Shear Strengthening of Reinforced Concrete Beams with Externally Bonded FRP Composites: Finite Element Modeling and Parametric Study

by

Amirali ABBASI

MANUSCRIPT-BASED THESIS PRESENTED TO ÉCOLE DE TECHNOLOGIE SUPÉRIEURE IN PARTIAL FULFILLMENT FOR THE DEGREE OF DOCTOR OF PHILOSOPHY
Ph.D.

MONTREAL, JANUARY 25, 2024

ÉCOLE DE TECHNOLOGIE SUPÉRIEURE
UNIVERSITÉ DU QUÉBEC

BOARD OF EXAMINERS

THIS THESIS HAS BEEN EVALUATED

BY THE FOLLOWING BOARD OF EXAMINERS

Mr. Omar Chaallal, Thesis Supervisor
Department of Construction Engineering at École de Technologie Supérieure

Mr. Georges El-Saikaly, Thesis Co-supervisor
Department of Construction Engineering at École de Technologie Supérieure

Mr. M. Hakim Bouzid, President of the Board of Examiners
Department of Mechanical Engineering at École de Technologie Supérieure

Mr. Amar Khaled, Member of the jury
Department of Construction Engineering at École de Technologie Supérieure

Mr. Hassan Aoude, External Evaluator
Department of Engineering, Faculty of Engineering, University of Ottawa

THIS THESIS WAS PRENSENTED AND DEFENDED

IN THE PRESENCE OF A BOARD OF EXAMINERS AND PUBLIC

ON JANUARY 3, 2024

AT ÉCOLE DE TECHNOLOGIE SUPÉRIEURE

ACKNOWLEDGMENTS

I would like to express my sincere appreciation to Professor Omar Chaallal who is a distinguished scholar, for accepting me as one of his PhD students and Georges El-Saikaly, my research co-supervisor, for their exceptional support and invaluable guidance during my PhD program. However, words cannot express my gratitude to my professors for their invaluable patience and feedback. I also could not have undertaken this journey without Professor Omar Chaallal and Georges El-Saikaly, who generously provided knowledge and expertise. I have been blessed with their continuous support to me during my PhD study; and for their patience, motivation and immense knowledge.

I would particularly like to thank Doctor Zine El Abidine Benzeguir who followed me and helped me throughout this research.

I would also like to thank Mr. Pier-Luc St-Onge (senior technicians) and calculquebec at École de technologie supérieure for their collaborations in conducting the numerical tests. Their continuous supports in my numerical program have assisted my research project and is highly appreciated.

The financial support of the Natural Sciences and Engineering Research Council of Canada (NSERC) and the Fonds de Recherche du Québec – Nature et Technologie (FRQNT) through operating grants is gratefully acknowledged.

Finally, I would like to acknowledge my family for their enduring support of me during my doctoral work and my dissertation.

Renforcement ā l'effort tranchant des poutres en béton armé avec des composites en PRF collés en surface: modélisation par éléments finis et étude paramétrique

Amirali ABBASI

RÉSUMÉ

La défaillance en cisaillement dans les poutres en béton armé (BA) a toujours été une préoccupation majeure pour les ingénieurs, en particulier dans les poutres profondes telles que les poutres en BA. Néanmoins, l'utilisation de composites en polymère renforcé de fibres (PRF) permet d'éviter ce type de défaillance. L'utilisation de composites PRF collés en surface (EB) pour le renforcement par cisaillement des poutres en BA exige une connaissance et une expérience suffisantes, compte tenu de la défaillance prématurée de la liaison, du comportement complexe de la couche d'interface entre les composites PRF et le substrat en béton, ainsi que de la mécanique de la rupture du béton non homogène. De nombreuses expériences ont été menées pour évaluer les contributions au cisaillement des EB-PRF pour le renforcement en cisaillement, même si les essais en laboratoire sont longs et coûteux. Cependant, en développant des modèles numériques et en obtenant des résultats de haute précision validés par les essais expérimentaux, les logiciels d'analyse par éléments finis sont devenus une alternative valable aux essais expérimentaux.

D'autre part, les modèles analytiques proposés dans les guides de conception existants ne sont pas compatibles avec les résultats obtenus à partir des essais expérimentaux, car de nombreux paramètres ne sont pas pris en compte dans ces modèles. Par exemple, l'interaction inverse entre les EB-PRF et les étriers en acier, l'effet d'échelle, les contraintes d'adhérence en cisaillement à l'interface entre le béton et les EB-PRF et entre les étriers en acier et le béton, les angles des fissures de cisaillement variant en fonction des renforts de cisaillement internes et externes, ainsi que la distribution des fissures de cisaillement conduisant à un décollement prématuré.

L'objectif de cette recherche est d'obtenir une compréhension approfondie de la charge maximale transférée par la couche d'interface et, par conséquent, de la charge ultime supportée par les poutres en BA renforcées en cisaillement avec des composites EB-PRF grâce à des approches analytiques et par éléments finis (FE). Les résultats obtenus à partir des méthodes susmentionnées seront validés avec des données expérimentales antérieures. Enfin, de nouvelles relations mathématiques seront proposées en tenant compte de tous les paramètres contribuant au renforcement par cisaillement des poutres en BA avec EB-PRF et au comportement de la couche d'interface. Pour cette raison, dans la première phase de cette recherche, une revue de la littérature est effectuée sur les recherches numériques précédentes pour évaluer leurs lacunes et leurs mérites dans la simulation des poutres susmentionnées. Cela nous permettra de mieux comprendre les hypothèses mises en œuvre dans ces études de recherche ainsi que le type d'analyse (statique ou dynamique).

Une simulation numérique est menée dans la deuxième phase de cette étude pour incorporer les paramètres ayant des influences essentielles sur les contributions au cisaillement des EB-PRF à la résistance ultime au cisaillement des poutres en BA renforcées à l'aide des EB-PRF. Ces paramètres comprennent l'effet d'échelle et l'interaction inverse entre les EB-PRF et les étriers en acier. Tous les résultats obtenus à partir des simulations numériques sont validés par les essais expérimentaux menées par l'équipe. Des études paramétriques sont ensuite réalisées pour obtenir les déformations effectives appropriées, plus proches de celles obtenues à partir des essais en laboratoire que des résultats analytiques.

Pour obtenir les déformations effectives appropriées, les résultats paramétriques sont évalués par régression des essais expérimentaux précédents. Des modèles analytiques pour les déformations effectives sont ensuite proposés pour combler l'écart entre les modèles existants dans les guides de conception, en tenant compte de la distribution des fissures de cisaillement et la distribution des contraintes sur les fibres interceptées par la fissure de cisaillement principale.

Mots-clés: structures en béton armé, feuille en PRFC, analyse par éléments finis, analyse analytique, renforcement par cisaillement, charges statiques, contrainte effective, couche cohésive, liaison PRF-béton, liaison étriers en acier-béton, distribution des contraintes, distribution des fissures de cisaillement, contrainte sur la fibre, contrainte sur les étriers en acier

Shear strengthening of reinforced concrete beams with externally bonded FRP composites: finite element modeling and parametric study

Amirali ABBASI

ABSTRACT

Shear failure in reinforced concrete (RC) beams has always been a major concern for engineers to deal with, particularly in deep beams such as RC girders. Nevertheless, with the use of fiber-reinforced polymer (FRP) composites, this type of failure can be avoided. Using externally bonded (EB) FRP composites for shear strengthening of RC beams requires sufficient knowledge and experience given the premature bond failure, the complex behavior of interface layer between FRP composites and the concrete substrate, as well as fracture mechanics of non-homogeneous concrete. Many experimental conducts have been carried out to evaluate the shear contributions EB-FRP in shear strengthening even though laboratory tests are time-consuming and expensive. However, by developing numerical models and obtaining high-precision results validated by experimental testing, finite element analysis softwares have become a valid alternative to experimental testing. On the other hand, the analytical models proposed in existing design guidelines are not consistent with the results obtained from experimental tests, as many parameters are not taken into account in these models. For example, the inverse interaction between EB-FRP and steel stirrups, the size effect, shear bond stresses at the interface between concrete and EB-FRP and between steel stirrups and concrete, shear crack angles varying with internal and external shear reinforcements, and the distribution of shear cracks leading to premature debonding.

The aim of this research is to have an in-depth insight into the maximum load transferred through interface layer and consequently, the ultimate load carried by RC beams strengthened in shear with EB-FRP composites through analytical and finite element (FE) approaches. The results obtained from the aforementioned methods will be validated with previous experimental data. Finally, new mathematical relationships will be proposed considering all the parameters contributing to the shear strengthening of RC beams with EB-FRP and the behavior of the interface layer. For this reason, in the first phase of this research, the literature-review is carried out on the previous numerical research to evaluate their deficiencies and merits in simulating the aforementioned beams. This will give us a better understanding of the assumptions implemented in these research studies, as well as the type of analysis (static or dynamic).

A numerical simulation is carried out in the second phase of this study to incorporate the parameters with essential influences on shear contributions of EB-FRP to the ultimate shear strength of RC beams strengthened using EB-FRP. These parameters include the size effect and the inverse interaction between EB-FRP and steel stirrups. All the results obtained from the numerical tests are validated through the experimental conducts. Parametric studies are then carried out to obtain the appropriate effective strains closer to those obtained from laboratory tests than from analytical results.

To obtain the appropriate effective strains, parametric results are evaluated by regression of previous experimental tests. Analytical models for the effective strains are then proposed to bridge the gap between the existing models in the design guidelines, taking into account the distribution of shear cracks and the distribution of stresses on the fibers intercepted by the main shear crack.

Keywords: RC structures, CFRP sheet, finite element analysis, analytical analysis, shear strengthening, static loads, effective strain, cohesive layer, FRP-to-concrete bond, steel stirrups-to-concrete bond, strain distributions, shear crack distribution, strain on fiber, strain on steel-stirrups

TABLE OF CONTENTS

Page

LIST OF TABLES

Page

LIST OF FIGURES

LIST OF ABREVIATIONS AND ACRONYMS

ACI	American Concrete Institute
ASCE	American Society of Civil Engineers
ASTM	American Society for Testing and Materials
AFRP	Aramid Fiber Reinforced Polymer
AVE	AVERAGE
BC	Brittle Cracking
CDP	Concrete Damage Plasticity
CEB	Comité Européen du Béton
CFRP	Carbon Fiber Reinforced Polymer
COH2D4	Four-node Cohesive Element
CNR	National Research Council
COV	Covariance
CSA	Canadian Standard Association
EB	Externally Bonded
EB FRP	Externally Bonded Fiber Reinforced Polymer
ETS	Externally Through-section Method
FIB	Fédération Internationale du Béton
FRP	Fiber Reinforced Polymer
FE	Finite Element
FEA	Finite Element Analysis
FEM	Finite Element Method
FIB	Fédération Internationale du Béton

GFRP	Glass Fiber Reinforced Polymer
HB	Design handbook for RC structures retrofitted with FRP and metal plates
JCI	Japanese Concrete Institute
JSCE	Japan Society of Civil Engineers
NES	Near End Supported
NSM	Near Surface Methods
RC	Reinforced Concrete
STD	Standard deviation of the data set
T2D2	Two-node 2D Truss elements

LIST OF SYMBOLS AND UNITS OF MEASUSERMENT

A_{FRP}	Area of the cross section of a FRP sheet or strip= $2n.t_f.w_f$
A_{fv}	Area of the cross section of a FRP sheet or strip= $2n.t_f.w_f$
b_w	Effective width of beam
d	Effective depth of the beam
d_f	Effective depth of FRP
d_{FRP}	Distance from the extreme compression fiber to the centroid of tension
d_f	Distance from the extreme compression fiber to the centroid of tension
D_{frp}	Stress distribution factor
$d_{frp,t}$	Distance from the compression face of beam to the top edge of the FRP
d_{fv}	Effective depth of FRP shear reinforcement, in. (mm)
E_a	Elasticity modulus of cohesive layer
E_c	Elasticity modulus of cohesive concrete
E_f	Elasticity modulus of FRP
E_f	Elastic modulus of FRP in the principal fiber-orientation direction
E_{FRP}	Young’s modulus of the FRP
E_s	Elastic modulus of steel stirrups rebars
F_{bsm}	Bond force per length
f_{bsm}	Mean bond stress of reinforcing steel
f_c'	Cylinder compressive strength of concrete
f_{ck}	Concrete characteristic cylinder strength
$f_{f,e}$	Average stress of FRP crossed by the shear crack
f_{dd}	FRP-to-concrete bond strength
f_{ed}	Effective debonding strength
f_{fed}	Design value for the FRP effective stress
F_{frp}	Force within the FRP composites at the ultimate limit
f_{ctm}	Concrete mean tensile strength
f_{cm}	Mean compressive strength of concrete
f_{fbwd}	Strength of the fibre reinforcement

$f_{fwd,c}$	Bond strength
f_{fwd}	The load-bearing capacity of three-sided FRP
f_{fbk}	Characteristic maximum bond strength
f_{fu}	Ultimate FRP tensile stress
G_a	Shear modulus for adhesive layer
G_c	Concrete shear modulus
G_f	Facture energy of the FRP-to-concrete bonded interface
$h_{f,e}$	Effective height of the FRP sheets/plates on the web of the beam
h_w	Beam web depth
K	Shear reinforcing efficiency of continuous fiber sheets coefficient
k_1	Concrete-strength modification factor
k_2	Wrapping-scheme modification factor
K_b	Covering/scale coefficient
K_p	Factor related to the width of the bonded plate and the width of the concrete
k_v	Bond-reduction coefficient
K_{nn}	Stiffness failure mode 1
K_{ss}	Stiffness of shear direction failure mode 2
K_{tt}	Stiffness of shear direction failure mode 3
K_{vb1}	Parameters of bond conditions
K_{vb2}	Parameters of bond conditions
L_e	Effective anchorage length of FRP
l_e	Effective bond length of FRP strips
l_e	Maximum bond length
$l_{e,0}$	Transfer length of the reinforcing steel
$l_{t,max}$	Anchorage length required to develop the full anchorage capacity
m	Number of strips for which the bond length is less than effective bond length
M_{cr}	Cracking moment
n	Number of strips crossed by the shear crack
n_f	Number of EB-FRP layers

$n_{s,i}$	Number of steels rebars
p_f	FRP centre-to-centre spacing measured orthogonally to the fiber orientation
R	Reduction factor
R^2	Ratio of FRP effective width to total FRP width
r_c	Corner radius of the section to be wrapped
R_{ck}	Concrete characteristic cubic strength
S_f	Center-to-center spacing of the FRP strips
s_{FRP}	Spacing of externally bonded FRP bands on concrete (mm)
S_r	Prediction of the crack spacing for reinforced concrete members
t_a	Thickness of cohesive layer
t_c	Thickness of concrete substrate detached in debonding mode
t_f	Thickness of EB-FRP
t_{FRP}	Thickness of FRP composite
V	Ultimate shear capacity of EB-RC beam
V_c	Shear contribution of concrete
V_s	Shear contribution of steel stirrups
V_f	Shear contribution of FRP
V_{fcal}	Contribution of FRP to shear as calculated by models
V_{fd}	Design value for the ultimate FRP stress
V_{fdd}	Design value for the FRP debonding stress
V_{fexp}	Experimental contribution of FRP to shear
$W_{C,0}$	Section modulus of the uncracked concrete cross section
w_f	Width of the FRP strips in the direction normal to the fibre orientation
$w_{f,e}$	Effective width of FRP sheet (for discrete FRP strips)
z	Lever arm length (generally may be set to d/1.15)
z	Internal lever arm
Z_b	Upper edge to the effective FRP(0.9d)
Z_t	Lower edge of the effective FRP
$Z_{rid.eq}$	Vertically projected length of the FRP strip, minus the effective bond length

α	Orientation of Fibers to horizontal axis of beam
β	Angle of the fiber direction
β_c	Concrete-cracking coefficient based on transverse-steel and FRP rigidity values
β_L	Coefficient to compensate for insufficient FRP anchorage length
β_w	FRP-width-to-spacing-ratio coefficient
γ_{fb}	Safety factor
γ_{rd}	Partial factor for the resistance model
ε_{fe}	Effective strain of FRP
$\varepsilon_{frp,e}$	Effective strain in FRP
ε_{fu}	Tensile strain in FRP at failure
$\varepsilon_{frp,u}$	FRP rupture strain
θ	Orientation of shear crack
$\sigma_{f,max}$	Maximum stress that can be reached in the FRP strips intersected by shear crack
ρ_f	FRP strengthening ratio = $\left(2n.\frac{t_f}{b}\right).(w_f/S_f)$
ρ_s	Transverse-steel ratio= $A_v/(b_w.s)$
ρ_{frp}	Ratio of steel stirrups
τ_{eff}	Average bond shear stress at failure
τ_{b1k}	Characteristic values of the shear strength
ϕ_{FRP}	Resistance factor for FRP components
$\emptyset_R$	Reduction factor due to local stress in corners
$\emptyset_{s,i}$	Diameter of steels rebars

INTRODUCTION

Shear failure in reinforced concrete (RC) beams has been a longstanding concern in structural engineering due to its complex behavior under loading and its tendency to brittle rupture without warning. As a result, structural engineers often prioritize understanding the sequence in which flexural failure occurs before shear failure. The absence of sufficient shear strength in RC beams can be attributed to various interrelated factors. Underestimating the real loads in the design process, lack of accuracy in the construction phase, natural disaster due to winds and earthquakes are examples of such factors. In recent years, the use of fiber reinforced polymer (FRP) composites has become a mainstream in the construction industry. FRP composites have high strength in tension, which can compensate for the shear and tensile deficiencies of RC beams. Researchers have applied various configurations of FRP sheets and bars through the common approach of bonding FRP sheets to the surface of RC beams, namely, externally bonded (EB) method. However, the lack of the numerical studies, expensive, and time-consuming laboratory tests may explain the existence of divergence between the experimental results and models offered by existing guidelines. The results obtained from finite element analysis (FEA) are extensive and can provide a better insight into the behavior of bond, which include evaluation of the response of interface layer, strain on all the fibers, prediction of the right angle of shear cracks, distributions of shear cracks, determination of the failure mode such as debonding and delamination of fibers, and plenty more outcomes during loading process. Therefore, some of the essential parameters affecting the shear contribution of EB-FRP include inverse interaction between EB-FRP and steel stirrups with respect to their proportion, size effect, shear stress on bond between contrite-to-EB-FRP as well as bond between steel stirrups-to-concrete, right angle of shear cracks variating based on internal and external shear reinforcements, and distribution of shear cracks leading to premature debonding. The current research study concentrates on the numerical investigations on the size effect, inverse interaction between EB-FRP and steel-stirrups, and distributions of shear cracks as the ratios of external shear reinforcement-to-internal shear reinforcement increases under static load. This publication aims to develop analytical models by incorporating the parameters, less employed in the literature and introduce new effective strains to solve the complexity of shear contributions of EB-FRP during propagations of shear cracks and size effects through the numerical tests. The following chapters represent a sketch of content debated in the existing research study:

- Chapter 1 provides an elucidation of the context through a description of the problem and research objectives, and discusses the methodology employed for the current study.

- Chapter 2 involves the assessment of existing design models found in guidelines, examining both their strengths and weaknesses. Furthermore, this chapter includes a comprehensive review and evaluation of previously proposed models from the literature that pertain to the enhancement of shear capacity in RC beams using EB-FRP strengthening techniques.

- Chapter 3 focuses on an article entitled "Shear Strengthening of RC Beams with FRP Composites: Database of FE Simulations and Analysis of Studied Parameters." The primary objective of this chapter is to compile a comprehensive database encompassing all studies that have employed finite element analysis (FEA) to investigate the shear strengthening of RC beams using EB-FRP composites. Furthermore, this chapter aims to assess the strengths and weaknesses of these studies by analyzing various parameters that were studied in their respective analyses.

- Chapter 4 presents the findings in an article entitled "FE Modeling and Simulation of the Size Effect of RC T-Beams Strengthened in Shear with Externally Bonded FRP Fabrics." This chapter delves into the results of a nonlinear finite element numerical study conducted on nine RC beams that underwent shear strengthening using EB-CFRP composites. These beams were tested in a laboratory setting under three different series. The study aims to meticulously examine the impact of various factors, including the response of the interface layer, the strain distribution along the fiber, and the fibers intersected by the main diagonal shear crack, on the size effect observed in the beams. The research also explores failure modes, load-deflection responses, and the pattern of shear cracks. One notable aspect of this study is its focus on investigating the size effect using finite element analysis and revealing the development of shear stress and strain in the interface layers and fibers during the loading process. Additionally, by analyzing the strain distribution curve on the fibers intercepted by the main shear crack, the study aims to quantify the distribution factor responsible for the effective strain experienced. This effective strain differs significantly from the values typically recommended in codes and guidelines.

- Chapter 5 discusses the findings from an article entitled "Inverse Interaction between Steel Stirrups and EB-CFRP in RC Beams Strengthened in Shear: Development of Analytical and Numerical Models." This chapter consolidates previous experimental results and conducts advanced nonlinear numerical tests to develop an analytical model for reinforced concrete (RC) beams strengthened in shear with externally bonded carbon fiber reinforced polymer (EB-CFRP). This model accounts for the negative inverse interaction that occurs between the steel stirrups and EB-CFRP as the ratios of EB-CFRP to steel stirrups increase. The study proposes reliable effective strains by considering this interaction parameter, which enhances the accuracy of calculating the shear contribution of the EB-CFRPs. The results are presented in various aspects, including shear crack patterns, load-midspan deflections, shear stresses, strain responses along the fibers, maximum strain profiles for all the CFRPs and specimens, applied shear forces-strain relationships for both steel stirrups and EB-CFRPs, and the interactions between steel stirrups and EB-CFRPs. These interactions are based on their respective maximum strain contributions at the point of maximum shear forces and the maximum strain they experience after shear failures.

In conclusion, the findings from this thesis project, along with recommendations for potential future research endeavors, are consolidated and presented, respectively.

CHAPTER 1

DESCRIPTION OF RESEARCH

1.1 Context

In North America, a significant portion of engineering structures, particularly reinforced concrete (RC) bridges that are still in operation, were built during the period spanning from 1960 to 1980. Currently, more than one-third of these bridges fall into the categories of being either structurally deficient or functionally obsolete. This classification is based on evaluating the condition of their structural components and their ability to meet modern design standards. These evaluations utilize a thorough assessment approach that incorporates condition and functionality indices as the benchmark criteria (El-Saikaly, 2015).

1.1.1 Shear cracks and shear strengthening with externally bonded FRP

The behavior of RC beams strengthened in shear using FRP composites is influenced by various parameters, making it a complex and challenging area of study. Some of these parameters include:

(a) Cross section, (b) Size effect, (c) Interface (concrete-to-FRP), (d) Interface (concrete-to-steel stirrups), (e) Crack shape function, (f) Types of configurations in shear, (g) different FRP materials, (h) Concrete strength, (i) Ratio of longitudinal steel reinforcements ρ_w, steel stirrups ρ_s, to those of EB-FRP ρ_{FRP}, (j) Types of the failure (debonding, delamination, rapture), (k) Interaction between Components, etc.

Shear-Strengthening Techniques: The method used for applying FRP composites, such as U-bonded, side-bonded, or fully wrapped, can significantly affect the shear performance of the beam. Despite extensive research, there is no unanimous agreement on a single design model for evaluating the shear contribution of Externally Bonded (EB) FRP composites. This complexity is acknowledged in industry standards. Currently, two main approaches are used for shear evaluation:

a) a) Simplified Hypothesis: This approach assumes that each component of the beam (concrete, stirrups, longitudinal bars, and FRP composites) contributes separately to the shear strength. The total shear resistance (V) is calculated as the sum of the contributions from these components:

$$V = V_c + V_s + V_f \tag{1.1}$$

V_c and V_s are calculated based on established codes and standards for reinforced concrete structures.

The challenge lies in accurately calculating the contribution of FRP composites (V_f) to the shear strength of EB RC beams.

b) Experimental Tests: This method involves conducting physical tests on shear-strengthened RC beams to determine their actual shear capacity. These tests provide valuable empirical data but can be resource-intensive and time-consuming.

In summary, the behavior of RC beams strengthened in shear by FRP composites is influenced by several factors, and hence there is ongoing research to develop reliable design models that consider the complex interaction of these components. The choice between a simplified approach and experimental testing depends on the specific project requirements and available resources.

1.1.2 Shear strengthening configurations

Externally bonded fiber reinforced polymer is a common method for boosting the shear strength of RC beams. FRP sheets/plates are normally attached to the web of the RC beams. As a result, they can compensate for the shear deficiency of the RC beams when diagonal shear cracks emerge in the web of beams. Initially, the FRP strips are inactive before the occurrence of cracking. With the appearance of cracking, FRP composites contribute to the shear strengthening alongside stirrups and concrete. In addition, these FRP composites can be attached to the bottom of beam to resist flexural tension of RC beams. In this technique of shear strengthening, FRP composites are attached to the surface of RC beams via resin epoxy.

They can be attached in the form of either continuous or non-continuous (separate) strips. When used in separate configuration these strips can be positioned with different orientation depending on the angle of shear cracks. Also, fully wrapped, and U-shaped methods are classified in this category. Nevertheless, the fully-wrapped method is not a common approach for shear-strengthening of current RC beams due to the restriction in practical applications. Indeed, the bond interface layer plays a crucial role in the ultimate strength of proposed beams. Ahmed Godat et al. (2013) and Valerio et al. (2009) conducted research on Embedded through-section technique effective way of boosting shear-strengthening of RC FRP beams in comparison to other methods employed. Because common failure in RC beams strengthened with FRP composites is debonding between FRP composites and concrete, this technic is an appropriate substitution to the other methods of shear strengthening by FRP. The debonding failure is considered as a drawback in RC FRP beams strengthened by external FRP composites since it triggers the failure of such structures before reaching the full capacity of their rehabilitation systems. Unlike other measures of shear strengthening of RC beams externally strengthened using FRP composites, externally through-section method technique (ETS), FRP bars pass through the core of drilled concrete in which debonding is not concerning issue because of the strong bond between concrete and FRP bars (Figure 1.1). Furthermore, due to the fact that the concrete core is stronger than its surface, more confinement is expected from this bond compared to externally bonded (EB) methods. Simple installation and high efficiency are some of the merits of this method. The only drawback associated with this approach is that the strength of concrete reduces because of the damage caused by drilling the hole. However, it can be minimized if whole of the procedure of drilling is performed based on the CSA/S806-02 codes of practice. More finite element analysis by software is required to comparing FE with experimental results.

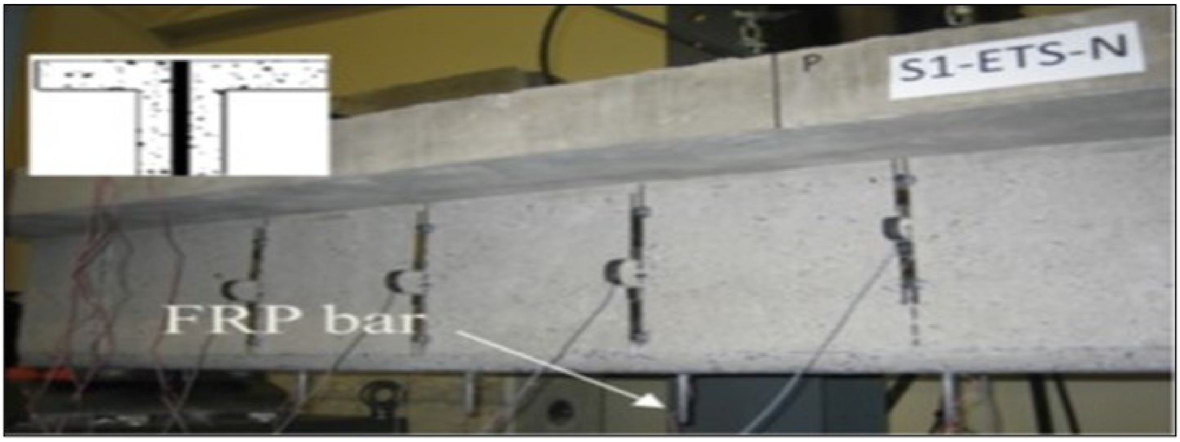

Figure 1.1 Shear strengthening of reinforced concrete beams via ETS approach
Taken from Ahmed Godat et al. (2013)

Even though the near-surface Methods cannot enhance shear strengthening of RC beams as much as ETS approach, the probability of debonding in this method is less than externally bonded techniques. Furthermore, as FRP RC beams are not homogenous structures in terms of materials, it is obvious that failure and yielding in materials do not take place at the same time. It means that steel stirrups cannot contribute to bearing external load and without reaching their ultimate capacity, failure occurs. NSM approach turns out to be a fruitful technique to improve contribution of steel stirrups and FRP Bars in bearing shear tensions in RC beams. As a matter of fact, ductility, shear-strengthening as well as strong bond are some of merits of this approaches which highlight it in comparison to externally bonded (EB) method. Overall layout and details of NSM methods and arrangement of materials toward each other are shown in Figure 1.2.

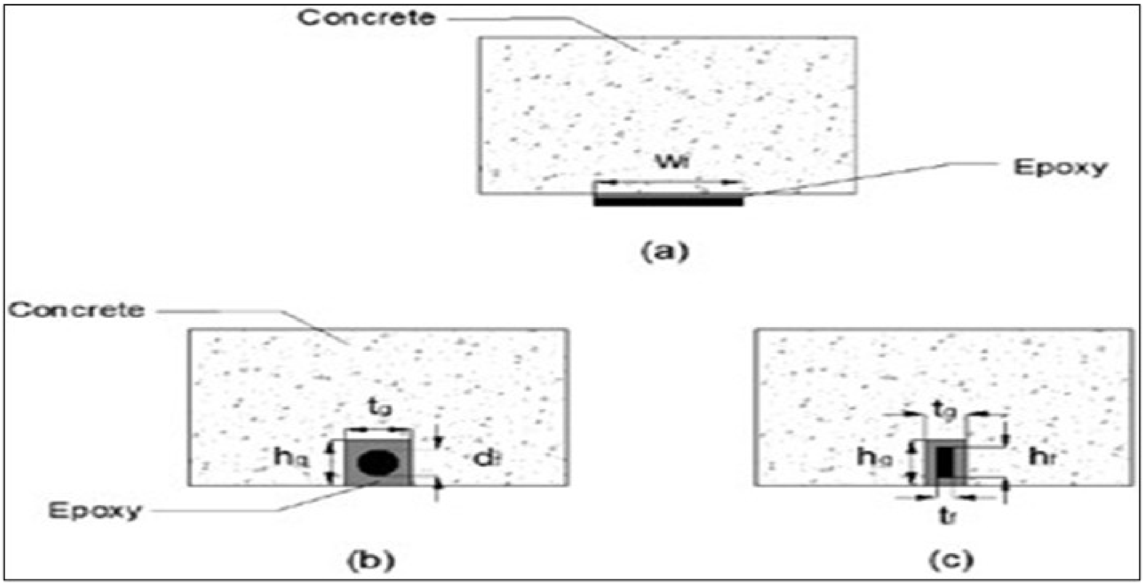

Figure 1.2 Detail of installation FRP bars in RC beam
Taken from Parvin and Syed Shah (2016)

1.1.3 Failure modes in RC beam strengthened with EB-FRP

By adopting traction-separation law in the ABAQUS, it is possible to assign the parameters of Lu et al. (2005) 's FRP-to-concrete bond-slip relationship to the cohesive layer already defined as an interface layer. Since the interface layer is subjected to three modes of failure shown in Figure 1.3, the envelope of all three modes has to be defined into the ABAQUS.

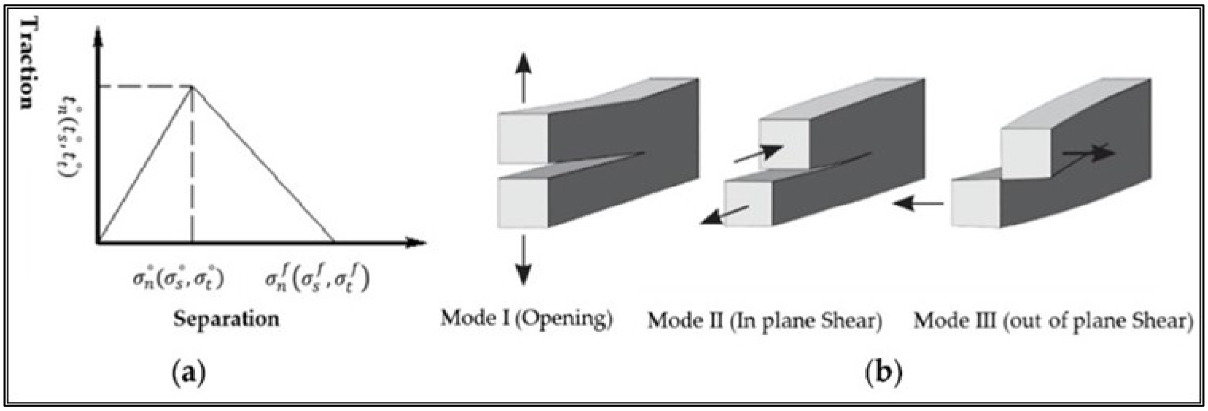

Figure 1.3 Traction-separation envelope exiting in ABAQUS (a) and modes of failure at interface layer (b)
Taken from Hokelekli and Yilmaz (2019)

As can be shown in Figure 1.4 typical bilinear traction-separation law in the ABAQUS has three parts that have to be specified by the users, which are initial stiffness, initiation of the damage, and damage evolution.

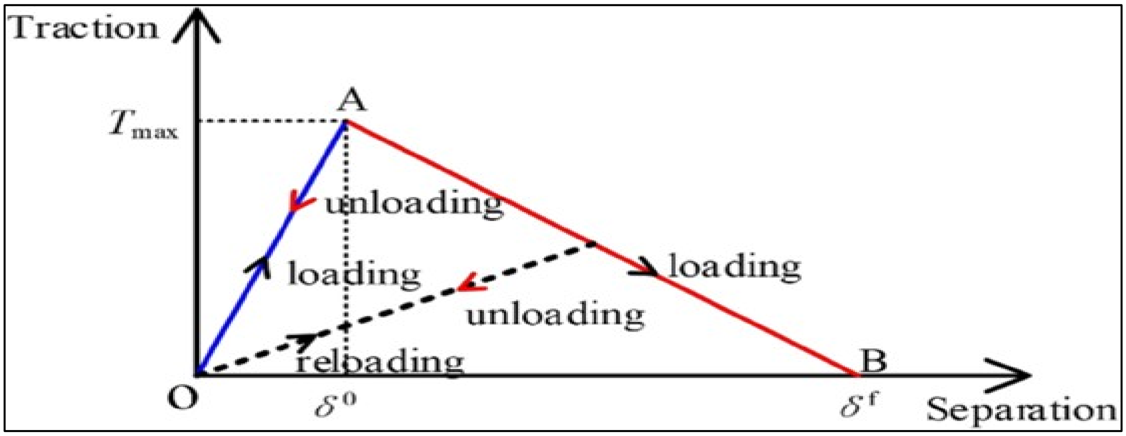

Figure 1.4 Typical damage-separation law envelope
Taken from Fang et al. (2023)

This damage-separation curve has to be defined in all three modes of failure in the ABAQUS since all these three modes have an effect on the final response of interface layer between concrete and CFRP plate (Figure 1.5).

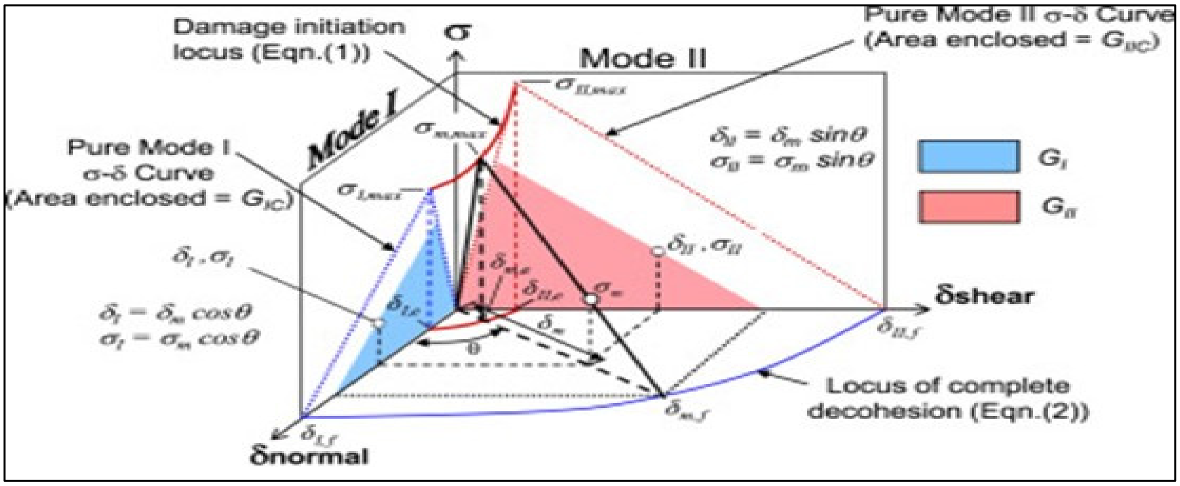

Figure 1.5 Typical traction-separation envelope for the all-failure modes
Taken from Harper and Hallett (2010)

In order to calculate the stiffness of this curve in the normal direction, the model proposed by Guo et al. (2005) was applied as follows:

$$K_{nn} = \frac{1}{{t_a}/{E_a} + {t_c}/{E_c}} \tag{1.2}$$

where E_a is the elasticity modulus, t_a is the thickness of the adhesive layer, E_c is the elasticity modulus and t_c is the thickness of concrete.

To calculate the stiffness in the two shear directions corresponding to failure mode2 and mode3, following model was employed:

$$K_{ss} = K_{tt} = \frac{1}{{t_a}/{G_a} + {t_c}/{G_c}} \tag{1.3}$$

Where G_a is the shear modulus, t_a is the thickness of the adhesive layer, G_c is the shear modulus and t_c is the thickness of concrete. In the following section, the theory of traction-separation law will be elaborated.

1.2 Problem statement

Reinforced concrete (RC) is a versatile composite and one of the most widely used materials in modern construction. Concrete is a relatively brittle material that is strong under compression but less so in tension. Concrete infrastructures entail constant maintenance and rehabilitation due to the deterioration of concrete and steel bars, structural damage, and insufficient ductility. Therefore, maintenance of these infrastructures is of paramount importance to the engineers.

These deteriorations give rise to a reduction of strength in these structures and failing to withstand service load. In the past years, the retrofitting of existing RC beams was carried out by conventional materials. Steel plate jacketing and section enlargement by shotcrete were among common techniques to enhance shear strength of existing deficient RC beams. However, these techniques are both costly and difficult to execute. FRP composites have taken the place of conventional methods since they have reduced the cost of rehabilitation in these beams. Ever since fiber reinforced polymers were introduced as retrofitting materials, their application in the construction industry has grown due to their high strength to weight ratio, high tensile strength and resistance to corrosion. Having said that, their interaction with reinforced concrete structures is convoluted when it is used for shear strengthening of existing RC beams. Furthermore, the design codes are based on experimental conduct, not covering all the parameters having an influence on the interaction between concrete and FRP plates and sheets. Indeed, the behavior of RC beams strengthened in shear with FRP plates and sheets has not been fully documented because all the experimental, simulating, analytical and numerical conducts have been based on simplified pull-off test not considering the behavior of the interface layer between concrete and FRP composites when FRP composites are applied for shear strengthening of RC beams. Moreover, previous studies did not consider fracture mechanic of concrete when interface layers were subjected to shear stresses in two directions. Therefore, the common pull-off test cannot capture the whole process of debonding between concrete and FRP composites when FRP plates and sheets are employed for shear strengthening of RC beams leading to incomplete results. Combined stress field at the interface layer and fracture mechanic of concrete are two main components affecting the outcome of the analysis. Given the fact that various techniques for EB shear strengthening configurations (vertical and inclined strips, continuous sheets, L and U-shaped plates) have been introduced, having a different interaction with the concrete substrate, current codes and standards are not able to offer comprehensive solutions for upgrading existing RC beams strengthened in shear with FRP plates and sheets. Therefore, an accurate design model, validated with FEA and experimental tests with the inclusion of influencing factors is clearly a need in current codes and standards.

1.3 Research objectives

Due to the shortage of the numerical study in the field of RC beams strengthened in shear with EB-FRP, the present research study aims to carry out a FEA while proving its efficiency in terms of time and cost in comparison with experimental conducts without compromising the accuracy of results. Furthermore, this study intends to develop a numerical simulation of the aforementioned beams and finally, develop an analytical model accounting for the shear contribution of EB-FRP through a parametric study.

1.3.1 Main objective

The research aims to propose a comprehensive analytical and numerical models for the shear resistance of RC beams strengthened using EB-FRP plates/sheet (Figure 1.6). While existing studies have improved shear strengthening methods, a more inclusive model considering all shear failure modes and strengthening schemes is needed. The interaction between FRP sheets and plates will be extensively studied using advanced FE methods. This includes addressing challenges related to the interaction between FRP composites and concrete, as well as the inverse interaction between EB-FRP and steel stirrups. Various influencing factors on the behavior of the interface layer will be explored, such as fracture mechanics of concrete, dimensions, and FRP composite configuration. The study seeks to determine the impact of these factors on the interface layer's behavior and, consequently, the ultimate load-carrying capacity of beams. New theoretical and mathematical approaches will be developed to replace current design models in codes and standards, providing a more comprehensive design method for practicing engineers. The proposed approaches are anticipated to enhance current design models in codes and standards by considering all relevant parameters.

1.3.2 Specific objectives

- To develop advanced precise numerical models and realistic assumptions for simulation of existing RC beams strengthened in shear with EB-FRP using FE software.
- To perform parametric numerical analysis on inverse interaction between EB-FRP and steel stirrups to evaluate the maximum stress transferred trough the bond between concrete and EB-FRP as the ratio of external shear reinforcement (EB-FRP) to internal shear reinforcement (steel stirrups) increases.

- To investigate the effect of maximum shear stress on bond between concrete and EB-FRP as well as concrete and steel stirrups. In addition to consider the maximum strain experienced by EB-FRP and steel stirrups at ultimate states in order to develop new closed form model based on aforementioned parameters.
- To propose new models for North American design codes for RC beams strengthened in shear with EB-FRP.
- To consider the size effect on the contribution of EB-FRP based on interfacial shear stress and strain profile along the direction of fibers.

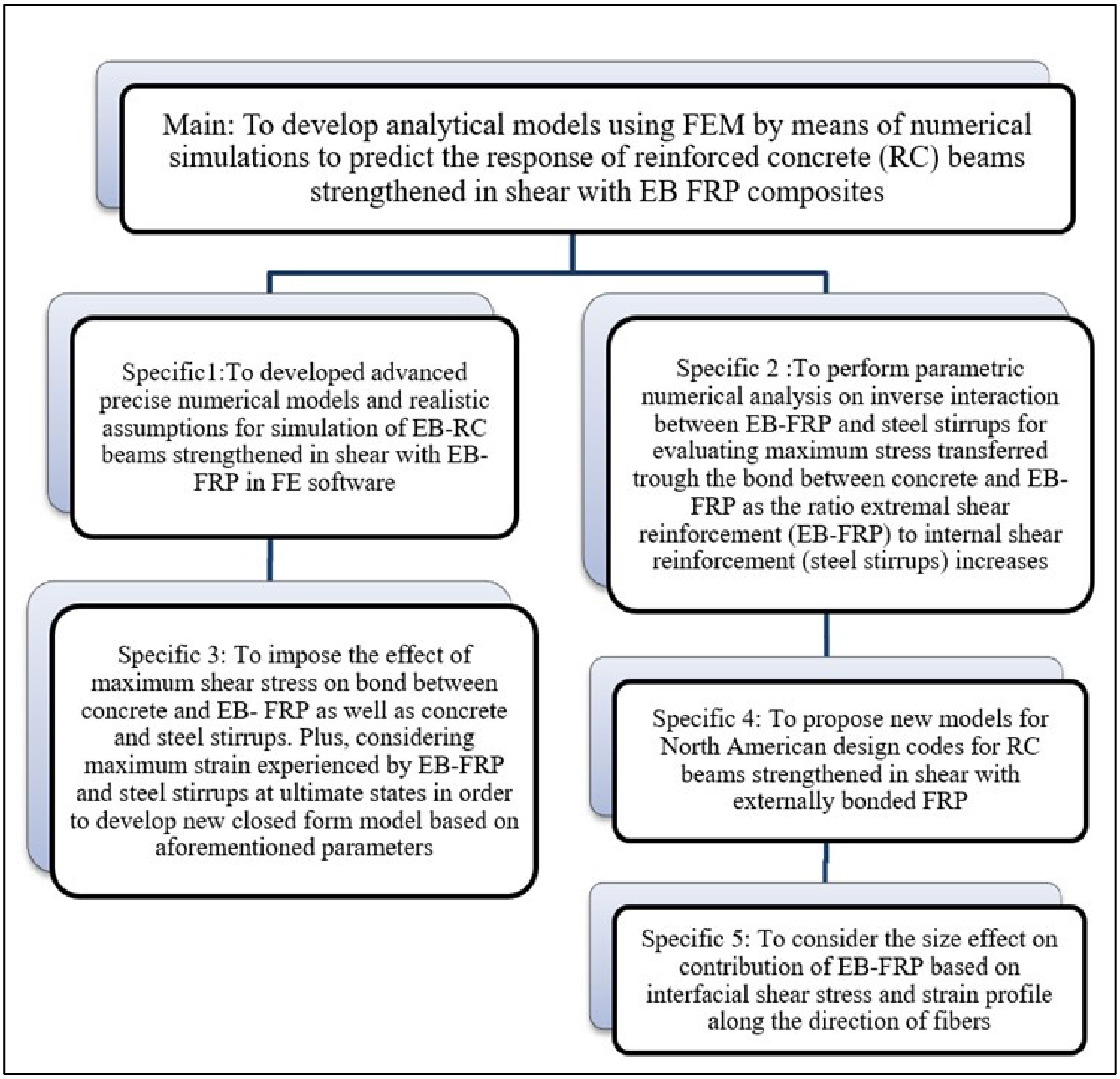

Figure 1.6 Research objectives

1.4 Methodology

Figure 1.7 illustrates the methodology employed in the present research study. Despite the fact that the laboratory tests are integral parts to evaluate the response of RC beam strengthen with EB-FRP, an array of features from above-mentioned beams are ambiguous through conducting laboratory studies. The proposed research follows a scientific procedure aimed at obtaining the results validated with available database in the literature. In this research study, the implementation of FEA models is reliable and less time-consuming option compared to experimental research demonstrating to achieve higher recognition of response of RC beams strengthened with EB-FRP. FEA models enable to develop parametric conducts resulting in creating more comprehensive data and enhancing accountable design model that reliably captures the shear contribution of EB-FRP to the ultimate load-carrying capacity of the above-mentioned beams. The two influencing parameters affecting the shear contribution of EB-FRP and where there is lack of numerical research studies are the size effect and inverse interactions between steel-stirrups and EB-FRP. Also, this research study is aimed to bridge the gaps between experimental and numerical studies due to limited numerical research. It starts with reviewing all the research regarding codes and standards of some countries about shear strengthening of RC beams with FRP composites, bond-slip law, behavior of interface layer between concrete and EB-FRP, fracture mechanic of concrete, constitutive models of FE software about simulating behavior of interface layer and concrete damage parameters.

For this reason, in the first section of this research study nine specimens are selected for the evaluation of the size effect. The study focuses on assessing the effectiveness of using EB-FRP for strengthening RC-T beams of various sizes and comparing the performance of strengthened beams to control beams through simulation and experimental testing. The goal is likely to provide insights into the behavior and performance of these beams under different strengthening conditions. There has been significant advancement in numerical models, enabling them to accurately capture various aspects, such as the interfacial shear stress along the bond, the strain profile along the fibers, and the normalized main diagonal shear cracks. The outcomes of a nonlinear finite element (FE) numerical investigation conducted on nine reinforced concrete (RC) beams that underwent shear strengthening using EB-CFRP composites. These beams were subjected to laboratory testing, grouped into three series, each comprising RC beams of different sizes (small, medium, and large) but geometrically similar. The findings demonstrate that numerical simulations exhibit a high level of accuracy in predicting experimental results. Additionally, they validate that as the size of the beams increases, both the shear strength of concrete and the contribution of CFRP to shear resistance decrease.

Another parameter where there is lack of analytical and numerical investigation is the inverse interaction between steel-stirrups and EB-FRP. This research considers both experimental and numerical testing methods to formulate an analytical model designed for reinforced concrete (RC) beams shear strengthened using EB-CFRP. Special attention is given to studying the adverse inverse relationship that arises between the steel stirrups and EB-CFRP as the ratios of EB-CFRP to steel stirrups increase. Notably, this particular interaction is not accounted for in the design models outlined in most existing guidelines, despite its significant impact on the shear resistance as projected by these guidelines.

Most current design guidelines do not account for this interaction, even though it significantly impacts the shear resistance predicted by these guidelines. Specifically, the contribution of EB-CFRP to shear resistance decreases as the ratio of EB-CFRP to steel stirrups increases. Therefore, proposing accurate effective strains by incorporating this parameter enhances the calculated shear contribution of EB-CFRPs.

To address this, an analytical model is introduced for determining the effective strain of CFRP, taking into consideration the inverse interaction between EB-CFRP and steel stirrups. Subsequently, this proposed model is validated using experimental data through a parametric study that explores the increasing trends in the EB-CFRP-to-steel-stirrups ratio. Additionally, a numerical finite element model is presented to calculate the reduction factor and the corresponding effective strain, accounting for the inverse interactions between EB-CFRPs and steel stirrups. These results are then compared against various existing guidelines.

The findings are presented in terms of shear crack patterns, midspan deflections under load, shear stresses, strain responses along the fibers, maximum strain profiles for all CFRPs and specimens, applied shear forces-strain relationships for both steel stirrups and EB-CFRPs, and the interactions between steel stirrups and EB-CFRPs based on their maximum strain contributions at the point of maximum shear forces and the maximum strain they endure after shear failures. Figure 1.7 and Figure 1.8 display both the simulating and analytical framework and flowchart and the assessed variables.

Figure 1.9 a-c and Figure 1.10 a-d demonstrate schematic two and three-dimensional models simulated in ABAQUS programme to investigate the size effect and the inverse interaction between steel stirrups and EB-FRP. After simulating the specimens, they are validated with experimental tests in terms of pattern of shear cracks, load-deflection curves, maximum strains on steel stirrups and EB-FRP.

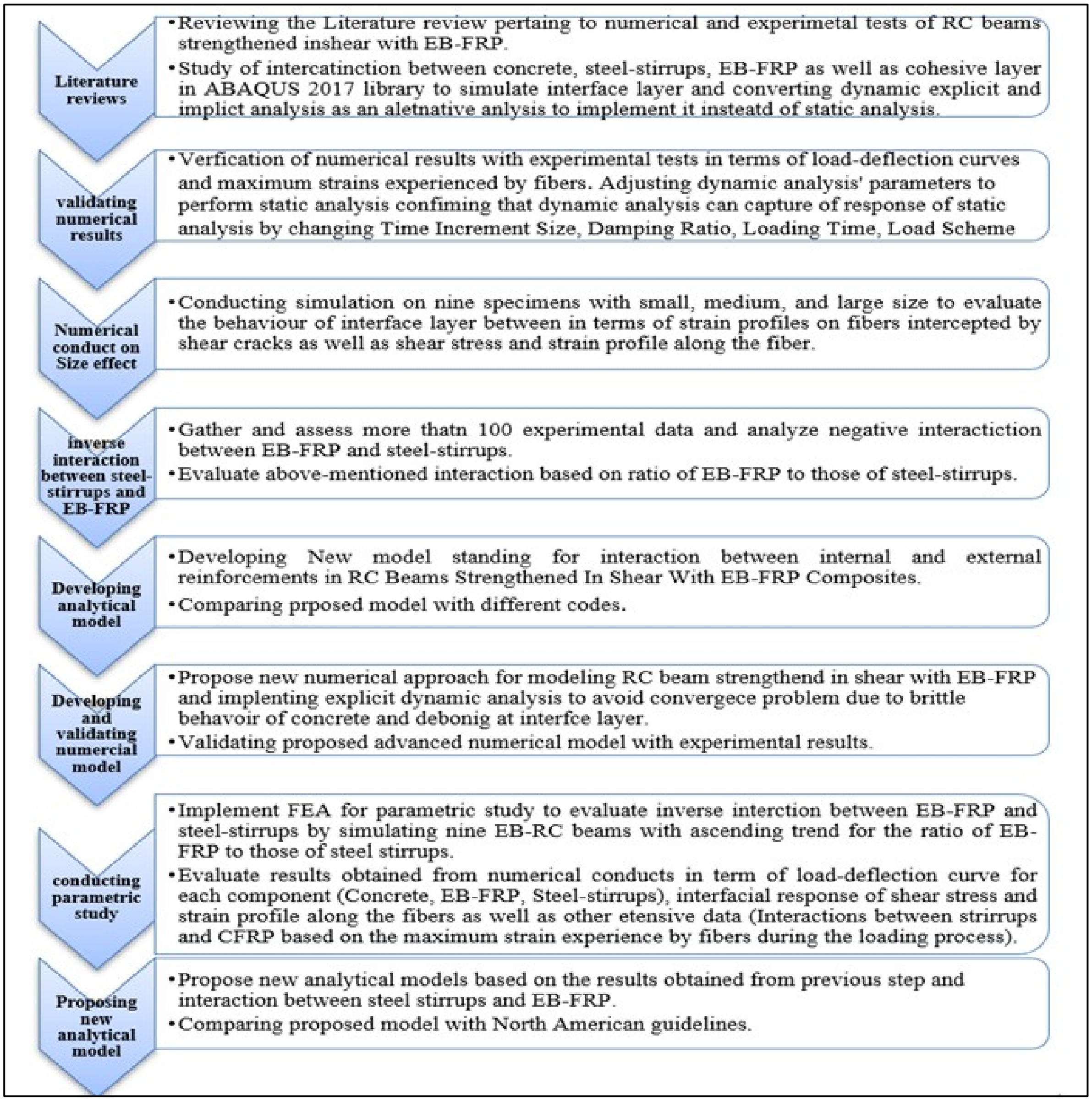

- Reviewing the Literature review pertaing to numerical and experimetal tests of RC beams strengthened inshear with EB-FRP.
- Study of intercatinction between concrete, steel-stirrups, EB-FRP as well as cohesive layer in ABAQUS 2017 library to simulate interface layer and converting dynamic explicit and implict analysis as an aletnative anlysis to implement it insteatd of static analysis.

- Verfication of numerical results with experimental tests in terms of load-deflection curves and maximum strains experienced by fibers. Adjusting dynamic analysis' parameters to perform static analysis confiming that dynamic analysis can capture of response of static analysis by changing Time Increment Size, Damping Ratio, Loading Time, Load Scheme

- Conducting simulation on nine specimens with small, medium, and large size to evaluate the behaviour of interface layer between in terms of strain profiles on fibers intercepted by shear cracks as well as shear stress and strain profile along the fiber.

- Gather and assess more thatn 100 experimental data and analyze negative interactiction between EB-FRP and steel-stirrups.
- Evaluate above-mentioned interaction based on ratio of EB-FRP to those of steel-stirrups.

- Developing New model standing for interaction between internal and external reinforcements in RC Beams Strengthened In Shear With EB-FRP Composites.
- Comparing prposed model with different codes.

- Propose new numerical approach for modeling RC beam strengthend in shear with EB-FRP and implenting explicit dynamic analysis to avoid convergece problem due to brittle behavoir of concrete and debonig at interfce layer.
- Validating proposed advanced numerical model with experimental results.

- Implement FEA for parametric study to evaluate inverse interction between EB-FRP and steel-stirrups by simulating nine EB-RC beams with ascending trend for the ratio of EB-FRP to those of steel stirrups.
- Evaluate results obtained from numerical conducts in term of load-deflection curve for each component (Concrete, EB-FRP, Steel-stirrups), interfacial response of shear stress and strain profile along the fibers as well as other etensive data (Interactions between strirrups and CFRP based on the maximum strain experience by fibers during the loading process).

- Propose new analytical models based on the results obtained from previous step and interaction between steel stirrups and EB-FRP.
- Comparing proposed model with North American guidelines.

Figure 1.7 Methodology of the doctoral research project

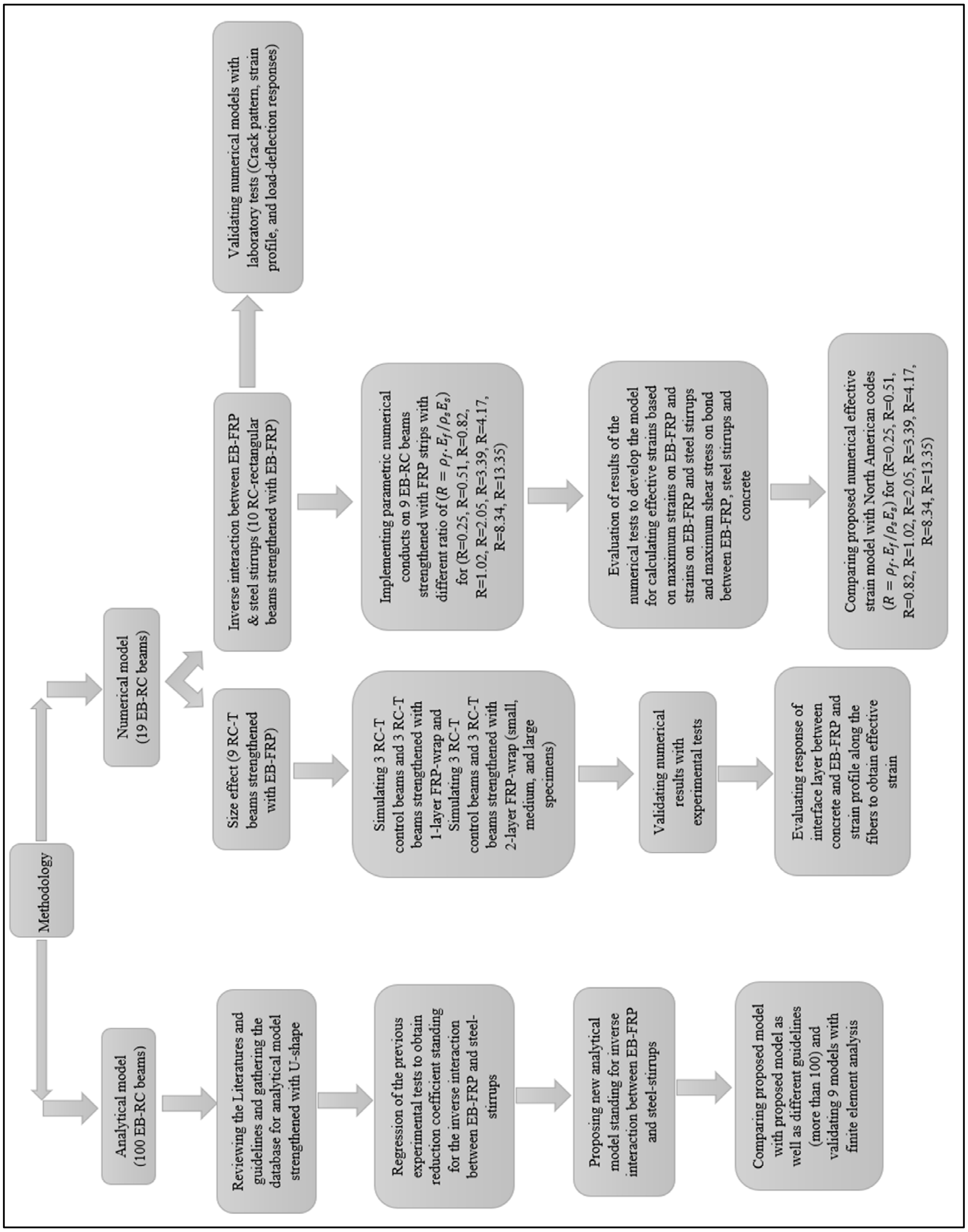

Figure 1.8 Numerical program identified within the doctoral research

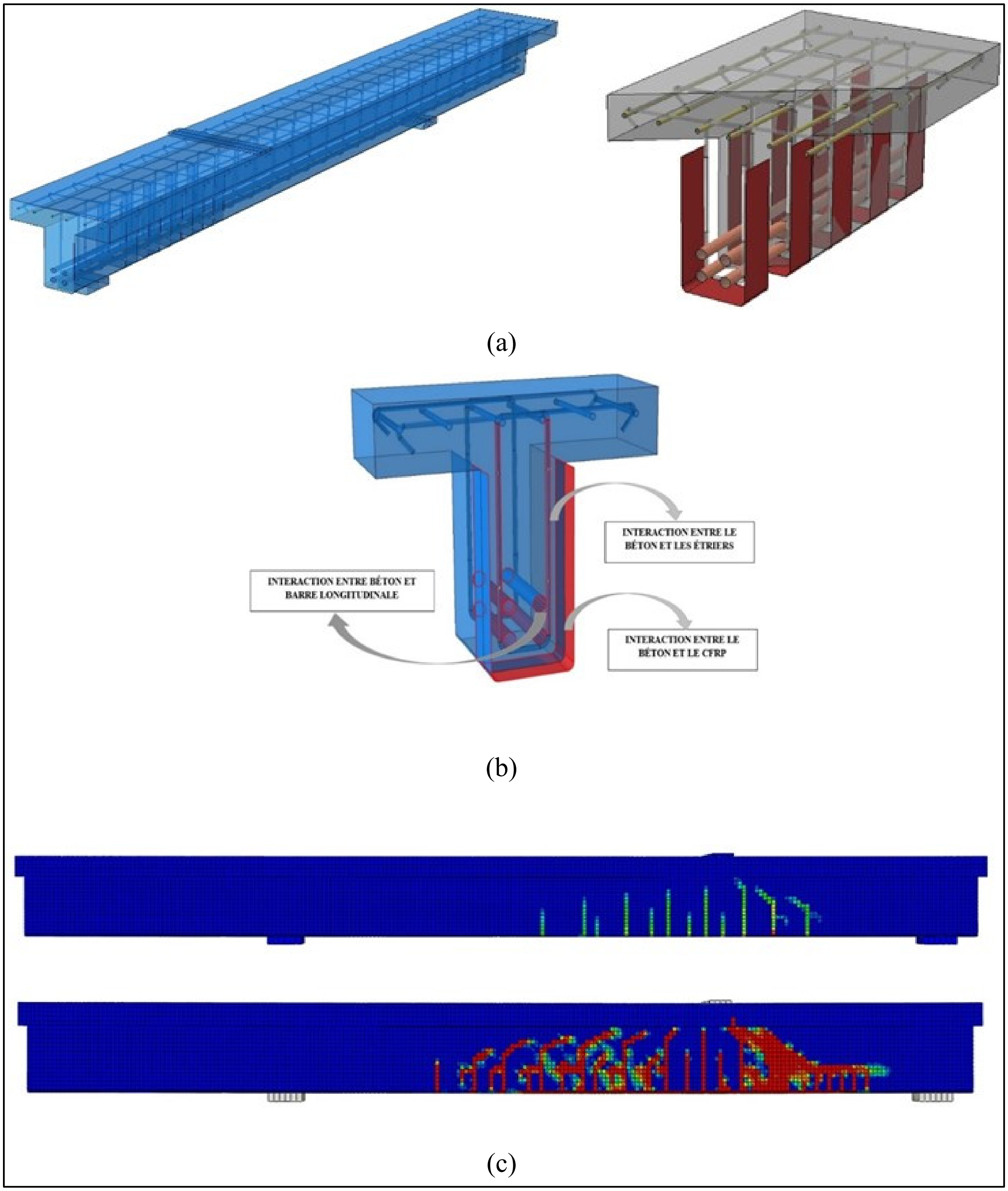

Figure 1.9 Schematic of three-dimensional simulated and analyzed RC-T beam strengthened in shear with EB-FRP under three-point loads (a) simulated specimen and position of steel stirrups and EB-FRP under three-point loads (b) situation of defined cohesive layer (c) initiation and propagation of flexural and shear cracks during load procedure

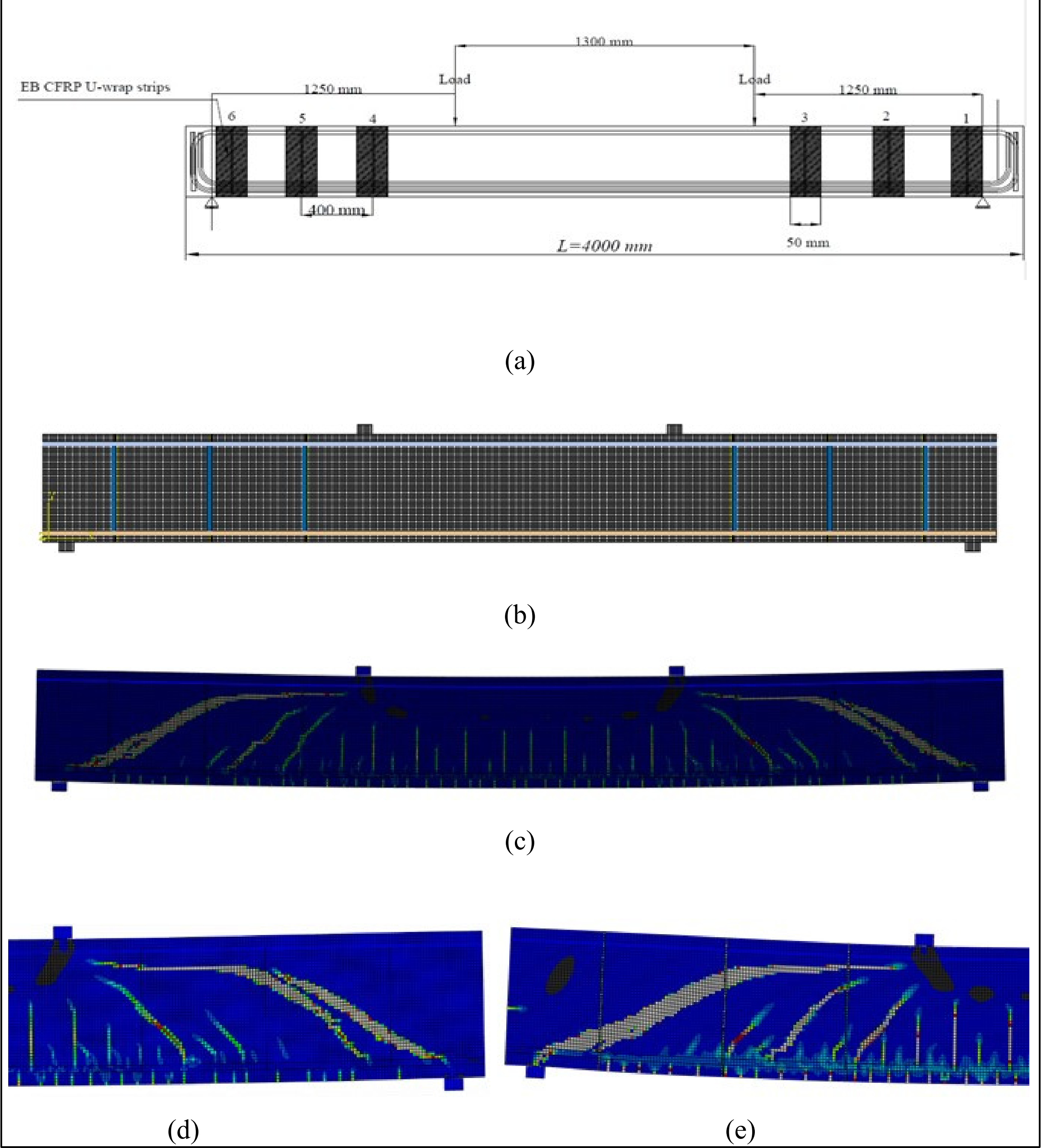

(a)

(b)

(c)

(d)

(e)

Figure 1.10 (a) elevation of rectangular specimen for parametric study (b) Schematic of two-dimensional simulated and analyzed RC beam strengthened in shear with EB-FRP under four-point loads (c) shear cracks in control beam (d) shear crack pattern in control beam at ultimate state (d) shear crack pattern in strengthened beam with EB-FRP at ultimate state

CHAPTER 2

RESEARCH BACKGROUND

2.1 Introduction

This section offers an overview of the existing information concerning RC beams strengthened, externally bonded in shear by FRP composites and their contributions in codes and standards is presented. The chapter begins with a synopsis of currently available models for predicting the shear strength of RC beams strengthened in shear with EB-FRP. The summary focuses on selective shear strength models, specifically those grounded in clear failure mechanisms or supported by significant experimental validation, rather than attempting to encompass all available models. Following that, the chapter concentrates on examining prior FE investigations concerning the shear failure of reinforced beams that have undergone strengthening.

2.2 Models for predicting shear strength currently in Use

Chaallal et al. (1998) Model

Chaallal et al. (1998) proposed the model utilized to determine the shear force carried by FRP composites in both side-bonded and U-wrap configurations. This model relies on the truss analogy as its fundamental principle.

$$V_f = \frac{2F_{frp}(\sin\beta + \cos\beta)d}{s_f} \tag{2.1}$$

The model incorporates several key parameters. F_{frp} represents the force within the FRP composites at the ultimate limit, determined by the average shear stress between the FRP composites and the concrete substrate. β signifies the angle of the fiber direction, d denotes the effective depth of the beam, and S_f is the center-to-center spacing of the FRP strips.

It's important to note that the average shear stress at the interface layer should not exceed fifty percent of the maximum shear stress at that interface layer. However, there are two notable deficiencies in this model.

The first deficiency pertains to the determination of the maximum shear stress at the interface layer, which relies on Roberts (1989) model. This model assumes that bond behavior is elastic and failure occurs in the adhesive layer, which contradicts the assumption that failure occurs in a thin layer of the concrete substrate close to the FRP composites. The second deficiency is related to the maximum shear stress at the bond. The model suggests that the maximum strength of the FRP can be fully utilized if there is adequate bond length. However, it's essential to consider the effective bond length, beyond which shear stress does not increase in the FRP composites (Guangming Chen, 2010).

Triantafillou (1998) Model

Triantafillou (1998) introduced a model to estimate the shear contribution of FRP composites to the shear strength of FRP reinforced concrete (RC) beams.

$$V_f = 0.9\rho_{frp}E_f\varepsilon_{frp,e}b_w d(1 + cot\beta)sin\beta \qquad (2.2)$$

This model is rooted in the failure mechanism of FRP composites. Triantafillou (1998) utilized an experimental approach to determine the shear contribution of FRP, employing an indicator termed "effective strain." This indicator was obtained through regression tests for this specific purpose.

$$\varepsilon_{frp,e} = 0.0119 - 0.0205\rho_{frp}E_f + 0.0104\left(\rho_{frp}E_f\right)^2 \qquad for \;\; 0 \le \rho_{frp}E_f < 1 \qquad (2.3)$$

$$\varepsilon_{frp,e} = -0.00065\rho_{frp}E_f + 0.00245 \qquad for \;\; \rho_{frp}E_f \ge 1 \qquad (2.4)$$

An inherent limitation of this model is its inability to distinguish between various configurations of shear strengthening and different failure modes (FRP debonding and rupture). Consequently, the model assumes a uniform shear contribution of FRP composites across all schemes, which may not accurately represent the real-world variations in shear behavior (Guangming Chen, 2010).

Khalifa et al. (1998) Model

Khalifa et al. (1998) introduced a model that incorporates two distinct failure mechanisms observed in shear-strengthened EB RC beams. This model serves as an amendment to Triantafillou's original model and accounts for two modes of failure, namely, FRP rupture and debonding. To facilitate this, Khalifa introduced two key parameters: "effective strain" ($\varepsilon_{frp,e}$) and the "reduction factor" (R). The reduction factor is determined by dividing the strain in the FRP at the point of rupture by the effective strain in the FRP, which is derived through regression analysis of experimental data. This is expressed as follows:

$$R = 0.5622\left(\rho_{frp}E_f\right)^2 - 1.2188\rho_{frp}E_f + 0.788 \leq 0.50 \tag{2.5}$$

Regarding debonding, Khalifa introduced a bond mechanism approach, which is based on the model initially proposed by Maeda (1997). This approach leads to the following expression for the reduction factor:

$$R = \frac{0.0042{f_c'}^{2/3}w_{f,e}}{(E_f t_f)^{0.58}\varepsilon_{frp,u}d_f} \tag{2.6}$$

Khalifa et al. (1998) suggested utilizing the lesser value between equations 2-5 and 2-6 to address debonding, while reserving Equation 2-5 exclusively for rupture analysis. Khalifa et al. (1998) model exhibits two notable deficiencies: firstly, Equation 2-5 relies on regression analysis of experimental data encompassing both failure modes (rupture and debonding), even though it was originally introduced solely for rupture analysis. This discrepancy arises because the mechanisms governing debonding and rupture differ. Secondly, the incorporation of Maeda

(1997) model as Equation 2-6 lacks precision in determining the effective bond length (Guangming Chen, 2010).

Triantafillou and Antonopoulos (2000) Model

Triantafillou and Antonopoulos (2000) introduced an alternative model that distinguishes between both failure modes and incorporates two distinct terms for computing effective strain. Additionally, they took into account various types of Fiber-Reinforced Polymer (FRP) materials within their model.

$$\varepsilon_{frp,e} = 0.65\left(\frac{\acute{f_c}^{2/3}}{\rho_{frp}E_f}\right)^{0.65} \times 10^{-3} \qquad CFRP\ debonding \qquad (2.7)$$

$$\varepsilon_{frp,e} = 0.17\left(\frac{\acute{f_c}^{2/3}}{\rho_{frp}E_f}\right)^{0.3} \times 10^{-3} \qquad CFRP\ rapture \qquad (2.8)$$

$$\varepsilon_{frp,e} = 0.048\left(\frac{\acute{f_c}^{2/3}}{\rho_{frp}E_f}\right)^{0.47} \times 10^{-3} \qquad AFRP\ rapture \qquad (2.9)$$

The problems with the model can be summarized as follows:

- Lack of Discrimination among shear strengthening FRP configurations: One issue is the failure to differentiate between various configurations of shear strengthening using FRP. This is problematic because each configuration can contribute differently, assuming all other parameters remain consistent, as noted by Teng et al. (2002b).

- Inconsistent model performance due to overlapping calibration and evaluation data: Another problem arises from the model's inconsistent performance when the same data is employed for both calibration and evaluation (Guangming Chen, 2010).

Chen and Teng (20003a, b) Model

J.-F. Chen and J. Teng (2003) and J. F. Chen and J. Teng (2003) introduced a model that differentiates between debonding and rupture modes. A noteworthy aspect of their model is its foundation in the actual failure process, as opposed to relying on the regression of experimental test data, as highlighted by Guangming Chen (2010).

$$V_f = 2f_{f,e}t_f w_f \frac{h_{f,e}(cot\theta + cot\beta)sin\beta}{s_f} \tag{2.10}$$

In which θ is the sign showing the orientation of shear crack and β represents the inclination of the fiber orientation, $h_{f,e} = Z_b - Z_t$ is the effective height of the FRP sheets/plates on the web of the beam, where:

$$Z_t = d_{frp,t} \tag{2.11}$$

$$Z_b = \left[d - \left(h - d_{frp}\right)\right] - 0.9d \tag{2.12}$$

They also demonstrated that stress within the FRP composites is not evenly distributed when debonding or rupture occurs. They put forth a model to calculate the average stress in the FRP material intersected by the crack, which is as follows:

$$f_{f,e} = D_{frp} . \sigma_{f,max} \tag{2.13}$$

Where $\sigma_{f,max}$ is the maximum tensile stress in FRP crossed by crack and D_{frp} is the coefficient for distributed stress.

$$D_{frp} = \frac{f_{f,e}}{\sigma_{f,max}} \tag{2.14}$$

Their model has several shortcomings (Guangming Chen, 2010):

- It relies on simplified assumptions, and it necessitates validation since it's constructed based on an analysis of the final state.
- Concerning FRP rupture, they presumed that FRP composites attain their peak tensile strength at the ultimate state. However, there is a likelihood that the ultimate state may occur either before or after the rupture of FRP strips.
- They posited that V_c, V_s, and V_f achieve their ultimate strength simultaneously. Nevertheless, due to the substantial strain in FRP composites during rupture, it's probable that V_c reaches its maximum strength before the rupture of FRP composites, possibly due to factors such as crack width and the loss of aggregate interlock.
- They assumed that FRP sheets/plates fully develop their bond lengths during debonding, which does not accurately reflect reality.
- It has been demonstrated that after debonding, FRP composites can reach their maximum tensile strength, a facet not accounted for in their study. Therefore, it is imperative to conduct a comprehensive analysis of the entire debonding process in EB RC beams.

Monti and Liotta (2007) Model

Giorgio Monti (2007) developed their model by building upon J.-F. Chen and J. Teng (2003) and J. F. Chen and J. Teng (2003) model, which acknowledges that the stress distribution along the FRP composites intersected by a crack is not uniform. Their model is based on two hypotheses: firstly, that the crack width increases linearly from the tip to the end of the crack, and secondly, that the number of slips at the top and bottom of the crack is equal. They introduced an analytical and mathematical model to establish a relationship between effective stress and the inclination of the shear crack for both U-wrap and side-bonded configurations. As part of their model, they presented the following equation to describe the shear contribution of FRP composites (Guangming Chen, 2010):

Side-bonded configuration:

$$V_f = \{\min 0.9d,\ h_w\}. f_{ed}. 2. t_f. \frac{sin\beta}{sin\theta}. \frac{w_f}{p_f} \tag{2.15}$$

Where

$$f_{ed} = f_{dd}. \frac{z_{rid.eq}}{\{\min 0.9d, h_w\}}. (1 - 0.6\sqrt{\frac{l_{eq}}{z_{rid.eq}}})^2 \tag{2.16}$$

$$z_{rid.eq} = z_{rid} + l_{eq} \tag{2.17}$$

$$z_{rid} = \{\min 0.9d, h_w\} - l_{eq}. sin\beta \tag{2.18}$$

$$l_e = \frac{s_f}{f_{dd}/E_f}. sin\beta \tag{2.19}$$

$$f_{dd} = \sqrt{\frac{2E_f.G_f}{t_f}} \tag{2.20}$$

$$G_f = 0.03K_b. \sqrt{f_{ck}f_{ctm}} \tag{2.21}$$

$$K_b = \sqrt{\frac{2-w_f/p_f}{1+w_f/400}} \tag{2.22}$$

In which $f_{dd}$is the strength of the bond between concrete and FRP composites, l_e is the effective bond length of the FRP composites, $G_f$is the fracture energy at the interface layer between concrete and FRP, K_b is the covering/scale coefficient, P_f is the FRP center-to-center spacing measured orthogonally to the fiber orientation, $h_w$is the beam web depth, $f_{ck}$is the concrete characteristic cylinder strength, and the concrete mean tensile strength $f_{ctm} = 0.27. R_{ck}^{2/3}$ (R is the concrete characteristic cube strength).

U-wrap configuration:

$$V_f = 0.9d. f_{ed}. 2. t_f. (cot\theta + cot\beta). \frac{w_f}{p_f} \tag{2.23}$$

And the effective stress is as follow:

$$f_{ed} = f_{dd}.\left[1 - \frac{1}{3}.\frac{l_e.sin\beta}{min\{0.9d, h_w\}}\right] \qquad (2.24)$$

And for the completely wrapped, effective stress is as follow:

$$f_{ed} = f_{dd}.\left[1 - \frac{1}{6}.\frac{l_e.sin\beta}{min\{0.9d, h_w\}}\right] + \frac{1}{2}(\emptyset_R.f_{fd} - f_{dd})\left[1 - \frac{1}{3}.\frac{l_e.sin\beta}{min\{0.9d, h_w\}}\right] \qquad (2.25)$$

Where

$$\emptyset_R = 0.2 + 1.6.\frac{r_c}{b_w} \qquad 0 \leq \frac{r_c}{b_w} \leq 0.5 \qquad (2.26)$$

In which r_c is the radius of section's corner

There are still some deficiencies as to this model: first and foremost, their closed-form model has a restriction to consider final state (not the whole process of failure). It means that they considered that failure of the EB FRP RC beams takes place when some of the FRP plates already debonded which is not accurate because the final state of the beam might happen before full debonding of all the FRP plates. Second, they employed some simplifying assumptions for their model which did not consider bond length under and top of the effective bond length, underestimating FRP contribution to shear capacity of the beam. Third, for modeling the behavior of interface layer between concrete and FRP composites, they used the simplified bond-slip model of Giorgio Monti et al. (2004) and Liotta (2006) which underestimate the shear contribution of FRP composites in shear contribution, particularly for side-bonded configuration. Forth, regarding similar slip on two sides of crack contributes to inaccurate result as to debonding process of the U-wrapped configuration (Guangming Chen, 2010).

Mofidi and Chaallal Model (2010)

Accounting on experimental data, Mofidi and Chaallal (2010) proposed a model for the shear contribution of FRP composites considering different configurations (U-wrapped, side-bonded). They assumed that effective bonded FRP was defined by a trapezoidal area illustrated by Figure 2.1.

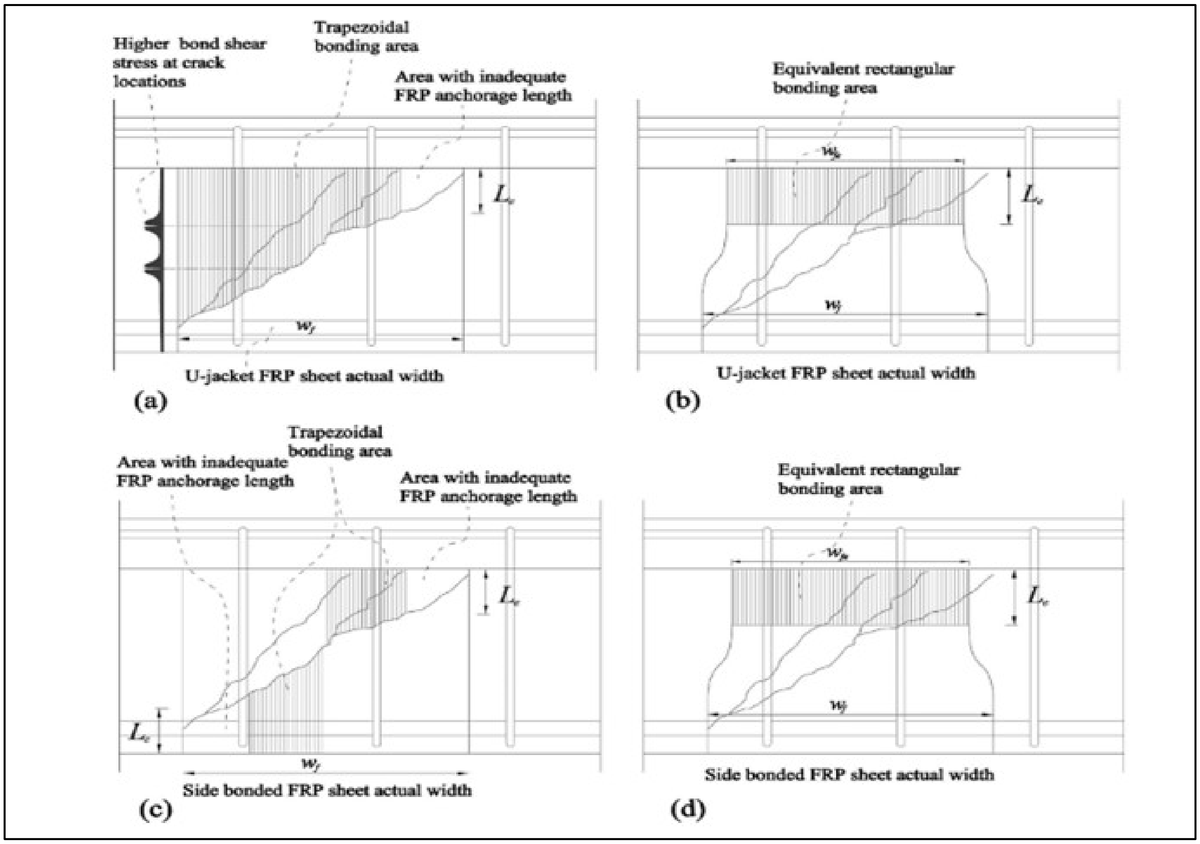

Figure 2.1 Typical configuration of effective FRP width in beams strengthened in shear with EB continuous FRP sheet: (a) actual bonding area for U-jacket; (b) equivalent bonding area for U-jacket; (c) actual bonding area for side-bonded FRP; and (d) equivalent bonding area for side-bonded FRP
Taken from Mofidi and Chaallal (2010)

Mofidi and Chaallal (2010) replaced these trapezoidal areas with the rectangular areas in which dimension of this rectangular area by effective length (L_e) and effective width(w_{fe}). The effective length is obtained based on the model of Neubauer and Rostasy (1997):

$$L_e = \sqrt{\frac{E_f t_f}{2 f_{ct}}} \tag{2.27}$$

$$f_{ct} = 0.53\sqrt{\acute{f_c}} \tag{2.28}$$

To calculate w_{fe}, they demonstrated that both the quantity of stirrups (($\rho_s E_s$)) and the stiffness of FRP composites ($\rho_f E_f$) influence the crack pattern. Furthermore, they established that the crack pattern impacts the bond length in FRP composites. When cracks develop in a distributed manner, fewer FRP composites contribute their entire bond length. Therefore, it's essential for the effective width to be sufficient in order to provide an effective bond length, especially as anchorage length decreases. For determining $\beta_c$and w_{fe}, they applied the struts-and-tie method while considering the angle of the shear crack to be 45° degrees. Mofidi and Chaallal (2010) introduced the definitions of the effective width and the cracking modification factor for each configuration (U-wrapped and side-bonded) as follows:

$$w_{fe} = \frac{0.6}{\sqrt{\rho_f E_f + \rho_s E_s}} \times d_f \qquad U - Wrapped \tag{2.29}$$

$$w_{fe} = \frac{0.43}{\sqrt{\rho_f E_f + \rho_s E_s}} \times d_f \qquad side - bonded \tag{2.30}$$

$$\beta_c = \frac{w_{fe}}{d_f} = \frac{0.6}{\sqrt{\rho_f E_f + \rho_s E_s}} \qquad U - Wrapped \tag{2.31}$$

$$\beta_c = \frac{w_{fe}}{d_f} = \frac{0.43}{\sqrt{\rho_f E_f + \rho_s E_s}} \qquad side - bonded \tag{2.32}$$

The effective strain is given by the following model:

$$\varepsilon_{fe} = \frac{\beta_c . \beta_L . \beta_w . \tau_{eff} . L_e}{t_f E_f} = 0.31\beta_c . \beta_L . \beta_w \sqrt{\frac{\sqrt{\acute{f_c}}}{t_f E_f}} \leq \varepsilon_{fu} \tag{2.33}$$

The contribution of FRP composites for non-continuous sheets can be calculated using the following model:

$$V_f = \frac{2t_f.w_f.\varepsilon_{fe}.E_f.(\cot\theta + \cot\alpha).sin\alpha.d_f}{s_f} = \rho_f.E_f.\varepsilon_{fe}.b.d_f.(cot\theta + cot\alpha).sin\alpha \qquad (2.34)$$

The problem with this model is that it does not show how the distribution of shear cracks changes when the ratio of EB-FRP to steel-stirrups increases. Since this model is based on the total ratio (internal and external ratio of shear reinforcement), it is important to evaluate the reduction of shear contribution of EB-FRP as function of the steel-stirrups ratio. In addition, the inverse interaction between steel-stirrups and FRP is not considered in the model proposed by Mofidi and Chaallal (2010).

2.3 Reviewing current codes and guidelines regarding RC beams strengthened in shear with EB-FRP composites

The objective of this study section is to examine the guidelines outlined in most recent publications of relevant building codes pertaining to the shear strengthening of reinforced concrete (RC) beams using externally bonded Fiber-Reinforced Polymer (EB-FRP) materials.

CAN/CSA-S6-19

CAN/CSA-S6-19 proposes the following model for the shear contribution EB-FRP:

$$V_f = \frac{\phi_{FRP}.E_{FRP}.\mathcal{E}_{FRP}.A_{FRP}.d_{FRP}(\cot\theta + \cot\beta).\sin\alpha}{s_{FRP}} \qquad (2.35)$$

In which the effective strain $\mathcal{E}_{FRPe}$is the function of k_1, k_2, k_v and V_f is the shear contribution of FRP composites in which the angel of the shear crack (Θ) is assumed 42 º and the upper limits of effective strain for U-shape configurations are given by:

U-wrapped scheme: $\varepsilon_{FRPe}.k_v \leq 4000\mu\varepsilon$

$$k_1 = (f_c^{'}/27)^{2/3} \tag{2.36}$$

$$k_2 = (d_{FRP} - L_e)/d_{FRP} \tag{2.37}$$

$$k_v = (k_1.k_2.L_e)/(11900\varepsilon_{FRPu}) \tag{2.38}$$

$$L_e = 23300/(t_{FRP}.E_{FRP})^{0.58} \tag{2.39}$$

where L_e is the effective bond length of EB-FRP that is reduced by increasing the elasticity and the thickness of EB CFRP because of more distributed shear cracks.

CAN/CSA-S806-12

In the Technical Committee on the rules of calculation and construction of building structures, containing fiber-reinforced polymers, the model for the shear contribution of the EB-FRP is similar to CAN/CSA-S6-19, but the angel of the shear crack (ϴ) is considered 35 º.

ACI 440.2R 2017

In the American code (ACI 440.2R 2017), the effective strain in FRP wrap failing by FRP rupture is limited to 0.004 in order to avoid loss of aggregate interlocking (Priestley et al., (1998). With regard to side-bonded and U-shaped schemes. In this code, the model of Khalifa et al., (1998) is used with slight corrections. The FRP shear contribution is given by:

$$V_f = \frac{A_{fv}.f_{fe}.(sin\alpha + cos\alpha).d_{fv}}{s_f} \tag{2.40}$$

For side-bonded and U-wrap configurations:

$$\varepsilon_{fe} = K_v \varepsilon_{fu} \leq 0.004 \tag{2.41}$$

$$K_v = \frac{k_1 k_2 L_e}{11900\varepsilon_{fu}} \leq 0.75 \tag{2.42}$$

$$L_e = \frac{23300}{(n_f t_f E_f)^{0.58}} \tag{2.43}$$

$$k_1 = \left(\frac{f_{cm}}{27}\right)^{2/3} \tag{2.44}$$

$$k_2 = \begin{cases} \frac{d_f - L_e}{d_f} & U-wrap \\ \frac{d_f - 2L_e}{d_f} & side-bonded \end{cases} \tag{2.45}$$

CEB- *fib*-TG 5.1-19

In the CEB- *fib*-TG 5.1-19, the proposed models for U-shape strips and wrap configurations (Figure 2.2) are considered the bilinear bond-law model which stand for the interaction between EB-FRP and concrete and the presented models are as follows:

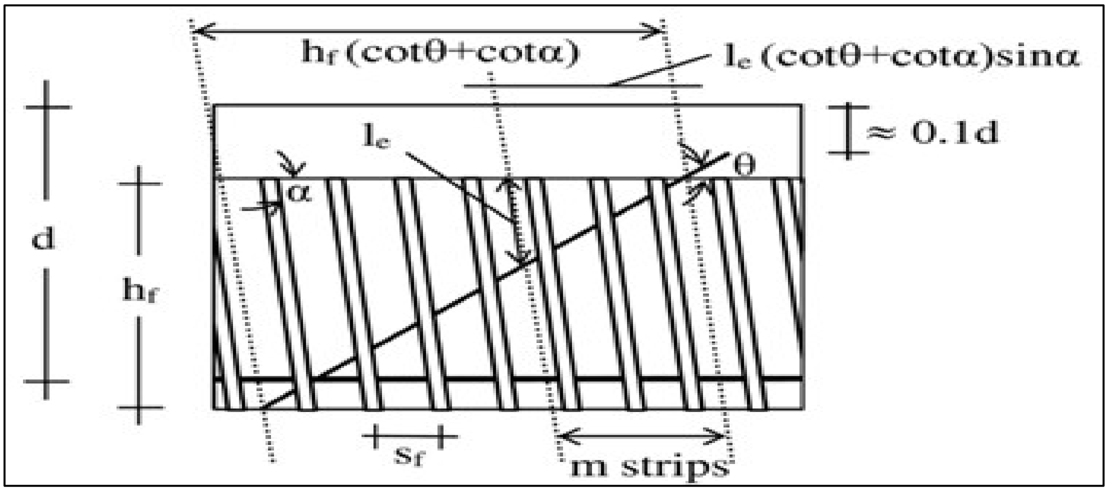

Figure 2.2 Strips crossed by the shear crack
Taken from Matthys and Group (2019)

$$f_{fwd} = \min\,(f_{fbwd}, f_{fwd,c}) \tag{2.46}$$

Regarding U-shape strip configuration where $\frac{h_f}{\sin\alpha} \geq l_e$ and $\frac{S_f}{\cot\theta+\cot\alpha\sin\alpha} \leq l_e$ i.e. If certain FRP strips intersected by the shear crack possess bond lengths are greater or equal to l_e while others have different bond lengths which are less than l_e, shear contribution of EB-FRP is as follow:

$$f_{fbwd} = (1 - \left(1 - \frac{2mS_f}{3l_e}\right)\frac{m}{n})\frac{f_{fbk}}{\gamma_{fb}} \tag{2.47}$$

And for U-shape configuration strips in which $\frac{h_f}{\sin\alpha} \leq l_e$ and $\frac{S_f}{(\cot\theta+\cot\alpha)\sin\alpha} \leq \frac{h_f}{\sin\alpha}$ i.e. If all the FRP strips crossed by the shear crack share the bond length less than l_e, the proposed closed-form model is as follow:

$$f_{fbwd} = \left(\frac{2nS_f/((\cot\theta+\cot\alpha)\sin\alpha)}{3l_e}\right)\frac{f_{fbk}}{\gamma_{fb}} \tag{2.48}$$

The scenario involving full-area bonding, represented by continuous FRP sheets, can be regarded as a specific case of FRP strips with $S_f = b_f/\sin\alpha$, which shear contributions of EB-FRP are calculated as following models:

$$if \quad \frac{h_f}{\sin\alpha} \geq l_e \quad f_{fbwd} = \left(1 - \frac{l_e}{3\,(h_f \sin\alpha)}\right)\frac{f_{fbk}}{\gamma_{fb}} \tag{2.49}$$

$$if \quad \frac{h_f}{\sin\alpha} \leq l_e \quad f_{fbwd} = \left(\frac{2h_f/\sin\alpha}{3l_e}\right)\frac{f_{fbk}}{\gamma_{fb}} \tag{2.50}$$

Where n = number of strips crossed by the shear crack = integer quotient $hf\ (cot\theta + cot\alpha)/sf$, m = number of strips for which the bond length is less than l_e= integer quotient $l_e(\cot\theta + \cot\alpha)\sin\alpha/S_f$, l_e = maximum bond length and f_{fbk}= characteristic maximum bond strength which can be obtained from following equations:

$$f_{fbk}(S_r) = \begin{cases} \sqrt{\frac{E_f . f_{0k} . \tau_{b1k}}{t_f}} \times \frac{S_r}{l_e}\left(2 - \frac{S_r}{l_e}\right) & if \quad S_r < l_e \\ \sqrt{\frac{E_f . f_{0k} . \tau_{b1k}}{t_f}} & if \quad S_r \geq l_e \end{cases} \tag{2.51}$$

$$l_e = \frac{\pi}{2} \times \sqrt{\frac{E_f . t_f . s_{0k}}{\tau_{b1k}}} \tag{2.52}$$

Above-mentioned parameters (the characteristic shear strength (τ_{b1k}) and the ultimate slip (s_{0k}) values) can be extracted from following tables (Table 2.1 and Table 2.2):

Table 2.1 Parameters of the bilinear $\tau_b - s$ constitutive law for bond
Taken from Matthys and Group (2019)

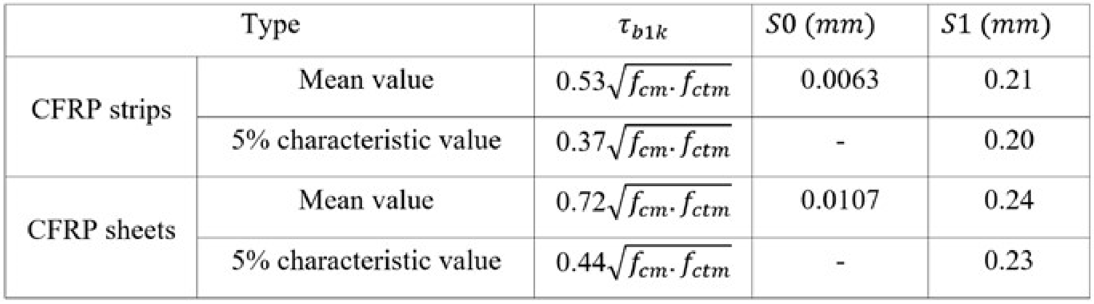

Type		τ_{b1k}	$S0\ (mm)$	$S1\ (mm)$
CFRP strips	Mean value	$0.53\sqrt{f_{cm} \cdot f_{ctm}}$	0.0063	0.21
	5% characteristic value	$0.37\sqrt{f_{cm} \cdot f_{ctm}}$	-	0.20
CFRP sheets	Mean value	$0.72\sqrt{f_{cm} \cdot f_{ctm}}$	0.0107	0.24
	5% characteristic value	$0.44\sqrt{f_{cm} \cdot f_{ctm}}$	-	0.23

Table 2.2 Material safety factors for bond
Taken from Matthys and Group (2019)

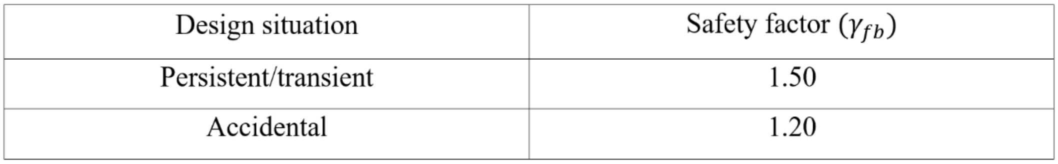

Design situation	Safety factor (γ_{fb})
Persistent/transient	1.50
Accidental	1.20

Where the estimation of the crack spacing (S_r) for reinforced concrete members, which can be calculated as follow:

$$S_r = 1.5 l_{e,0} \tag{2.53}$$

In which $l_{e,0}$ represents the transfer length of the reinforcing steel, which is equal to

$$1.5l_{e,0} = \frac{M_{cr}}{Z_s.F_{bsm}} \tag{2.54}$$

In this context, M_{cr} stands for the cracking moment, Z_s is approximately equal to 0.85 times the total member height (h), and F_{bsm} represents the bond force per unit length. In reinforced concrete members, the cracking moment can be estimated as:

$$M_{cr} = K_{fl}.f_{ctm}.W_{C,0} \tag{2.55}$$

In this context, K_{fl} is defined as $(1.6 - h/1000)$, with h measured in millimeters, and $W_{C,0}$ represents the section modulus of the uncracked concrete cross-section (the moment of inertia divided by the distance of the extreme tensile fiber from the neutral axis). When calculating M_{cr} for T-beams, it's important to consider the effective flange width. The bond force per unit length can be computed as:

$$F_{bsm} = \sum_{i=1}^{n} n_{s,i}.\pi.\emptyset_{s,i}.f_{bsm} \tag{2.56}$$

Where, f_{bsm} represents the mean bond stress of the reinforcing steel and is related to the diameter of the steel bars ($\emptyset_{s,i}$). When dealing with a single bar with an equivalent diameter equal to the square root of 2 times $\emptyset_s$, the number of steels rebars to be used for double bars is determined. Equation 2-56 is formulated under the assumption of uniform bond stress along the reinforcing bar, extending from the cracked section up to the midpoint between successive cracks. The mean bond stress (f_{bsm}) can be determined in the following manner:

$$f_{bsm} = \begin{cases} 0.43.K_{vb1}.f_{cm}^{2/3} & for\ ribbed\ bars \\ 0.28.K_{vb2}.\sqrt{f_{cm}} & for\ smooth\ bars \end{cases} \tag{2.57}$$

The values of the parameters K_{vb1} and K_{vb2} are contingent on the bond conditions and can be selected as follows:
For good bond conditions, K_{vb1} and K_{vb2} are both set to 1.0. For medium bond conditions, κvb1 is assigned a value of 0.7, and κvb2 is assigned a value of 0.5.

CNR-DT 200/2004

The model in Italian codes (CNR-DT 200/2004) depends on equations proposed by (G Monti et al., 2003) with some corrections. The upgrade model, mentioned in CNR-DT 200 (2004) was presented in (Giorgio Monti, 2007). In this guideline, the contribution of FRP composites to shear strengthening is classified into three categories based on different scheme.

1. For completely wrapped scheme

$$V_{fd} = \frac{1}{\gamma_{rd}}.0.9d.f_{fed}.2t_f.(cot\theta + cot\alpha).\frac{w_f}{s_f} \tag{2.58}$$

$$f_{fed} = f_{fdd}.\left[1 - \frac{1}{6}.\frac{L_e sin\alpha}{\min\{0.9d;h_w\}}\right] + \frac{1}{2}\left(\emptyset_R f_{fd} - f_{fdd}\right)\left[1 - \frac{L_e sin\alpha}{\min\{0.9d;h_w\}}\right] \tag{2.59}$$

$$\emptyset_R = 0.2 + 1.6\frac{r_c}{b_w}; \qquad 0 \leq \frac{r_c}{b_w} \leq 0.5 \tag{2.60}$$

$$G_{fk}0.03k_b.\sqrt{f_{ck}.f_{ctm}}; \qquad f_{dd} = \frac{0.80}{\gamma_{fd}}.\sqrt{\frac{2-w_f/s_f}{1+w_f/400}} \geq 1 \tag{2.61}$$

2. For a U-wrapped scheme

$$f_{fed} = f_{fdd}.[1 - \frac{1}{3}.\frac{L_e sin\alpha}{\min\{0.9d;h_w\}} \tag{2.62}$$

3. For a side-bonded scheme

$$V_{fd} = \frac{1}{\gamma_{rd}}.\min\{0.9d;h_w\}.f_{fed}.2.t_f.\frac{sin\alpha}{sin\theta}.\frac{w_f}{s_f} \tag{2.63}$$

$$f_{fed} = f_{fdd} \cdot \frac{z_{red.eq}}{\min\{0.9d; h_w\}} \cdot [1 - 0.6\sqrt{\frac{L_{eq}}{z_{red.eq}}}]^2 \quad (2.64)$$

In which

$$Z_{red.eq} = Z_{red} + L_{eq} \quad (2.65)$$

$$z_{red} = \min\{0.9d; h_w\} - L_e sin\alpha \quad (2.66)$$

$$L_{eq} = \frac{s_{uf}}{f_{fdd}/E_f} . sin\alpha \quad (2.67)$$

JSCE (2007)

In the JSCE (2007), the contribution of FRP composites to the shear resistance is given by:

$$V_f = K . \left[A_f . f_{fu} . (sin\alpha_f + cos\alpha_f)/s_f\right] . z \quad (2.68)$$

$$K = 1.68 - 0.67R \quad (2.69)$$

$$R = (\rho_f E_f)^{1/4} (\frac{f_{fu}}{E_f})^{2/3} (\frac{1}{f_c})^{1/3} \quad (2.70)$$

$$\rho_f = A_f/(b_w . s_f) \quad (2.71)$$

In which K is the shear reinforcing efficiency of continuous fiber sheets, α_f is the angle of the directions of the fibers with respect to the horizontal axis of the beam, and $z = J/1.15$ is the lever arm length (generally may be set to $d/1.15$). The model is based on experimental data, which did not include some failure modes such as FRP rupture, debonding of FRP composites, and crushing of struts in concrete obviously. A shortcoming of this model is that the different failure modes are not regarded properly. It is noteworthy that this standard suggests another technique for calculating the FRP shear contribution and the behavior of bond-slip between concrete and FRP according to the numerical approach Guangming Chen (2010).

Having said that, Mofidi and Chaallal (2010) proposed a new model by considering the effect of the total shear reinforcement on the distribution of the shear cracks since the effective bond length reduces as the amount of the total shear reinforcement increases. The accuracy of this model demonstrates the better prediction of the shear contribution of the EB-FRP in comparison to the guidelines that are already reviewed. This model replaces these trapezoidal areas with rectangular areas of effective length (L_e) and effective width (w_{fe}). The effective length was obtained based on the model of Neubauer and Rostasy (1997) :

$$L_e = \sqrt{\frac{E_f t_f}{2 f_{ct}}} \qquad (2.72)$$

$$f_{ct} = 0.53\sqrt{f_c'} \qquad (2.73)$$

For calculating w_{fe}, this model proves that both the amounts of stirrups $(\rho_s E_s)$ and the rigidity of FRP composites $(\rho_f E_f)$ affect the distributions of the shear cracks. Moreover, the proposed model shows that the crack pattern affects the bond length in FRP composites in a way that as cracks propagate, less bond length is available and leading thereby to less FRP contribution to the shear resistance. Therefore, the effective width should be sufficient to provide the effective bond surfaces anchorage length. To calculate β_c and w_{fe} , the strut-and-tie method is adopted with an angle of the shear crack of 45°. The modification factor for each configuration (U-wrapped and side-bonded) is defined by the effective width and the distribution of the shear cracks as follows:

$$w_{fe} = \frac{0.6}{\sqrt{\rho_f E_f + \rho_s E_s}} \times d_f \qquad U - Wrapped \qquad (2.74)$$

$$w_{fe} = \frac{0.43}{\sqrt{\rho_f E_f + \rho_s E_s}} \times d_f \qquad side - bonded \qquad (2.75)$$

$$\beta_c = \frac{w_{fe}}{d_f} = \frac{0.6}{\sqrt{\rho_f E_f + \rho_s E_s}} \qquad U - Wrapped \qquad (2.76)$$

$$\beta_c = \frac{w_{fe}}{d_f} = \frac{0.43}{\sqrt{\rho_f E_f + \rho_s E_s}} \qquad side - bonded \tag{2.77}$$

The effective strain is given by:

$$\varepsilon_{fe} = \frac{\beta_c . \beta_L . \beta_w . \tau_{eff} . L_e}{t_f E_f} = 0.31\beta_c . \beta_L . \beta_w \sqrt{\frac{f_c'}{t_f E_f}} \leq \varepsilon_{fu} \tag{2.78}$$

The contribution of FRP composites in the shear resistance can be determined using the following equation:

$$V_f = \frac{2t_f . w_f . \varepsilon_{fe} . E_f . (\cot\theta + \cot\alpha) . sin\alpha . d_f}{s_f} = \rho_f . E_f . \varepsilon_{fe} . b . d_f . (cot\theta + cot\alpha) . sin\alpha \tag{2.79}$$

The problem with this model is that it doesn’t mention how the distribution of the shear crack changes when the ratio of EB-FRP to the steel stirrups increases. Since this model is based on the total ratio of the internal and the external ratio of the shear reinforcement, we need to know how the shear contribution of EB-FRP reduces as the ratio of the steel stirrups increases.

HB 305 2008

In the Australian code (HB 305 2008), (J. Chen & J. Teng, 2003) are adopted, in which the contribution of FRP composites to shear strengthening is obtained by the following model:

$$V_f = 2f_{fed} . t_f . \frac{w_f}{s_f} . h_{fe} . (cot\theta + cot\alpha) sin\alpha \tag{2.80}$$

$$h_{fe} = Z_b - Z_t; \quad Z_b = 0.9d - d_{fb}; \quad Z_t = d_{ft} \tag{2.81}$$

$$f_{fed} = D_f . f_{fd,max} \tag{2.82}$$

For a completely wrapped scheme:

$$f_{fd,max} = \begin{cases} \frac{1}{\gamma_f}.\emptyset_R.f_{fu}; & \varepsilon_f \leq 1.5\% \\ \frac{1}{\gamma_f}.\emptyset_R.E_f.f_{fu}; & \varepsilon_f > 1.5\% \end{cases} \tag{2.83}$$

$$D_f = 0.5(1 + \frac{z_t}{z_b}) \tag{2.84}$$

For U-wrapped and side-bonded schemes:

$$D_f = \begin{cases} \frac{2}{\pi.\lambda}.\frac{1-\cos(\frac{\pi}{2}.\lambda)}{\sin(\frac{\pi}{2}.\lambda)}; & \lambda = \frac{L_{max}}{L_e} \leq 1 \\ 1 - \frac{\pi-2}{\pi.\lambda}; & \lambda = \frac{L_{max}}{L_e} > 1 \end{cases} \tag{2.85}$$

$$L_{max} = \begin{cases} \frac{h_{fe}}{sin\alpha} & for \quad U - shape\ scheme \\ \frac{h_{fe}}{2sin\alpha} & for \quad side - bonded\ scheme \end{cases} \tag{2.86}$$

$$L_e = \sqrt{\frac{E_f.t_f}{\sqrt{f_{ck}}}} \tag{2.87}$$

$$f_{fd.max} = min \begin{cases} \frac{1}{\gamma_f}.\emptyset_R.f_{fu} \\ \frac{1}{\gamma_f}.0.35.\beta_L.\beta_w.\sqrt{\frac{E_f.\sqrt{f_{ck}}}{t_f}} \end{cases} \tag{2.88}$$

$$\beta_L = \begin{cases} \lambda, & \lambda \leq 1 \\ 1, & \lambda > 1 \end{cases}; \quad \beta_w = \sqrt{\frac{2 - w_{f/(s_f.sin\alpha)}}{1 + w_{f/(s_f.sin\alpha)}}} \tag{2.89}$$

In which $\emptyset_R = 0.80\ and\ \gamma_f = 1.25$

UK code

In Concrete society 2004, the shear contribution of FRP for all kinds of failure modes is obtained by the following model:

$$V_f = E_f . \varepsilon_{f,e} . A_f \frac{\left(d_f - \frac{n}{3} l_{t,max}\right)}{s_f} (sin\beta + cos\beta) \tag{2.90}$$

$$\varepsilon_{fe} = \min \{0.5\varepsilon_f, 0.64\sqrt{\frac{f_{ctm}}{E_f . t_f}}\ , 0.004\} \tag{2.91}$$

$$l_{t,max} = 0.7\sqrt{\frac{E_f t_f}{f_{ctm}}} \tag{2.92}$$

In which ε_{fe} is the effective stain of FRP composites intersected by shear crack, n is a coefficient representing the strengthening scheme (n= 0 for the completely wrapped scheme, n = 1.0 for FRP U-shape scheme and n = 2.0 for side-bonded FRP strips), $l_{t,max}$ is the bond length needed to extend the whole anchorage length. Three strain models are used in this model to ensure the safety of FRP composites against different failure modes:

1. First, effective stain restricts failure mode regarding the rapture of FRP
2. Second effective strain restricts debonding failure mode in FRP composites
3. The third effective strain put a restriction in order to prevent loss of interlock between aggregate in concrete.

This model is quite conservative in comparison to experimental results.

2.4 Finite element analysis (FEA)

When FRP composites were first introduced in the construction industry, computer programs and finite element packages were not as advanced as they are today. Consequently, most assessments of the effectiveness of reinforcing RC (reinforced concrete) beams with EB-FRP (Externally Bonded Fiber-Reinforced Polymer) composites relied on laboratory experiments.

Consequently, the impact of various factors on the overall behavior of these tested beams often remained undetermined. This challenge was particularly pronounced when certain factors interacted with one another, leading to complex and not easily understandable beam behavior. Furthermore, once finite element programs became available, most research using these tools primarily focused on strengthening RC beams in flexure using EB-FRP composites. Theoretical research regarding the performance of reinforced concrete beams strengthened in shear using FRP composites is relatively scarce compared to studies on FRP flexural strengthening. Due to the cost and time demands associated with laboratory testing, there is a limited availability of such investigations. Given the costly and time-intensive nature of laboratory tests, there is a clear benefit to having precise numerical methods that can effectively replicate the intricate behavior of these structures. Effective numerical models provide an additional advantage in that they can be leveraged to enhance our comprehension of diverse failure mechanisms and the impact of significant controlling factors.

Accurate and trustworthy models should have the capacity to accommodate the numerous intricacies of concrete behavior, including non-linear behavior in compression, post-failure characteristics in tension, and the bond-slip connections inherent in both the steel-to-concrete and FRP-to-concrete interface layer.

2.4.1 Numerical softwares

So far, a variety of accessible finite element software have been employed to investigate the performance of beams reinforced with FRP in shear. Some of the outstanding research implementing FEA software are ABAQUS (Amir, 1998; GM Chen et al., 2012; GM Chen et al., 2013; GM Chen, Teng, & Chen, 2010; GM Chen et al., 2015; Kaliakin et al., 1996), ANSYS (Elyasian et al., 2006; Kachlakev et al., 2001; Santhakumar et al., 2004) and DIANA (Al-Mahaidi et al., 2001; T. K. Lee, 2003; T. K. Lee et al., 2000) ADINA (Ahmed Godat, 2008; Ahmed Godat et al., 2013; A Godat et al., 2008, 2012). A clear benefit of using finite element software lies in their adaptability. These tools typically provide a broad selection of element kinds and possess the capacity to handle a diverse array of intricate structural challenges.

2.4.2 FRP-strengthened beams' simulation

2.4.2.1 Simulation of concrete

Concrete damage plasticity (CDP): The primary purpose of developing the concrete damaged plasticity model was to create a versatile tool for analyzing concrete structures subjected to cyclic or dynamic loads. Although this model can also be applied to the analysis of other quasi-brittle materials such as rock, mortar, and ceramics, this section concentrates primarily on concrete to demonstrate various aspects of the constitutive theory. When exposed to low confining pressures, concrete displays a brittle behavior characterized by two primary failure mechanisms: the formation of tension-induced cracks and compression-induced crushing. However, as the confining pressure surpasses a certain threshold, crack propagation is impeded, and the brittle nature of concrete diminishes. Under these conditions, failure occurs due to the consolidation and collapse of the microstructure within the concrete. This results in a macroscopic response that resembles the behavior of a ductile material, including work hardening.

The plastic-damage model under consideration does not include the modeling of concrete behavior under high hydrostatic pressures. Rather, the constitutive theory in this section is tailored to capture the outcomes of irreversible damage resulting from failure mechanisms in concrete and comparable quasi-brittle materials when exposed to relatively modest confining pressures, usually below four or five times the ultimate compressive stress observed in uniaxial compression loading. These consequences manifest in the following macroscopic properties:

Distinct Yield Strengths: Yield strengths in tension and compression are dissimilar, with the initial yield stress in compression being notably higher, often exceeding the initial yield stress in tension by a factor of 10 or more (Abaqus, 2011).

- Tension Softening: Concrete exhibits softening behavior in tension, contrasting with initial hardening followed by softening in compression.
- Elastic Stiffness Degradation: There is varying degradation in the elastic stiffness between tension and compression.
- Stiffness Recovery Effects: During cyclic loading, there are stiffness recovery effects, which means that the material may regain some of its stiffness after unloading.

- Rate Sensitivity: The material's response is sensitive to loading rates, especially showing an increase in peak strength with higher strain rates.
- These properties are essential considerations when modeling the behavior of concrete and quasi-brittle materials, and they are addressed in the discussed constitutive theory.

The plastic-damage model employed in ABAQUS is rooted in the models originally proposed by J Lubliner et al. (1989) and subsequently extended by J. Lee and Fenves (1998) (Figure 2.3). The following sections in this segment will elucidate this model. Firstly, there will be an overview of the fundamental elements of the model, followed by a comprehensive examination of the various aspects within the constitutive model (Abaqus, 2011).

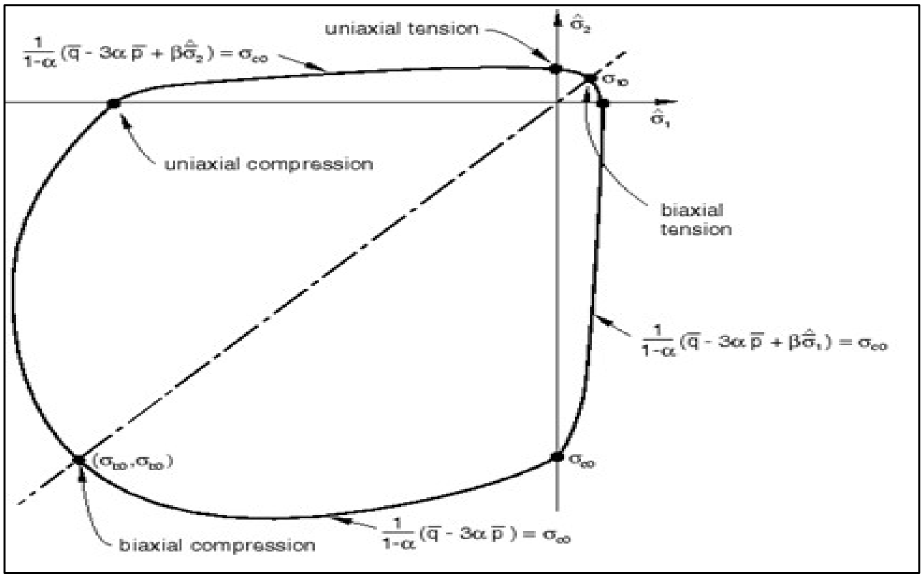

Figure 2.3 Yield surface in plane stress
Taken from Abaqus (2011)

Smeared crack model: This model employs a smeared crack approach to represent the discontinuous brittle behavior observed in concrete. Rather than tracking individual "macro" cracks, the model conducts constitutive calculations independently at each material point within the finite element model. The presence of cracks influences these calculations by modifying the stress and material stiffness associated with each material point (Abaqus, 2011).

For the sake of simplicity in this section's discussion, the term "crack" refers to a direction where cracking has been identified at the specific material calculation point under consideration. The closest conceptual representation is that there exists a network of micro-cracks surrounding the point, oriented as determined by the model. It is assumed that the anisotropy introduced by cracking plays a significant role in the simulations for which the model is designed (Abaqus, 2011).

Brittle cracking (BC): The purpose of this option is to define properties related to cracking and the subsequent post-cracking behavior within the brittle cracking material model. It's crucial to emphasize that the brittle cracking option should be employed in conjunction with the brittle cracking option, and it should immediately precede it in the input sequence. Moreover, if needed, the brittle cracking option can be used together with the brittle failure option to establish a brittle failure criterion. The brittle cracking model in ABAQUS/Explicit exhibits the following key characteristics (Abaqus, 2011):

- Versatile Application: It can be used to simulate concrete behavior across a wide range of structural types, including beams, trusses, shells, and solids.
- Broad Material Applicability: Beyond concrete, it can effectively model other brittle materials such as ceramics or brittle rocks.
- Tensile Cracking Emphasis: Specifically designed for situations where the predominant behavior is governed by tensile cracking.
- Linear Elastic Compression: Assumes that the material retains linear elastic behavior in compression under all circumstances.
- Linear Elastic Material Model: It necessitates use in conjunction with the linear elastic material model, which comprehensively characterizes material behavior before cracking occurs.
- Accuracy in Brittle Behavior: Its precision is highest when applied to scenarios where brittle behavior predominates, making the assumption of linear elastic compression satisfactory.
- Suitable for Plain Concrete: While its primary focus is on analyzing reinforced concrete structures, it can also be effectively employed for plain concrete materials.

- Element Removal Capability: It enables the removal of elements based on a brittle failure criterion, enhancing simulation accuracy.
- Comprehensive Documentation: Detailed information and guidance about this model

2.4.2.2 Simulation of interface between concrete-to-FRP and concrete-to-steel stirrups:

Cohesive element:

The decent approach for modeling the interface layer between EB-FRP and concrete as well as steel stirrups and concrete involves assigning cohesive elements to the interface layer. This allows for the properties of the bond-slip curve obtained from experimental results to be attributed to the interface layer (Figure 2.4). Several research studies that have adopted this method are outlined below:

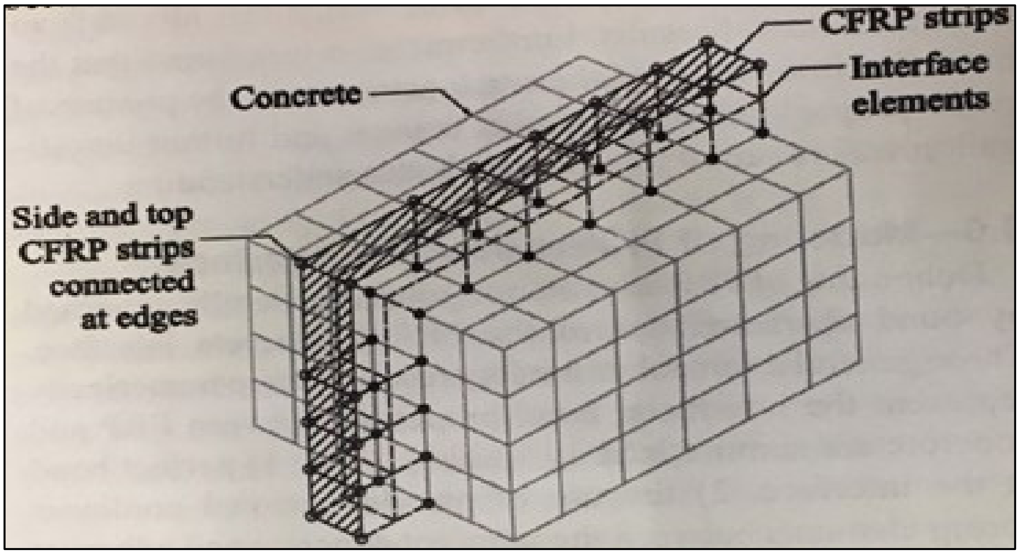

Figure 2.4 Connection between FRP and concrete via interface element
Taken from Hii (2006)

Obaidat et al. (2010) conducted a FE study on the behavior of RC beams retrofitted by CFRP plates using ABAQUS software. To simulate the behavior of bond-slip, they applied bilinear traction-separation law introduced the traction τ versus opening displacement δ constitutive law illustrated in Figure 2.5.

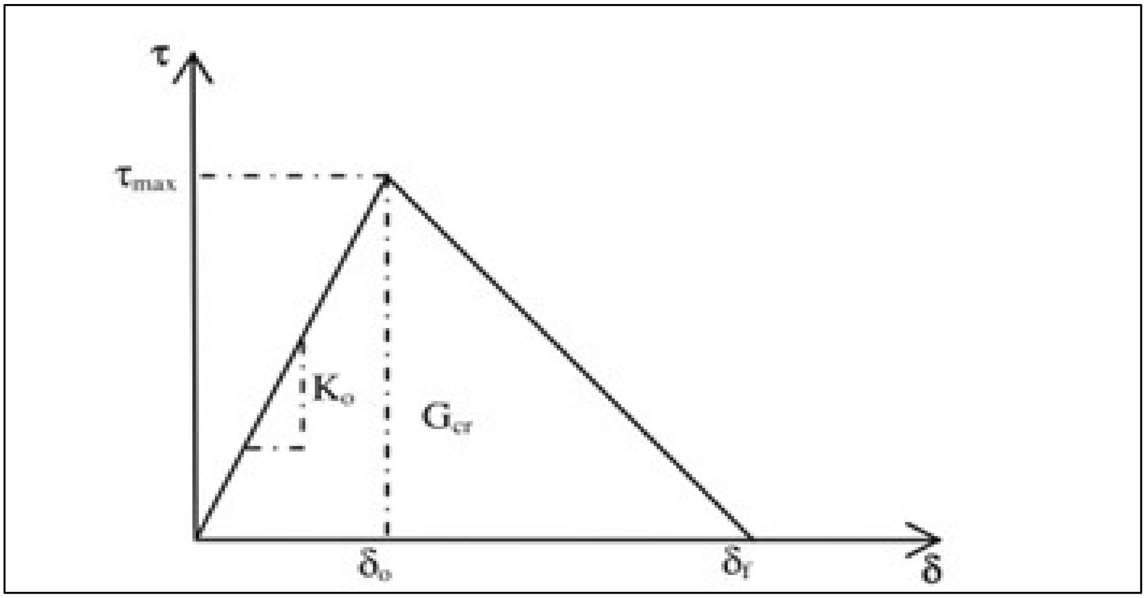

Figure 2.5 Bilinear traction–separation constitutive law
Taken from Obaidat et al. (2010)

In the modeling approach, the interface layer is represented with a relatively negligible thickness, and the ascending stiffness of the curve, denoted as K_0, is determined based on the method proposed by Guo et al. (2005).

$$K_0 = \frac{1}{(K_a + K_c)} \tag{2.93}$$

$$K_a = \frac{G_a}{t_a} \tag{2.94}$$

$$K_c = \frac{G_c}{t_c} \tag{2.95}$$

In their research study, the following values for the parameters you mentioned were used:
G_a: Shear modulus of the concrete substrate.
t_a: Thickness of the concrete substrate (approximately 5 mm).
G_c: Shear modulus of the adhesive.
t_c: Thickness of the adhesive.
However, the specific numerical values for these parameters are not provided in the information you've given. These values would typically depend on the particular experimental

setup and materials used in their study which are t_a = 1 mm, t_c = 5 mm, G_a = 0.665 GPa, and G_c = 10.8 GPa.

Obaidat et al. (2010) used a cohesive element for the interface layer, as depicted in Figure 2.6. This cohesive element consists of two surfaces separated by a certain thickness. The relative displacement between the upper and lower surfaces of this thickness represents the opening or closing behavior of the interface. This cohesive element is employed to model the bond-slip behavior and interactions between materials at the interface accurately.

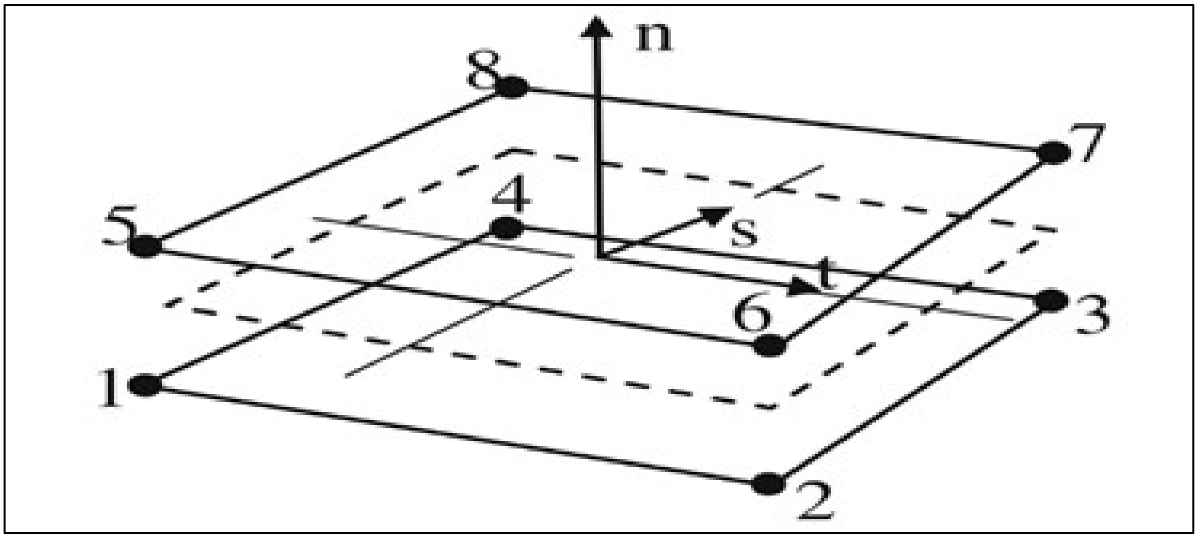

Figure 2.6 Element used in the numerical analysis (8-node 3-D cohesive element)
Taken from Obaidat et al. (2010)

GM Chen et al. (2012) conducted a finite element analysis focusing on the behavior of reinforced concrete (RC) beams strengthened in shear using FRP composites with the assistance of ABAQUS software. The primary objective of their study was to assess the interaction between stirrups and externally bonded FRP (EB-FRP) composites. They explored various bond-slip behavioral laws for the interface layer to understand their impact on the overall behavior of RC beams strengthened in shear with EB-FRP composites.

To simulate the contact between FRP and concrete, they employed a two-dimensional cohesive element (COH2D4) and a perfect bond model. For modeling the bond-slip behavior of the cohesive element, they utilized model introduced by Lu et al. (2005), as illustrated in Figure

2.7. This allowed them to effectively simulate the bond-slip behavior and interactions between the FRP and concrete in their analysis.

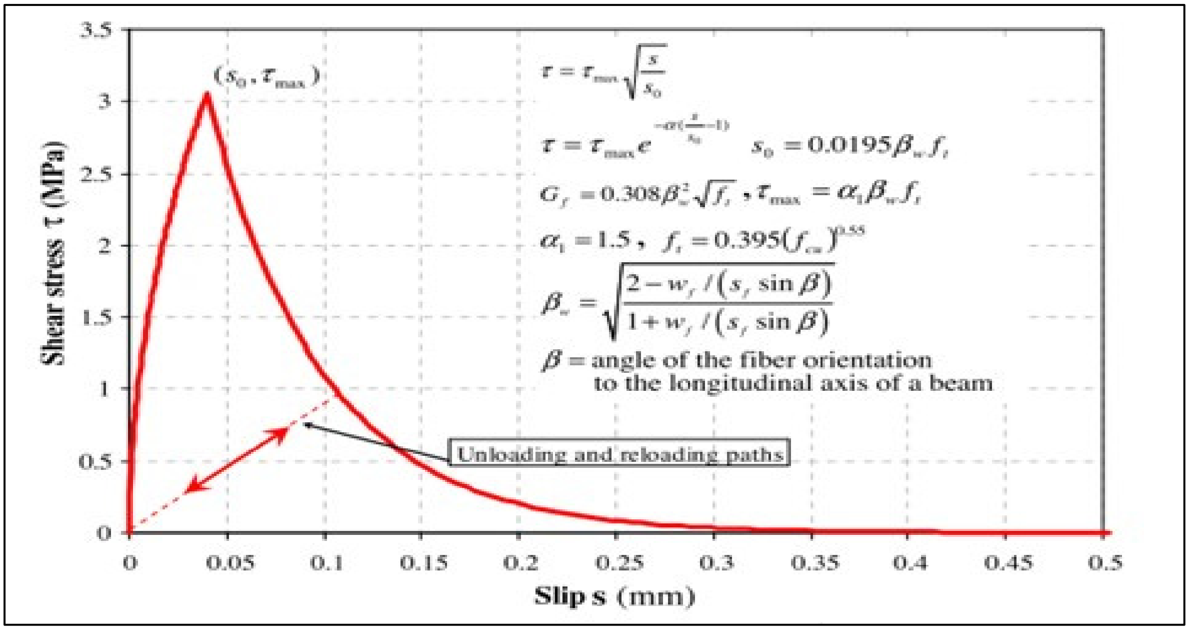

Figure 2.7 Bond–slip model between concrete and CFRP proposed by Lu et al. (2005)
Taken from GM Chen et al. (2012)

CHAPTER 3

SHEAR STRENGTHENING OF RC BEAMS WITH FRP COMPOSITES: DATABASE OF FE SIMULATIONS AND ANALYSIS OF STUDIED PARAMETERS

Amirali Abbasi[1], Omar Chaallal[2] and Georges El-Saikaly[3]

[1,2,3] Department of Construction Engineering, École de Technologie Supérieure
1100 Notre-Dame St W, Montreal (Quebec) H3C 1K3, Canada

Paper published in Journal of *Modelling and Simulation in Engineering*, Volume 27, Issue 1, January 2022

3.1 Abstract

The use of externally bonded fiber-reinforced polymer (EB-FRP) composites for shear strengthening of reinforced concrete (RC) beams presents many challenges given the complex phenomena that come into play. Premature bond failure, the behavior of the interface layer between FRP composites and the concrete substrate, the complex and brittle nature of shear cracks, and the adverse interaction between internal steel stirrups and EB-FRP are some of these phenomena. Compared to experimental investigations, the finite element (FE) technique provides an accurate, cost-effective, and less time-consuming tool, enabling practicing engineers to perform efficient, accurate nonlinear and dynamic analysis as well as parametric studies on RC beams strengthened with EB-FRP. Since 1996, many numerical studies have been carried out on the response of RC beams strengthened using FRP. However, only a few have been related to RC beams strengthened in shear using EB-FRP composites. In addition, the analytical models that have been reported so far have failed to address and encompass all the factors affecting the contribution of EB-FRP to shear resistance because they have mostly been based on experimental studies with limited scopes. The aim of this paper is to build an extensive database of all the studies using finite element analysis (FEA) carried out on RC beams strengthened in shear with EB-FRP composites and to evaluate their strengths and weaknesses through various studied parameters.

Keywords: finite element analysis (FEA); reinforced concrete beams; shear strengthening; externally bonded; fiber-reinforced polymer (FRP)

3.2 Introduction

Given its complexity and its propensity to brittle failure without warning, the shear behavior of reinforced concrete (RC) beams has long been a major concern in the field of structural engineering. Therefore, practicing engineers often privilege the sequence by which flexural failure occurs before shear failure. The lack of shear resistance in RC beams can be due to various interacting factors. Underestimating the real applied loads in the design process, lack of accuracy in the construction phase, and damage due to winds and earthquakes are examples of such factors. In recent years, fiber-reinforced polymer (FRP) composites for rehabilitation and strengthening of RC beams have gained in popularity and have reached worldwide acceptance since their first use as externally bonded (EB) fabrics/laminates to strengthen existing deficient structures in the late 1990s. Their success has been due to the high strength-to-weight ratio and the tensile strength they offer, which can compensate for the shear resistance deficiency of RC beams. Researchers have investigated various FRP shapes such as fabrics, laminates, bars, and rods. However, the EB method consisting of bonding FRP fabrics/laminates to the substrate of RC beams is the most common approach. Other techniques for shear strengthening of RC beams include the embedded through section (ETS) method as well as the near-surface (NSM) method. If the tensile strength of the concrete substrate is insufficient, mechanical anchorage systems in addition to resin epoxy are generally required. The interaction between concrete and EB-FRP composites depends on various complex interacting factors. There have been some finite element analysis (FEA) studies of RC beams strengthened in flexure. In contrast, due to the brittle nature of shear cracks and the complex behavior of the bond between concrete and EB-FRP laminates/fabrics, very few studies have considered FEA on RC beams strengthened in shear with EB-FRP. Because it is more cost-effective and less time-consuming than experimental studies, FEA has gained increasing attention in the last few years. Research conducted on RC beams strengthened in shear using EB-FRP has been very restricted. Some of previous studies also used simplistic assumptions, such as perfect bonding between components and a restrictive definition of shear cracks, leading to inaccurate prediction of the number and angles of shear cracks in RC beams affecting the effective bond length, further leading to inaccurate results. Finally, the other merit of FEA is that the response of all specimen components can be recorded during loading, resulting in an insightful comprehension of the complex relations between concrete, steel stirrups, longitudinal tensile reinforcement, and EB-FRP fabrics/laminates, which is impossible to attain by laboratory testing. The database built in the present study evaluates all the FEA carried out on RC beams strengthened in shear using FRP composites, including all the EB, NSM, and ETS strengthening techniques, with a special emphasis on the externally bonded method (EB). An evaluation has also been carried out on the parameters used in previous research studies as follows: type of FRP materials and shear strengthening configurations; size effect; interaction between components and types of interface element; analytical approach in FE simulations; number, size, and type of elements in simulation; ratio of EB-FRP, longitudinal, and transverse steel reinforcement; failure modes in concrete and EB-FRP (debonding, delamination, or rupture); effective stress, strain, and bond length; stress and strain distributions along the shear cracks; shape function of the crack, crack width, and crack pattern; and load-deflection response. Emphasis will be placed on showing the paramount importance of these parameters for the development of an analytical model to calculate the contribution of FRP laminates/fabrics to the ultimate shear capacity of RC beams shear-strengthened with EB-FRP.

3.3 Important Issues in Modeling RC Beams Strengthened with EB-FRP

To assess the crucial issues related to RC beams strengthened in shear with FRP composites, particularly their failure modes, a review of previous studies has been carried out. Among the few FE research studies related to this type of beam, only those that exhaustively described the main simulation assumptions and validated them with experimental tests were considered in this study. Modeling concrete and its cracks as an inhomogeneous material in FE models has always been a controversial issue. However, the development of FEM has paved the way for other solutions, such as implementing concrete damage plasticity theory (CDP) in the model programming. The plastic-damage model in concrete depends on the models developed by

Jacob Lubliner et al. (1989) and J. Lee and Fenves (1998). The CDP model can analyze concrete structures subjected to dynamic loading. Furthermore, it is appropriate for evaluating quasi-brittle materials like rock, mortar, and ceramics. The two main failure modes in concrete are cracking in tension and crushing in compression. The constitutive model of CDP can capture the influence of irretrievable damage related to the failure mechanisms that happen in concrete as well as in quasi-brittle materials. Modeling RC beams and their cracks on the one hand and the interaction between concrete, steel reinforcement, and FRP composites on the other are critical parts of a simulation. Generally, two models are used to describe concrete cracking: (i) the discrete crack model and (ii) the smeared crack model.

3.3.1 Discrete Crack Approach:

The discrete crack approach depends on the geometry of the model in which crack propagation spreads among the existing borders of each element when discontinuities are defined in FE discretization. Therefore, a crack's growth and angle rely on the size and shape of the mesh in FE programs, so that this method is mesh objective. The solution to overcome this objectivity is to define auto-remeshing programs, which lead to increased computational challenges by changing the mesh topology (GM Chen et al., 2012).

3.3.2 Smeared Crack Approach:

Unlike the discrete crack model that propagates among the discontinuities in an element, the smeared crack model grows through the continuity of the material and consequently through elements, by reducing the stiffness of discretized elements. The smeared crack model can be further divided into two categories: the fixed smeared crack model and the rotated smeared crack model. The former model does not change the crack angle, and as the load increases, a crack propagates during the whole calculation process. In the rotated smeared crack model, on the other hand, the orientation of the crack changes as the load increases, and new orientations are determined based on directions of updated main stresses and strains. Nevertheless, the smeared crack method leads to localization of strain, which means that when the element dimension is close to zero, the energy consumption approaches zero. This issue was solved by introducing the crack band model, which links the fracture energy to the constitutive law of concrete. Therefore, the fracture energy during crack propagation does not rely on the dimension of the element and the mesh, making this technique not mesh-objective (GM Chen et al., 2012).

3.3.3 Interactions between Steel Reinforcement and Concrete:

Studies conducted by previous researchers have shown that there is an inverse interaction between EB-FRP and steel reinforcement, particularly steel stirrups, which means that when the number of steel stirrups increases, the contribution of EB-FRP to shear resistance decreases (GM Chen et al., 2012). Furthermore, it has been shown that assuming a perfect bond model between the longitudinal steel reinforcement and the concrete results in more distributed crack patterns, leading to a narrower crack width. This affects the debonding process, which occurs in a later stage than without the assumption and consequently overestimates the ultimate shear resistance of the beam (GM Chen et al., 2012). However, noticeable disparities have been observed on the overall load-displacement curves of the specimens. The bond-slip model introduced in the European CEB-FIP Model Code 1990 (Code, 1993) is an appropriate indication of interaction between the concrete and the steel reinforcement (GM Chen et al., 2012).

3.3.4 Interface between EB-FRP and Concrete:

To predict the ultimate shear capacity of RC beams strengthened in shear using EB-FRP, the interaction between concrete and FRP composites should be defined precisely, because otherwise debonding mechanism between concrete and FRP composites cannot be detected. In addition, an accurate definition of the concrete-FRP interaction affects the angle and distribution of shear cracks. Indeed, the assumption of perfect bonding results in distributed diagonal shear cracks, whereas the correct bond model definition leads to one main diagonal shear crack. Therefore, assuming a perfect bond model between concrete and EB-FRP composites overestimates the ultimate load-carrying capacity of the beam (GM Chen et al., 2012). This demonstrates the importance of defining the bond model between concrete and FRP composites with high precision and accuracy.

3.4 Review and Synthesis of Previous Work on FE Modeling

When FRP composites were introduced in the construction industry, computer programs and FE packages were not developed as much as today. As a result, most evaluations of the efficiency of RC beams strengthened in shear with EB-FRP composites were based on laboratory tests, and hence the effect of many parameters on the overall response of these tested beams could not be detected. This was particularly true when some of these parameters interacted with each other, making the behavior of these beams complex and difficult to fully understand. In addition, once FE programs were developed, most studies that used them concentrated on strengthening in flexure of RC beams using EB-FRP composites. In this section, the main FE studies carried out on RC beams strengthened in shear, as well as the major parameters affecting the response of these beams and their components, are gathered and presented in Figure 3.1.

Figure 3.1 includes 34 studies from 1996 to 2020, with a total of 239 RC beams strengthened in shear using FRP composites, six of them were subjected to microscopic studies in which the stress and strain distributions along fictional diagonal shear cracks and the effective bond length were examined (GM Chen, Teng, et al., 2010; Lu et al., 2009), and the rest (233 beams) were simulated using FE software. The details of these 239 shear-strengthened RC beams subjected to FEA are presented in Table 3.1, Table 3.2, and Table 3.3. Generally, in terms of depth, RC beams are generally classified into three groups depending on their shear span-to-depth ratio (a/d), as follows: (i) a/d less than 1 is a deep beam; (ii) a/d between 1 and 2.5 is a moderately deep beam, with shear failure likely occurring before flexure failure; and (iii) a/d equal to or greater than 2.5 is a flexural slender beam that often exhibits flexure before shear failure.

The shape of RC beams is designed based on their applications and the load they carry. For example, beams with an I cross section are generally used by the road and bridge construction industries in which shear strength is of paramount importance, whereas beams with a T cross section can be designed for either the road building or the housing industry. Figure 3.2 presents a histogram of 233 RC beams strengthened in shear using EB-FRP and studied by FEA to evaluate the shear contribution of FRP to the ultimate shear capacity of beams. The histogram shows that, among the 233 beams, 46 were T-shaped, 175 were rectangular, and 12 were I-shaped cross-sections, representing 19.7%, 75.1%, and 5.1% respectively of all the shear-strengthened RC beams. Therefore, despite their generalized use in practice, few FE studies focused on T cross-sectional beams (19.7%), indicating the need for more research on the response of these beams and their influencing parameters. Shear span-to-depth ratio plays a crucial role in the behavior of these beams, and, as illustrated in the histogram, 110 (47.2%) and 118 (52.9%) of the beams belong to the moderately deep ($1 < a/d < 2.5$) and the flexural slender ($a/d \geq 2.5$) beam categories, respectively, showing that more research is needed on deep beams ($a/d \leq 1$) where shear failure usually occurs before flexure failure.

The configuration type of shear strengthening using EB-FRP is to some extent a function of the cross section of RC beams. For instance, the full-wrap technique cannot be used for shear strengthening of T-shaped or I-shaped section beams because the flange of these beams is generally not accessible. To this end, other effective methods of shear strengthening can be used for these beam cross section shapes, such as side-bonded, U-shaped, ETS, or NSM techniques. As for the interaction between stirrups and FRP composites, experimental tests show that the ETS configuration leads to a greater contribution to shear resistance compared to EB-FRP. In addition, because the concrete core is generally stronger than its surface, more confinement is expected on the ETS bond than with externally bonded (EB) methods. Simple installation and high efficiency are some of the merits of this method. Among the 239 RC beams of all studies presented in Figure 3.1, 221 (92%) beams were subjected to FE studies that focused on shear strengthening using the EB method (Side-bonded, U-wrap and Full-wrap EB-FRP configurations) (Table 3.1), and only 18 (8%) beams corresponded to the ETS and NSM methods (Table 3.2). In addition, as illustrated in Figure 3.3, among the 239 RC beams shear-strengthened with FRP, only 39 beams (16.3%) were T-shaped cross-sections, indicating the research needs for FEA to study the parameters affecting the response of such beams.

3.5 Main Studied Parameters Using FEA of Shear-Strengthened Beams

With the advantages of FEA, many of the shear responses of RC beams strengthened using FRP composites that cannot be captured by experiments can be studied from initiation of loading to ultimate failure while recording the whole failure process and its mechanisms. Most of the results derived from laboratory tests were based on the load-deflection response of the beam and the strain on the FRP composite obtained from strain gauges installed on FRP laminates, fabrics, and bars. In contrast, more parameters can be observed and studied using FEA, as illustrated in Figure 3.4, which highlights the variations in all components of the shear strengthened beams. In addition, the complex interactive behavior between the components (concrete, longitudinal steel reinforcement, steel stirrups, and FRP composite) of the studied beams and their interrelations can be interpreted to achieve a more precise closed-form model that integrates all these factors.

3.5.1 Shape Function of the Crack, Crack Pattern, and Crack Width:

Because the width of a crack along its propagation path is not constant, the strain and stress distributions on FRP laminates/fabrics are not uniform. This nonuniformity of stresses and strains influences the response of steel stirrups and FRP laminates/fabrics. This means that the steel stirrups crossed by the shear crack reach the yielding point, and then, the FRP laminates/fabrics crossed by the shear cracks reach their maximum tensile strength, leading to rupture. Therefore, J. F. Chen and J. Teng (2003) introduced a distribution factor to calculate the effective stress and strain in FRP laminates/fabrics:

$$f_{FRP,e} = D_{FRP} \times f_{FRP} \tag{3.1}$$

			Geometry			Beam type			Interface		Crack type			Studied parameters											Types of configuration in shear					
Author	(a)	(b)	(c)	(d)	(e)	(f)	(g)	(h)	(i)	(j)	(k)	(l)	(m)	(n)	(o)	(p)	(q)	(r)	(s)	(t)	(u)	(v)	(w)	(x)	(y)	(z)	(ab)	(ac)	(ad)	(af)
(Kaliakin et al.)	1996	8		●				●			●												●			●				
(Arduini et al.)	1997	1	●					●			●										●		●							
(Amir)	1998	1	●					●			●			●			●	●			●							●		
(Vecchio et Bucci)	1999	1	●				●				●												●					●		
(Lee et al.)	2000	2		●				●					●								●		●	●					●	
(Kachlakev et al.)	2001	2	●					●			●			●						●	●		●	●		●				
(Wong et Vecchio)	2003	4	●					●	●		●				●			●	●			●	●						●	
(Santhakumar et al.)	2004	2	●					●			●									●			●	●		●				
(Elyasian et al.)	2006	4	●					●			●			●	●		●						●		●					
(Otoom et al.)	2006	1	●					●	●			●									●		●							●
(Qu et al.)	2006	1	●				●		●		●										●		●							●
(Smith et al.)	2006	1	●						●												●		●							●
(Godat et al.)	2007	11	●	●				●	●		●			●			●	●	●		●		●			●		●	●	●
(Godat et al.)	2008	3	●				●		●		●										●		●	●						●
(Lee et al.)	2008	3	●					●	●		●												●	●		●				●
(Lu et al.)	2009	8	●						●					●	●			●			●			●					●	●
(Chen et al.)	2010	2	●						●	●				●				●		●				●					●	●
(Godat et al.)	2010	4	●				●		●		●			●	●				●		●		●		●					●
(Hawileh et al.)	2011	1	●					●	●														●				●			
(Hawileh et al.)	2011	7		●				●	●		●			●			●				●		●	●		●			●	
(You et al.)	2011	10			●			●	●			●									●		●							●
(Hawileh et al.)	2012	4	●			●			●		●			●					●				●	●		●		●		
(Chen et al.)	2012	2	●						●	●		●									●	●	●							●
(Dirar et al.)	2012	5		●				●	●			●					●			●	●		●	●		●				
(Godat et al.)	2012	17	●	●			●	●	●		●			●	●		●		●				●			●		●	●	●
(Godat et al.)	2012	4	●					●	●		●										●	●	●			●			●	
(Imperatore et al.)	2012	2		●				●	●	●	●										●		●							●
(Godat et al.)	2013	3		●				●	●		●				●		●				●		●				●			
(Sayed et al.)	2013	55	●				●		●		●			●	●		●		●						●	●		●	●	●
(Manos et al.)	2014	8	●					●	●		●								●		●		●							●
(Qapo et al.)	2015	2			●			●	●		●				●		●					●	●	●						●
(Qapo et al.)	2016	6		●				●	●		●				●							●	●	●			●			
(Ibars et al.)	2018	8	●					●	●		●				●			●	●			●	●		●					●
(Hawileh et al.)	2019	6	●			●	●	●	●		●				●						●		●				●			
(Al Jawahery et al.)	2019	10	●				●	●	●	●		●			●				●				●	●						●
(Jin et al.)	2020	28	●				●		●	●				●	●		●						●	●					●	
(Shomali et al.)	2020	2	●				●		●		●				●		●		●	●	●		●	●			●			

Note: (a) Year, (b) No. of specimens, (c) Rectangular section, (d) T-section, (e) I-section, (f) $a/d \leq 1$, (g)$1 < a/d < 2.5$, (h) $a/d \geq 2.5$, (i) Interface (concrete-to-FRP), (j) Interface (concrete-to-steel), (k) Smeared crack model, (l) Smeared + crack band, (m) Discrete crack model, (n) Types of configuration in shear & different FRP materials, (o) Size effect, concrete strength, (p) Analysis approach types of solvers in FEA (dynamic versus static), (q) Ratio of longitudinal steel reinforcements ρ_w, steel stirrups ρ_s, and EB FRP ρ_{FRP}, (r) Effective stress and strain, bond-length, distribution factors, (s) Types of the failure (debonding, delamination, rapture), (t) number, size, types of elements in simulation, (u) Strain, stress and slip distribution along t he vertical, horizontal axis of the beam or along diagonal crack on FRP fabrics/laminates, (v) Interaction between Components, types of interface elements, (w) Load-deflection curve, total shear capacity, (x) Shape function of the crack, crack pattern, crack width, (y) Full wrap, (z) Continuous U wrap, (ab) NSM, ETS, (ac) Continuous side-bonded, (ad) Side-bonded strips, (af) U strip

Figure 3.1 Summary of parameters studied on RC beams strengthened in shear by FRP composites by FEA

Table 3.1 Database of numerical studies assessing parameters of RC beams strengthened in shear with externally bonded FRP composites and validating with and without experimental tests

Specimen	Section	d_{fv}	h_f	h_w	b_w	d	nt_f	a/d	f'_c	$\rho_{\mathrm{FRP}}(\%)$	$\rho_w(\%)$	$\rho_s(\%)$	Configuration	β(degree)	Fiber	E_s	E_{FRP}	ε_{fu}	$V_{t(\exp)}$	$V_{t(\mathrm{NUM})}$
Kaliakin et al. [25]																				
C1	T	88.9	63.5	127	63.5	152.4	—	2.67	59.6	0	2.05	0	—	—	—	200	—	—	38.3	37.7
C2	T	88.9	63.5	127	63.5	152.4	—	2.67	74.3	0	2.05	0	—	—	—	200	—	—	39.8	39.3
C3	T	88.9	63.5	127	63.5	152.4	—	2.67	54.5	0	2.05	0	—	—	—	200	—	—	38.5	38
C4	T	88.9	63.5	127	63.5	152.4	—	2.67	56.5	0	2.05	0	—	—	—	200	—	—	36	35.5
A1	T	88.9	63.5	127	63.5	152.4	1.04	2.67	54.5	3.28	2.05	0	CT-U	90	A	200	11.03	0.0225	77.4	78.4
A2	T	88.9	63.5	127	63.5	152.4	1.04	2.67	58.0	3.28	2.05	0	CT-U	90	A	200	11.031	0.0225	60.1	—
E1	T	88.9	63.5	127	63.5	152.4	0.46	2.67	50.2	1.44	2.05	0	CT-U	90	E-G	200	14.27	0.0134	73.5	—
E2	T	88.9	63.5	127	63.5	152.4	0.46	2.67	58.0	1.44	2.05	0	CT-U	90	E-G	200	14.27	0.0134	67.9	61.5
G1	T	88.9	63.5	127	63.5	152.4	0.58	2.67	52.7	1.833071	2.05	0	CT-U	90	G	200	20.96	0.0095	71	64.3
G2	T	88.9	63.5	127	63.5	152.4	0.58	2.67	56.6	1.833071	2.05	0	CT-U	90	G	200	20.960	0.0095	72.9	66
45G1	T	88.9	63.5	127	63.5	152.4	0.58	2.67	56.6	1.833071	2.05	0	CT-U	45	G	200	20.960	0.0095	75.1	68
45G2	T	88.9	63.5	127	63.5	152.4	0.58	2.67	50.2	1.833071	2.05	0	CT-U	45	G	200	20.960	0.0095	94.5	85.6
Arduini et al. [26]																				
B4	R	350	—	400	300	350	0.51	3.14	39.6	0.113333	0.37	0.28	CT-U	90	C	200	400	0.0075	—	—
Amir [27]																				
IF	R	175	—	200	127	175	2	2.61	36.5	3.149606	1.80	0.21	CTS	45	C	200	34.13	—	—	—
Vecchio and Bucci [28]																				
Beam 1	R	935	—	1000	550	935	—	2.16	44.7	—	0.81	0.06	—	—	—	492	—	—	1700	1800
Beam 2	R	935	—	1000	550	935	1	2.16	44.7	0.363636	0.81	0.06	CTS	90	C	492	230	0.0142	2528	—
Lee et al. [29]																				
Model 1	T	192.8	75	230	140	267.8	—	2.98	25	—	4.46	0.18	—	—	—	200	—	—	—	64
Model 2	T	192.8	75	230	140	267.8	—	2.98	25	—	4.46	0.18	—	—	—	200	—	—	—	48
Model 3	T	192.8	75	230	140	267.8	1.2	2.98	25	0.337458	4.46	0.18	ST-U	90	C	200	165	0.014	—	78
Model 4	T	192.8	75	230	140	267.8	1.2	2.98	25	0.337458	4.46	0.18	ST-U	90	C	200	165	0.014	—	93
Kachlakev et al. [30]																				
Control beam	R	—	—	768.35	305	704.85		2.59	16.7	0	0.54	0	—	—	—	200	—	—	476	454
Shear beam	R	679.45	—	768.35	305	704.85	5.2	2.59	14.7	3.409836	0.54	0	CTS	90	Glass	200	21	—	689	525
Flexure/shear beam	R	679.45	—	768.35	305	704.85	5.2	2.59	13.0	3.409836	0.54	0	CTS + flexural strengthening	90	C/ glass	200	62-21	—	712	930
Wong and Vecchio [31]																				
RWOA-1	R	470	—	560	305	470	0.84	3.89	22.6	0.367213	1.67	—	ST-S	90	C	217.87	72.4	0.011	493	—
RWOA-2	R	470	—	560	305	470	0.84	4.86	25.9	0.367213	2.16	—	ST-S	90	C	217.87	72.4	0.011	457	—
RWOA-3	R	470	—	560	305	470	0.84	6.80	43.5	0.367213	2.65	—	ST-S	90	C	205.46	72.4	0.011	436	—
Beam 1 (De rose)	R	935	—	560	550	935		2.16	44.7	—	0.81	0.06	—	—	—	492	—	—	1700	1800
Beam 2 (De rose)	R	935	—	560	550	935	1	2.16	44.7	0.363636	0.81	0.06	CTS	90	C	492	230	0.0142	2528	2465
Santhakumar et al. [32]																				
C48	R	164.05	—	203.2	127	164.05	—	2.78	36.5	—	1.93	0.21	—	—	—	200	—	—	—	—
IIIFu	R	164.05	—	203.2	127	164.05	1.49	2.78	36.5	2.36063	1.93	0.21	CT-U	45	C	200	28.3	0.009	—	—
IE	R	164.05	—	203.2	127	164.05	2.18	2.78	36.5	3.43937	1.93	0.21	CT-U	90	C	200	34.1	0.009	—	—

Table 3.1 Database of numerical studies assessing parameters of RC beams strengthened in shear with externally bonded FRP composites and validating with and without experimental tests (Continued)

Specimen	Section	d_{fv}	h_f	h_w	b_w	d	nt_f	a/d	f'_c	ρ_{FRP}(%)	ρ_w(%)	ρ_s(%)	Configuration	β(degree)	Fiber	E_s	E_{FRP}	ε_{fu}	$V_{t(\exp)}$	$V_{t(\mathrm{NUM})}$
Elyasian et al. [33]																				
SB-90	R	320.5	—	380	230	320.5	0.18	2.85	31	0.156522	1.33	0.18	CTW	90	C	200	228	0.018	451	—
SB-90-0	R	320.5	—	380	230	320.5	0.36	2.85	31	0.313043	1.33	0.18	CTW	90	C	200	228	0.018	468	—
SB-45	R	320.5	—	380	230	320.5	0.18	2.85	31	0.156522	1.33	0.18	CTW	45	C	200	228	0.018	529	—
SB-45-0	R	320.5	—	380	230	320.5	0.36	2.85	31	0.313043	1.33	0.18	CTW	45	C	200	228	0.018	528	—
Otoom et al. [34]																				
S03-1	R	260	—	305	150	260		2.92	28	—	4.12	—	—	—		200	—	—	154	—
S03-2	R	260	—	305	150	260	0.16	2.92	28	0.088	4.12	—	ST-U	90	C	200	228	0.0165	262	265
Qu et al. [35]																				
S0-2-0	R	260	—	—	—	260	—	2.15	31.8	—	2.9	0.19	—	0	—	—	—	—	—	—
S-CU-2-1	R	260	—	—	—	260	—	2.15	37.6	0.074	2.9	0.19	ST-U	90	C	—	235	—	—	—
Smith et al. [36]																				
BS3	—	—	—	—	—	—	—	—	—	—	—	—	—	—	—	—	—	—	—	—
BS5	—	—	—	—	—	—	—	—	—	—	—	—	ST-U	—	—	—	—	—	—	—
Godat et al. [37]																				
B-1	R	—	—	200	150	170		3	30.5	—	2.98	—	—	—	—	182	—	—	40	41
B-8	R	170	—	200	150	170	0.16	3	35.4	0.222667	2.98	—	CT-U	90	C	182	230	0.015	86	90
TR30D1	R	250	—	300	150	250		3	31.4	—	—	0.33	—	—	—	210	—	—	322	323
TR30D3	R	250	—	300	150	250	0.16	3	31.4	0.22	—	0.33	CTS	90	C	210	233.6	0.015	323	336
TR30D4	R	250	—	300	150	250	0.33	3	31.4	0.44	—	0.33	CTS	90	C	210	233.6	0.015	400	399
TR30D2	R	250	—	300	150	250	0.49	3	31.4	0.66	—	0.33	CTS	90	C	210	233.6	0.015	422	414
BT1	T	256.66	100	305	150	356.66	—	3	35	—	2.30	—	—	—	—	200	—	—	178	184
BT2	T	256.66	100	305	150	356.66	0.16	3	35	0.22	2.30	—	CT-U	90	C	200	228	0.0166	309	313
BT3	T	256.66	100	305	150	356.66	0.33	3	35	0.44	2.30	—	CT-U	90	C	200	228	0.0166	310	313
BT4	T	256.66	100	305	150	356.66	0.16	3	35	0.088	2.30	—	ST-U	90	C	200	228	0.0166	324	325
BT5	T	256.66	100	305	150	356.66	0.16	3	35	0.088	2.30	—	ST-S	90	C	200	228	0.0166	243	247
BT6	T	256.66	100	305	150	356.66	0.16	3	35	0.22	2.30	—	CT-U + anchorage	90	C	200	228	0.0166	442	453
US	R	216	—	250	150	216		2.5	35	—	—	—	—	—	—	200	—	—	114	119
RS90	R	216	—	250	150	216	1	2.5	35	0.666667	—	—	ST-S	90	C	200	150	0.014	184	197
RS135	R	216	—	250	150	216	1	2.5	35	0.444444	—	—	Inclined ST-S	45	C	200	150	0.014	194	202
Godat et al. [38]																				
RC1	R	—	—	200	100	166		2.04	51.2	—	4.1	—	—	90	—	200	235	—	160	166
U4	R	166	—	200	100	166	0.111	2.04	51.2	0.1332	4.1	—	ST-U	90	C	200	235	0.0151	203	213
RC2	R	—	—	400	200	330		2.06	49.7	—	4.5	—	—	90	—	200	235	—	709	745
U5	R	330	—	400	200	330	0.222	2.06	51.2	0.1332	4.5	—	ST-U	90	C	200	235	0.0151	809	813
RC3	R	—	—	600	300	498		2.04	50.5	—	4.2	—	—	90	—	200	235	—	1626	1659
U6	R	498	—	600	300	498	0.33	2.04	51	0.1332	4.2	—	ST-U	90	C	200	235	0.0151	2018	2053
Lee et al. [39]																				
SO3-1	R	253.33	—	305	150	253.33		3	27.5	—	4.23	—	—	90	—	200	—	—	154	—
SO3-2	R	253.33	—	305	150	253.33	0.16	3	27.5	0.088	4.23	—	ST-U	90	C	200	228	0.0166	262	—
SO3-4	R	253.33	—	305	150	253.33	0.16	3	27.5	0.22	4.23	—	CT-U	90	C	200	228	0.0166	289	—
SO3-5	R	253.33	—	305	150	253.33	0.33	3	27.5	0.44	4.23	—	CT-U	90	C	200	228	0.0166	339	—

Table 3.1 Database of numerical studies assessing parameters of RC beams strengthened in shear with externally bonded FRP composites and validating with and without experimental tests (Continued)

Specimen	Section	d_{fv}	h_f	h_w	b_w	d	nt_f	a/d	f'_c	$\rho_{FRP}(\%)$	$\rho_w(\%)$	$\rho_s(\%)$	Configuration	β(degree)	Fiber	E_s	E_{FRP}	ε_{fu}	$V_{t(exp)}$	$V_{t(NUM)}$
Godat et al. [40]																				
RC1	R	—	—	200	100	166		2.04	51.2	—	4.1	—	—	90	—	200	235	—	160	166
U4	R	166	—	200	100	166	0.11	2.04	51.2	0.1332	4.1	—	ST-U	90	C	200	235	0.0151	203	213
RC2	R		—	400	200	330		2.06	49.7	—	4.5	—	—	90	—	200	235	—	709	745
U5	R	330	—	400	200	330	0.22	2.06	51.2	0.1332	4.5	—	ST-U	90	C	200	235	0.0151	809	813
RC3	R	—	—	600	300	498		2.04	50.5	—	4.2	—	—	90	—	200	235	—	1626	1659
U6	R	498	—	600	300	498	0.33	2.04	51	0.1332	4.2	—	ST-U	90	C	200	235	0.0151	2018	2053
W7	R	498	—	600	300	498	0.33	2.04	51	0.222	4.2	—	CTW	90	C	200	235	0.0151	2221	2203
You et al. [41]																				
T4-12-control	I	817	—	—	152	944	—	2.9	68.5	0	—	0.31	—	—	—	178	210	—	894	903
T4-18-control	I	817	—	—	152	944	—	2.9	68.7	0	—	0.2	—	—	—	178	210	—	912	858
T4-18-S90-NA	I	817	—	—	152	944	0.31	2.9	69.1	0.14	—	0.2	ST-U	90	C	178	210	0.017	983	961
T4-18-S90-CMA	I	817	—	—	152	944	0.31	2.9	69.8	0.14	—	0.2	ST-U	90	C	178	210	0.017	1085	1010
T4-18-S90-DMA	I	817	—	—	152	944	0.31	2.9	70	0.14	—	0.2	ST-U	90	C	178	210	0.017	1005	1023
T4-12-control-deck	I	817	—	—	152	944	—	2.9	73.5	0	—	0.31	—	—	—	178	210	—	1090	1112
T4-12-S90-SDMA	I	817	—	—	152	944	0.31	2.9	71.2	0.14	—	0.31	ST-U	90	C	178	210	0.017	1139	1174
T3-12-control	I	655	—	—	152	782	—	3.4	61.3	0	—	0.31	—	—	—	178	210	—	1121	1014
T3-12-S90-NA	I	655	—	—	152	782	0.31	3.4	61.4	0.14	—	0.31	ST-U	90	C	178	210	0.017	1201	1152
T3-12-S90-NA-PC	I	655	—	—	152	782	0.31	3.4	65.3	0.14	—	0.31	ST-U	90	C	178	210	0.017	1085	1143
T3-12-S90-DMA	I	655	—	—	152	782	0.31	3.4	71.6	0.14	—	0.31	ST-U	90	C	178	210	0.017	1108	1143
T3-18-control	I	655	—	—	152	782	—	3.4	66.1	0	—	0.2	—	—	—	178	210	—	1121	912
T3-18-S90-NA	I	655	—	—	152	782	0.31	3.4	69.8	0.14	—	0.2	ST-U	90	C	178	210	0.017	943	907
T3-18-S90-HS	I	655	—	—	152	782	0.31	3.4	70.2	0.14	—	0.2	ST-U	90	C	178	210	0.017	979	894
T3-18-S90-SDMA	I	655	—	—	152	782	0.31	3.4	71.9	0.14	—	0.2	ST-U	90	C	178	210	0.017	1045	907
Hawileh et al. [42]																				
TB 1-60-90°	T	260	120	75	285	335	0.12	5	32.4	0.1666	0.98	0	ST-S	90	C	205	231	0.017	57.17	55.07
TB 1-0-90°	T	260	120	75	285	335	0.12	5	32.4	0.2	0.98	0	CT-S	90	C	205	231	0.017	—	65.13
TB 1-17-90°	T	260	120	75	285	335	0.12	5	32.4	0.58	0.98	0	ST-S	90	C	205	231	0.017	—	60
TB 1-153-90°	T	260	120	75	285	335	0.12	5	32.4	0.06	0.98	0	ST-S	90	C	205	231	0.017	—	47
TB 2-60-90°	T	260	120	75	285	335	0.24	5	32.4	0.333	0.98	0	ST-S	90	C	205	231	0.017	—	58
TB 3-60-90°	T	260	120	75	285	335	0.36	5	32.4	0.5	0.98	0	ST-S	90	C	205	231	0.017	—	63
TB 1-60-45° X	T	260	120	75	285	335	0.12	5	32.4	0.166	0.98	0	Inclined ST-S	45	C	205	231	0.017	—	65
Hawileh et al. [43]																				
FS-200-C	R	400	—	80	500	400	0.381	0.8	21	0.95	1.54	0.46	CT-U	90/0	C	200	230	0.015	270.5	270
FS-250-C	R	400	—	80	500	400	0.381	0.8	21	0.95	1.54	0.46	CT-U	90/0	C	200	230	0.015	182	186
FS-250-T	R	400	—	80	500	400	0.381	0.8	21	0.95	1.54	0.46	CT-U	90/0	C	200	230	0.015	219.4	219.3
FS-250-B	R	400	—	80	500	400	0.381	0.8	21	0.95	1.54	0.46	CT-U	90/0	C	200	230	0.015	186.6	185.5

Table 3.1 Database of numerical studies assessing parameters of RC beams strengthened in shear with externally bonded FRP composites and validating with and without experimental tests (Continued)

Specimen	Section	d_{fv}	h_f	h_w	b_w	d	nt_f	a/d	f'_c	$\rho_{\text{FRP}}(\%)$	$\rho_w(\%)$	$\rho_s(\%)$	Configuration	β(degree)	Fiber	E_s	E_{FRP}	ε_{fu}	$V_{t(\text{exp})}$	$V_{t(\text{NUM})}$
Chen et al. [3]																				
SO3-1	R	260	—	305	150	260	—	2.92	27.5	—	4.12	—	—	—	—	200	—	—	154	—
SO3-2	R	260	—	305	150	260	0.16	2.92	27.5	0.088	4.12	—	ST-U	90	C	200	228	0.0166	262	—
BS3	R	403.22	—	450	200	403.22	—	3.1	37.5	—	2.33	0.07	—	—	—	200	—	—	136.6	—
BS5	R	403.22	—	450	200	403.22	0.11	3.1	36	0.013875	2.33	0.07	ST-U	90	C	200	233	0.015	170	—
Dirar et al. [44]																				
F/295/LP1/4.5	T	295	105	245	105	295	0.39	3.8	24	0.249524	4.5	0.21	CT-U	90	C	200	238	0.018	135	114.8-134.4-134.4
F/295/LP2/4.5	T	295	105	245	105	295	0.39	3.8	27	0.249524	4.5	0.21	CT-U	90	C	200	238	0.018	133.5	127.2-153.6-142.4
F/215/LP1/4.6	T	215	105	165	105	215	0.39	3.8	32	0.249524	4.6	0.21	CT-U	90	C	200	238	0.018	122.5	113-132.6-132.4
F/215/LP2/4.6	T	215	105	165	105	215	0.39	3.8	25	0.249524	4.6	0.21	CT-U	90	C	200	238	0.018	102.5	96.6-115.6-109
F/295/LP1/3.3	T	295	105	245	105	295	0.39	3.8	28	0.249524	3.3	0.21	CT-U	90	C	200	238	0.018	96.5	125-108-119
Godat et al. [45]																				
SGU-1-1	R	—	—	—	150	—	—	1.5	—	—	—	—	—	—	—	—	—	—	355	368
S0-2-0	R	—	—	—	150	—	—	1.5	—	—	—	—	—	—	—	—	—	—	222	230
SGU-2-1a	R	—	—	—	150	—	—	1.5	—	—	—	—	—	—	—	—	—	—	301	300
SGU-2-1b	R	—	—	—	150	—	—	1.5	—	—	—	—	—	—	—	—	—	—	516	515
SGU-2-2	R	—	—	—	150	—	—	2.15	—	—	—	—	—	—	—	—	—	—	285	301
SGU-2-3	R	—	—	—	150	—	—	2.15	—	—	—	—	—	—	—	—	—	—	347	366
SCU-2-1	R	—	—	—	150	—	—	2.15	—	—	—	—	—	—	—	—	—	—	294	291
SGO-2-1	R	—	—	—	150	—	—	2.15	—	—	—	—	—	—	—	—	—	—	530	538
SGUB-2-1	R	—	—	—	150	—	—	2.8	—	—	—	—	—	—	—	—	—	—	306	314
SGU-3-1	R	—	—	—	150	—	—	2.8	—	—	—	—	—	—	—	—	—	—	221	239
R1	T	—	—	—	225	—	—	2.8	—	—	—	—	—	—	—	—	—	—	495	515
0.75D	T	—	—	—	225	—	—	3	—	—	—	—	ST-U	—	—	—	—	—	762	804
0.6D	T	—	—	—	225	—	—	3	—	—	—	—	ST-U	—	—	—	—	—	797	816
0.5D	T	—	—	—	225	—	—	3	—	—	—	—	ST-U	—	—	—	—	—	892	940
RC1	R	166	—	200	100	166	—	2.04	51.2	—	4.1	—	—	90	—	200	235	—	160	166
U4	R	166	—	200	100	166	0.11	2.04	51.2	0.1332	4.1	—	ST-U	90	C	200	235	0.0151	203	213
RC2	R	330	—	400	200	330	—	2.06	49.7	—	4.5	—	—	90	—	200	235	—	709	745
U5	R	330	—	400	200	330	0.22	2.06	51.2	0.1332	4.5	—	ST-U	90	C	200	235	0.0151	809	813
RC3	R	498	—	600	300	498	—	2.04	50.5	—	4.2	—	—	90	—	200	235	—	1626	1659
U6	R	498	—	600	300	498	0.33	2.04	51	0.1332	4.2	—	ST-U	90	C	200	235	0.0151	2018	2050
W7	R	498	—	600	300	498	—	3	—	—	—	—	—	—	—	—	—	0.0151	2221	2203
B-1	R	170	—	200	150	170	—	3	30.5	—	2.98	—	—	—	—	182	—	—	40	41
B-8	R	170	—	200	150	170	0.16	3	35.4	0.222667	2.98	—	CT-U	90	C	182	230	0.015	86	90
TR30D1	R	250	—	300	150	250		3	31.4	—	—	0.33	—	—	—	210	—	—	322	323
TR30D3	R	250	—	300	150	250	0.16	3	31.4	0.22	—	0.33	CTS	90	C	210	233.6	0.015	323	336
TR30D4	R	250	—	300	150	250	0.33	3	31.4	0.44	—	0.33	CTS	90	C	210	233.6	0.015	400	399
TR30D2	R	250	—	300	150	250	0.49	3	31.4	0.66	—	0.33	CTS	90	C	210	233.6	0.015	422	414
BT1	T	256.66	100	305	150	356.66		3	35	—	2.30	—	—	—	—	200	—	—	178	184
BT2	T	256.66	100	305	150	356.66	0.16	3	35	0.22	2.30	—	CT-U	90	C	200	228	0.0166	309	313

Table 3.1 Database of numerical studies assessing parameters of RC beams strengthened in shear with externally bonded FRP composites and validating with and without experimental tests (Continued)

Specimen	Section	d_{fv}	h_f	h_w	b_w	d	nt_f	a/d	f'_c	$\rho_{\text{FRP}}(\%)$	$\rho_w(\%)$	$\rho_s(\%)$	Configuration	β(degree)	Fiber	E_s	E_{FRP}	ε_{fu}	$V_{t(\text{exp})}$	$V_{t(\text{NUM})}$
BT3	T	256.66	100	305	150	356.66	0.33	3	35	0.44	2.30	—	CT-U	90	C	200	228	0.0166	310	313
BT4	T	256.66	100	305	150	356.66	0.16	3	35	0.088	2.30	—	ST-U	90	C	200	228	0.0166	324	325
BT5	T	256.66	100	305	150	356.66	0.16	3	35	0.088	2.30	—	ST-S	90	C	200	228	0.0166	243	247
BT6	T	256.66	100	305	150	356.66	0.16	3	35	0.22	2.30	—	CT-U + anchorage	90	C	200	228	0.0166	442	453
US	R	216	—	250	150	216		2.5	35	—	1.63	0.21	—	—	—	200	—	—	114	119
RS90	R	216	—	250	150	216	1	2.5	35	0.666667	1.63	0.21	ST-S	90	C	200	150	0.014	184	197
RS135	R	216	—	250	150	216	1	2.5	35	0.444444	1.63	0.21	Inclined ST-S	45	C	200	150	0.014	194	202
Godat et al. [46]																				
B-1	R	170	—	200	150	170	—	3	30.5	—	2.98	—	—	—	—	182	—	—	80	82-82
B-8	R	170	—	200	150	170	0.16	3	35.4	0.222667	2.98	—	CT-U	90	C	182	230	0.015	172	180-159
TR30D1	R	250	—	300	150	250	—	3	31.4	—	—	0.33	—	—	—	210	—	—	322	323-323
TR30D3	R	250	—	300	150	250	0.16	3	31.4	0.22	—	0.33	ST-S	90	C	210	233.6	0.015	323	336-300
US	R	216	—	250	150	216	—	2.5	35	—	1.63	0.21	—	—	—	200	—	—	114	119-119
RS90	R	216	—	250	150	216	1	2.5	35	0.666667	1.63	0.21	ST-S	90	C	200	150	0.014	184	162-176
RS135	R	216	—	250	150	216	1	2.5	35	0.444444	1.63	0.21	Inclined ST-S	45	C	200	150	0.014	194	202-184
Imperatore et al. [47]																				
TM1	T	273	210	315	260	483	—	—	19.1	—	0.72	0.15	ST-U	45	C	—	65.5	0.00822	450	—
TM2	T	268	210	310	260	478	—	—	25.5	—	0.72	0.15	ST-U	45	C	—	65.5	0.00822	500	—
Sayed et al. [48]																				
2S-1	R	360	—	400	200	360	0.1	1.8	30	0.05	2.05	0.25	ST-S	90	C	240	200	0.015	—	163.1
2S-2	R	360	—	400	200	360	0.2	1.8	30	0.1	2.05	0.25	ST-S	90	C	240	200	0.015	—	174.3
2S-3	R	360	—	400	200	360	0.3	1.8	30	0.15	2.05	0.25	ST-S	90	C	240	200	0.015	—	180.8
2S-4	R	360	—	400	200	360	0.2	1.8	30	0.066667	2.05	0.25	ST-S	90	C	240	200	0.015	—	163.0
2S-5	R	360	—	400	200	360	0.2	1.8	30	0.05	2.05	0.25	ST-S	90	C	240	200	0.015	—	152.3
2S-6	R	360	—	400	200	360	0.2	1.8	30	0.2	2.05	0.25	CT-S	90	C	240	200	0.015	—	218.8
2S-7	R	360	—	400	200	360	0.2	1.8	30	0.1	2.05	0.25	ST-S	90	C	240	200	0.015	—	162.9
2S-8	R	360	—	400	200	360	0.2	1.8	30	0.1	2.05	0.25	ST-S	90	C	240	200	0.015	—	178.8
2S-9	R	360	—	400	200	360	0.2	1.5	30	0.1	2.05	0.25	ST-S	90	C	240	200	0.015	—	178.7
2S-10	R	360	—	400	200	360	0.2	2.25	30	0.1	2.05	0.25	ST-S	90	C	240	200	0.015	—	172.9
2S-11	R	360	—	400	200	360	0.2	1.8	30	0.333333	2.05	0.25	CT-S	90	C	240	200	0.015	—	198.3
2S-12	R	360	—	400	200	360	0.2	1.8	30	0.1	2.05	0.25	CT-S	90	C	240	200	0.015	—	280.2
2S-13	R	360	—	400	200	360	0.1	1.8	20	0.05	2.05	0.25	ST-S	90	C	240	200	0.015	—	141.4
2S-14	R	360	—	400	120	360	0.1	1.8	50	0.05	2.05	0.25	ST-S	90	C	240	200	0.015	—	190.4
2S-15	R	360	—	400	400	360	0.2	1.8	30	0.2	2.05	0.25	CT-S	90	C	240	200	0.015	—	182.1
2S-16	R	360	—	400	200	360	0.2	1.8	30	0.2	2.05	0.25	CT-S	90	C	240	200	0.015	—	197.8
2S-17	R	280	—	300	200	280	0.1	1.8	30	0.1	2.05	0.25	CT-S	90	C	240	200	0.015	—	143.2
2S-18	R	360	—	400	200	360	0.1	1.8	30	0.1	2.05	0.25	CT-S	90	C	240	200	0.015	—	172.9
2S-19	R	560	—	600	200	560	0.1	1.8	30	0.1	2.05	0.25	CT-S	90	C	240	200	0.015	—	247.9
U-jac.-1	R	360	—	400	200	360	0.1	1.8	30	0.05	2.05	0.25	ST-U	90	C	240	200	0.015	—	206.5
U-jac.-2	R	360	—	400	200	360	0.2	1.8	30	0.1	2.05	0.25	ST-U	90	C	240	200	0.015	—	229.1
U-jac.-3	R	360	—	400	200	360	0.3	1.8	30	0.15	2.05	0.25	ST-U	90	C	240	200	0.015	—	247.0
U-jac.-4	R	360	—	400	200	360	0.2	1.8	30	0.066667	2.05	0.25	ST-U	90	C	240	200	0.015	—	211.7

Table 3.1 Database of numerical studies assessing parameters of RC beams strengthened in shear with externally bonded FRP composites and validating with and without experimental tests (Continued)

Specimen	Section	d_{fv}	h_f	h_w	b_w	d	nt_f	a/d	f'_c	$\rho_{\mathrm{FRP}}(\%)$	$\rho_w(\%)$	$\rho_s(\%)$	Configuration	β(degree)	Fiber	E_s	E_{FRP}	ε_{fu}	$V_{t(\exp)}$	$V_{t(\mathrm{NUM})}$
U-jac.-5	R	360	—	400	200	360	0.2	1.8	30	0.05	2.05	0.25	ST-U	90	C	240	200	0.015	—	205.9
U-jac.-6	R	360	—	400	200	360	0.2	1.8	30	0.2	2.05	0.25	CT-U	90	C	240	200	0.015	—	268.8
U-jac.-7	R	360	—	400	200	360	0.2	1.8	30	0.1	2.05	0.25	ST-U	90	C	240	200	0.015	—	201.9
U-jac.-8	R	360	—	400	200	360	0.2	1.8	30	0.1	2.05	0.25	ST-U	90	C	240	200	0.015	—	231.8
U-jac.-9	R	360	—	400	200	360	0.2	1.5	30	0.1	2.05	0.25	ST-U	90	C	240	200	0.015	—	242.7
U-jac.-10	R	360	—	400	200	360	0.2	2.25	30	0.1	2.05	0.25	ST-U	90	C	240	200	0.015	—	225.0
U-jac.-11	R	360	—	400	200	360	0.2	1.8	30	0.333333	2.05	0.25	CT-U	90	C	240	200	0.015	—	209.1
U-jac.-12	R	360	—	400	200	360	0.2	1.8	30	0.1	2.05	0.25	CT-U	90	C	240	200	0.015	—	360.2
U-jac.-13	R	360	—	400	200	360	0.1	1.8	20	0.05	2.05	0.25	ST-U	90	C	240	200	0.015	—	172.1
U-jac.-14	R	360	—	400	120	360	0.1	1.8	50	0.05	2.05	0.25	ST-U	90	C	240	200	0.015	—	243.9
U-jac.-15	R	360	—	400	400	360	0.2	1.8	30	0.2	2.05	0.25	CT-U	90	C	240	200	0.015	—	211.9
U-jac.-16	R	360	—	400	200	360	0.2	1.8	30	0.2	2.05	0.25	CT-U	90	C	240	200	0.015	—	246.7
U-jac.-17	R	280	—	300	200	280	0.1	1.8	30	0.1	2.05	0.25	CT-U	90	C	240	200	0.015	—	185.2
U-jac.-18	R	360	—	400	200	360	0.1	1.8	30	0.1	2.05	0.25	CT-U	90	C	240	200	0.015	—	210.5
U-jac.-19	R	560	—	600	200	560	0.1	1.8	30	0.1	2.05	0.25	CT-U	90	C	240	200	0.015	—	278.7
Wrapped-1	R	360	—	400	200	360	0.1	1.8	30	0.05	2.05	0.25	ST-W	90	C	240	200	0.015	—	255.4
Wrapped-2	R	360	—	400	200	360	0.2	1.8	30	0.1	2.05	0.25	ST-W	90	C	240	200	0.015	—	301.8
Wrapped-3	R	360	—	400	200	360	0.3	1.8	30	0.15	2.05	0.25	ST-W	90	C	240	200	0.015	—	322.8
Wrapped-4	R	360	—	400	200	360	0.2	1.8	30	0.066667	2.05	0.25	ST-W	90	C	240	200	0.015	—	272.2
Wrapped-5	R	360	—	400	200	360	0.2	1.8	30	0.05	2.05	0.25	ST-W	90	C	240	200	0.015	—	252.8
Wrapped-6	R	360	—	400	200	360	0.2	1.8	30	0.2	2.05	0.25	CT-W	90	C	240	200	0.015	—	355.8
Wrapped-7	R	360	—	400	200	360	0.2	1.8	30	0.1	2.05	0.25	ST-W	90	C	240	200	0.015	—	270.5
Wrapped-8	R	360	—	400	200	360	0.2	1.8	30	0.1	2.05	0.25	ST-W	90	C	240	200	0.015	—	305.7
Wrapped-9	R	360	—	400	200	360	0.2	1.5	30	0.1	2.05	0.25	ST-W	90	C	240	200	0.015	—	307.6
Wrapped-10	R	360	—	400	200	360	0.2	2.25	30	0.1	2.05	0.25	ST-W	90	C	240	200	0.015	—	272.1
Wrapped-11	R	360	—	400	200	360	0.2	1.8	30	0.333333	2.05	0.25	CT-W	90	C	240	200	0.015	—	288.3
Wrapped-12	R	360	—	400	200	360	0.2	1.8	30	0.1	2.05	0.25	CT-W	90	C	240	200	0.015	—	482.0
Wrapped-13	R	360	—	400	200	360	0.1	1.8	20	0.05	2.05	0.25	ST-W	90	C	240	200	0.015	—	209.1
Wrapped-14	R	360	—	400	120	360	0.1	1.8	50	0.05	2.05	0.25	ST-W	90	C	240	200	0.015	—	313.1
Wrapped-15	R	280	—	300	400	280	0.1	1.8	30	0.1	2.05	0.25	CT-W	90	C	240	200	0.015	—	217.8
Wrapped-16	R	360	—	400	200	360	0.1	1.8	30	0.1	2.05	0.25	CT-W	90	C	240	200	0.015	—	282.8
Wrapped-17	R	560	—	600	200	560	0.1	1.8	30	0.1	2.05	0.25	CT-W	90	C	240	200	0.015	—	435.0
Manos et al. [49]																				
CRB	R	322	—	360	200	322	—	2.79	22.4	—	2.43	—	—	—	—	202.7	—	—	39.44	39.44
CRBs	R	322	—	360	200	322	—	2.79	25.9	—	2.43	0.33	—	—	—	202.7	—	—	90.60825	87.89
RB200C	R	322	—	360	120	322	0.13	2.79	22.4	0.109167	2.43	—	ST-U	90	C	202.7	41.784	0.009	97.99	97.99
RB200Ca	R	322	—	360	120	322	0.13	2.79	22.4	0.109167	2.43	—	ST-U + anchorage	90	C	202.7	41.784	0.009	115.3301	118.79
RB200S	R	322	—	360	120	322	0.11	2.79	25.9	0.098667	2.43	—	ST-U	90	SFRP	202.7	36.35	0.009	94.12903	87.54
RB200Sa	R	322	—	360	120	322	0.11	2.79	25.9	0.098667	2.43	—	ST-U + anchorage	90	SFRP	202.7	36.35	0.009	122.25	112.47
RB150C	R	322	—	360	120	322	0.13	2.79	22.4	0.145556	2.43	—	ST-U	90	C	202.7	41.784	0.009	100.6566	99.65
RB150Ca	R	322	—	360	120	322	0.13	2.79	22.4	0.145556	2.439125	—	ST-U + anchorage	90	C	202.7	41.784	0.009	123.0408	120.58
RB150S	R	322	—	360	120	322	0.11	2.79	22.4	0.131556	2.439125	—	ST-U	90	SFRP	202.7	36.35	0.009	103.1383	96.95

Table 3.1 Database of numerical studies assessing parameters of RC beams strengthened in shear with externally bonded FRP composites and validating with and without experimental tests (Continued)

Specimen	Section	d_{fv}	h_f	h_w	b_w	d	nt_f	a/d	f'_c	$\rho_{\mathrm{FRP}}(\%)$	$\rho_w(\%)$	$\rho_s(\%)$	Configuration	β(degree)	Fiber	E_s	E_{FRP}	ε_{fu}	$V_{t(\exp)}$	$V_{t(\mathrm{NUM})}$
RB150Sa	R	322	—	360	120	322	0.11	2.79	22.43	0.131556	2.439125	—	ST-U + anchorage	90	SFRP	202.7	36.35	0.009	118.7692	123.52
Qapo et al. [50]																				
Control	I	457.2	—	—	102	457.2	—	2.5	—	—	1.23	0	—	90	—	186.6-204.5	—	—	117.4	129,5
IB-05	I	457.2	—	—	102	457.2	1.25	2.5	70.8	1.466728	1.23	0	ST-U	90	C	186.6-204.6	6.585	0.015	161.9	162
IB-10	I	457.2	—	—	102	457.2	1.25	2.5	70.8	0.733364	1.23	0	ST-U	90	C	186.6-204.7	6.585	0.015	119.2	149.7
Ibars et al. [51]																				
U90S5-a	R	250	—	420	250	370	0.29	3.5	36.9	0.88	2.03	0.10	ST-U	90	C	200	240	0.015	341	341
U90S5-b	R	250	—	420	250	370	0.29	3.5	28.0	0.88	2.03	0.10	ST-U	90	C	200	240	0.015	326	315
U90S3-a	R	250	—	420	250	370	0.17	3.5	20.5	0.53	2.03	0.10	ST-U	90	C	200	240	0.0155	285	263
U90S3-b	R	250	—	420	250	370	0.17	3.5	22.5	0.53	2.03	0.10	ST-U	90	C	200	240	0.0155	204	—
U90S3-c	R	250	—	420	250	370	0.17	3.5	28.0	0.53	2.03	0.10	ST-U	90	C	200	240	0.0155	320	311
W90S5	R	370	—	420	250	370	0.29	3.5	49.9	0.88	2.03	0.10	ST-W	90	C	200	240	0.015	383	402
W90S3-ab	R	370	—	420	250	370	0.17	3.5	37	0.53	2.03	0.10	ST-W	90	C	200	240	0.0155	432	408
W90S3-b	R	370	—	420	250	370	0.17	3.5	37	0.53	2.03	0.10	ST-W	90	C	200	240	0.0155	394	408
Al Jawahery et al. [52]																				
Rf1 * U90	R	—	—	—	150	260	0.3	2.4	44.5	0.177778	1.546154	—	ST-U	90	C	200	240	0.0204	233.24	225
A1 – 5INJ *	R	—	—	—	150	210-260	—	2.97-2.4	60	—	1.94-1.54	—	—	—	—	200	240	0.0204	113.5	118.2
A1-10U90	R	—	—	—	150	160-260	0.3	3.9-2.4	49	0.1	2.51-1.54	—	ST-U	90	C	200	240	0.0204	173.21	170.5
A2-10U45	R	—	—	—	150	160-260	0.3	3.9-2.4	51.5	0.1	2.51-1.55	—	ST-U	45	C	200	240	0.0204	171.523	160
A1 – 15U90 *	R	—	—	—	150	110-160	0.3	5.68-3.9	42.5	0.1	3.65-2.51	—	ST-U	90	C	200	240	0.0204	171.445	158
A2-15U45	R	—			150	110-260	0.3	5.68-2.4	60	0.1	3.65-1.54	—	ST-U	45	C	200	240	0.0204	168.149	164
Rf2U90	R	—	—	—	150	210	0.3	2.97	60.7	0.1	1.91	—	ST-U	90	C	200	240	0.0204	163.157	134
B1-5INJ	R	—	—	—	150	210-260	—	2.97-2.4	58.5		1.91-1.54	—	—	—	—	200	240	0.0204	108	152.8
B1-10U90	R	—	—	—	150	210-310	0.3	2.97-2.01	44	0.1	1.91-1.29	—	ST-U	90	C	200	240	0.0204	140.049	130.8
B2-10U45	R	—	—	—	150	210-310	0.3	2.97-2.02	61	0.1	1.91-1.30	—	ST-U	45	C	209 (assumed)	240	0.0204	153.45	110
B1-15U90	R	—	—	—	150	210-360	0.3	2.97-1.73	62	0.1	1.91-1.11	—	ST-U	90	C	200	240	0.0204	140.74	136
B2-15U45	R	—	—	—	150	210-360	0.3	2.97-1.73	50.1	0.1	1.91-1.11	—	ST-U	45	C	200	240	0.0204	119.664	110
Jin et al. [53]																				
CBF-S-0.0555	R	180	—	200	80	180	1	2	39.5	0.0555	1.24	0.12	ST-S	90	C	210	212	0.0198	—	—
CBF-M-0.0555	R	360	—	400	160	360	2	2	39.5	0.0555	1.24	0.12	ST-S	90	C	210	212	0.0198	—	—
CBF-L-0.0555	R	540	—	600	240	540	3	2	39.5	0.0555	1.24	0.12	ST-S	90	C	210	212	0.0198	—	—
CBF-U-0.0555	R	720	—	800	320	720	4	2	39.5	0.0555	1.24	0.12	ST-S	90	C	210	212	0.0198	—	—
CBF-S-0.111	R	180	—	200	80	180	2	2	39.5	0.111	1.24	0.12	ST-S	90	C	210	212	0.0198	—	—
CBF-M-0.111	R	360	—	400	160	360	4	2	39.5	0.111	1.24	0.12	ST-S	90	C	210	212	0.0198	—	—

Table 3.1 Database of numerical studies assessing parameters of RC beams strengthened in shear with externally bonded FRP composites and validating with and without experimental tests (Continued)

Specimen	Section	d_{fv}	h_f	h_w	b_w	d	nt_f	a/d	f'_c	$\rho_{\mathrm{FRP}}(\%)$	$\rho_w(\%)$	$\rho_s(\%)$	Configuration	β(degree)	Fiber	E_s	E_{FRP}	ε_{fu}	$V_{t(\exp)}$	$V_{t(\mathrm{NUM})}$
CBF-L-0.111	R	540	–	600	240	540	6	2	39.5	0.111	1.24	0.12	ST-S	90	C	210	212	0.0198	–	–
CBF-U-0.111	R	720	–	800	320	720	8	2	39.5	0.111	1.24	0.12	ST-S	90	C	210	212	0.0198	–	–
CBF-S-0.222	R	180	–	200	80	180	4	2	39.5	0.222	1.24	0.12	ST-S	90	C	210	212	0.0198	–	–
CBF-M-0.222	R	360	–	400	160	360	8	2	39.5	0.222	1.24	0.12	ST-S	90	C	210	212	0.0198	–	–
CBF-L-0.222	R	540	–	600	240	540	12	2	39.5	0.222	1.24	0.12	ST-S	90	C	210	212	0.0198	–	–
CBF-U-0.222	R	720	–	800	320	720	16	2	39.5	0.222	1.24	0.12	ST-S	90	C	210	212	0.0198	–	–
CBF-S-1.11	R	180	–	200	80	180	20	2	39.5	1.11	1.24	0.12	ST-S	90	C	210	212	0.0198	–	–
CBF-M-1.11	R	360	–	400	160	360	40	2	39.5	1.11	1.24	0.12	ST-S	90	C	210	212	0.0198	–	–
CBF-L-1.11	R	540	–	600	240	540	60	2	39.5	1.11	1.24	0.12	ST-S	90	C	210	212	0.0198	–	–
CBF-U-1.11	R	720	–	800	320	720	80	2	39.5	1.11	1.24	0.12	ST-S	90	C	210	212	0.0198	–	–
CBF-S-2.22	R	180	–	200	80	180	40	2	39.5	2.22	1.24	0.12	ST-S	90	C	210	212	0.0198	–	–
CBF-M-2.22	R	360	–	400	160	360	80	2	39.5	2.22	1.24	0.12	ST-S	90	C	210	212	0.0198	–	–
CBF-L-2.22	R	540	–	600	240	540	120	2	39.5	2.22	1.24	0.12	ST-S	90	C	210	212	0.0198	–	–
CBF-U-2.22	R	720	–	800	320	720	160	2	39.5	2.22	1.24	0.12	ST-S	90	C	210	212	0.0198	–	–
CBF-S-4.44	R	180	–	200	80	180	80	2	39.5	4.44	1.24	0.12	ST-S	90	C	210	212	0.0198	–	–
CBF-M-4.44	R	360	–	400	160	360	160	2	39.5	4.44	1.24	0.12	ST-S	90	C	210	212	0.0198	–	–
CBF-L-4.44	R	540	–	600	240	540	240	2	39.5	4.44	1.24	0.12	ST-S	90	C	210	212	0.0198	–	–
CBF-U-4.44	R	720	–	800	320	720	320	2	39.5	4.44	1.24	0.12	ST-S	90	C	210	212	0.0198	–	–
CBF-S-8.88	R	180	–	200	80	180	160	2	39.5	8.88	1.24	0.12	ST-S	90	C	210	212	0.0198	–	–
CBF-M-8.88	R	360	–	400	160	360	320	2	39.5	8.88	1.24	0.12	ST-S	90	C	210	212	0.0198	–	–
CBF-L-8.88	R	540	–	600	240	540	480	2	39.5	8.88	1.24	0.12	ST-S	90	C	210	212	0.0198	–	–
CBF-U-8.88	R	720	–	800	320	720	640	2	39.5	8.88	1.24	0.12	ST-S	90	C	210	212	0.0198	–	–

Table 3.2 Database of numerical studies assessing parameters of RC beams strengthened in shear with FRP bars and validating with experimental tests

Database of FE conducts on reinforce concrete beam strengthened by FRP bars

Geometry of beams					Properties of concrete			Configuration		Results	
Specimen	Section	d (mm)	Bw (mm)	a/d	f_c'	$\rho_w(\%)$	$\rho_s(\%)$	Fiber	Configuration	$V_{t(\exp\}}$ (KN)	$V_{t(\mathrm{NUM})}$ (KN)
Hawileh et al. [54]											
FE SPEC-1	R	320	200	5	25	1.79	0	G	NSM	92.68	95.05
Godat et al. [55]											
S0-ETS	T	350	152	3	25	0.35	0	C	ETS	273	301.4
S1-ETS	T	350	152	3	25	0.35	0.3779	C	ETS	397	417.9
S3-ETS	T	350	152	3	25	0.35	0.2543	C	ETS	425.5	428
Qapo et al. [56]											
S0-12d130s	T	350	152	3	25	0.35	0	C	ETS	180.8	179.6
1-12d260s	T	350	152	3	25	0.35	0.3779	C	ETS	266.6	271.5
R00	T	295	125	3.05	17.4	1.77	0.292	C	ETS	142	150.6
Specimen 8	R	189	110	3.17	47	0.934	0	A	ETS	32	33.3
Specimen 9	R	189	110	3.17	47	0.934	0	A	ETS	32	31.9
Specimen 10	R	189	110	3.17	47	0.394	0	A	ETS	30	31.5
Hawileh et al. [57]											
B1	R	200	300	3.5/11.5	52.3	0.28	0	C	FRP bars	84	81.1
B2	R	300	300	3.5/6.5	52.3	0.35	0	C	FRP bars	94	81.6
B3	R	400	300	3.5/4	52.3	0.58	0	C	FRP bars	102	91.9
B4	R	500	300	3.5/2.5	52.3	0.58	0	C	FRP bars	162	161.6
B5	R	400	300	6.5/1	52.3	0.58	0	C	FRP bars	381	417.5
B6	R	400	300	6/1.5	52.3	0.73	0	C	FRP bars	309	313.2
Shomali et al. [58]											
B3-NSM-30	R	262	200	2.29	32	1.79	0	C	NSM	210	224.7
B4-NSM-30	R	262	200	2.29	34	1.79	0.264	C	NSM	262	280.34

Table 3.3 Database of numerical studies assessing distribution of stress and strain on the interface and interaction between steel stirrups and FRP composites of RC beams strengthened in shear with externally FRP composites

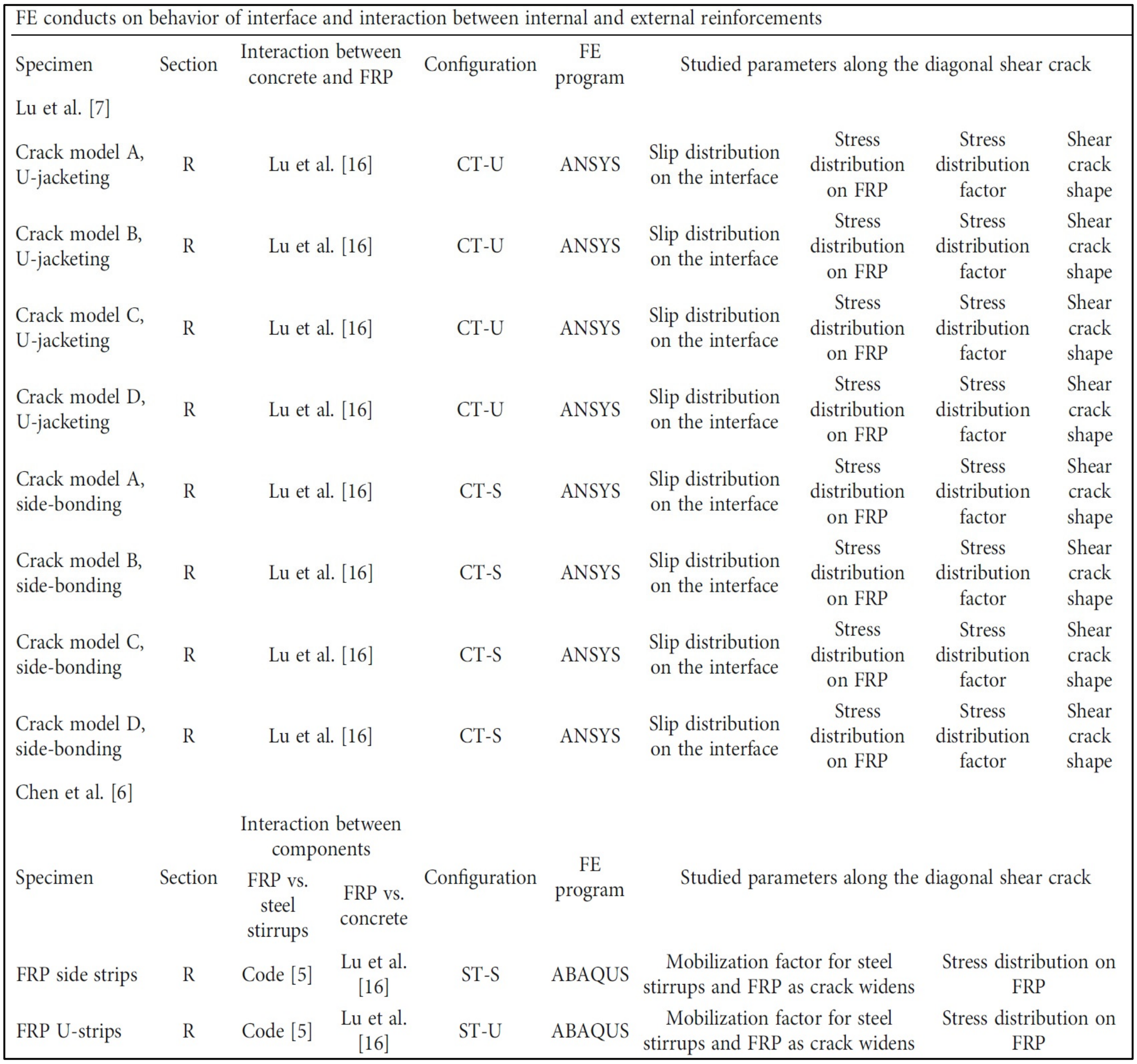

FE conducts on behavior of interface and interaction between internal and external reinforcements

Specimen	Section	Interaction between concrete and FRP	Configuration	FE program	Studied parameters along the diagonal shear crack			
Lu et al. [7]								
Crack model A, U-jacketing	R	Lu et al. [16]	CT-U	ANSYS	Slip distribution on the interface	Stress distribution on FRP	Stress distribution factor	Shear crack shape
Crack model B, U-jacketing	R	Lu et al. [16]	CT-U	ANSYS	Slip distribution on the interface	Stress distribution on FRP	Stress distribution factor	Shear crack shape
Crack model C, U-jacketing	R	Lu et al. [16]	CT-U	ANSYS	Slip distribution on the interface	Stress distribution on FRP	Stress distribution factor	Shear crack shape
Crack model D, U-jacketing	R	Lu et al. [16]	CT-U	ANSYS	Slip distribution on the interface	Stress distribution on FRP	Stress distribution factor	Shear crack shape
Crack model A, side-bonding	R	Lu et al. [16]	CT-S	ANSYS	Slip distribution on the interface	Stress distribution on FRP	Stress distribution factor	Shear crack shape
Crack model B, side-bonding	R	Lu et al. [16]	CT-S	ANSYS	Slip distribution on the interface	Stress distribution on FRP	Stress distribution factor	Shear crack shape
Crack model C, side-bonding	R	Lu et al. [16]	CT-S	ANSYS	Slip distribution on the interface	Stress distribution on FRP	Stress distribution factor	Shear crack shape
Crack model D, side-bonding	R	Lu et al. [16]	CT-S	ANSYS	Slip distribution on the interface	Stress distribution on FRP	Stress distribution factor	Shear crack shape

Chen et al. [6]

Specimen	Section	Interaction between components		Configuration	FE program	Studied parameters along the diagonal shear crack	
		FRP vs. steel stirrups	FRP vs. concrete				
FRP side strips	R	Code [5]	Lu et al. [16]	ST-S	ABAQUS	Mobilization factor for steel stirrups and FRP as crack widens	Stress distribution on FRP
FRP U-strips	R	Code [5]	Lu et al. [16]	ST-U	ABAQUS	Mobilization factor for steel stirrups and FRP as crack widens	Stress distribution on FRP

Where D_{FRP} is the distribution factor, which is function of the crack shape and varies with the amount of internal steel reinforcement. Therefore, the authors present the following equation to cover all shear crack shapes:

$$w = w_{max}\begin{cases} \frac{1-C_{\bar{z}}}{1-C} \times \bar{z} & 0 \leq C < \frac{1}{2} \\ 4C_{\bar{z}}(1 - C_{\bar{z}}) & \frac{1}{2} \leq C < 1 \end{cases} \tag{3.2}$$

where w = crack width, w_{max} = maximum crack width (Guangming Chen, 2010), $\bar{z} = z/z_b$ (normalized vertical coordinate where $z_b = 0.9\ d$, the effective depth of the beam), and C is the factor determining the shape of the strain distribution. Among the 239 studied beams, 102 beams (42.6%) were evaluated for their crack width, crack pattern, and shape function (Figure 3.4). However, only two studies (GM Chen, Teng, et al., 2010; Lu et al., 2009), involving 10 beams (4.1%), considered the effect of crack shape and crack function in their proposed shear model based on FEA. The rest (92 beams) focused on shear crack patterns. This indicates the need for more research related to shear crack shape functions, considering different crack shapes and their effect on the distribution factors and the effective stress and strain, to develop future predictive models.

3.5.2 Strain, Stress, and Slip Distribution along the Diagonal Crack on EB FRP

J. Chen and J. Teng (2003) showed that the width of the shear crack varies along its length, confirming thereby that the strain and stress distributions along the FRP laminates/fabrics are non-uniform. As for the issue that FRP laminates/fabrics crossed by the diagonal shear crack experience different ranges of strain and stress as the crack widens, it could be concluded that the amount of stress/strain in the fibers is influenced by the crack width, and hence the D_{FRP} distribution factor is not constant. Therefore, D_{FRP} depends on the location of the FRPs because the fibers located at the end of the crack experience more strain than those situated at the tip of the crack. Nevertheless, as mentioned in the previous section, the shape of the shear crack relies on the steel reinforcement, and hence the shear crack is not necessarily linear. The maximum width of the crack can be in the middle of the beam if the beam contains a high ratio of longitudinal steel reinforcement (Lu et al., 2009). The other factor affecting the fiber strain distribution is the FRP configuration type. For instance, when assuming U-shaped configurations, fibers located below the shear crack experience more strain than those located near the top of the crack because there is enough bond length on the lower side of crack compared to the upper side. However, for side-bonded configurations, with the same bond length at the bottom and top of the crack, the fibers on both sides of the crack experience the same strain distribution. Therefore, it is of paramount importance to consider the strain profile on the fibers to obtain the effective strain in FRP laminates/fabrics. On the other hand, studying slip profiles on the interface layer gives an insight into how the interface layer responds to increasing load and crack propagation. The slip distributions make it possible to understand how shear cracks form because fiber debonding occurs near the shear crack. Therefore, through a slip profile, shear crack propagation can be predicted by FEA, which is not possible by experimental tests. Among the 239 beams, 84 (35.1%) beams were subjected to FEA that evaluated the strain distribution along the fibers and the slip profile along the interface layer, of which 25 beams (10.4%) were T-shaped cross-sections (Figure 3.4). This indicates the need for more FE studies on the strain and slip profile for T cross-section beams.

3.5.3 Load-Deflection Curve

Most laboratory and FE results on RC beams strengthened in shear using FRP composites have been based on the load-deflection curve, particularly in experimental tests. Generally, the load-deflection response has become the way to evaluate the ultimate load-carrying capacity as well as the ductility and the behavioral features of EB-FRP shear-strengthened RC beams. In fact, the load-deflection response has become a criterion to validate the accuracy of FEA results against experimental results. However, it cannot be the only criterion for validating FEA and developing analytical models because it has been observed that, even if the load-deflection curves of shear-strengthened RC beams using EB-FRP were compatible when subjected to two different tests, their failure modes could be different. In addition, it has been established that specimens featuring the same load-deflection responses from different tests may present many discrepancies with regards to formation and number of shear cracks, strain profile along fibers, slip profiles along the interface as well as fiber strain distribution along the horizontal axis of the specimens. Nevertheless, the load-deflection response can be one of the indications to validate whether a simulated model is accurate. Among the 239 beams, 185 (77.4%) FE beams were studied in terms of load-deflection response, of which 125 (52.3%) were rectangular, 48 (20%) were T-shaped, and 12 (5%) were I-shaped cross-sections (Figure 3.4).

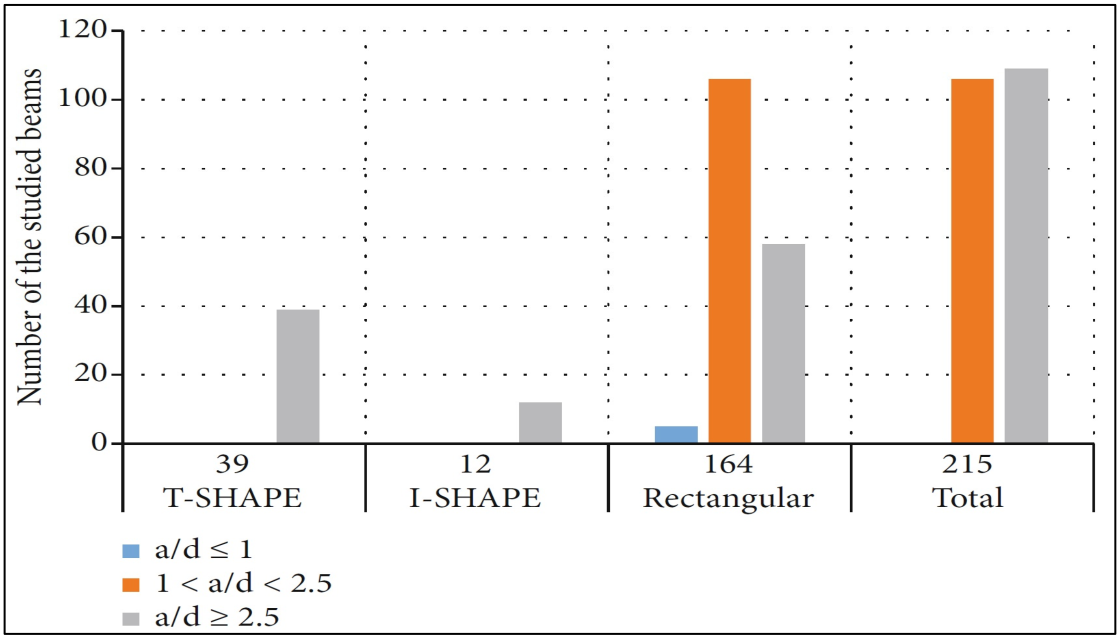

Figure 3.2 Number of cross-section types and a/d ratios considered in FEA

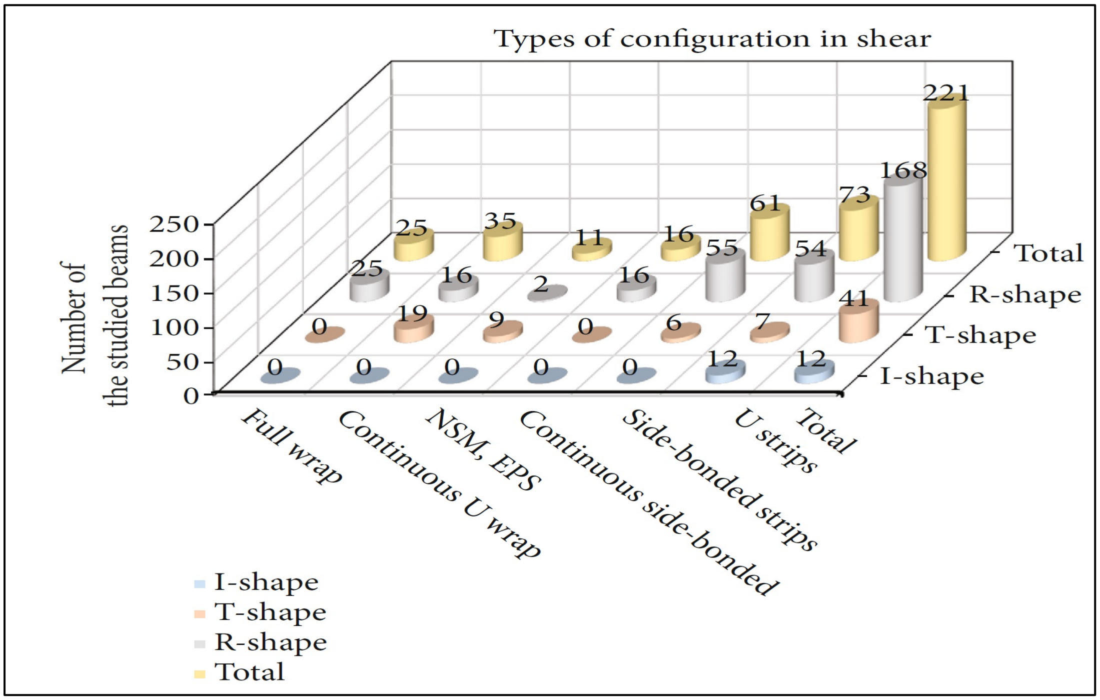

Figure 3.3 Number of cross-section types and configurations considered in FEA

3.5.4 Number, Size, and Types of Elements in Simulation

Selecting the right element in simulation for each component of the beam is of paramount importance in FE methods, which are highly sensitive to the size and type of the elements. As the size of elements is reduced, the time and cost for FEA will increase. Modeling EB-FRP RC beams can be classified into two categories: (i) three-dimensional simulation, which is time-consuming, but provides results that are representative of the real model; (ii) two-dimensional modeling, which takes advantage of the plane stress behavior that EB-FRP RC beams can exhibit. The two-dimensional model ignores the deflection of the beam into the normal direction to its plane and makes some further simplifying assumptions, reducing considerably the time and cost of FEA. In the three-dimensional model, the brick element is chosen for concrete, whereas for steel reinforcement, either the one-dimensional bar or the three-dimensional brick element can be considered. For EB-FRP laminates/fabrics, the two-dimensional shell element for EB-FRP and the one-dimensional link or bar elements would be appropriate. As for concrete-to-FRP and steel reinforcement-to-concrete interface elements, there are many options affecting the right choice, depending on the type of fibers in the EB-FRP (one-directional, two-directional) and ranging from the one-dimensional link element to three-dimensional cohesive elements depending on whether the model in question is three- or two-dimensional. Few investigations considered the effect of element type as a studied parameter in FE simulations. In fact, only 17 (7.1%) of the 239 beams underwent this study, of which 12 (5%) were rectangular and 5 (2%) were T-shaped cross-sections (Figure 3.4).

3.5.5 Effective Stress and Strain, Bond Length, and Distribution Factor (D)

The effective stress and strain experienced by FRP are essential components to calculate FRP contribution to shear resistance, which depends on the stress and strain distribution along the shear cracks, which in turn relies on the shape functions of cracks. As for the effective bond length of EB-FRP, which is the length of FRP that has not debonded and hence still contributes to the shear resistance, it is directly related to the shear crack distribution in the concrete. Indeed, the more the shear cracks are distributed, the shorter is the effective bond length of the FRP and the more likely the beam will exhibit a premature failure (Mofidi & Chaallal, 2010).

Many models based on the effective bond length have been reported in the literature. The models introduced by Neubauer and Rostasy (1997) and J.-F. Chen and J. Teng (2003) are some of the most reliable models, Among the 239 RC beams strengthened in shear using FRP composites, only 41 (17.1%) were considered to study the effective stress and strain, the bond length, and distribution factor (*D*), of which 29 (12.1%) were rectangular and 12 (5%) were T-shaped cross-sections (Figure 3.4).

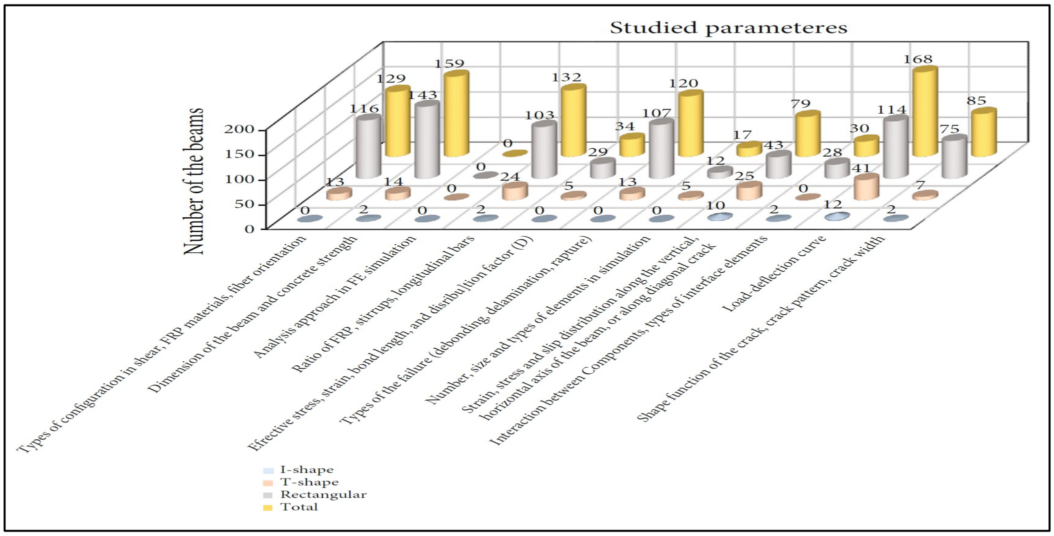

Figure 3.4 Number of studied beams evaluating the effect of each parameter on closed-form model for shear contribution of FRP composites by FEA

Which are expressed in the following Eq. 3-3 to Eq. 3-4 respectively:

$$L_e = \sqrt{\frac{E_f t_f}{2 f_{ct}}} \tag{3.3}$$

Where f_{ct} is the tensile strength of concrete (Mirza et al., 1979):

$$f_{ct} = 0.53\sqrt{\acute{f}_c} \tag{3.4}$$

$$L_e = \sqrt{\frac{E_{frp} t_{frp}}{\sqrt{f_c'}}} \tag{3.5}$$

3.5.6 Failure Modes in Concrete and EB-FRP (Debonding, Delamination, Rupture)

Failure of RC beams strengthened in shear using EB-FRP can be mainly related either to reinforced concrete (crushing of concrete struts, tensile shear failure, yielding and fracture of steel reinforcement) or to EB-FRP composites (debonding or rupture). In fact, the failure modes observed in EB-FRP specimens are: (i) rupture of FRP laminates/fabrics, which occurs usually in a fully wrapped FRP configuration; (ii) debonding of FRP due to lack of effective bond length near shear cracks; and (iii) failure of RC beams due to delamination of EB laminates/fabrics from the concrete substrate when EB-FRP still contributes to the shear resistance (Guangming Chen, 2010). Failure modes related to loss of concrete strength also depend on the shear span-to-depth ratio, according to Teng et al. (2002a). They can involve compressive or tensile shear failure of the RC beams, as well as failure of deep beams. The failure modes of 124 (51.8%) beams were subjected to FE studies, of which 113 (47.2%) were rectangular and only 11 (4.6%) were T-shaped cross-sections (Figure 3.4). The advantage of FE studies over experimental tests is that detection of failure modes using FEA is much easier than laboratory testing of shear-strengthened RC beams using EB-FRP. In addition, the post-failure response of the specimens can be captured using FEA, which is impossible in an experimental protocol.

3.5.7 Shear strengthening configurations, FRP materials and fiber orientation

There is an array of configurations for strengthening RC beams in shear, which are associated with the beam’s cross section, shear crack orientation, and accessibility to the surfaces of the beam to be strengthened. Three EB configurations are used in practice for strengthening RC beams in shear: (i) the side-bonded configuration where FRP laminates/fabrics are installed on the two lateral sides of the beam. The corresponding failure mode is mainly by FRP delamination from the concrete substrate; (ii) the U-shaped configuration where the FRP laminates/fabrics are installed on three surfaces of the beam (lateral sides and soffit of the beam). The corresponding failure mode is mainly by FRP debonding from the top side of the shear crack due to lesser effective bond length compared to the bottom side of crack; and (iii) the full-wrap configuration is usually labeled by the symbol W and involves wrapping FRP laminates/fabrics over the whole surface of the beam. The full-wrap configuration is more applicable to beams with easy access to all beam surfaces, such as rectangular RC beams and columns. All three configurations can be installed to the concrete substrate in the form of continuous or discontinuous (strips) bonded FRP composites. If bond length is insufficient, anchorages can be used to prevent premature debonding failure. Furthermore, various types of fibers are used for FRP composites, such as carbon, glass, and aramid. The fiber orientation in FRP laminates/fabrics can be horizontal, vertical, or diagonal at any angle to the axis of RC beams. When feasible, the optimal fiber orientation would cross the shear crack perpendicularly, providing more contribution to shear resistance. 140 (58.5%) of the 239 beams were subjected to FEA to evaluate the effect of shear strengthening configurations, type of FRP composites, and fiber orientation, of which 127 (53.1%) were rectangular and only 13 (5.4%) were T-shaped cross-sections (Figure 3.4).

3.5.8 Analytical approach in FE simulations

Solving problems using FEA can be classified into two techniques: (i) static solvers; and (ii) dynamic solvers, which can further be divided into dynamic implicit and dynamic explicit. Because ABAQUS/CAE 2017 was used in the majority of studies, the following description is concentrated on ABAQUS solvers. A dynamic analysis is to be privileged over static analysis because of many reasons and considerations, such as the brittle behavior of concrete, debonding phenomenon, delamination of concrete substrate, problem of reaching convergence in analysis, and the post-peak behavior of RC beams strengthened in shear using EB-FRP laminates/sheets. Nevertheless, results obtained from a dynamic approach should be verified against a general static analysis. When performing dynamic analysis on specimens, certain parameters should be considered to improve the accuracy of the results. These include the loading pattern (smoothing, stepping, or ramping), loading duration on the structure, amount of damping for EB-FRP RC beams, and time increment, among others (Guangming Chen, 2010). Figure 3.4 reveals that among all the FEA studies, none of them mentioned how these influencing parameters were selected to solve their models. Therefore, when the dynamic solver is used, an explanation should be provided of how these parameters were selected in the implicit or the explicit analysis.

3.5.9 Interaction between Components and Types of Interface Elements

Steel stirrups and EB-FRP composites are the two main factors that contribute to shear resistance in EB-FRP strengthened RC beams. Nevertheless, Bousselham and Chaallal (2004) showed an inverse interaction between EB-FRP and steel stirrups. The contribution of EB-FRP to shear resistance was found to decrease as the ratio of rigidity of steel stirrups to EB-FRP $(E_s\rho_s/E_f\rho_f)$ increased, confirming thereby the interaction between internal and external reinforcement. Guangming Chen (2010) introduced a model that explained this inverse shear interaction between steel stirrups and EB-FRP, and demonstrated that because of this inverse interaction, neither internal nor external reinforcement reaches its full capacity. Therefore, two mobilization factors were proposed by Guangming Chen (2010) for determining the contribution of steel stirrups and FRP in EB-FRP RC beams:

$$V_u = V_c + K_s V_s + K_f V_f \qquad (3.6)$$

where K_f and K_s are the mobilization factors accounting for FRP and steel stirrups and varying between 0 and 1. GM Chen, Teng, et al. (2010) investigated the response of these two mobilization factors and found that K_f and K_s could be functions of crack width. The authors then created artificial cracks and observed the response of the two mobilization factors as the cracks grew, using two configuration types (U-shaped and side-bonded). They showed that as the crack width increases, K_f was always greater than K_s, which means that when most of the FRP strips were already debonded or had reached their maximum strength, the steel stirrups had not yet reached their maximum strength.

They further showed that there was an opposite behavior between K_f and K_s, indicating an inverse interaction, in which K_s was always less than K_f, and that this inverse interaction reduced the FRP shear contribution more than when the effect of this interaction was not considered. Hence, if the effect of this inverse interaction on just the contribution of FRP strips is considered, based on the equation proposed by Guangming Chen (2010), the following equation can be derived, in which the effect of inverse interaction is considered by means of a coefficient *K*:

$$V_u = V_c + V_s + KV_f \tag{3.7}$$

Integrating Eq. (6) and Eq. (7), it follows that (Guangming Chen, 2010):

$$K = K_f + (K_s - 1) \times \frac{V_s}{V_f} = K_f + (K_s - 1) \times \mu \tag{3.8}$$

where:

$$\mu = \frac{V_s}{V_f} = \frac{f_y A_{sv}}{f_{f,e} A_{frp}} \tag{3.9}$$

This indicates that when the amount of steel stirrups, and consequently the value of μ increases, the value of K_f declines (Bousselham & Chaallal, 2004; Guangming Chen, 2010). From the database, approximately 100 EB-FRP RC beams were considered in this study to evaluate the response of inverse shear interaction between steel stirrups and EB-FRP, with different EB-FRP configurations (continuous U-shaped, strip U-shaped, fully wrapped, and side-bonded) and based on steel stirrups ratio, EB-FRP ratio, and gain in shear contribution, as shown in Figure . The figures show that the shear gain due to FRP decreased by increasing the ratio of steel stirrups, which confirms the research findings by Bousselham and Chaallal (2004). In addition to the ratio of steel stirrups and EB-FRP, other factors, like the FRP configuration or the size effect, could have affected this inverse shear interaction because this database considers all types of shear configurations and beam sizes.

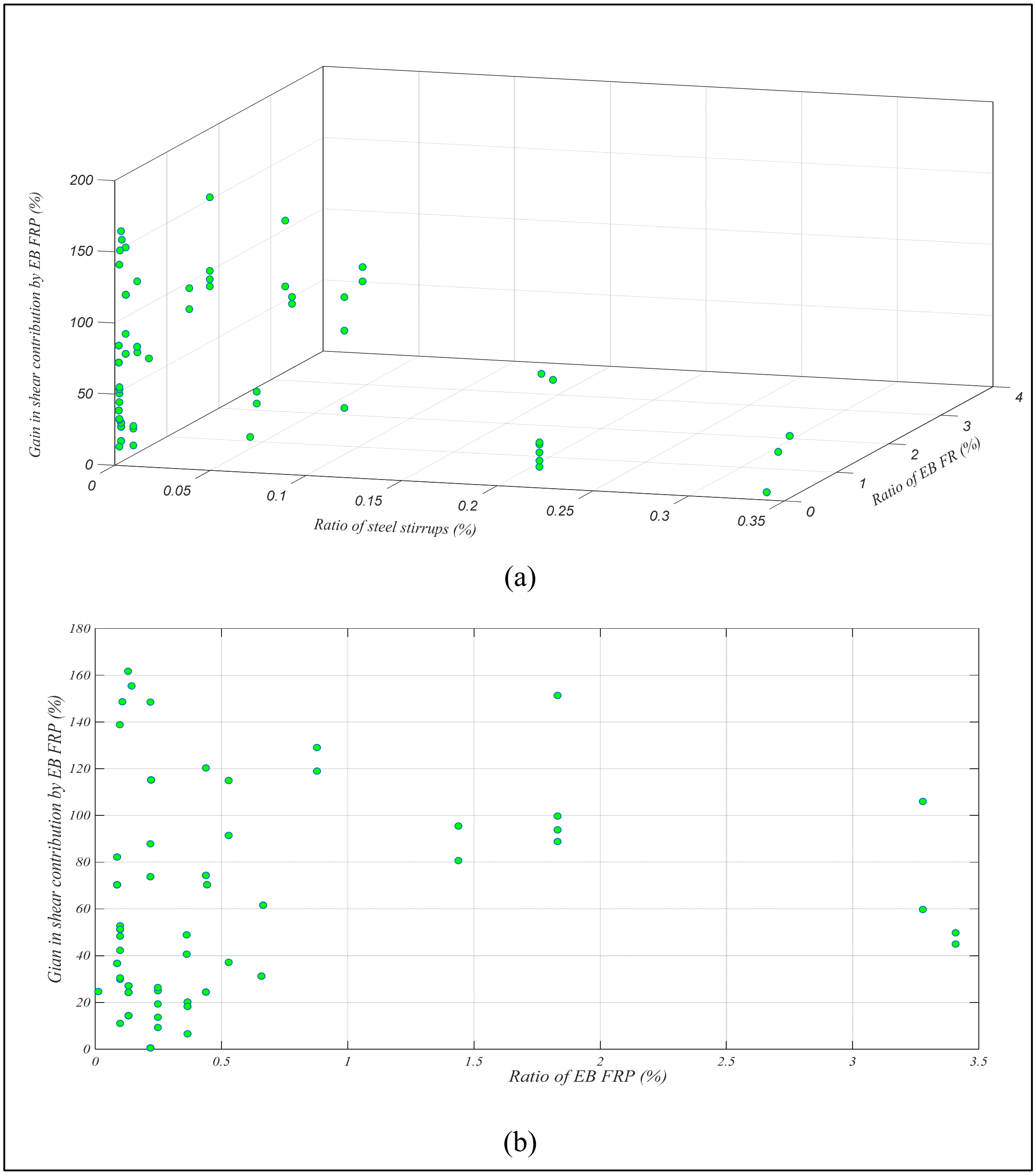

(a)

(b)

Figure 3.5 Interaction between steel stirrups and EB-FRP versus shear gain contributions (X= Ratio of steel stirrups (%) Y= Ratio of EB FRP (%) Z= Gain in shear contribution by EB FRP (%)

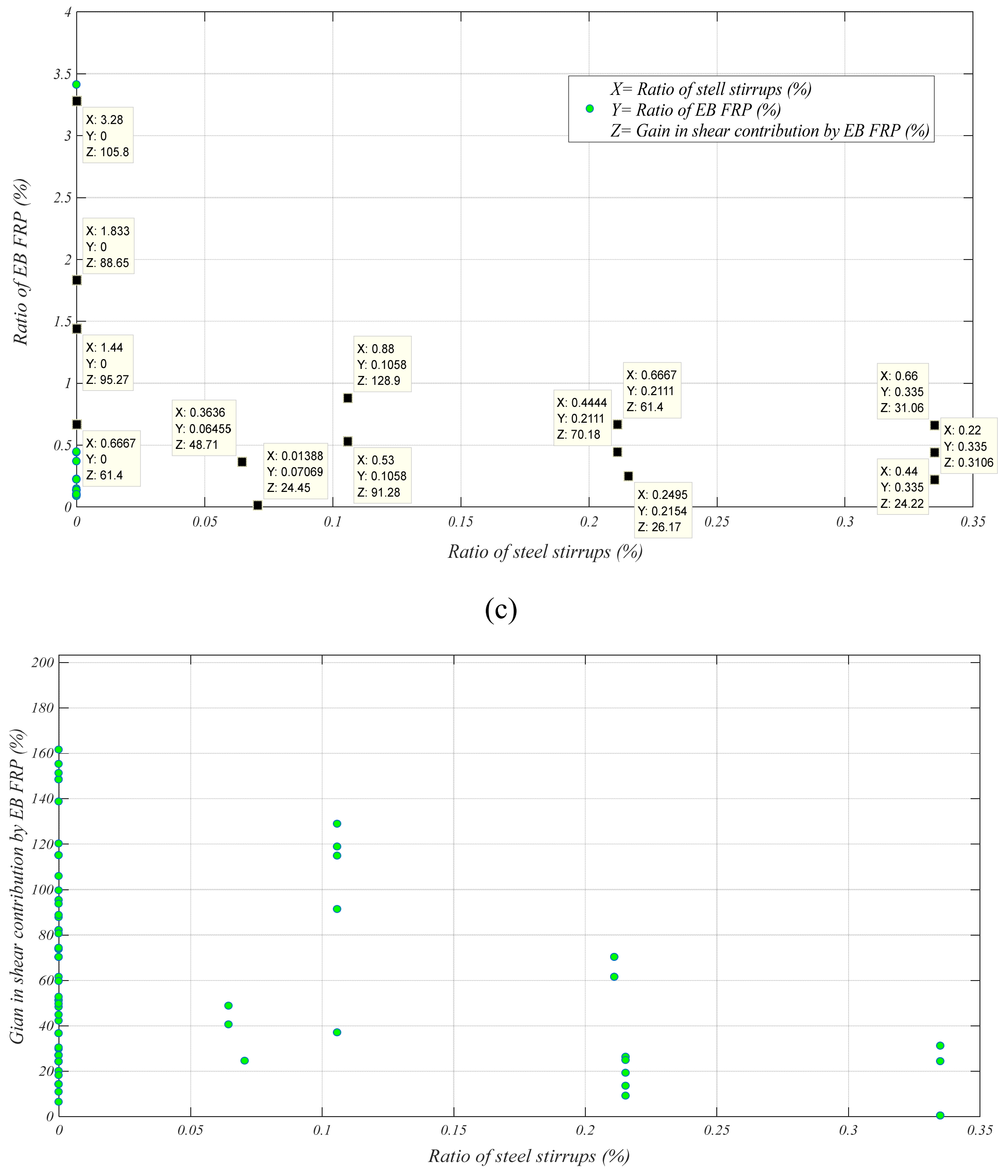

(c)

(d)

Figure 3.5 Interaction between steel stirrups and EB-FRP versus shear gain contributions (X= Ratio of steel stirrups (%) Y= Ratio of EB FRP (%) Z= Gain in shear contribution by EB FRP (%) (continued)

The FRP gain contribution can be computed as follows:

$$FRP\ gain\ contribution = V_f/(V_t - V_f) \tag{3.10}$$

Where V_t is the total shear resistance of the beam and V_f is the contribution of FRP to shear resistance.

Among the 239 beams, only 44 (20%) beams were subjected to FEA that considered the interaction between all components simultaneously (Concrete, steel reinforcement, and FRP composites), based on the modeling of concrete cracking, of which 12 (5%) beams assumed a properly defined bond-slip law using a smeared crack + crack band model for both concrete-to-FRP and concrete-to-steel interactions, as illustrated in Fig. 5. Moreover, for only 16 (6.7%) and 10 (4.1%) of the beams, a bond-slip law with smeared crack + crack band model was assumed for concrete-to-FRP and for concrete-to-steel interactions, respectively. Therefore, if the inverse interaction with concrete is considered as a fact in the overall response of RC beams strengthened in shear using FRP composites, both interactions for internal and external reinforcement should be introduced to the FE package alongside the smeared crack + crack band model. Accordingly, the simulated model would be representative of the real beam, and the results obtained from the FE package would be more reliable. In the current study, as the database shows, only 5% of all specimens were adequately and correctly modeled and simulated. Therefore, there is a need for more studies with precise and accurate simulations of RC beams strengthened in shear using FRP, and particularly the EB strengthening technique. The aim of these studies would be to measure the effective strains and stresses using precise FE simulations to incorporate their effects into a reliable closed-form model providing the contribution of FRP composites to shear resistance of FRP-strengthened RC beams.

3.5.10 Interface elements between concrete and FRP composites

There are few models in the FE software that can be introduced as an interface element between concrete and FRP, ranging from one-dimensional elements (e.g., link, spring, truss) to 2-dimensional or 3-dimentsional elements. They stand for the behavior of the interface layer (interfacial shear stress, slip profile along the interface layer). As for the 2-dimensional interface elements, cohesive elements existing in all FE software's could be an appropriate candidate to simulate the response of the interface layer in its plane. Indeed, precision of results obtained from the behavior of interface layer much depends on the model introduced to those elements, which can be obtained from both numerical and experimental tests.

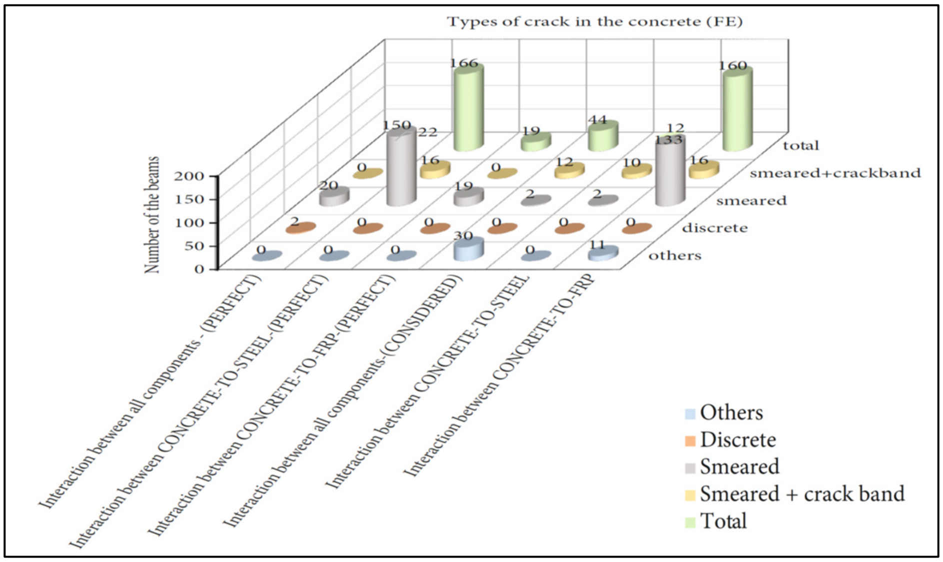

Figure 3.6 Number of studied beams evaluating bond-models based on definition of types of cracks for concrete by FEA

Few studies have been conducted on the response of bond-slip models, which are described hereafter. Since the failure modes at the interface layer could be different (debonding, delamination), the one-dimensional elements are not an appropriate representative for presenting the response of the debonding failure at the interface layer. However, most of the research studies carried out on the 2-dimensional interface elements (cohesive elements) concentrated on the behavior of the interface layer in its plane (failure modes 2 and 3), ignoring the delamination failure occurring normal to the cohesive plane (delamination phenomenon, failure mode 1). Therefore, it is of paramount importance that 2-dimensional or 3-dimensional elements should be implemented as an interface layer to consider all types of failure modes (1, 2, and 3), by representing the debonding in 2-directions of the interface elements at its plane, and the delamination normal to the interface elements. According to the study conducted by

Lu et al. (2005), the following are the most reliable models accounting for the response of bond-slip models.

The relationship proposed by Neubauer and Rostasy (1997) for the bond-slip model consisted of two parts:

$$\tau = \tau_{max}(\frac{s}{s_0}) \text{ If } \quad s \leq s_0 \quad \text{for the ascending part of the curve} \tag{3.11}$$

$$0 \quad \text{If} \quad s > s_0 \quad \text{for the descending part of curve}$$

Where

$$\tau_{max} = 1.8\beta_w f_t \tag{3.12}$$

$$s_0 = 0.202\beta_w \tag{3.13}$$

$$\beta_w = \sqrt{1.125(\frac{\left(\frac{2-b_f}{b_c}\right)}{\left(\frac{1+b_f}{400}\right)})} \tag{3.14}$$

Nakaba et al. (2001) proposed the following relationship in which both ascending and descending parts are shown as an integrated curve:

$$\tau = \tau_{max}(\frac{s}{s_0})\left[\frac{3}{(2+(\frac{s}{s_0})^3}\right] \quad \text{For both ascending and descending part} \tag{3.15}$$

Where

$$\tau_{max} = 3.5\acute{f}^{0.19} \tag{3.16}$$

, and $s_0 = 0.65$.

G Monti et al. (2003) applied two different equations for the ascending and descending part of the bond-slip curve:

$$\tau = \tau_{max}\left(\frac{s}{s_0}\right) \qquad \text{If} \qquad s \le s_0 \tag{3.17}$$

$$\tau = \frac{s_f - s}{s_f - s_0} \qquad \text{If} \qquad s > s_0 \tag{3.18}$$

Where

$$\tau_{max} = 1.8\beta_w f_t \tag{3.19}$$

$$s_0 = 2.5\tau_{max}\left(\frac{t_a}{E_a} + \frac{50}{E_c}\right) \tag{3.20}$$

$$s_f = 0.33\beta_w \tag{3.21}$$

, and

$$\beta_w = \sqrt{\frac{1.5\left(\frac{2-b_f}{b_c}\right)}{\left(\frac{1+b_f}{100}\right)}} \tag{3.22}$$

Savoia et al. (2003) employed just a united curve for both ascending and descending parts:

$$\tau_{max} = \left(\frac{s}{s_0}\right)\left[\frac{2.86}{\left(1.86+\frac{s}{s_0}\right)^{2.86}}\right] \qquad \text{For both ascending and descending part} \tag{3.23}$$

Where

$$\tau_{max} = 3.5\acute{f}^{0.19} \text{ , and } s_0 = 0.051 \tag{3.24}$$

Dai and Ueda (2003) proposed to separate the equations for the ascending and descending sections of the curve:

$$\tau = \tau_{max}(\frac{s}{s_0})^{0.575} \qquad \text{If} \qquad s \leq s_0 \tag{3.25}$$

$$\tau = \tau_{max}e^{-\beta(s-s_0)} \qquad \text{If} \qquad s > s_0 \tag{3.26}$$

Where

$$\tau_{max} = \frac{-1.575\alpha K_a + \sqrt{2.481\alpha^2 {K_a}^2 + 6.3\alpha\beta^2 K_a G_f}}{2\beta} \tag{3.27}$$

$$s_0 = \frac{\tau_{max}}{\alpha K_a} \tag{3.28}$$

$$\beta = 0.0035K_a(\frac{E_f T_f}{1000})^{0.34} \tag{3.29}$$

$$G_f = 7.554{K_a}^{-0.449}(\acute{f_c})^{0.343} \tag{3.30}$$

,and

$$K_a = \frac{G_a}{t_a} \tag{3.31}$$

Another model proposed by Ueda et al. (2003) in which the integrated equation is proposed for both ascending and descending parts of the curve:

$$\tau = 2UG_f(e^{-Us} - e^{-2Us}) \tag{3.32}$$

Where

$$U = 6.846(\frac{E_f t_f}{1000})^{0.108}(\frac{G_a/t_a}{1000})^{0.833} \tag{3.33}$$

, and

$$G_f = 0.446(\frac{E_f t_f}{1000})^{0.023}(\frac{G_a/t_a}{1000})^{-0.352}\acute{f}_c^{\,0.236} \tag{3.34}$$

Finally, the bond-slip model introduced by (Lu et al., 2005), which is the most accepted model used worldwide by researchers is as follow:
For ascending and softening parts of bond-slip curve following models are applied:

$$\tau = \tau_{max}\sqrt{\frac{s}{s_0}} \qquad \text{If} \qquad s \le s_0 \tag{3.35}$$

$$\tau = \tau_{max}e^{-\alpha(\frac{s}{s_0}-1)} \qquad \text{If} \qquad s > s_0 \tag{3.36}$$

Where

$$s_0 = 0.0195\beta_w f_t \tag{3.37}$$

$$G_f = 0.308{\beta_w}^2\sqrt{f_t} \tag{3.38}$$

, and

$$\alpha = \frac{1}{\frac{G_f}{\tau_{max} s_0} - \frac{2}{3}} \tag{3.39}$$

$$\beta_w = \sqrt{\frac{2-({w_f}/{(s_f \sin\beta)})}{1+({w_f}/{(s_f \sin\beta)})}} \tag{3.40}$$

and $\beta =$ Orientation of the fiber in direction normal to the cohesive layer, which is representative of delamination in the interface, the following is for estimation of initial stiffness of cohesive layer:

$$\mathrm{K_{nn}} = \frac{1}{\frac{\mathrm{t_{concrete}}}{\mathrm{E_{concrete}}} + \frac{\mathrm{t_{epoxy}}}{\mathrm{E_{epoxy}}}} \tag{3.41}$$

3.5.11 Interface elements between concrete and steel reinforcement

Unlike the interface layer between concrete and FRP where all 3 modes of failure should be defined (from one-dimensional to 2 and 3-dimensional elements), the interface between concrete and steel bars could be represented by one-dimensional elements (link, spring, truss) because experimental tests have proved that steel bars slip in their own direction (failure mode 2). Therefore, one-dimensional elements could simulate the response of the interface layer between concrete and steel reinforcement. However, 2 or 3-dimensional elements could be defined to the interface layer in a way that the stiffness of cohesive layer should be higher in comparison to mode 2, where there would be no slippage in modes 1 and 3. This later technique increases the time of the FE analysis. Telford (1993) proposed the most accepted model for both plane and deformed bars to implement the interface layer that account for ascending and softening parts. Since the deformed bars are now used for both stirrups and longitudinal bars, the following presents the model proposed by Telford (1993) for bond-slip relationship between concrete and deformed steel bars (Figure 3.7):

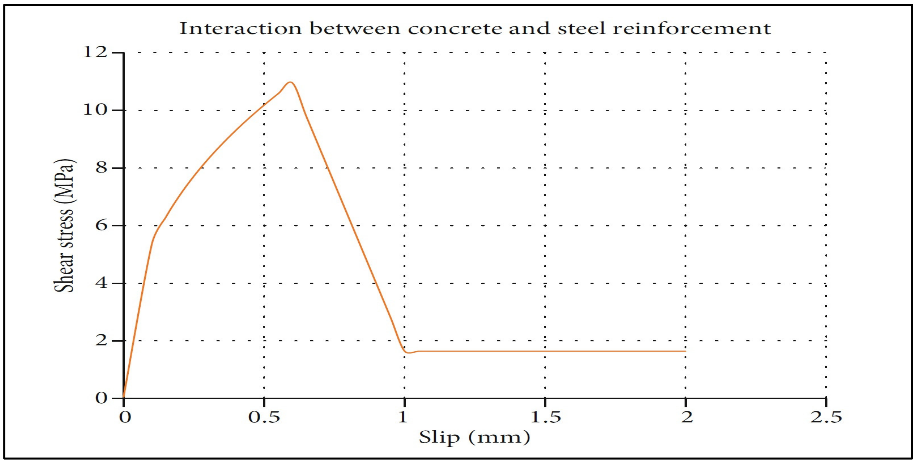

Figure 3.7 Telford model (Code, 1993) for bond-slip relation between concrete-deformed bars ($f_c' = 30\ MPa$)

$$\tau = \tau_{max}(\frac{s}{s_1})^{\alpha} \qquad \text{If} \qquad (s_0 \leq s \leq s_1) \tag{3.42}$$

$$\tau = \tau_{max} \qquad \text{If} \qquad (s_1 \leq s \leq s_2) \tag{3.43}$$

$$\tau = \tau_{max} - (\tau_{max} - \tau_f)(\frac{s-s_2}{s_3 - s_2}) \qquad \text{If} \qquad (s_2 \leq s \leq s_3) \tag{3.44}$$

$$\tau_{max} = \tau_f \qquad \text{If} \qquad (s_3 \leq s) \tag{3.45}$$

Where $\alpha = 0.4$, $s_1 = s_2 = 0.6\ mm, s_3 = 1\ mm$

$$\tau_{max} = 2.0 \times \sqrt{f_{ck}} \tag{3.46}$$

$$\tau_f = 1.5 \times \tau_{max} \tag{3.47}$$

3.5.12 Ratio of FRP, stirrups, and longitudinal bars

The ratio of FRP composites, longitudinal tensile steel reinforcement, and transverse steel stirrups affects the shear resistance of EB-FRP strengthened RC beams. In addition, the ultimate load-carrying capacity of the beam depends on the complex interaction among these reinforcing elements. Therefore, more FE parametric studies are required to clarify these interactions and their underlying mechanisms to achieve an optimized design model for the shear resistance of a beam. FEA is a powerful and cost-effective tool to perform such studies compared to experimental tests. For longitudinal steel reinforcement, it has been shown that assuming a perfect bonding model can reduce the shear resistance of specimens by reducing the shear contribution of EB-FRP in beams where the shear cracks are more distributed and inclined at a high angle with respect to the horizontal axis of the beam. Indeed, FRP laminates/fabrics crossed by shear cracks at a high angle are less solicited and result in less FRP contribution to shear resistance (GM Chen et al., 2012). More than 100 beams were selected from the database to evaluate the interaction between longitudinal reinforcement and EB-FRP, as illustrated in Figure . The figures reveal that the contribution of EB-FRP to shear resistance is reduced by increasing the amount of longitudinal tensile reinforcement, confirming the results reported by GM Chen et al. (2012). For steel stirrups, it has been demonstrated by Bousselham and Chaallal (2004) that the higher the stiffness of the steel stirrups, the less is the EB-FRP contribution to shear resistance. Finally, previous investigations (FEA, experimental tests, and analytical models) have demonstrated that, given the EB-FRP propensity to debonding failure, increasing the stiffness and cross section of EB-FRP could increase the FRP contribution to resistance up to a threshold, beyond which no increase in FRP contribution would occur because it is limited by the effective bond length (Guangming Chen, 2010). 138 (57.7%) of the 239 beams were subjected to FEA that evaluated the ratio of reinforcing components, of which only 33 (13.8%) were T-shaped, and 2 (less than 1%) were I-shaped cross-sections (Figure 3.4). There is a need for more FE studies to develop a reliable closed-form model for calculating the respective contributions of these shapes to shear resistance.

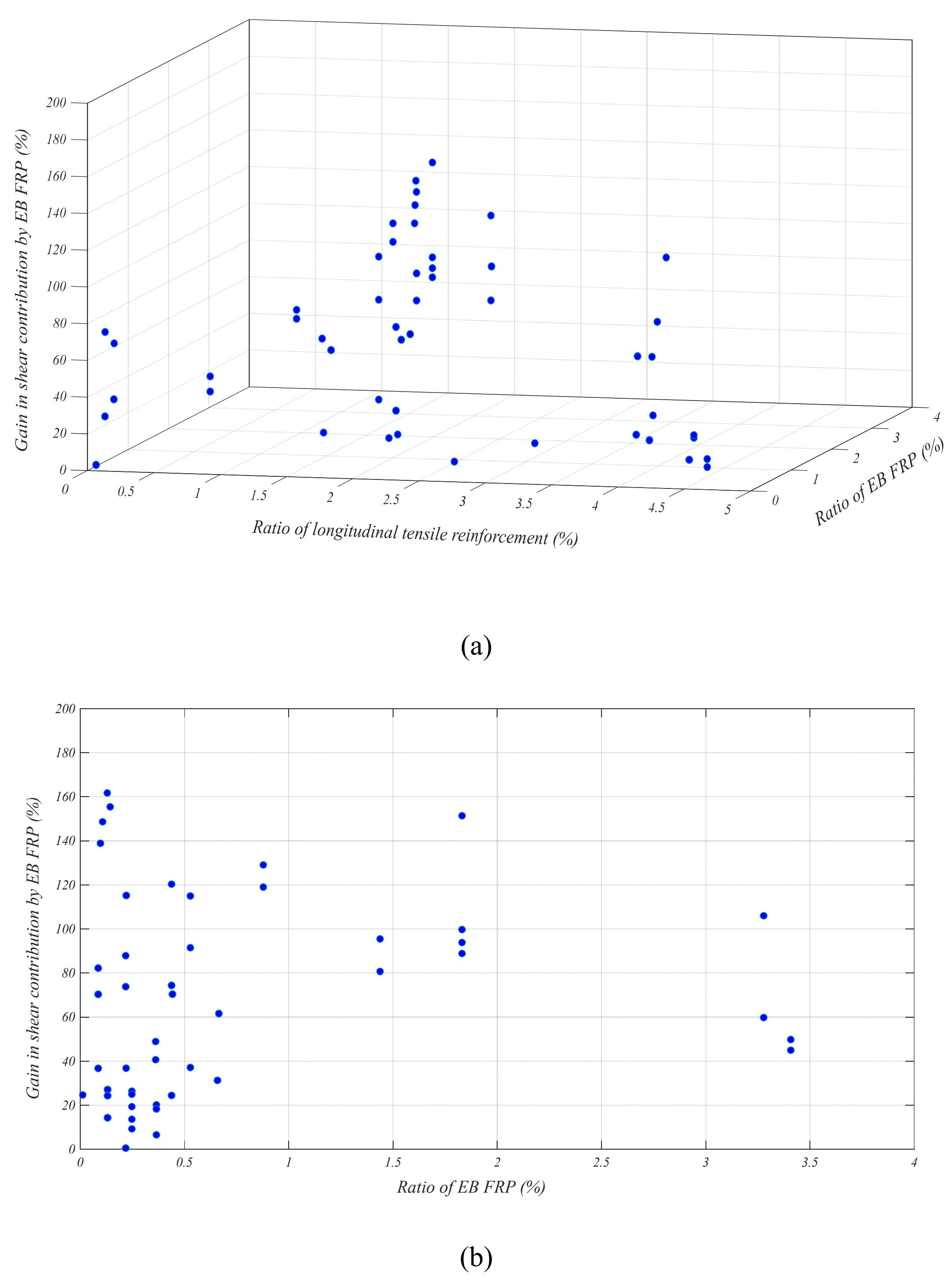

(a)

(b)

Figure 3.8 Interaction between longitudinal tensile reinforcement and EB-FRP versus shear gain contributions (X= Ratio of longitudinal reinforcement (%) Y= Ratio of EB FRP (%) Z= Gain in shear contribution by EB FRP (%))

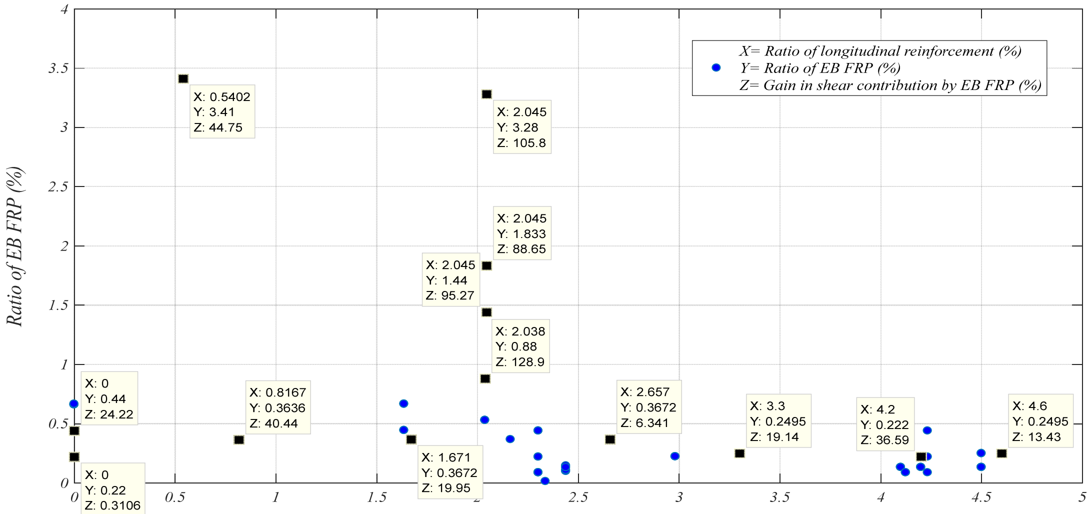

(c)

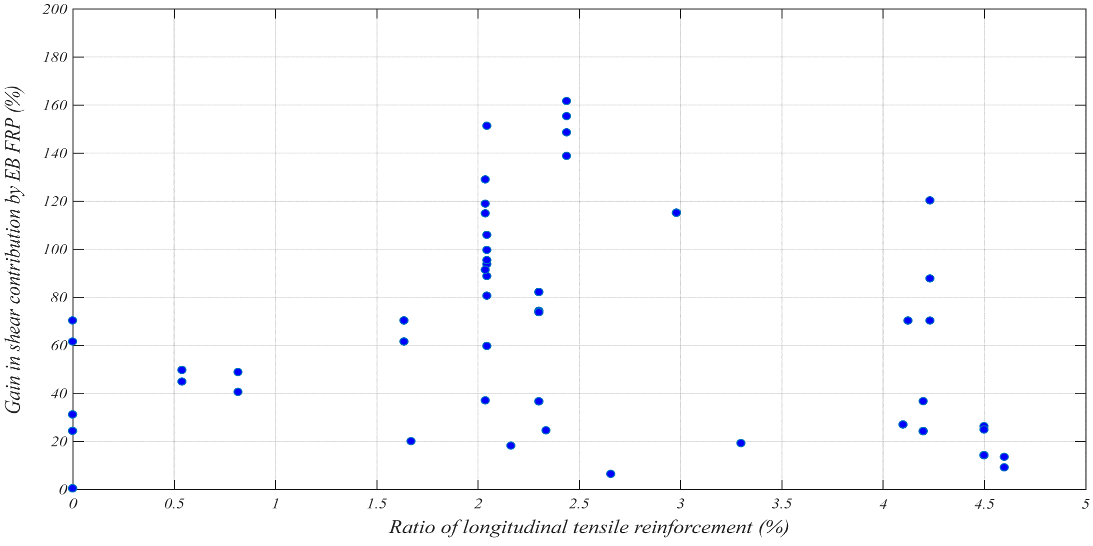

(b)

Figure 3.8 Interaction between longitudinal tensile reinforcement and EB-FRP versus shear gain contributions (X= Ratio of longitudinal reinforcement (%) Y= Ratio of EB FRP (%) Z= Gain in shear contribution by EB FRP (%)) (continued)

3.5.13 Dimension of the Beam (Size Effect)

The size effect is considered as a factor that can have a negative impact on the load-carrying capacity of RC beams. If all parameters are kept unchanged, the shear resistance of RC beams, particularly deep beams, will decrease as the beam's depth increases (Benzeguir et al., 2017). More than 100 specimens from the study database were considered to evaluate the relation between the beam depth and shear span-to-depth ratio versus normalized shear strength, as illustrated in Figure 3.9.

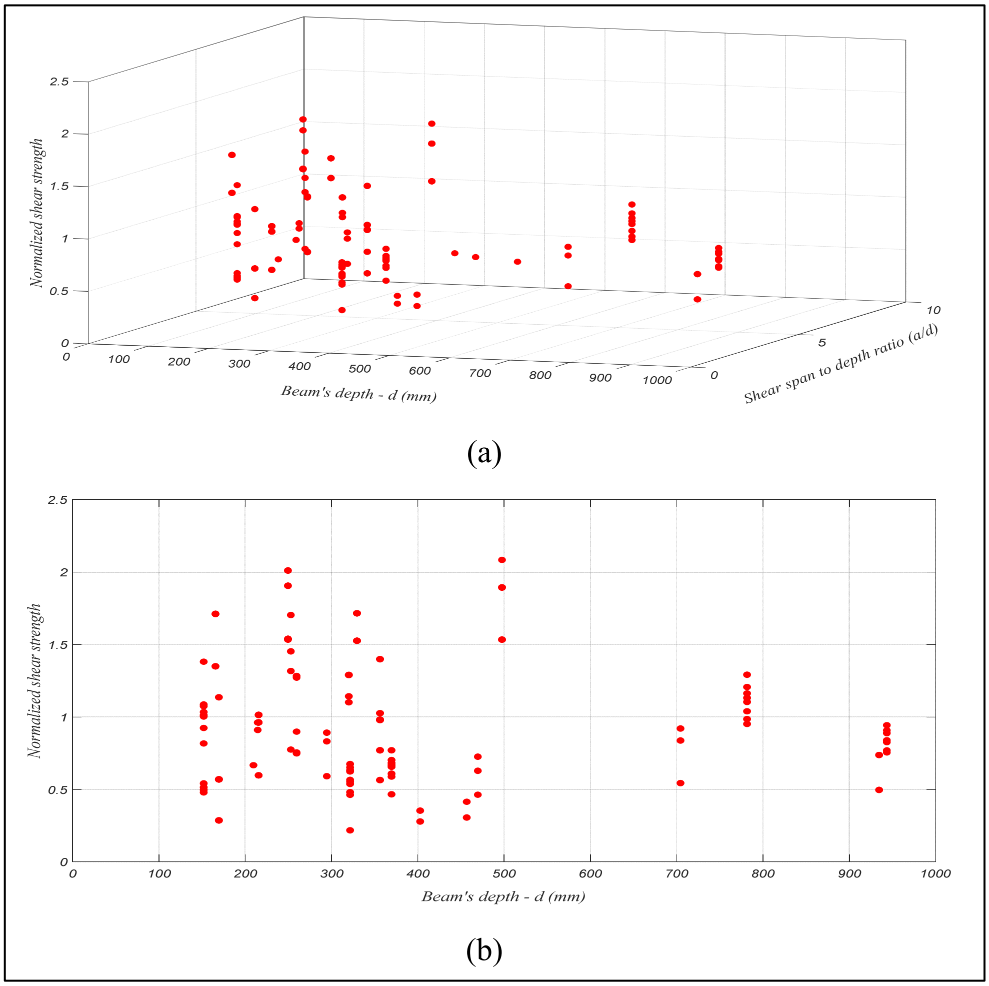

(a)

(b)

Figure 3.9 Effect of shear span-to-depth ratio on size effect versus normalized shear strength (X= Beam's depth (mm) Y= Shear span to depth ratio (a/d) Z= Normalized shear strength)

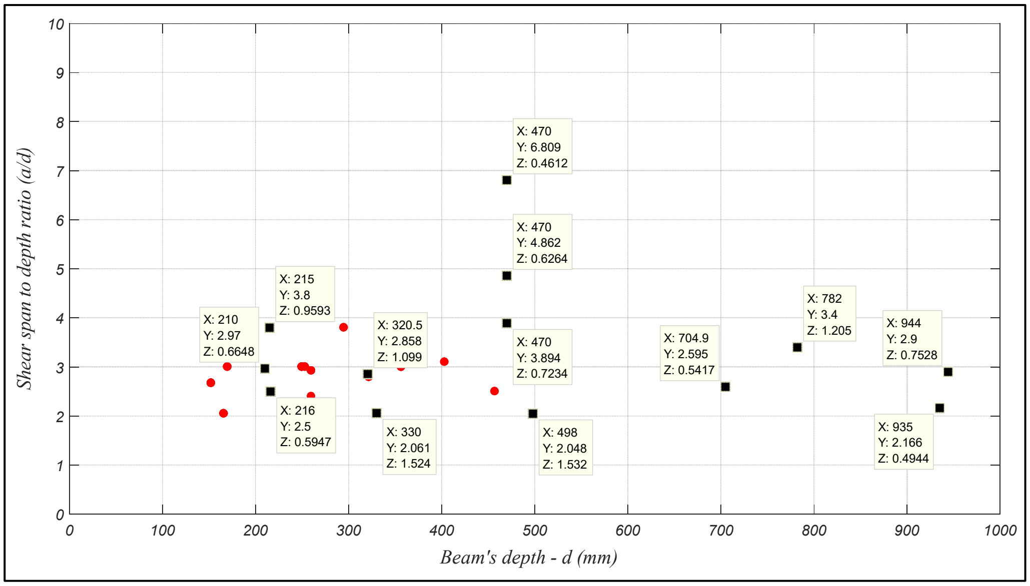

Figure 3.9 Effect of shear span-to-depth ratio on size effect versus normalized shear strength (X= Beam's depth (mm) Y= Shear span to depth ratio (a/d) Z= Normalized shear strength) (Continued)

The size effect is considered as a factor that can have a negative impact on the load-carrying capacity of RC beams. If all parameters are kept unchanged, the shear resistance of RC beams, particularly deep beams, will decrease as the beam’s depth increases (Benzeguir et al., 2017). More than 100 specimens from the study database were considered to evaluate the relation between the beam depth and shear span-to-depth ratio versus normalized shear strength, as illustrated in Figure 3.9. The figures reveal that, given the shear span-to-depth ratio (*a*/*d*), increasing the beam’s depth (*d*) reduces the normalized shear strength of the RC beam strengthened in shear using EB-FRP, which confirms the results obtained by Benzeguir et al. (2017). The database shows that few studies have been performed on the size effect of shear-strengthened RC beams using EB-FRP. Two known theories related to the size effect are generally used: the Weibull theory and the theory based on fracture mechanics. The model proposed by Bazant and Planas (1997) is the only closed-form model that considers this effect and can be expressed as:

$$\sigma_{Nu} = \frac{B\acute{f}_t}{\sqrt{1+D/D_0}} \tag{3.48}$$

A complete parametric study on the size effect on EB-FRP RC beams was conducted by Benzeguir et al. (2017), where five major factors influencing the size effect were evaluated: the shear-span-to depth ratio a/d, the aggregate size a_g, the ratio of longitudinal tension bars ρ_w, the ratio of steel stirrups ρ_s, and the concrete strength f'_c. Many numerical studies have been carried out on beams of different sizes. However, the aim of these numerical studies was not to evaluate the size effect in RC beams strengthened in shear using EB-FRP composites. 165 (69%) of the 239 beams in this study were analyzed by FEA to study the effect of beam dimension, of which 149 (62.3%) were rectangular, 14 (5.8%) were T-shaped, and 2 (less than 1%) were I-shaped cross-sections (Figure 3.4).

3.6 Synthesis, results and recommendations

FEA provides a powerful tool that can replace experimental tests if accurate assumptions are provided to the software and the required in-depth knowledge is obtained regarding parameters that affect dynamic analysis, such as loading pattern (smoothing, stepping, or ramping), impact loading duration, amount of damping for EB-FRP RC beams, and finally time increment when performing nonlinear dynamic analysis. FEA of RC beams strengthened in flexure is well documented. This does not hold true for RC beams strengthened in shear using EB-FRP composites, where clearly there is a need for more research studies. Indeed, first, the brittle behavior of shear cracks in RC beams is still unpredictable and becomes even more complex when RC beams are strengthened in shear with EB-FRP because the type of EB strengthening affects the shear crack pattern. Second, interactions between the components of such strengthened beams have not been fully documented, and indirect interactions between the components and their effects on each other are still not fully understood. Third, selecting the right type of finite element for each component of these beams is of paramount importance and needs a theoretical and experimental understanding of the response of each material when used for shear strengthening.

From existing FE studies on EB-FRP RC beams, it is obvious that early studies assumed perfect bond-slip models for their specimens and only 18.4% (44 beams) of all the FE studies considered bond-slip laws for both concrete-to-FRP and concrete-to-steel reinforcement interactions. This has led to incorrect results because Bousselham and Chaallal (2004) proved that increasing the rigidity of steel stirrups results in a reduction of EB-FRP contribution to shear resistance. Therefore, defining appropriate bond-slip laws between all the various materials involved in a study must be a priority. Furthermore, GM Chen, Teng, et al. (2010) showed that there is an inverse interaction between internal and external reinforcement and that its effect should be considered in a closed-form model, suggesting a need for research on this phenomenon.

Because of the unpredictable nature of shear cracking, most international guidelines recommend a crack angle of 45°, which is obviously overestimated, but conservative. The crack shape functions presented by Lu *et al*. (2009) are based on four simplified assumptions, leading to unrealistic stress and strain distributions for fibers intercepted by the shear crack. Moreover, from the data evaluated earlier, 35.1% (84 beams) of all FE studies considered the stress and strain distributions along the shear crack. In addition, the assumption of one main shear crack is to some extent unrealistic because experimental tests revealed more marginal distributed shear cracks that contributed to shorter effective bond length. Therefore, more research is needed to encompass the patterns and shapes of shear cracks for EB-FRP strengthened RC beams.

The smeared crack model in conjunction with the crack band model is an appropriate model for defining shear cracks in concrete. These should be considered alongside appropriate bond-slip laws between all components of EB-FRP RC beams to achieve an accurate simulation of the real specimen. It may be worth noting that, from the FE data already gathered, only 5% (12 beams) research studies have observed this phenomenon.

3.7 Validation of Numerical FEA and Experimental Tests

The validation of over 200 specimens strengthened with different configurations (side-bonded, U-shaped, fully wrapped, EB with anchorage, ETS, NSM), and unstrengthen (control beams) is carried out to evaluate the accuracy of the FEA results in terms of ultimate load-carrying capacity of the specimens. Figure 3.10 shows the numerical versus experimental results for total strength achieved by all the specimens. The results reveal that the FE studies predicted the experimental tests with good agreement because the square of the Pearson product-moment correlation coefficient (R^2) was greater than 99% for all beams.

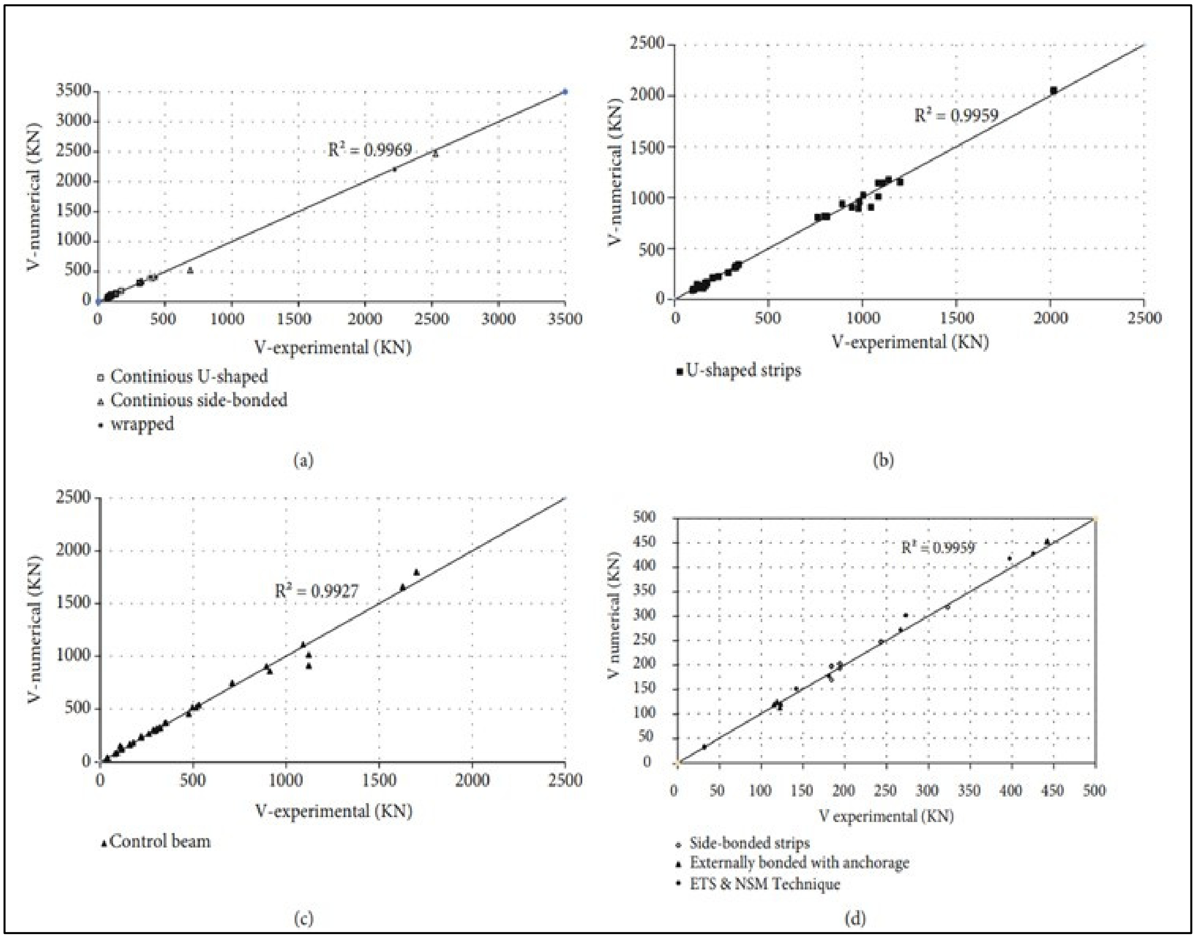

Figure 3.10 Numerical versus experimental ultimate load-carrying capacity of the specimens for: (a) continuous U-shaped, continuous side-bonded, fully-wrapped; (b) U-shaped strips; (c) Control beam; (d) Side-bonded strips, EB with anchorage, ETS and NSM methods

3.8 Conclusions

This study has concentrated on the evaluation of many factors affecting the accuracy of simulating RC beams strengthened in shear with EB-FRP and of parameters studied by researchers through FEA. To that end, an extensive database consisting of over 200 FE specimens validated by experimental tests was gathered and evaluated in this study. The most relevant features drawn from the FEA and the studied parameters were as follows:

- To achieve an accurate simulation reflecting the behavior of the real beam, the parameters and elements introduced in FEA should represent the real response of each component. Essential building blocks of FEA include the smeared crack model alongside the crack band model and the bond-slip law to describe concrete-to-FRP and concrete-to-steel reinforcement interactions, and dynamic analysis in which parameters such as the structure-damping ratio, the time increment, the crack pattern, and the loading duration are well characterized. Less than 6% of all FE studies addressed these parameters, and none of them described the implementation details.
- After FEA is performed on RC beams strengthened in shear with EB-FRP, the study parameters obtained from the output to develop the analytical model should be extracted precisely, and their complex effects on each other should be carefully examined. The angle of the shear crack in concrete, the interaction between components of specimens, the inverse interaction between internal and external reinforcements, the shape of the shear crack, the stress and strain distributions along the shear cracks, the size effect, and the type of FRP configuration are some of these important interacting parameters.
- The ultimate load-carrying capacity of a specimen is not the only good indication for evaluating the overall specimen response. FEA is a powerful and useful tool for evaluating other important response indicators, considering all the beam components during the process of loading. Therefore, based on the built database, studies are needed to consider the influencing parameters required to develop a reliable closed-form model to calculate with confidence the EB-FRP contribution to shear resistance.
- FEA can capture the real behavior of a beam, including details that can be important to the research community, such as the number and angle of shear cracks and the stress distribution along the shear cracks and fibers.
- By drawing comparisons between variations in the ratio of EB-FRP and in the ratio of steel stirrups, it is obvious that for each ratio of steel stirrups, there exists only one peak for the ratio of EB-FRP corresponding to the maximum gain due to FRP. This inverse interaction should be considered for optimal design.

- When drawing comparisons between FRP contributions to shear resistance in RC beams strengthened in shear using EB-FRP, the negative impact of size effect should be included in any final closed-form model.

3.9 Acknowledgements

Financial support from the Natural Sciences and Engineering Research Council of Canada (NSERC) and from the Fonds de recherche du Québec – Nature et technologie (FRQ-NT) through operating grants is gratefully acknowledged

CHAPTER 4

FE MODELLING AND SIMULATION OF THE SIZE EFFECT OF RC T-BEAMS STRENGTHENED IN SHEAR WITH EXTERNALLY BONDED FRP FABRICS

Amirali Abbasi[1], Zine El Abidine Benzeguir[2], Omar Chaallal[3] and Georges El-Saikaly[4]

[1,2,3,4] Department of Construction Engineering, École de Technologie Supérieure
1100 Notre-Dame St W, Montreal (Quebec) H3C 1K3, Canada

Paper published in Journal of *Composites Science*, Volume 116, Issue 6.4, April 2022

4.1 Abstract

The objective of this study is to conduct a finite-element (FE) numerical study to assess the effect of size on the shear resistance of reinforced concrete (RC) beams strengthened in shear with externally bonded carbon fibre-reinforced polymer (EB-CFRP). Although a few experimental studies have been done, there is still a lack of FE studies that consider the size effect. Experimental tests are time-consuming and costly and cannot capture all the complex and interacting parameters. In recent years, advanced numerical models and constitutive laws have been developed to predict the response of laboratory tests, particularly for issues related to shear resistance of RC beams, namely, the brittle response of concrete in shear and the failure modes of the interface layer between concrete and EB-CFRP (debonding and delamination). Numerical models have progressed in recent years and can now capture the interfacial shear stress along the bond and the strain profile along the fibres and the normalized main diagonal shear cracks. This paper presents the results of a nonlinear FE numerical study on nine RC beams strengthened in shear using EB-CFRP composites that were tested in the laboratory under three series, each containing three sizes of geometrically similar RC beams (small, medium, and large). The results reveal that numerical studies can predict experimental results with good accuracy. They also confirm that the shear strength of concrete and the contribution of CFRP to shear resistance decrease as the size of beams increases.

Keywords: size effect; reinforced concrete beams; finite-element method; shear strengthening; externally bonded carbon fibre-reinforced polymer (EB-CFRP) composites

4.2 Introduction

In the last two decades, very few FE studies have been dedicated to RC beams strengthened in shear EB-FRP or any types of strengthening with composite materials (Tan, 2014) made of CFRP (Kolanu et al., 2020; Rozylo, 2021). However, given the lack of accurate constitutive laws at that time, these early FE studies did not consider the bond between concrete and FRP, nor did they simulate the interaction between concrete and steel reinforcement(Amir, 1998; Arduini et al., 1997; Elyasian et al., 2006; Kachlakev et al., 2001; Kaliakin et al., 1996; T. K. Lee et al., 2000; Santhakumar et al., 2004; Vecchio & Bucci, 1999). Recently, some FE studies have concentrated on shear strengthening using embedded-through-section (ETS) and near-surface-mounted (NSM) techniques (Ahmed Godat et al., 2013; Qapo et al., 2016; Shomali et al., 2020). With recent advances in the development of high-performance FE programs and constitutive laws, numerical studies can better simulate and accurately predict the outcome of experimental tests in terms of load-deflection response, behavior of the interface between concrete and EB-FRP, and the strain distribution along fibres (Al Jawahery et al., 2019; GM Chen et al., 2012; GM Chen, Teng, et al., 2010; Dirar et al., 2012; A Godat et al., 2008, 2012; Ahmed Godat et al., 2012; Ahmed Godat et al., 2007; Ahmed Godat et al., 2010; Ibars et al., 2018; Imperatore et al., 2012; Jin et al., 2020; H.-K. Lee et al., 2008; Lu et al., 2009; Manos et al., 2014; Qapo et al., 2016; Qapo et al., 2015; Qu et al., 2006; Sayed et al., 2013; Smith et al., 2006; Wong & Vecchio, 2003; You et al., 2011). Nevertheless, among these studies, very few have considered either the size effect of EB-FRP-strengthened RC beams (Ahmed Godat et al., 2010; Jin et al., 2020) or the crack band model along with the concrete smeared crack model. This was the main impetus to carry out this study to assess the size effect by means of a numerical approach, by implementing both crack models in modelling the concrete and by considering the interface behavior between EB-FRP and the concrete substrate.

Given their complex behavior under loading, as well as their brittle rupture without warning, shear failure in RC beams has long been a major concern in structural engineering. Therefore, practicing engineers often privilege the sequence by which flexural failure occurs before shear failure. Lack of shear strength in RC beams can be due to various interacting factors. Neglecting the size effect in codes and guidelines and thereby overestimating the ultimate shear capacity in the design process is an example of the effect of such factors. In recent years, the trends towards using FRP composites for rehabilitation and strengthening of RC beams have become intensified due to the high strength-to-weight ratio and tensile strength of FRP composites, which can compensate for the shear-strength deficiency of existing RC beams. It has been established that when the beam size is increased, the shear strength decreases due to the so-called size effect (Bazant & Kazemi, 1991; Collins & Kuchma, 1999; Kani, 1967). Many parameters affect the size effect, either mitigating or amplifying it by controlling the width of the diagonal shear crack—for example, the rigidity of FRP sheets (Benzeguir et al., 2019). Even though comprehensive studies have been performed on the effect of size in RC beams, research studies related to the size effect on RC beams strengthened with EB-FRP are limited. FE analysis can be implemented instead of experimental testing to obtain an inside view of the shear-stress profile variation along the interface layer and the distribution of stress on the fibres during loading. Most analytical models proposed by codes and guidelines are based on experimental results and can be prone to errors (human error, defects in laboratory machines, restricted tools...). Therefore, the results obtained from these models are not as accurate as those from FE methods for capturing the shear resistance contribution of concrete and EB-FRP through appropriate evaluation of strain distributions on the fibres.

The FE method is a cost-effective and precise tool for replacing experimental tests as long as the models are simulated based on reliable and logical assumptions. A few FE studies have been performed on the size effect of RC beams strengthened in shear with EBCFRP, but either their assumptions were very simplistic, such as perfect bonding between concrete and EB-CFRP, which does not reflect the response of such a beam (location of the shear crack), or they fail to mention the assumptions used in their simulations. As explained in the following sections, the developed 2D-FE model was preferred to 3D models because it is less time-consuming and simulates the propagation of the shear crack in concrete with higher precision. Note that the shear crack is a major parameter in predicting the size effect.

As illustrated in Figure 1, the shear contributions of EB-FRP predicted by ACI 440.2R 2017 for over 50 beams with different depths varying from 80 mm to 682 mm strengthened in shear with continuous U-wrap and strips were compared with their corresponding experimental tests (see Appendix A Table A1 for details). The beams were classified into three categories depending on their depth (Figure 4.1). As the depth of the specimens and their corresponding EB-FRP bond lengths increased, the ACI 440.2R (2017) guidelines clearly overestimated the shear contribution of EB-FRP, which may indicate the existence of an additional size effect due to the contribution of EB-FRP to shear resistance. In fact, the models of most guidelines overestimate the contribution of EB-CFRP to shear resistance in large specimens.

In the current study, nine RC-T beams without steel stirrups (Benzeguir et al., 2019) were selected for simulation. The beams were grouped into three series (small, medium, large). In each series, one beam was considered a control (not strengthened with EB-FRP), and the others were strengthened with one and two layers of EB-FRP. The results from the simulated models were validated with experimental tests.

The objectives of the present study were to evaluate the size effect and the shear contributions of concrete and EB-FRP, as well as the effect of an increase in EB-FRP rigidity, on the three series of specimens (different sizes) through numerical investigation. Capturing the response of the interface layer between concrete and CFRP sheets, as well as the distribution of strain along the main fibre of CFRP fabrics during loading, is of paramount importance when using FEA, given their impact on the size effect. Therefore, the impact of the response of the interface layer, the strain distribution along the fibre, and the fibres intercepted by the main diagonal shear crack on the size effect will be studied carefully, along with the failure modes, the load-deflection response, and the pattern of shear cracks. The novelty of this study is to conduct FE research on the size effect and to show the development of the shear stress and strain in the interface layers and fibres during the loading process. Furthermore, by extracting the strain distribution curve on the fibres that intercepted the main shear crack, it would be possible to measure the distribution factor leading to the effective strain experienced, which is far lower than the effective strain introduced in codes and guidelines.

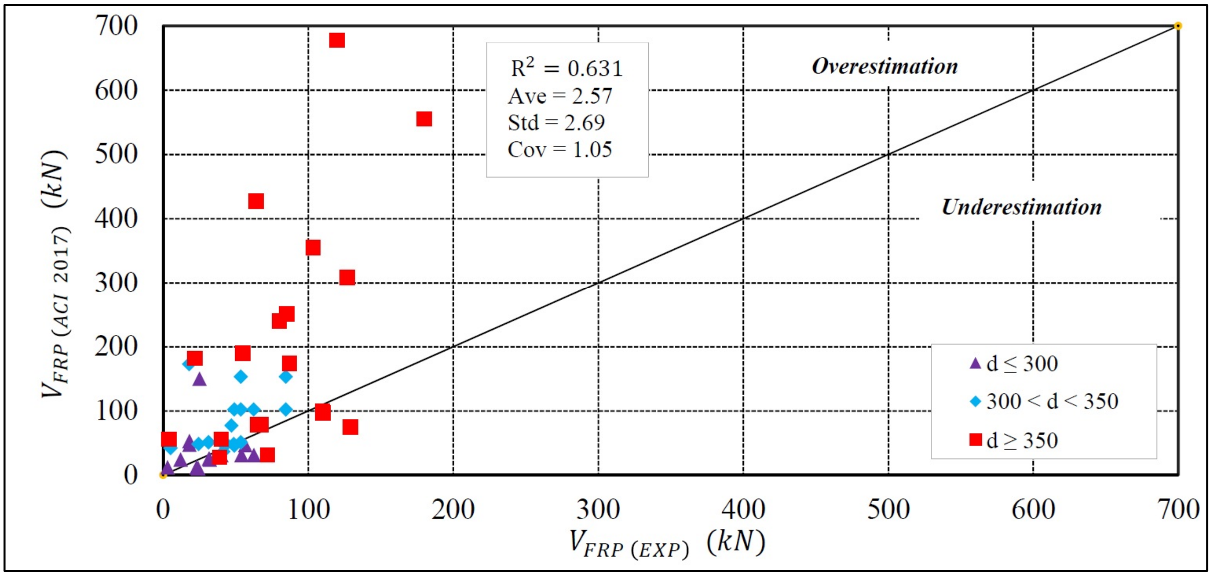

Figure 4.1 Comparison of the predicted ACI 440.2R 2017 code and experimental results

4.3 Finite-Element Modelling

4.3.1 Suggested FE Modelling

The assumptions implemented for a simulation related to the types of crack models for concrete, steel bar, CFRP sheets, and the interface layer between concrete and CFRP are described in the following sections. Because the beam was not under stress in the normal direction to the plane of the beam, the plane stress model was used for concrete. Steel bars and CFRP sheets were modelled by 2D truss elements that contributed to transferring the stress in the direction of the truss element. Dynamic implicit analysis was implemented to overcome the convergence problem. Indeed, because the divergence occurred due to the brittle behavior of concrete and the nonlinearity of the interface layer between concrete and CFRP (delamination and debonding), general static solvers (static, general and static, Riks) cannot capture the nonlinearity of materials during imposed targeted displacement. Details of the implicit dynamic analysis implementation are described in Guangming Chen (2010).

4.3.2 Constitutive Models of Materials

4.3.2.1 Concrete Cracking Models

Various types of concrete cracking models can be used with FEA. The discrete crack model, the rotating smeared crack model, and the fixed smeared crack model are some examples. Considering the discrete crack model, a crack is introduced into the model geometry, where crack propagation occurs along the border of the element in FEA, proving its mesh objectivity. Furthermore, the location of the crack in the model must be defined in advance, which shows the dependency of this technique on how the precise initiation of the crack is predicted. Unlike the discrete crack model, there is no need to predefine the cracking initiation location in the smeared crack model because probable cracking zones and directions are recognized through the smeared crack technique. Elements lose their stiffness as the crack propagates in the smeared crack approach, whereas the stress-strain relation in concrete considers cracks a continuum and predicts the deletion of elements when a crack path is detected. The smeared crack approach can be classified into two categories: the rotating smeared crack approach and the fixed smeared crack approach. The differences between them are their theories for crack direction and their shear retention factor. The deficiency of the smeared crack model is that when element size decreases, it leads to zero energy dissipation in the softening part of the stress–strain curve in the tensile concrete material, resulting in strain localisation (GM Chen et al., 2012). To address strain localisation, some limiters have been proposed, among which the crack band model implemented in the concrete damage plasticity framework has been proved to address mesh objectivity challenges resulting in convergence problems (Bažant & Becq-Giraudon, 2002). The function of the crack band model is to convert the width of the crack band to the cracking strain caused by the crack, as shown in Figure 4.2.

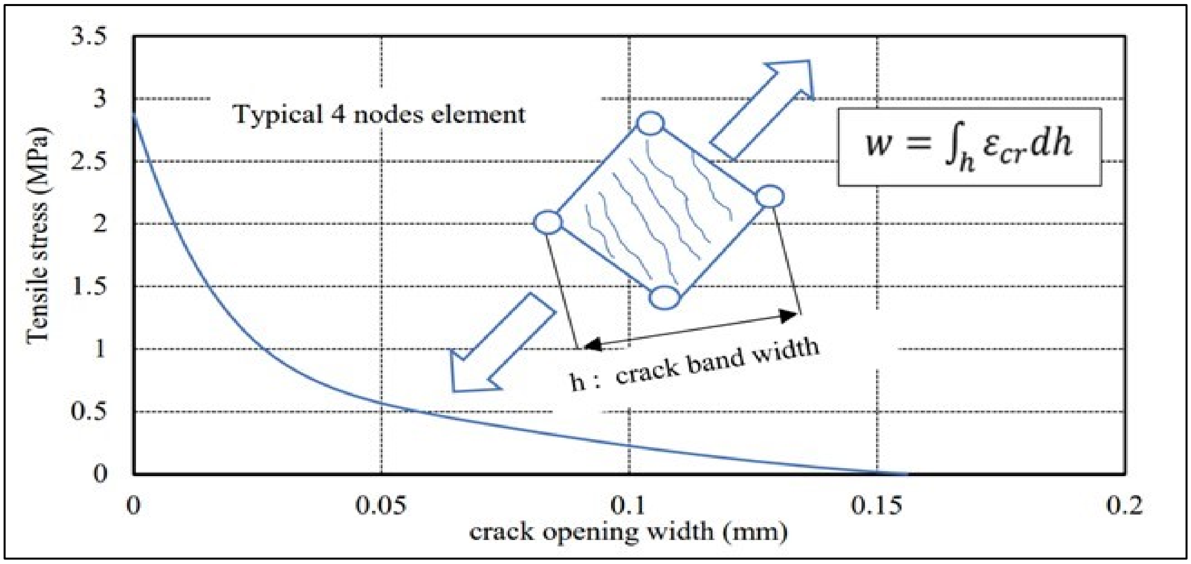

Figure 4.2 Relation between cracking width and tensile stress introduced by Hordijk (1991)

4.3.2.2 Concrete Response in Compression and Tension

Because the RC T-beams in the present study behave in their plane, a four-node plane stress element (CPS4) was implemented to simulate concrete. Various models have been proposed to represent the uniaxial behaviour of concrete in compression, among which the model introduced by Saenz (1964) (see Equation 1) features a decent prediction of the ascending and softening parts of the concrete material curve, as shown in Figure 4.3.

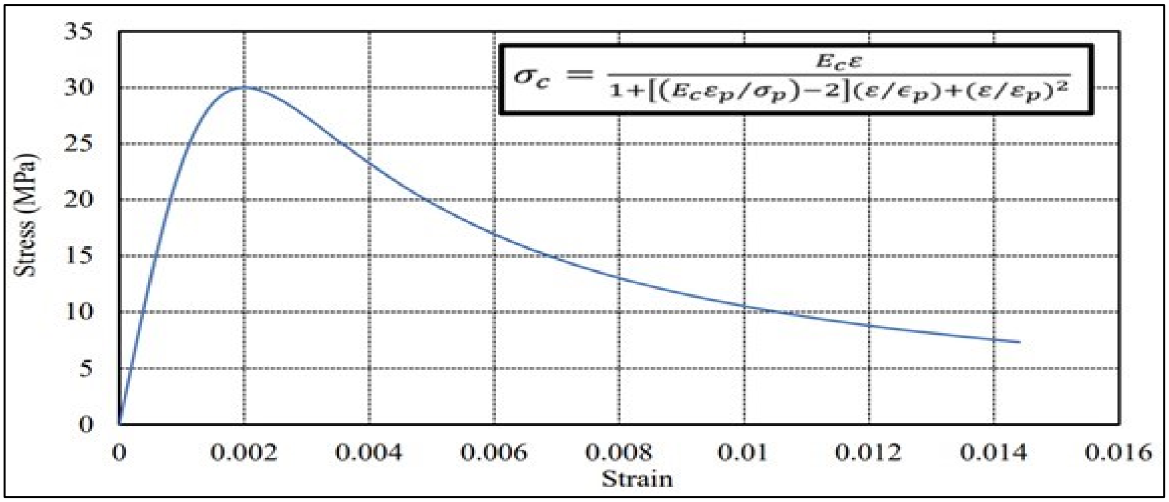

Figure 4.3 Stress-strain model for uniaxial compression in concrete introduced by Saenz (1964)

$$\sigma_c = \frac{\alpha\varepsilon}{1+[(\alpha\varepsilon_p/\sigma_p)-2](\varepsilon/\epsilon_p)+(\varepsilon/\varepsilon_p)^2} \tag{4.1}$$

where σ_p and ε_p are the maximum concrete compressive stress and strain obtained from experimental tests, equal to $f_c^{'} = 30$ MPa and 0.002 respectively; E_c is the concrete modulus of elasticity, $E_c = 4730\sqrt{f_c^{'}}$ (MPa) according to (ACI 318); σ and ε are the applied compressive stress and corresponding strain during loading of the cylindrical specimen.

To define tensile concrete behaviour in the descending and softening parts, the model introduced by Hordijk (1991) on the basis of numerous stress-crack displacement tests was implemented in this study as follows:

$$\frac{\sigma}{f_t} = \left[1 + \left(c_1\frac{w}{w_{cr}}\right)^3\right] e^{\left(-c_2\frac{w}{w_{cr}}\right)} - \frac{w}{w_{cr}}(1 + {c_1}^3)e^{-c_2} \tag{4.2}$$

$$w_{cr} = 5.14\frac{G_f}{f_t} \tag{4.3}$$

$$f_t = 1.4(\frac{f_c^{'}-8}{10})^{\frac{2}{3}} \tag{4.4}$$

$$G_f = (0.0469{d_a}^2 - 0.5d_a + 26)(\frac{f_c^{'}}{10})^{0.7} \tag{4.5}$$

where w is the crack width during loading; w_{cr} is the crack width at the moment when no stress can be transferred between the two sides of the crack; f_t is the maximum concrete tensile stress; σ is the tensile stress in the specimen during the stress-crack displacement test; G_f is the fracture energy, which in addition to Equation (5), can be obtained from the area of the stress-cracking displacement graph (Figure 2); $c_1 = 3$, $c_2 = 6.93$ are constant parameters proposed by Hordijk (1991); and d_a is the largest aggregate dimension.

4.3.2.3 Definition of Compressive and Tensile Damage to Concrete Damage Plasticity (CDP)

To define concrete damage in both compression and tension, represented by the softening part of the stress-strain curves, the proposed model introduced by Tao and Chen (2014) was considered as follows:

$$d_{t,c} = \begin{cases} \frac{(1-k)\varepsilon^{P}}{(1-k)\varepsilon^{P}+\sigma/E_0} & if \quad \dot{\varepsilon}^{P} \geq 0 \\ \frac{\varepsilon^{P}-(\varepsilon-\bar{\varepsilon}_{cr}^{e})}{\varepsilon^{P}-(\varepsilon-\bar{\varepsilon}_{cr}^{e})+\sigma/E_0} & if \quad \dot{\varepsilon}^{P} < 0 \end{cases} \tag{4.6}$$

where $d_{t,c}$ is the damage parameter in both tension and compression; $\dot{\varepsilon}^{P}$ is the plastic strain rate; k is the rate of inelastic strain when stiffness degrades ($\bar{\varepsilon}^{P}$) to inelastic strain when stiffness is constant (ε^{P}); $\bar{\varepsilon}_{cr}^{e}$ is the cracking strain when the plastic strain rate is zero. The smeared crack model is implemented in the concrete damage plasticity (CDP) framework. Therefore, the stress-strain behaviour of concrete in tension is transformed to stress-cracking displacement through the crack band model, $\varepsilon_t^p = w_t/h$ (Tao & Chen, 2014). Furthermore, the graphs in Figure 4.4 obtained from Equation 4-6 are applied for both tensile and compressive damage in concrete versus cracking displacement and plastic strain respectively (for 10-mm element size).

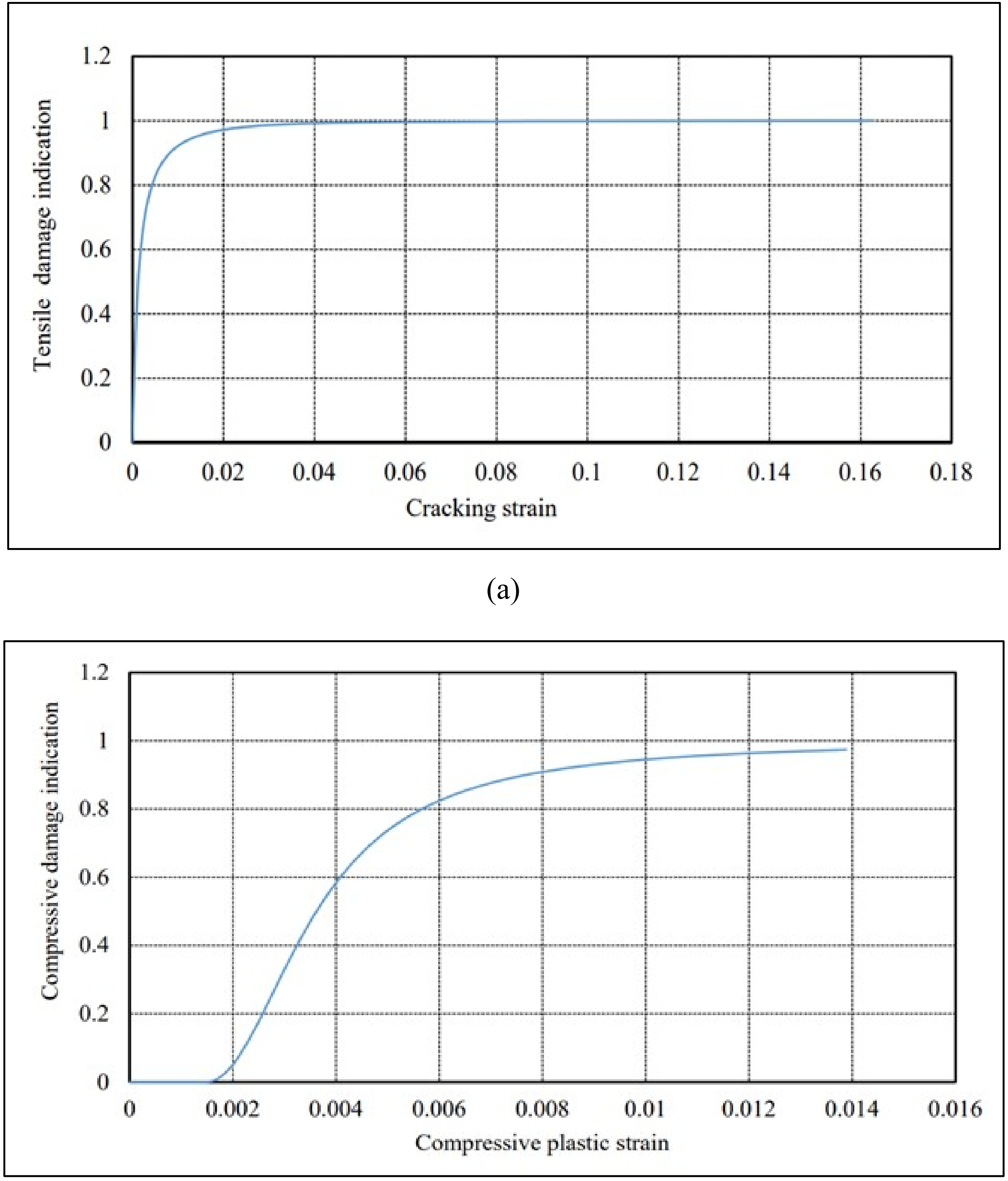

(a)

(b)

Figure 4.4 Tensile concrete damage model (for 10 mm element size): (a) compressive concrete damage models; (b) proposed by Tao and Chen (2014)

4.3.2.4 Bond-Slip Model for Concrete–Steel Reinforcement and Concrete–CFRP

To predict the ultimate shear capacity of an RC beam shear-strengthened with EB-FRP, the interaction between concrete and FRP composites should be defined precisely; otherwise, the software cannot identify the potential failure modes between concrete and CFRP, such as debonding and delamination. Early simulations assumed a perfect bond between the components of such beams, resulting in overestimation of the load-carrying capacity of the specimens. In addition, the perfect bond model between concrete and EB-CFRP has an effect on the distribution, direction, and position of shear cracks, leading to incorrect debonding and delamination. Because no slips were observed between concrete and longitudinal bars, a perfect bond model was assumed between the concrete and the longitudinal steel reinforcement. As for the bond between the concrete substrate and EB-CFRP, a two-dimensional, four-node cohesive element (COH2D4) that could capture both debonding and delamination failures in the model was implemented in ABAQUS. To define the properties of the cohesive elements, a simplified bond-slip law introduced by Lu *et al.* (2005) was implemented in this study (Figure 4.5). The ascending and softening parts of the bond-slip curves were defined as follows:

$$\tau = \tau_{max}\sqrt{\frac{s}{s_0}} \qquad \text{if} \qquad s \leq s_0 \tag{4.7}$$

$$\tau = \tau_{max}e^{-\alpha(\frac{s}{s_0}-1)} \qquad \text{if} \qquad s > s_0 \tag{4.8}$$

where $s_0 = 0.0195\beta_w f_t$; $G_f = 0.308\beta_w{}^2\sqrt{f_t}$; $\alpha = \frac{1}{\frac{G_f}{\tau_{max}s_0}-\frac{2}{3}}$; $\beta_w = \sqrt{\frac{2-({}^{w_f}/_{(s_f\,sin\,\beta)})}{1+({}^{w_f}/_{(s_f\,sin\,\beta)})}}$; and $\beta =$ fibre orientation. In the direction normal to the cohesive layer, which is representative of interface delamination, the following model was implemented for the cohesive layer to estimate the initial stiffness:

$$K_{nn} = \frac{1}{\frac{t_{concrete}}{E_{concrete}}+\frac{t_{epoxy}}{E_{epoxy}}} \tag{4.9}$$

where $t_{concrete}$ is the substrate thickness of concrete, t_{epoxy} is the thickness of epoxy, and $E_{concrete}$ and E_{epoxy} are respectively the concrete and epoxy moduli of elasticity. The maximum tensile strength normal to the cohesive layer was also assumed equal to the maximum strength of concrete in tension.

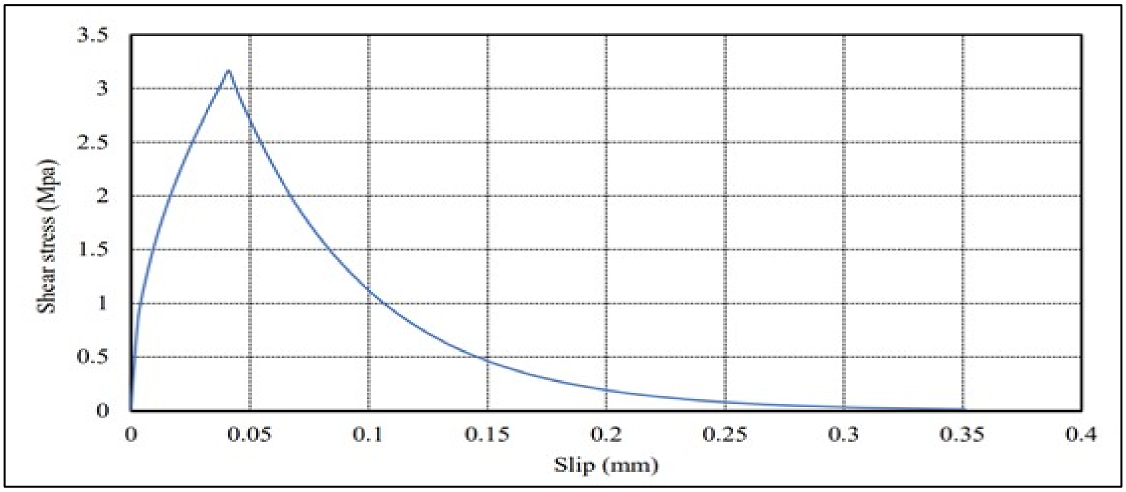

Figure 4.5 Bond–slip model between concrete and CFRP proposed by Lu et al. (2005)

4.3.2.5 Modelling Internal Steel Reinforcement and EB-CFRP

To model the internal steel reinforcement and the external CFRP fabric, two-node 2D truss elements (T2D2) were implemented in the current study. Details of the simulation are illustrated in Figure 4.6. The elastic–plastic material was assigned to the steel reinforcement where bilinear response of the stress–strain behavior of steel bars in tension was assumed instead of nonlinear behavior after reaching the elastic limit to reduce calculation time (Figure 4.7 a). As for EB-CFRP, the material was considered elastic until rupture in such a way that CFRP fibres could contribute to shear resistance through their tensile strength (Figure 4.7 b) while their compression strength was zero. Based on Guangming Chen (2010), it was assumed that when FRP wrap is modelled by truss elements, the space between truss elements should be approximately $S_f = {}^{h_{f,e}}/_{20}$ to achieve reasonable agreement with continuous FRP fabrics. Therefore, the space between the truss elements modelling CFRP fibres was set to 10 mm, 10 mm, and 5 mm for large, medium, and small beams, respectively.

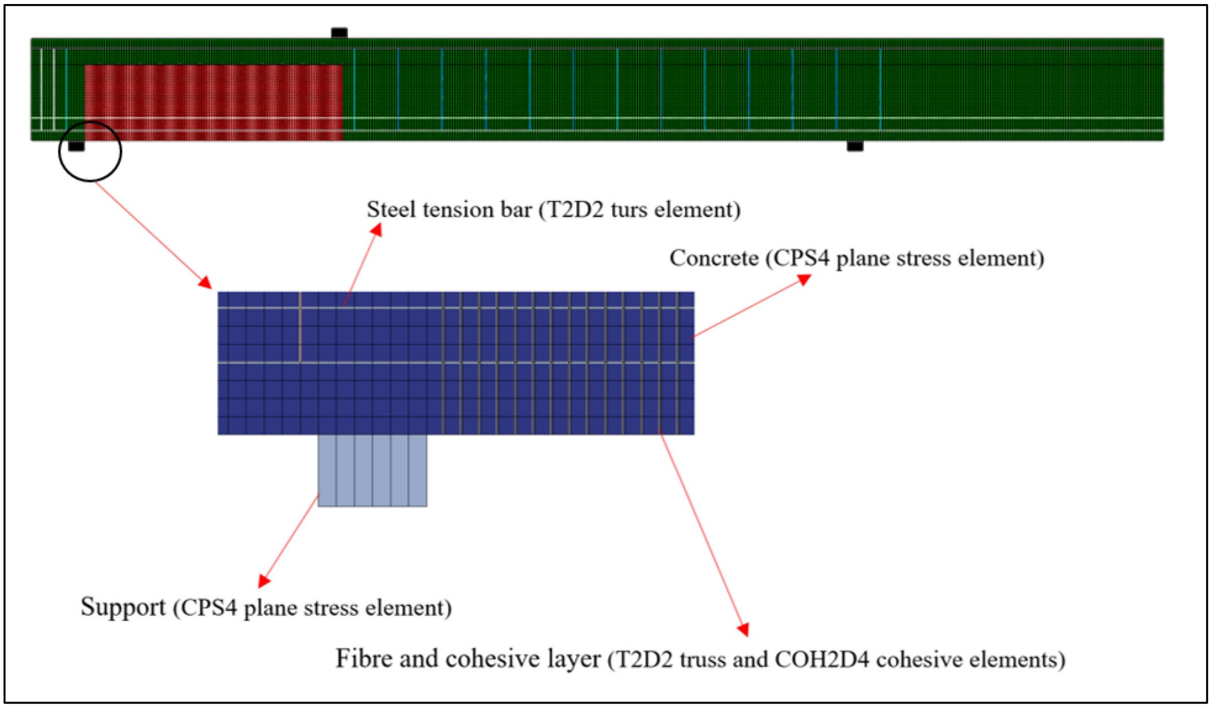

Figure 4.6 2D simulation of the strengthened RC T-beams and their defined elements in ABAQUS

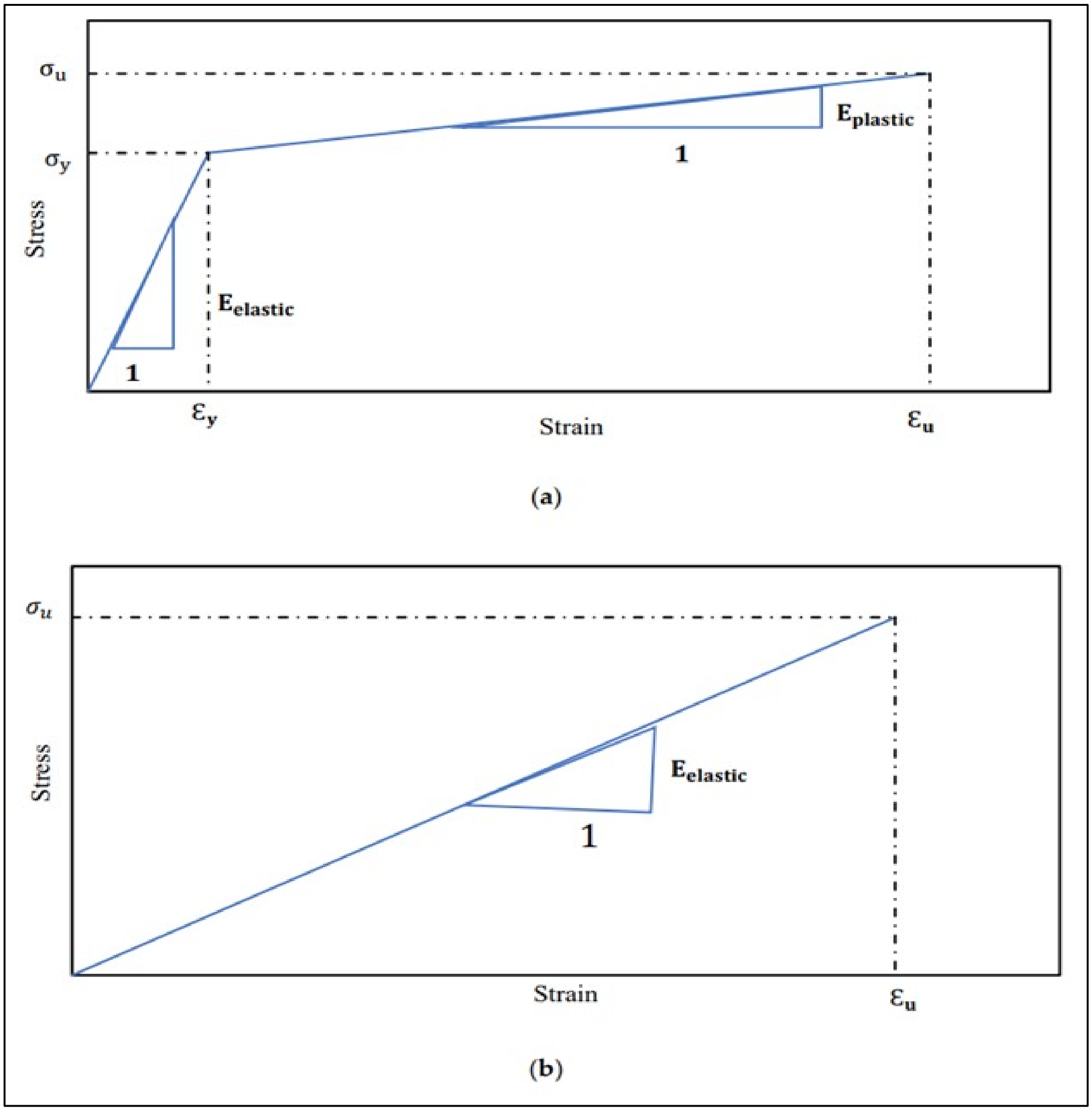

Figure 4.7 Stress–strain relation for (a) steel reinforcement and (b) CFRP fabrics

4.4 Experimental Investigation

Nine RC T-beams without steel stirrups were selected from the experimental tests (control and strengthened using EB-CFRP) conducted by Benzeguir et al. (2019) to investigate the size effect by means of FEA. In addition, this study assessed the impact of increasing the rigidity of EB-CFRP on its contribution to the shear resistance of RC beams. The results are presented in terms of (1) load-deflection responses, (2) strain profiles along the normalized diagonal shear cracks, (3) strain profiles along the fibre direction, and (4) variation of interfacial shear stress profiles along the cohesive layer. Details of the geometry, steel reinforcement position, and configuration of EB-CFRP are illustrated in Figure 4.8. These beams were grouped into three series of RC T-beams that were geometrically similar, but of different sizes: large, medium, and small, abbreviated as L, M, and S, respectively. One beam in each series was not strengthened and served as a control beam. The specimens were subjected to a three-point loading scheme. The geometry and properties of the nine selected specimens are presented in Table 4.1.

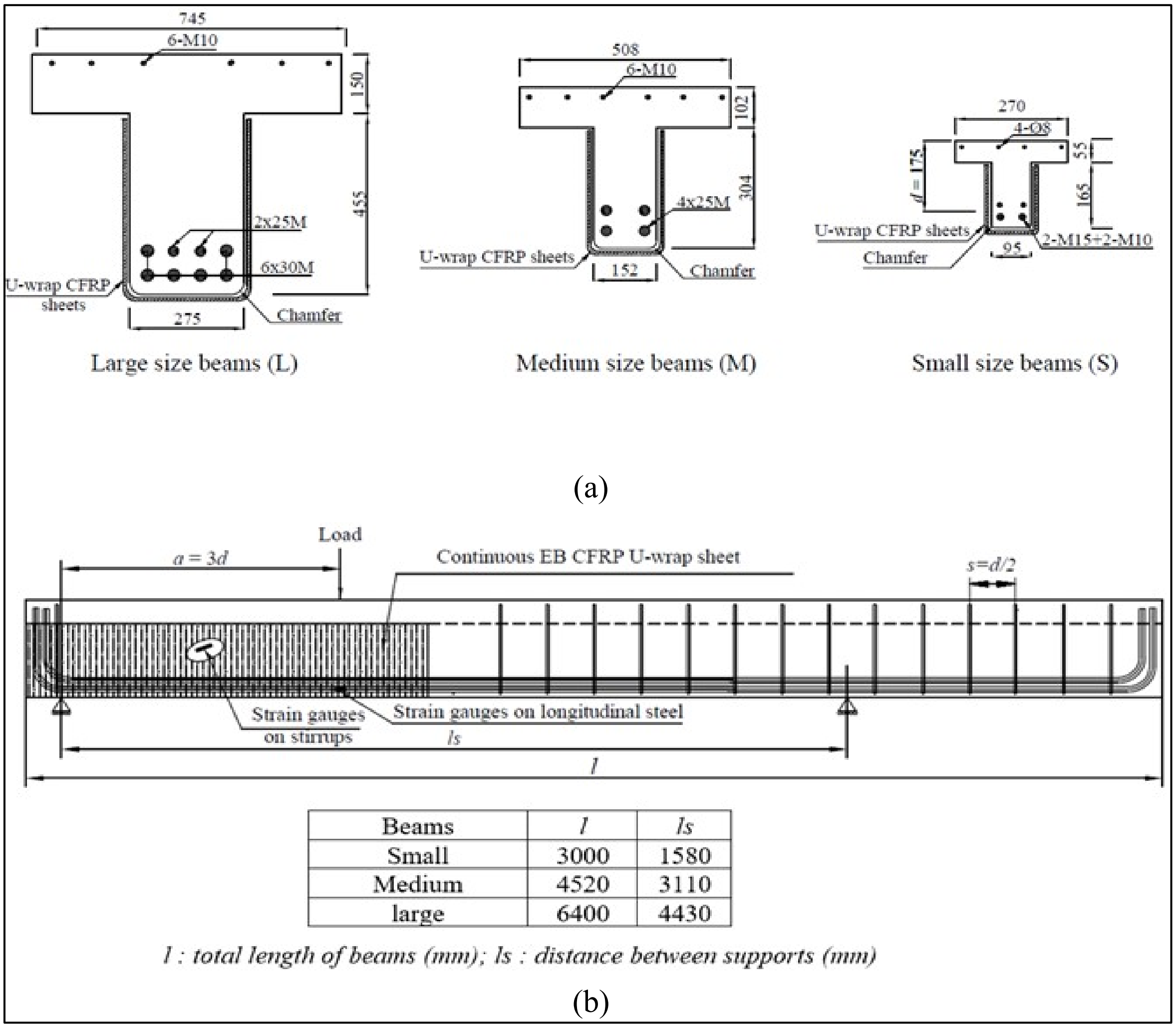

Beams	l	ls
Small	3000	1580
Medium	4520	3110
large	6400	4430

l : total length of beams (mm); ls : distance between supports (mm)

Figure 4.8 Details of beams: (a) cross-sections of large, medium, and small specimens (mm) and (b) elevation of beam and position of three-point loading conducted by Benzeguir et al. (2019)

Table 4.1 Geometry and property of material in studied beams by Benzeguir et al. (2019)

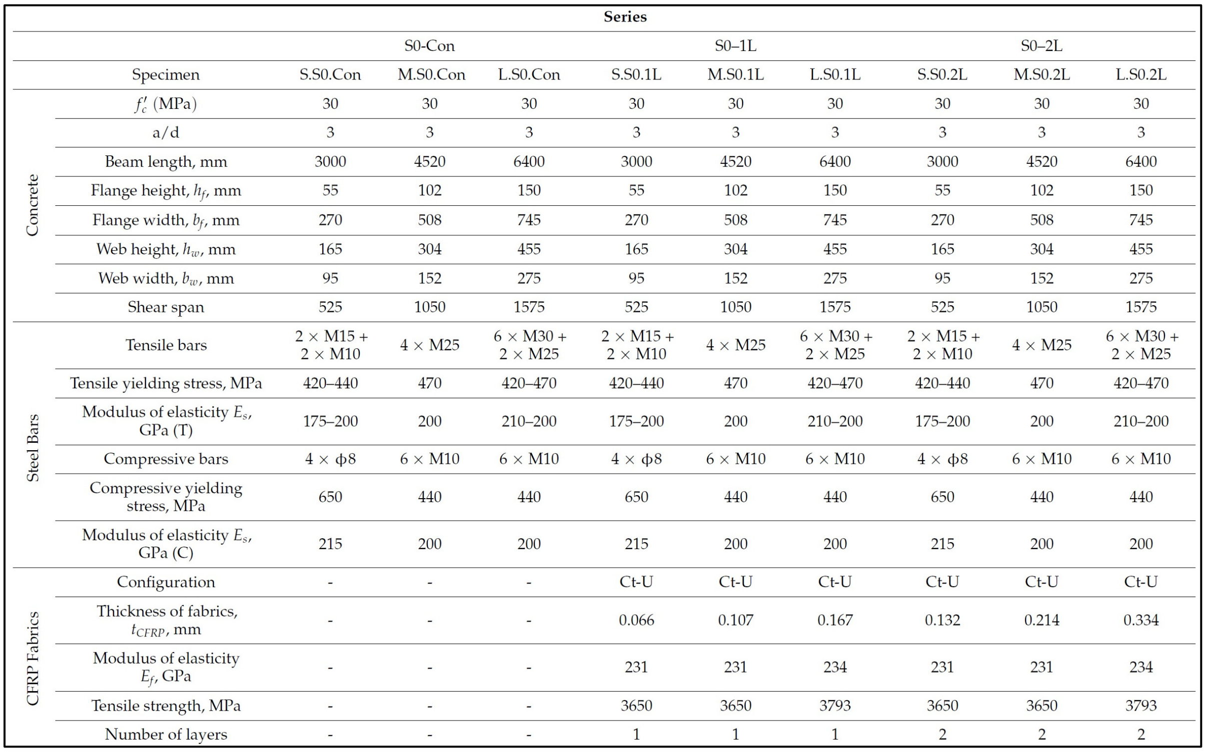

		Series								
		S0-Con			S0–1L			S0–2L		
	Specimen	S.S0.Con	M.S0.Con	L.S0.Con	S.S0.1L	M.S0.1L	L.S0.1L	S.S0.2L	M.S0.2L	L.S0.2L
Concrete	f'_c (MPa)	30	30	30	30	30	30	30	30	30
	a/d	3	3	3	3	3	3	3	3	3
	Beam length, mm	3000	4520	6400	3000	4520	6400	3000	4520	6400
	Flange height, h_f, mm	55	102	150	55	102	150	55	102	150
	Flange width, b_f, mm	270	508	745	270	508	745	270	508	745
	Web height, h_w, mm	165	304	455	165	304	455	165	304	455
	Web width, b_w, mm	95	152	275	95	152	275	95	152	275
	Shear span	525	1050	1575	525	1050	1575	525	1050	1575
Steel Bars	Tensile bars	2 × M15 + 2 × M10	4 × M25	6 × M30 + 2 × M25	2 × M15 + 2 × M10	4 × M25	6 × M30 + 2 × M25	2 × M15 + 2 × M10	4 × M25	6 × M30 + 2 × M25
	Tensile yielding stress, MPa	420–440	470	420–470	420–440	470	420–470	420–440	470	420–470
	Modulus of elasticity E_s, GPa (T)	175–200	200	210–200	175–200	200	210–200	175–200	200	210–200
	Compressive bars	4 × ϕ8	6 × M10	6 × M10	4 × ϕ8	6 × M10	6 × M10	4 × ϕ8	6 × M10	6 × M10
	Compressive yielding stress, MPa	650	440	440	650	440	440	650	440	440
	Modulus of elasticity E_s, GPa (C)	215	200	200	215	200	200	215	200	200
CFRP Fabrics	Configuration	-	-	-	Ct-U	Ct-U	Ct-U	Ct-U	Ct-U	Ct-U
	Thickness of fabrics, t_{CFRP}, mm	-	-	-	0.066	0.107	0.167	0.132	0.214	0.334
	Modulus of elasticity E_f, GPa	-	-	-	231	231	234	231	231	234
	Tensile strength, MPa	-	-	-	3650	3650	3793	3650	3650	3793
	Number of layers	-	-	-	1	1	1	2	2	2

4.5 Validation with Experimental Tests

As mentioned earlier, the simulated model has been validated by the experimental tests carried out by Benzeguir et al. (2019). The element size for discretization of the small beams (one- and two-layer strengthening) and the control beam was 5 mm, 10 mm, and 10 mm for small, medium, and large beams, respectively. These sizes have shown good agreement between numerical and experimental results (Failure modes, crack patterns, and ultimate load-carrying capacity). Negative strain shows as compression in concrete, which mainly occurs around the supports and the load plate. Figure 4.9 shows the numerical results, which illustrate the main shear crack distributions in all strengthened beams by means of the principal logarithmic plastic strain in the plane of the beams. As shown in Figure 4.9, regardless of size, the patterns of shear cracks for small, medium, and large beams strengthened with two CFRP layers were similar (Figure 4.9 a-b-e), starting in the mid-depth of the web and extending to the support and the web/flange intersection to propagate horizontally towards the load plate. The results for the medium and large strengthened specimens with one CFRP layer (Figure 4.9 c-d) followed the same trend.

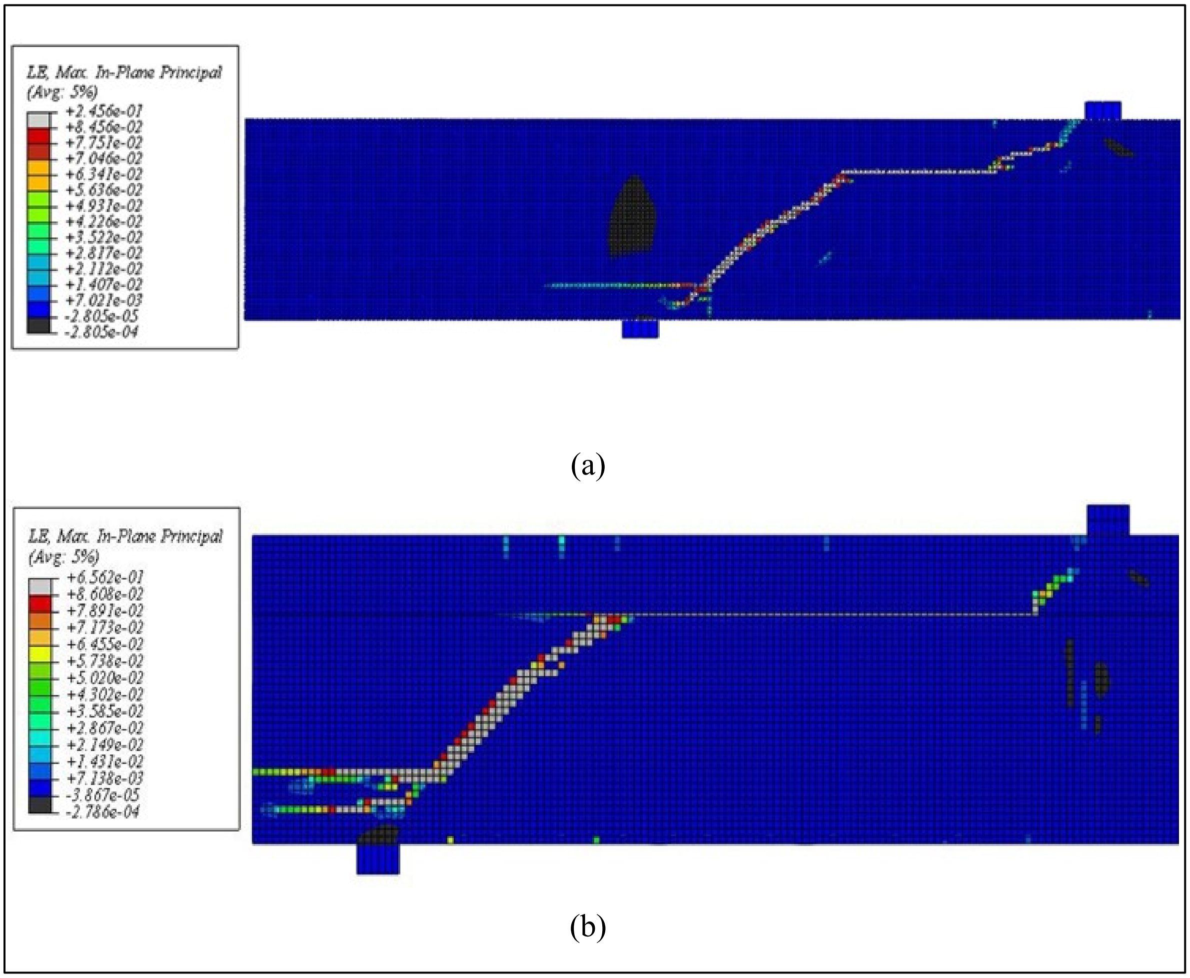

(a)

(b)

Figure 4.9 Crack pattern obtained from simulation in ABAQUS for specimen at complete failure: (a) specimen S.S0.2L; (b) specimen M.S0.2L; (c) specimen M.S0.1L; (d) specimen L.S0.2L; (e) specimen

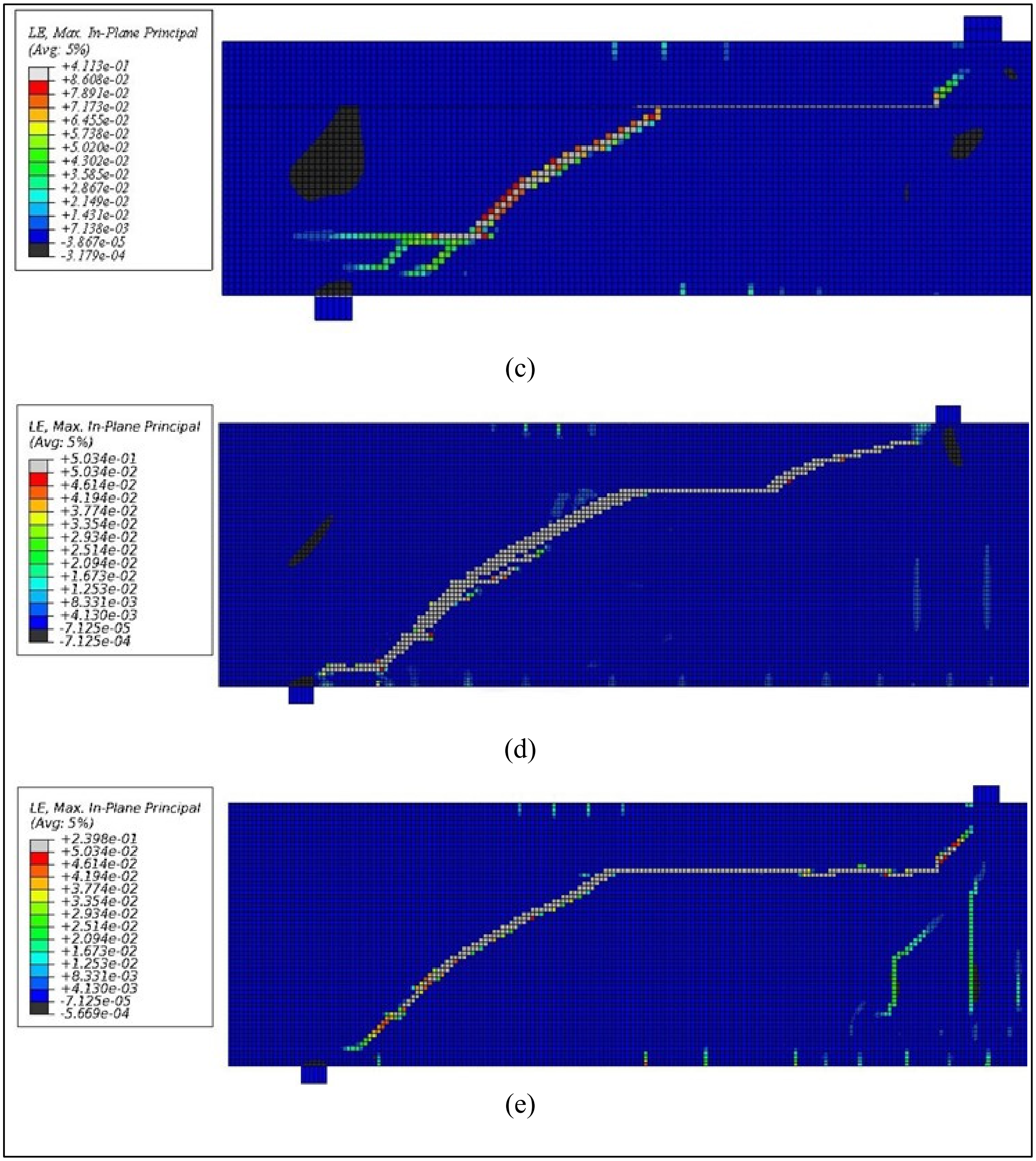

(c)

(d)

(e)

Figure 4.9 Crack pattern obtained from simulation in ABAQUS for specimen at complete failure: (a) specimen S.S0.2L; (b) specimen M.S0.2L; (c) specimen M.S0.1L; (d) specimen L.S0.2L; (e) specimen (Continued)

Experimental tests of the control beams (small, medium, large) showed similar crack angle patterns with one single diagonal shear crack, appearing as a crack band at mid-height of the web and propagating toward the web soffit (support) and the flange (load application point) of the beam. As shown in Figure 10, the maximum crack angle occurred at mid-depth of the beams and then decreased as the crack extended towards the support and the load application point. The crack patterns predicted through numerical analysis were in good agreement with experimental results (Figure 4.10 a-c). The failure thresholds of the control specimens with increasing load are presented in Table 4.2.

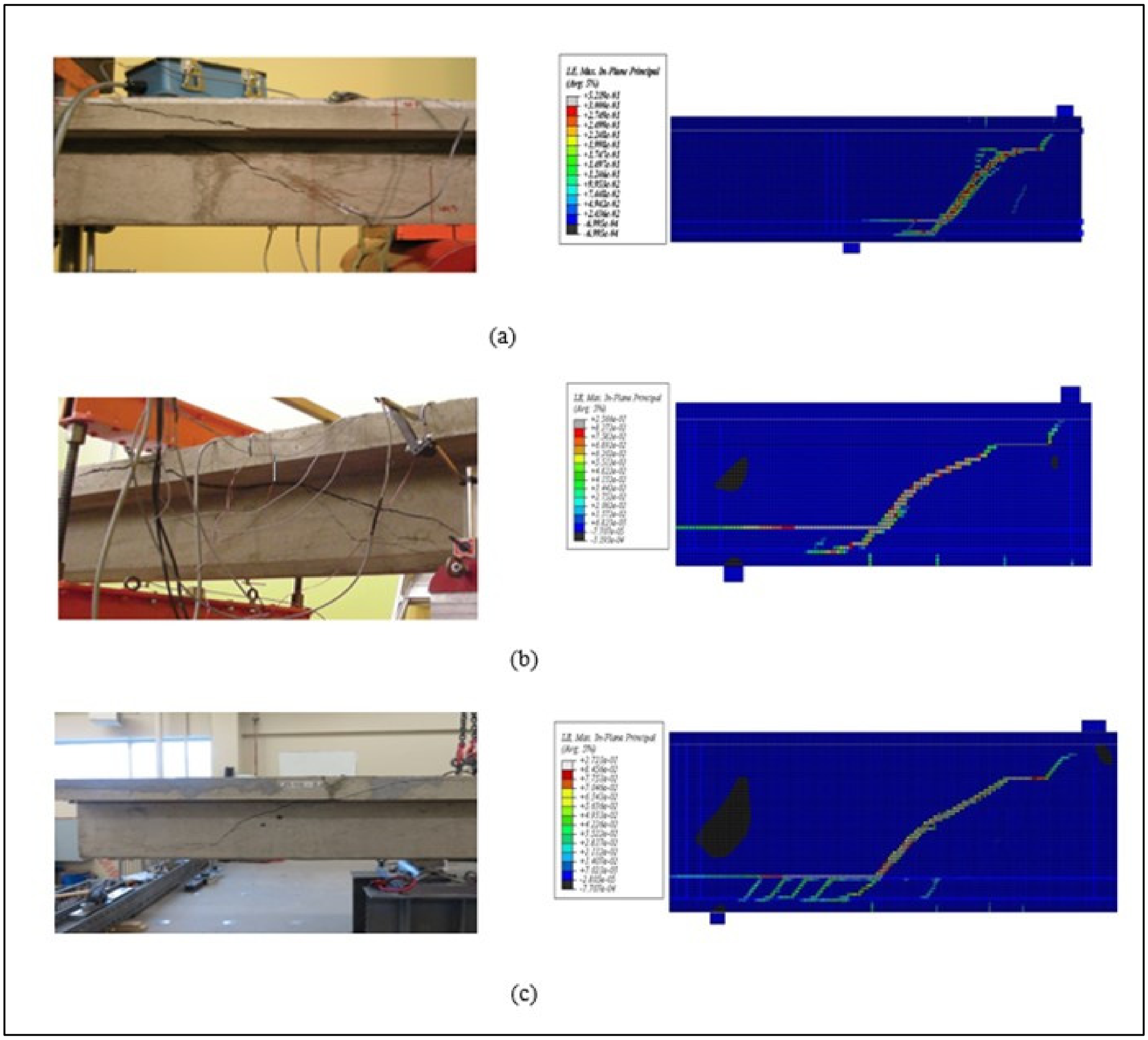

Figure 4.10 Crack pattern obtained from FEA and experimental testing for control beams at ultimate states: (a) S.0L.Con; (b) M.0L.Con; (c) L.0L.Con

Table 4.2 Failing procedure of control specimens as increasing load for experimental and numerical tests

Imposed Load					
	Experimental Test		Numerical Prediction		
Specimen	Failure Load (kN)	Shear Cracks (kN)	Shear Cracks (kN)	Failure Load (kN)	$P_{num.}/P_{exp.}$
S.S0.Con	58	19 (31%)	25 (40%)	62	1.06
M.S0.Con	130	45 (35%)	60 (46%)	128	0.98
L.S0.Con	283	73 (25%)	89 (30%)	293	1.03

Note that the flexural and shear cracks in the small and medium specimens occurred at approximately the same ratio of ultimate loads. However, this ratio decreased considerably for large beams, indicating the possible existence of a size effect in large specimens that reduced their shear strength capacities as depth increased. Numerical results showed that the ultimate load of the medium beam was 106% higher than that of the small beam, and that the ultimate load of the large beam was 372% and 128% higher than those of the small and medium ones respectively. The failure loads occurred at 62, 128, and 293 kN, whereas shear cracks formed at 25 kN, 60 kN, and 89 kN applied loads for small, medium, and large beams respectively. This was in good agreement with experimental results (see Table 4.2). Single diagonal shear cracks formed in control beams (small, medium, and large), giving rise to shear failure in all specimens. This confirms the results obtained by Pellegrino and Modena (2002). Moreover, based on the experimental results, the shear crack angles in small, large, and medium beams were 42°, 37°, and 24° respectively, which are comparable with the numerical results (Figure 4.10 a-c). As shown in Figure 4.10, crack patterns in all control specimens were similar regardless of specimen size. However, the large beams featured more distributed minor cracks, probably due to wider cracking and the resulting loss of aggregate interlock (Figure 4.10 c). Delamination of the interface layer occurred in all strengthened specimens when the stresses normal to the interface layer exceeded their maximum resistance (2.3 MPa). The delamination started from the top edge of the CFRP wrap located at the web/flange intersection and then extended horizontally and propagated vertically towards the top parts of the main diagonal shear crack. The stress normal to the interface layer at the web/flange intersection exceeded 2.3 MPa, which is the maximum strength in the normal direction of the interface layer.

As beam depths decreased from 525 mm to 350 mm and then to 175 mm, the behaviour of the specimens changed from brittle to ductile, as indicated by the load-deflection response with a plateau (Figure 4.11 a). Numerical results commonly overestimate the load-carrying capacity of a beam by approximately 6% because the bond between longitudinal bars and concrete is assumed perfect and an implicit dynamic is implemented to solve the model, thus amplifying deflection and load in the dynamic analysis (Guangming Chen, 2010; GM Chen et al., 2012). However, as long as the parameters in the dynamic analysis are defined appropriately (time increment, loading time, and loading scheme), it can be an appropriate replacement for static analysis (Guangming Chen, 2010; GM Chen et al., 2012).

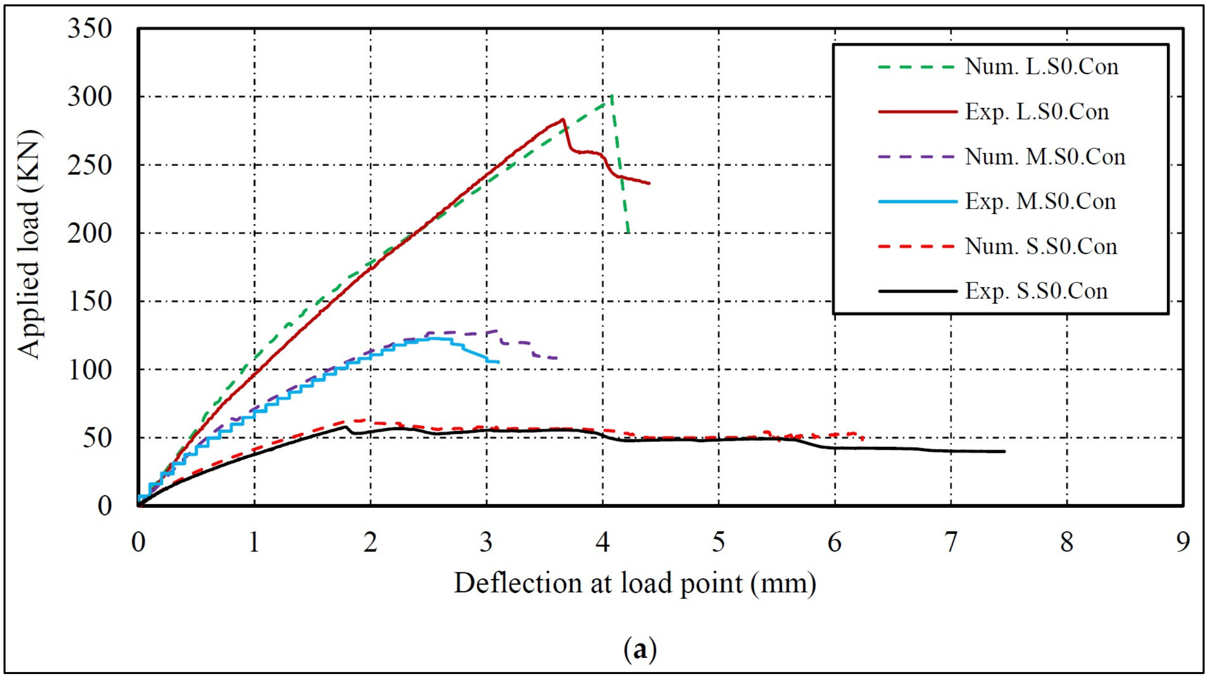

(**a**)

Figure 4.11 Numerical vs. experimental load-deflection response: (a) control beams; (b) beams strengthened with one CFRP layer; (c) beams strengthened with two CFRP layers

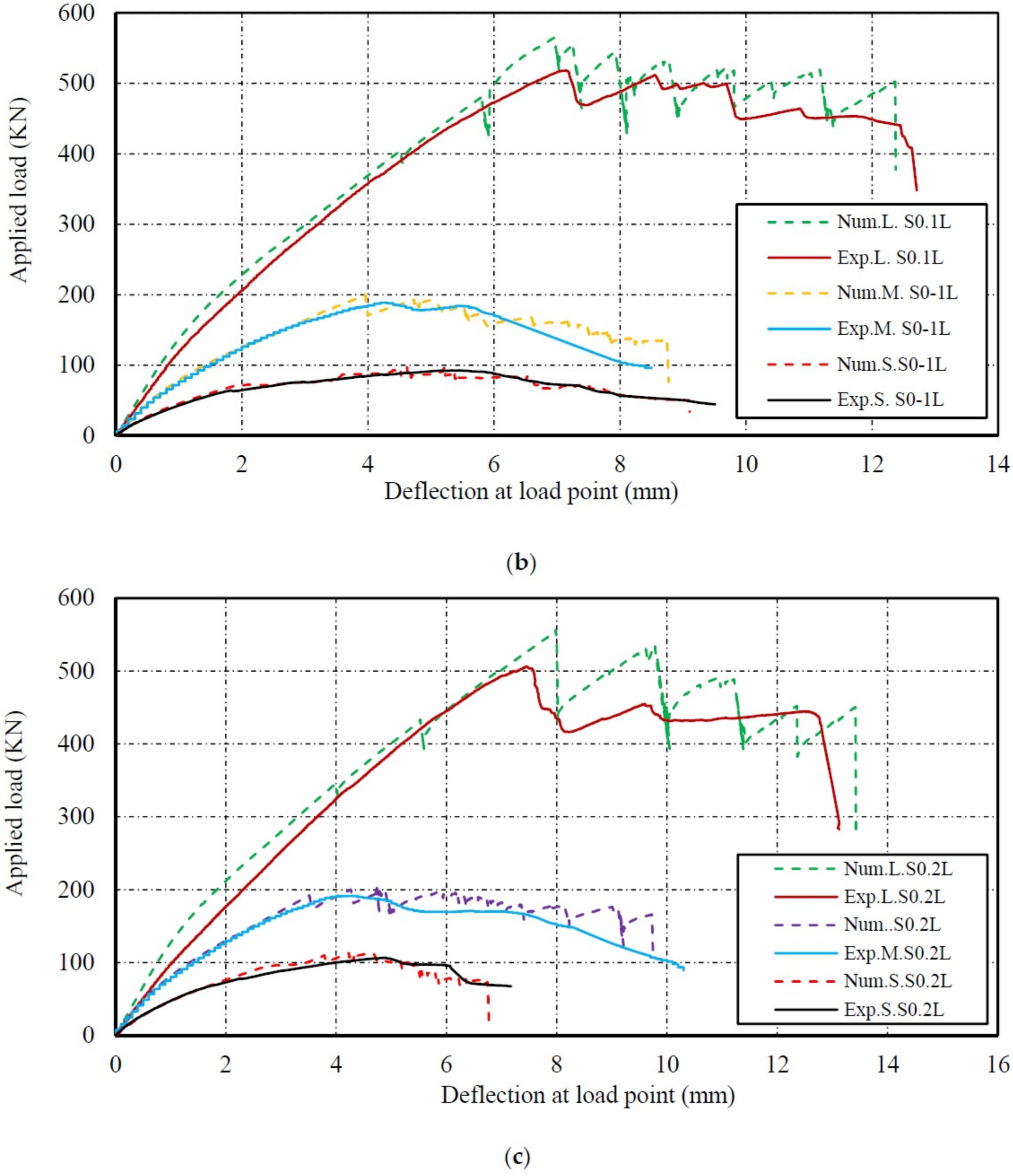

Figure 4.11 Numerical vs. experimental load-deflection response: (a) control beams; (b) beams strengthened with one CFRP layer; (c) beams strengthened with two CFRP layers (Continued)

The results of the numerical and experimental tests are summarized in Table 4.3 and Table 4.4 in terms of ultimate load (P_{max}), deflection at P_{max}, shear contribution of CFRP (V_{CFRP}), shear gain due to CFRP (G_{CFRP}), maximum shear force (V_T), maximum shear stress in the section $\nu = V_T/(b_w \times d)$, loss of shear stress in medium and large specimens with respect to the small beam ν (%), and ultimate strain contributed by CFRP fabrics in each specimen.

Table 4.3 Comparison between experimental and numerical results in terms of load deflection and ultimate shear strength contributed by concrete and CFRP fabrics

	P_{max} (kN)		$\Delta_{P_{max}}$(mm)		V_T(kN)		V_{CFRP} (kN)		P_{num}/P_{max}	Failure Mode	
Specimens	**Exp.**	**Num.**	**Exp.**	**Num.**	**Exp.**	**Num.**	**Exp.**	**Num.**		**Exp.**	**Num.**
S.S0.Con	58	62	1.8	1.9	38	41	-	-	1.06	Shear	Shear
M.S0.Con	130	128	2.6	3.1	86	85	-	-	0.98	Shear	Shear
L.S0.Con	283	293	3.7	4	182	189	-	-	1.03	Shear	Shear
S.S0.1L	93	98	5.4	5.2	62	65	23	24	1.05	Shear	Shear
M.S0.1L	189	195	4.2	3.9	125	130	39	45	1.03	Shear	Shear
L.S0.1L	518	550	7.1	7.2	334	354	151	165	1.06	Shear	Shear
S.S0.2L	106	112	4.9	4.23	71	75	32	34	1.05	Shear	Shear
M.S0.2L	191	202	4.1	4.8	127	134	40	49	1.05	Shear	Shear
L.S0.2L	506	543	7.5	8	326	349	144	160	1.07	Shear	Shear

Table 4.4 Comparison between numerical and experimental results in terms of shear gain and loss

	Shear Gain Due to FRP (%)		**Shear Stress in Concrete**		**Loss in Shear Stress with Respect to Control Beam (ν%)**	
Specimens	**Exp.**	**Num.**	**Exp.**	**Num.**	**Exp.**	**Num.**
S.S0.Con	-	-	2.31	2.46	-	-
M.S0.Con	-	-	1.62	1.59	30	35
L.S0.Con	-	-	1.26	1.31	45	47
S.S0.1L	60	58	3.71	3.91	-	-
M.S0.1L	45	52	2.35	2.44	37	38
L.S0.1L	83	87	2.31	2.45	38	37
S.S0.2L	84	83	4.26	4.51	-	-
M.S0.2L	47	58	2.38	2.51	44	44
L.S0.2L	79	85	2.26	2.41	47	47

4.5.1 Load-Deflection Responses

Figure 4.11 compares experimental and numerical results in terms of ultimate load-carrying capacities and displacements for the nine specimens. Note that shear strengthening with EB-CFRP fabrics showed higher levels of strength in specimens strengthened with one layer by about 58%, 52%, and 88% for small, medium, and large beams respectively with respect to control beams. Furthermore, the deflections corresponding to the maximum load (Δ_{pmax}) of specimens strengthened with one EB-CFRP layer increased by 173%, 25%, and 80% with respect to control beams, which could be attributed to the fact that CFRP fabrics control the deflection of specimens (Figure 4.11). Nevertheless, by adding two CFRP layers, no considerable additional deflections were observed in the specimens compared to those strengthened with one layer. The results of the load-deflection data obtained from numerical analysis are highly comparable with experimental observations, showing that the simulated model can predict laboratory tests with high accuracy.

4.6 FE Simulations and Results

This section is dedicated to FE simulations and analyses. The results are presented in terms of (a) shear strength for control and strengthened beams, (b) distribution of strain on the fibres along the diagonal shear crack, and (c) strain distributions along the CFRP fabric and interfacial shear stress at the cohesive layer.

4.6.1 Shear Strength and Loss in Control and Strengthened Beams

This section presents the FEA results for shear strength and shear loss due to the size effect. The size effect had an impact on strengthened beams in the way that the shear stress contributed by CFRP fabric decreased in specimens strengthened with one CFRP layer, from 1.45 MPa in S.S0.1L to 1.14 MPa in L.S0.1L. Table 4.4 compares the numerical and experimental results. The specimens of the third series, which were strengthened by two layers, resulting in higher CFRP rigidity, showed similar results, with shear stress decreasing from 2.05 MPa in S.S0.2L to 1.1 MPa in L.S0.2L. As illustrated in Figure 4.12, adding a second layer of EB-CFRP increased the shear stress in the small beam before delamination by 30%, that is, from 1.45 MPa to 2.05 MPa. This gain in shear stress decreased in the medium specimen by 7% and in the large specimen by 3%, indicating that the size effect has an impact on the shear stress contributed by both concrete and CFRP. Nevertheless, more investigations are required to clarify the relation between the size effect and the rigidity of CFRP as the specimen dimension increases.

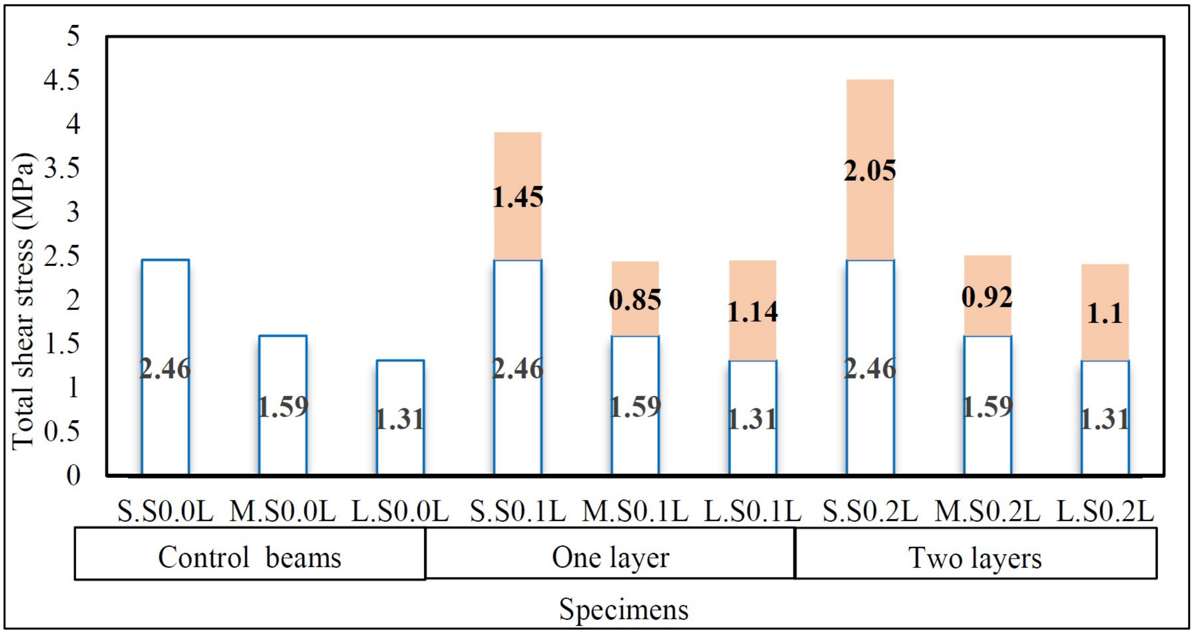

Figure 4.12 Shear stress contributed by concrete and CFRP fabric (FE results)

4.6.2 Distribution of Strain on the Fibres along the Diagonal Shear Crack by FEA

Assessing the strain profile along the main diagonal shear crack resulted in a better understanding of the behavior of fibres and their contribution to shear strengthening as the size of specimens and the rigidity of CFRP fabrics increased. By evaluating the strain distribution along the shear crack path, it is possible to locate the maximum crack width and to understand how debonding and delamination occur on both sides of the crack. The main diagonal shear cracks had an almost linear pattern for specimens strengthened with two layers of CFRP fabric and a semi-parabolic shape for those strengthened with one CFRP layer (Figure 4.9 and Figure 4.10, respectively). Because the strain distribution on the fibres along the main diagonal shear crack constitutes the basis on which the distribution factors for the strain are established, the response of the strain in fibres intersected by the normalized shear crack is evaluated in this section. Note that the distribution factor D_{FRP} introduced by J.-F. Chen and J. Teng (2003) is a function of the average strain on the fibres intercepted by the shear crack and the maximum strain experienced by fibres at a specific load, as follows:

$$D_{FRP} = \frac{\sum_{i=1}^{n} \varepsilon_{FRP,i}}{n\varepsilon_{max}} \tag{4.10}$$

Where $\varepsilon_{FRP,i}$ is the strain in the i^{th}specific fibre intercepted by the shear crack, n is the number of fibres crossed by the diagonal shear crack, and ε_{max} is the maximum strain experienced by the fibre at ultimate state.

The formula introduced by J. Chen and J. Teng (2003) for the shear contribution of EB-FRP is:

$$V_f = 2f_{f,e}t_f w_f \frac{h_{f,e}(\cot\theta + \cot\beta)\sin\beta}{s_f} \tag{4.11}$$

where $f_{f,e}$ is the effective stress in the FRP intercepted by the main shear diagonal shear crack that can be obtained through the distribution factor (D_{FRP}) given by (Chen 2010):

$$f_{f,e} = E_f \varepsilon_{f,e} = E_f \varepsilon_{max} \mathrm{D_{FRP}} \tag{4.12}$$

in which $\varepsilon_{f,e}$ is the effective strain in FRP wrap, E_f is the FRP modulus of elasticity, and D_{FRP} is the distribution factor obtained from Equation 4-10.

As shown in Figure 4.13a-f, the strain distributions along the shear crack are illustrated by four displacement levels corresponding to four phases: (1) initiation of crack at mid-depth of the web; (2) all fibres intercepted by shear cracks are in active phase (experiencing strain) just before initiation of delamination at the tip of the crack; (3) delamination at the cohesive layer already formed and developed at mid-distance of shear crack paths (effective bond lengths start to decrease); and (4) one of the fibres intercepted by the shear crack is exposed to maximum strain during the loading process.

Regarding the series of small specimens, as displacements reached 2.23 mm and 2.79 mm in specimens strengthened with one and two layers respectively, the shear crack initiated at mid-distance of the shear crack path from the end of the normalized distance. Then it propagated toward the bottom edge of the beams and the edge of the intersection between webs and flanges. When the displacements at the loading points reached 3.92 mm and 3.81 mm, the maximum strains on CFRP fabrics were 0.00637 and 0.00246 in S.S0.1L and S.S0.2L respectively (Figure 4.13a-b). At this stage, shear cracks had completely formed, and all the fibres intersected by shear cracks were in the active phase (from the tips to the ends of the shear crack). The strain values on fibres intersected by the shear crack on the top part of the crack then dropped suddenly to zero due to delamination and to the short bond length compared to the bottom part of the crack. During that process, the cracks at the edge of the intersection between the flange and the web propagated horizontally.

The maximum strains experienced by fibres before entirely losing the CFRP shear contribution were 0.00866 and 0.00266 in S.S0.1L and S.S0.2L respectively. These values are in good agreement with the corresponding experimental results, that is, 0.00714 and 0.00216, corresponding to 45% and 13% of CFRP ultimate strain. Note that the values of strains on fibres obtained from numerical analysis are larger than those obtained from experimental tests because dynamic implicit analysis was used to solve the models from which the amplified strains were recorded, whereas such an amplification did not exist in the static analysis (Guangming Chen, 2010). Furthermore, strain gauges installed on EB-CFRP fabrics measure the average strains, which are lower than the maximum strain obtained from FEA (GM Chen et al., 2012). For the medium beams, shear cracks appeared at mid-distance of the shear crack path when displacements at the loading points reached 3.36 mm and 3.15 mm in beams strengthened with one and two layers of CFRP fabric respectively. When the displacements reached 4.73 mm and 5.44 mm in M.S0.1L and M.S0.2L respectively (Figure 4.13c-d), the main diagonal shear cracks in both specimens became complete, and at this stage, all fibres crossed by shear cracks (from the tips to the ends of the cracks) experienced stress and strain. The maximum strains experienced by the fibres just before delamination were 0.0032 and 0.0033 in M.S0.1L and M.S0.2L respectively, as presented in Figure 4.13c-d, representing 20% and 21% of the ultimate strain of the fibres. After these maximum strains were reached, an inactive zone where more fibres lost their contribution to shear strengthening (zero strain) developed at the support. The maximum strains obtained from numerical analysis were in good agreement with experimental results (i.e., 0.00248 and 0.0027 in M.S0.1L and M.S0.2L respectively). The same scenario was observed for the large specimens, from initiation of shear cracks to complete failure of EB-CFRP. Therefore, all fibres were in active modes as complete shear cracks formed, and at this stage, displacements reached 7.26 mm and 8.27 mm in L.S0.1L and L.S0.2L respectively (Figure 4.13a-f)) just before delamination.

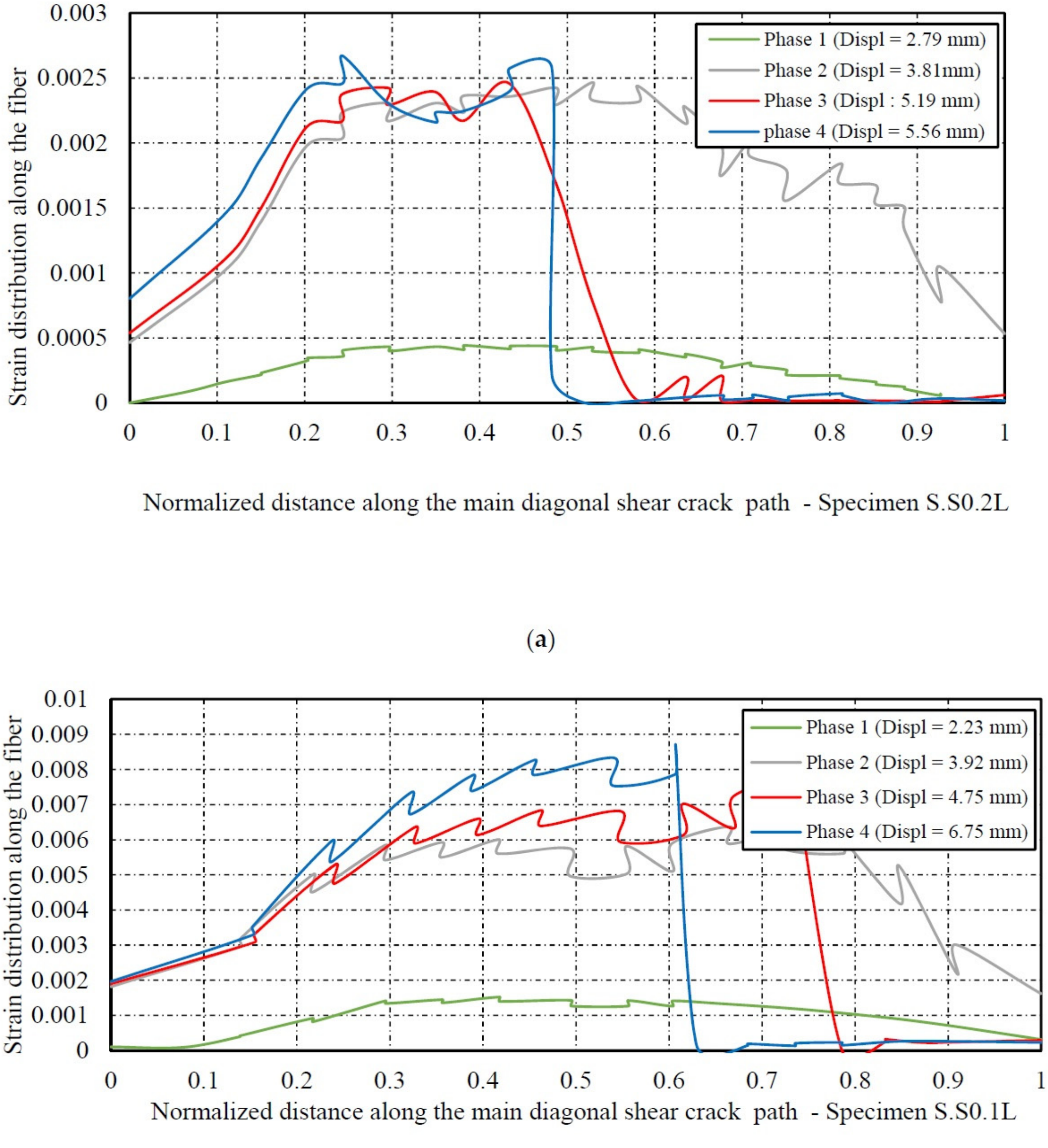

(**a**)

(**b**)

Figure 4.13 Distributions of strains on fibres crossed by normalized distance along the main diagonal shear path: (a) specimen S.S0.1L; (b) specimen S.S0.2L; (c) specimen M.S0.1L; (d) specimen M.S0.2L; (e) specimen L.S0.1L; (f) specimen L.S0.2L. Phase 1: initiation of main diagonal shear crack. Phase 2: all the fibres intersected by shear crack in an active phase. Phase 3: development of the loss of the shear contribution of the fibres at tips of the shear crack. Phase 4: the maximum strain recorded on fibres before the complete loss of the shear contribution of the fibres at the top part of the shear crack

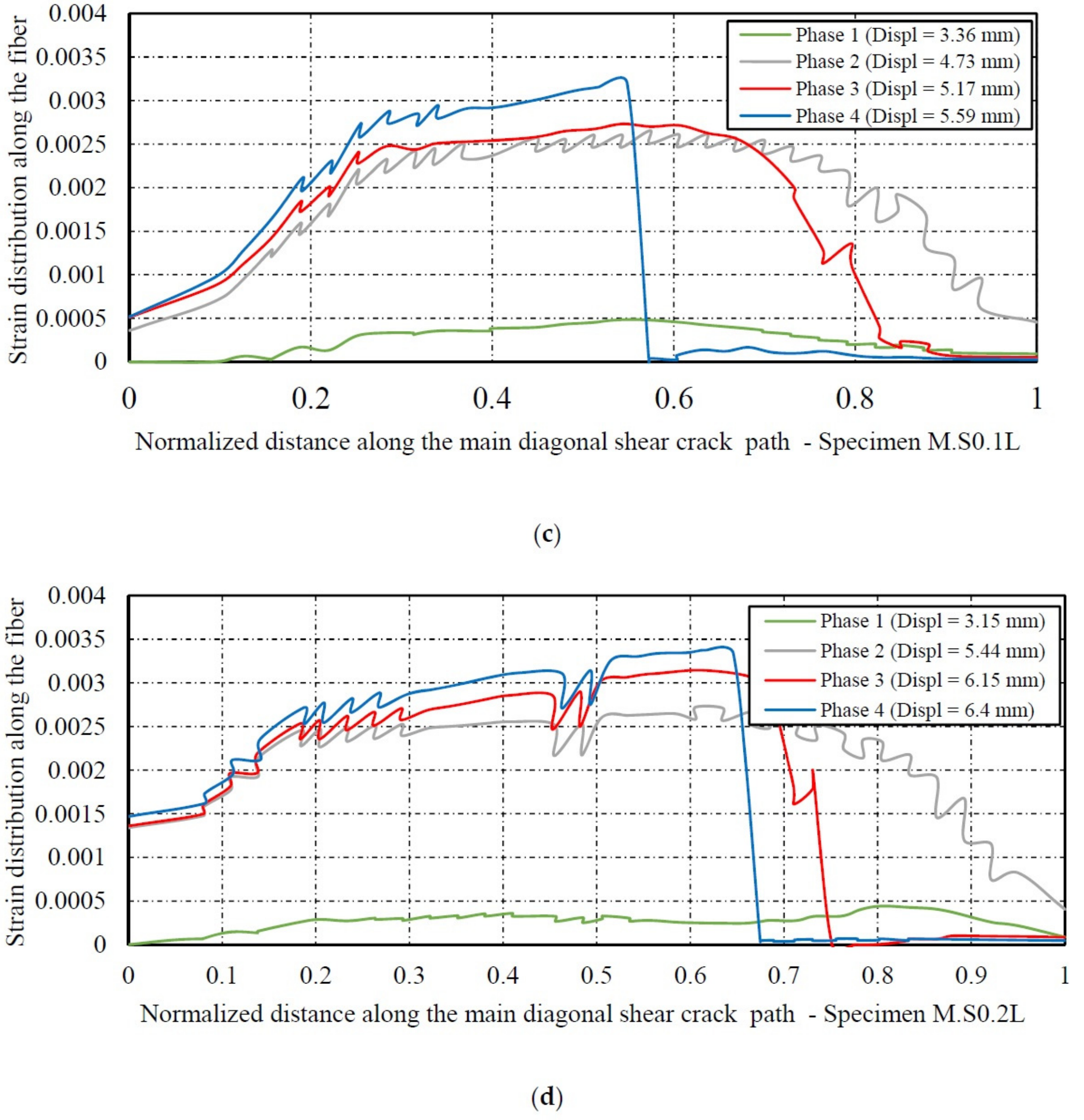

Figure 4.13 Distributions of strains on fibres crossed by normalized distance along the main diagonal shear path: (a) specimen S.S0.1L; (b) specimen S.S0.2L; (c) specimen M.S0.1L; (d) specimen M.S0.2L; (e) specimen L.S0.1L; (f) specimen L.S0.2L. Phase 1: initiation of main diagonal shear crack. Phase 2: all the fibres intersected by shear crack in an active phase. Phase 3: development of the loss of the shear contribution of the fibres at tips of the shear crack. Phase 4: the maximum strain recorded on fibres before the complete loss of the shear contribution of the fibres at the top part of the shear crack (Continued)

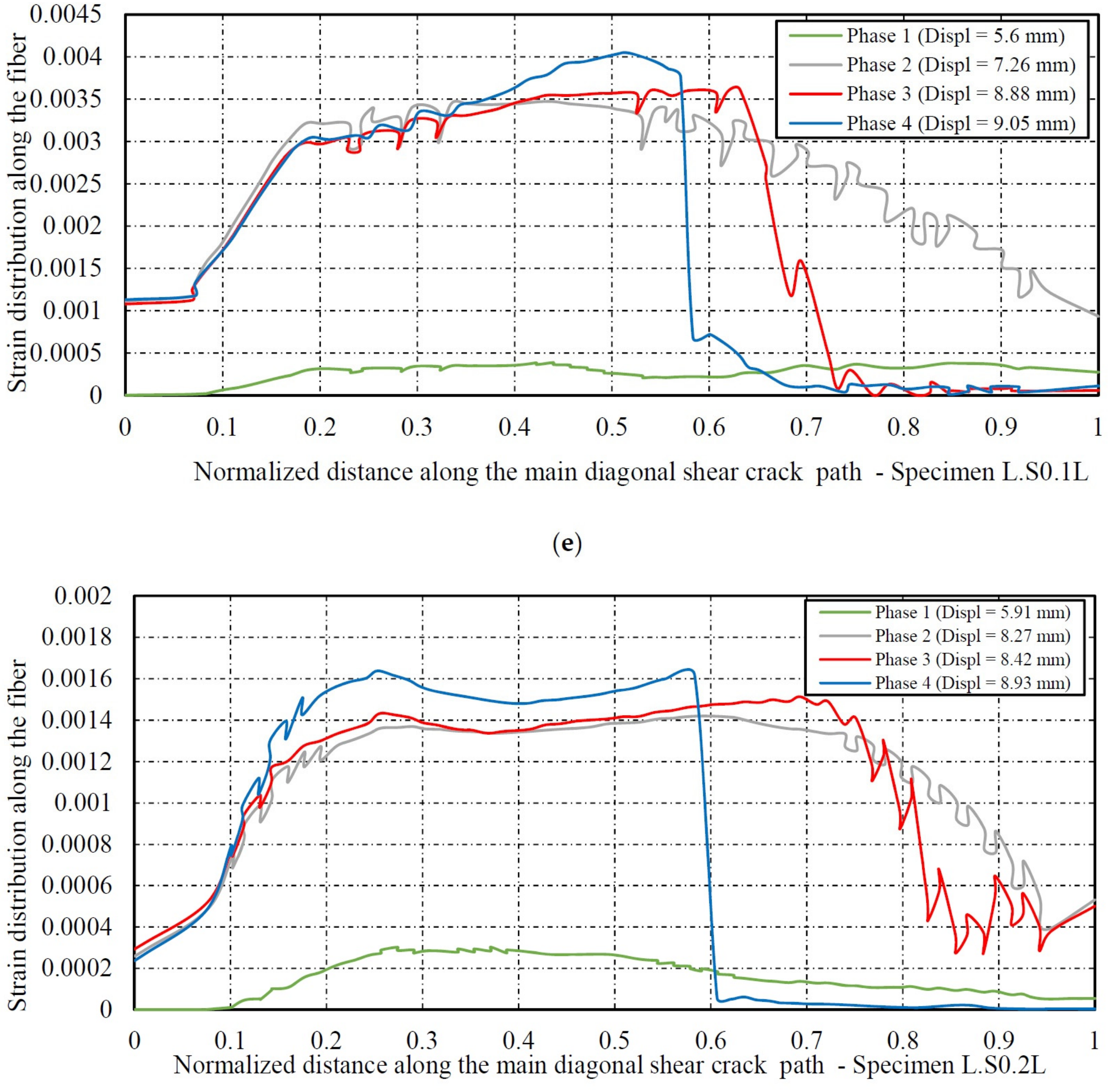

(**e**)

(**f**)

Figure 4.13 Distributions of strains on fibres crossed by normalized distance along the main diagonal shear path: (a) specimen S.S0.1L; (b) specimen S.S0.2L; (c) specimen M.S0.1L; (d) specimen M.S0.2L; (e) specimen L.S0.1L; (f) specimen L.S0.2L. Phase 1: initiation of main diagonal shear crack. Phase 2: all the fibres intersected by shear crack in an active phase. Phase 3: development of the loss of the shear contribution of the fibres at tips of the shear crack. Phase 4: the maximum strain recorded on fibres before the complete loss of the shear contribution of the fibres at the top part of the shear crack (Continued)

The maximum strains experienced by the fibres were 0.00415 and 0.00161 in L.S0.1L and L.S0.2L, respectively, which were very close to experimental values (0.00369 and 0.0016, respectively). Therefore, the maximum strains reached on EB-CFRP in large specimens (L.S0.1L, L.S0.2L) decreased in comparison to small beams by 53% and 40% in beams strengthened with one and two layers, respectively, resulting in a size effect on both concrete and CFRP shear contributions. Likewise, in the control beams (Figure 4.10 a–c), the pattern of shear cracks at the final states in strengthened specimens as obtained from numerical analysis was in good agreement with experimental tests, confirming that the assumptions applied for simulation were accurate (Figure 4.9 a–e).

4.6.3 Strain distributions along the CFRP fabric and interfacial shear stress at the cohesive layer

By evaluating the strain distribution on fibres along with the normalized distance of the crack path, it is possible to locate the maximum vertical crack width. Those fibres that experience more strain before losing their shear contributions are located at the maximum crack width. Moreover, the vertical width of the crack can be calculated by summation of interfacial slip along the two sides of the crack and the deformation of CFRP fabric in the debonding area (GM Chen et al., 2012). Therefore, after the maximum crack width has been located and calculated, the strain distribution and the interfacial shear stress along the fibre intersected by the shear crack at its maximum width were evaluated to further investigate the size effect on the shear contribution of EB-CFRP.

The FEA strain profile along the fibre and the shear stress profile along the interface layer for L.S0.1L and L.S0.2L are presented in Figure 4.14a-b and Figure 4.15a-b respectively. The results are presented in terms of strain development along the fibre direction and the interfacial shear stress along the interface layer in which debonding can be observed. Each graph shows the strain distributions and the interfacial shear stress at six displacement stages, in which the first three steps are related to initiation and development of the shear crack just before delamination, and the next three steps represent the initiation of delamination to complete loss of strain in the fibre. This yields six curves corresponding to six levels of displacement. As shown in Figure 4.14a-b and Figure 4.15a-b, there is a similarity between the strain distribution along the main fibre direction and the strain response obtained from the pullout tests.

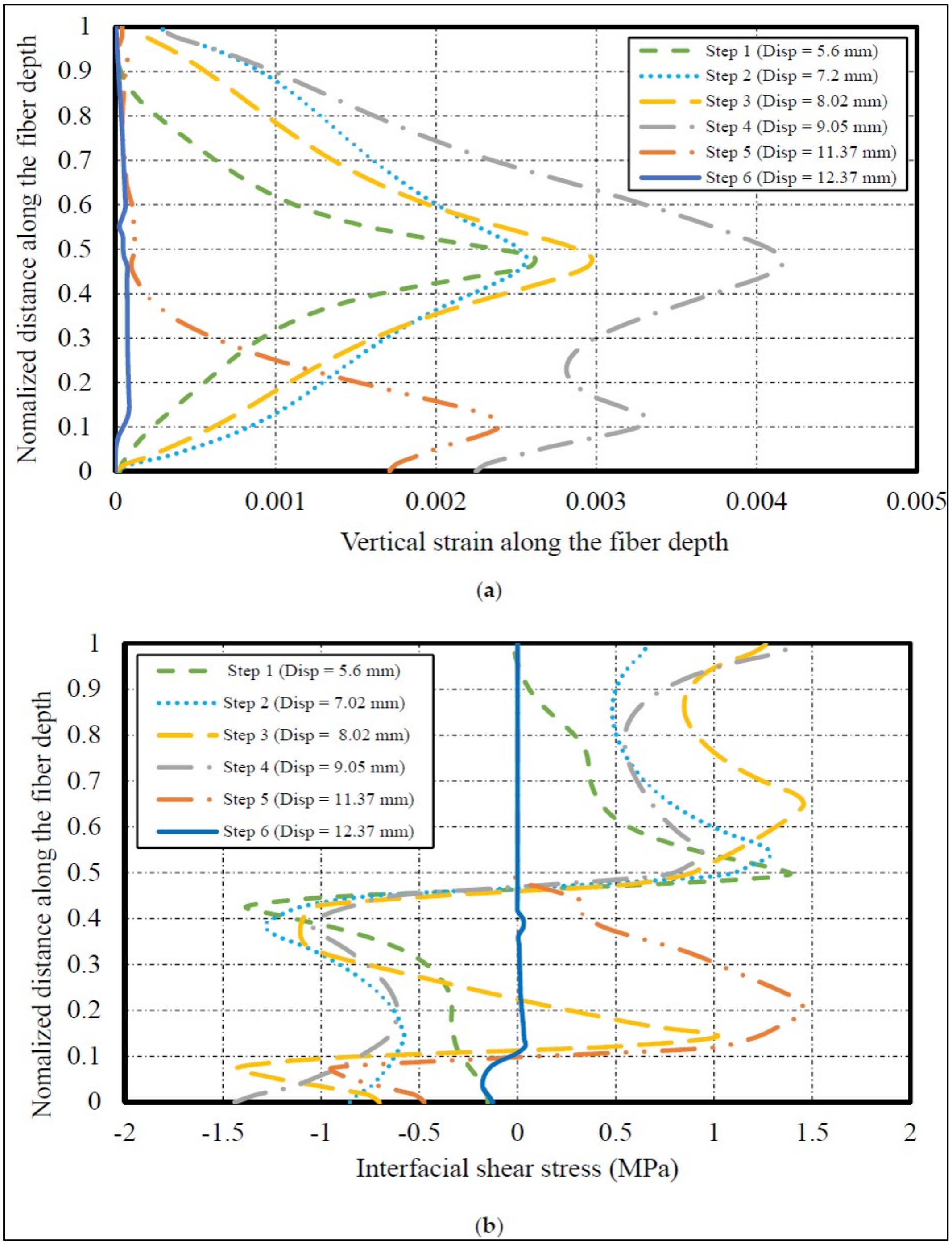

(a)

(b)

Figure 4.14 Strain profile and interfacial shear stress along the fibre and interface layer intercepted by maximum crack width (specimen L.S0.1L)

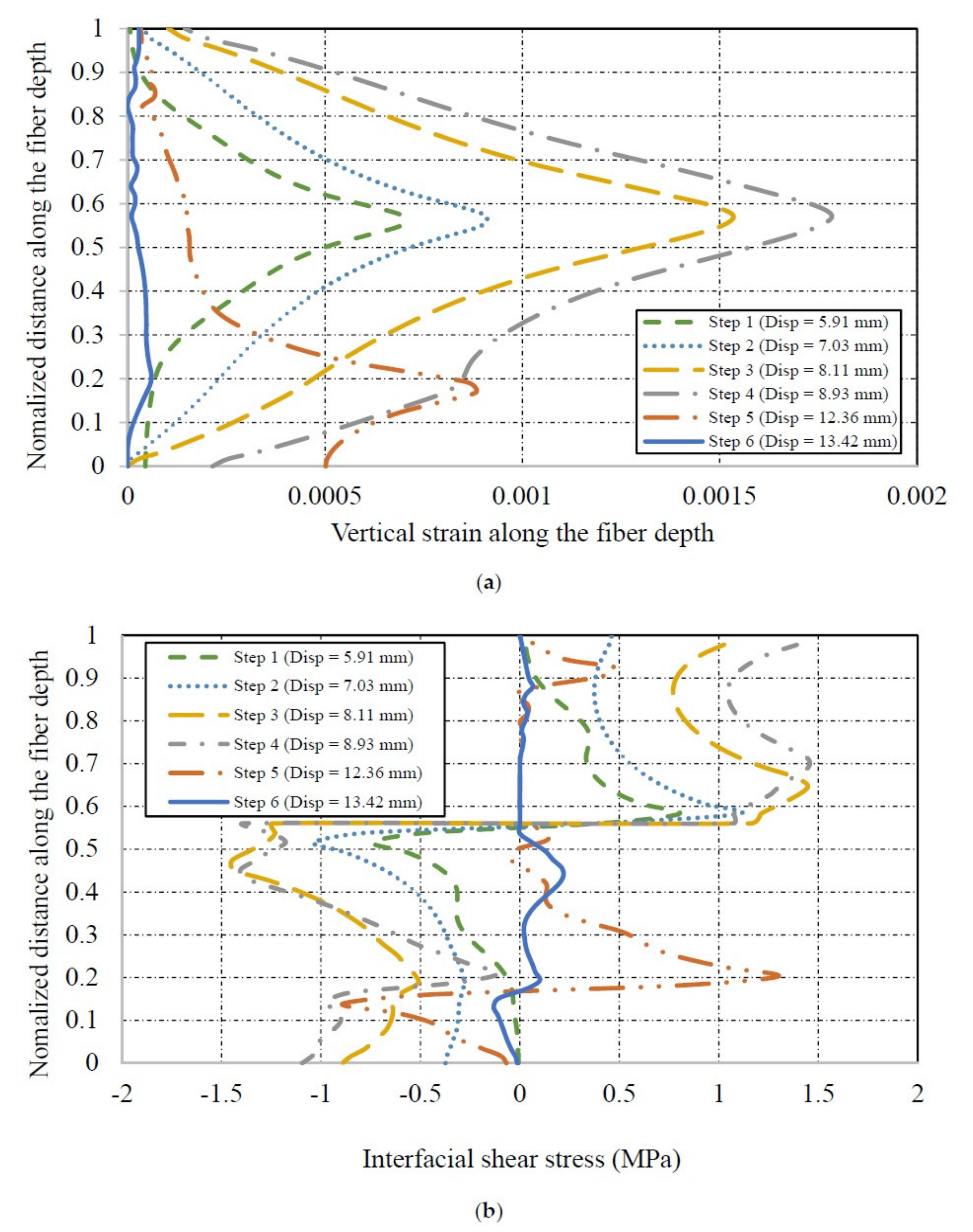

(a)

(b)

Figure 4.15 Strain profile and interfacial shear stress along the fibre and interface layer intercepted by maximum crack width (specimen L.S0.2L). Steps 1,2,3: the initiation and development of the shear crack just before the delamination procedures. Step 4,5,6: the procedure from the initiation of the delamination to the complete loss of strain in the fibre

As soon as the shear crack appeared in L.S0.1L at 5.6 mm displacement, the fibre started to contribute to shear resistance. By increasing the load and the corresponding displacement, the amount of strain increased to a maximum of 0.00415. The maximum strain occurred at mid-depth of the specimen and then decreased gradually toward the top edge of the web/flange intersection. The amount of strain experienced by the lower part increased more than that on the top edge of the fibre because there was more effective bond length in the bottom crack part of the U-wrap configuration, in which the fibres below the shear crack were fixed.

Note that at the peak of the strain profile and when strain was constant, interfacial shear stress was zero, indicating the delaminated zone. At the third stage, during development of the delaminated area, this zone propagated in the top part of the crack, as evidenced by zero interfacial shear stress and zero strain in the strain profile (Figure 4.14 and Figure 4.15). As the displacement reached 12.37 mm, complete delamination occurred in specimen L.S0.L1, and likewise in specimen L.S0.2L. In addition, the amount of strain on the fibres along the main diagonal shear crack decreased in all specimens strengthened with two CFRP layers compared to specimens strengthened with one CFRP layer. Unlike the medium specimens, where increasing rigidity did not significantly change the maximum strains on the fibres, the maximum strains in all the small and large specimens (strengthened with one and two CFRP layers) decreased with increasing size, indicating the existence of an additional size effect on CFRP shear contribution. However, there is a need for more investigations regarding the relation between the size effect and the increase in CFRP rigidity. To compare maximum strain results on the contribution of CFRP fabrics to the ultimate specimen shear strength, the following dimensionless value $V_T/(b_w \times d \times f_c^{'})$ was introduced (Ahmed Godat et al., 2010). This formula defines a dimensionless unit of the ultimate shear capacity of the beam versus the maximum strain on fibres. Therefore, it can evaluate the impact of the size effect on the ultimate specimen shear capacity (Figure 4.16 a, b). The maximum vertical strains were measured at the widest parts of the shear cracks. As shown in Figure 4.16 a, b, both small specimens (S.S0.1L, S.S0.2L) showed more shear contribution of EB-CFRP than the medium and large beams. This confirms the existence of a size effect because it was expected that by increasing beam size and consequently FRP bond length, more FRP shear contribution should be obtained. In addition, despite their longer effective bond lengths, large specimens experienced less vertical strain on the fibre than small specimens, which confirms the results of previous investigations (Benzeguir et al., 2019; Ahmed Godat et al., 2010) that as beam size increases, the shear strength contribution of CFRP decreases.

In conclusion, absorption of vertical strains through the fibres is greater in smaller than in larger specimens despite the fact that both beam sizes have the same ratio of CFRP fabric.

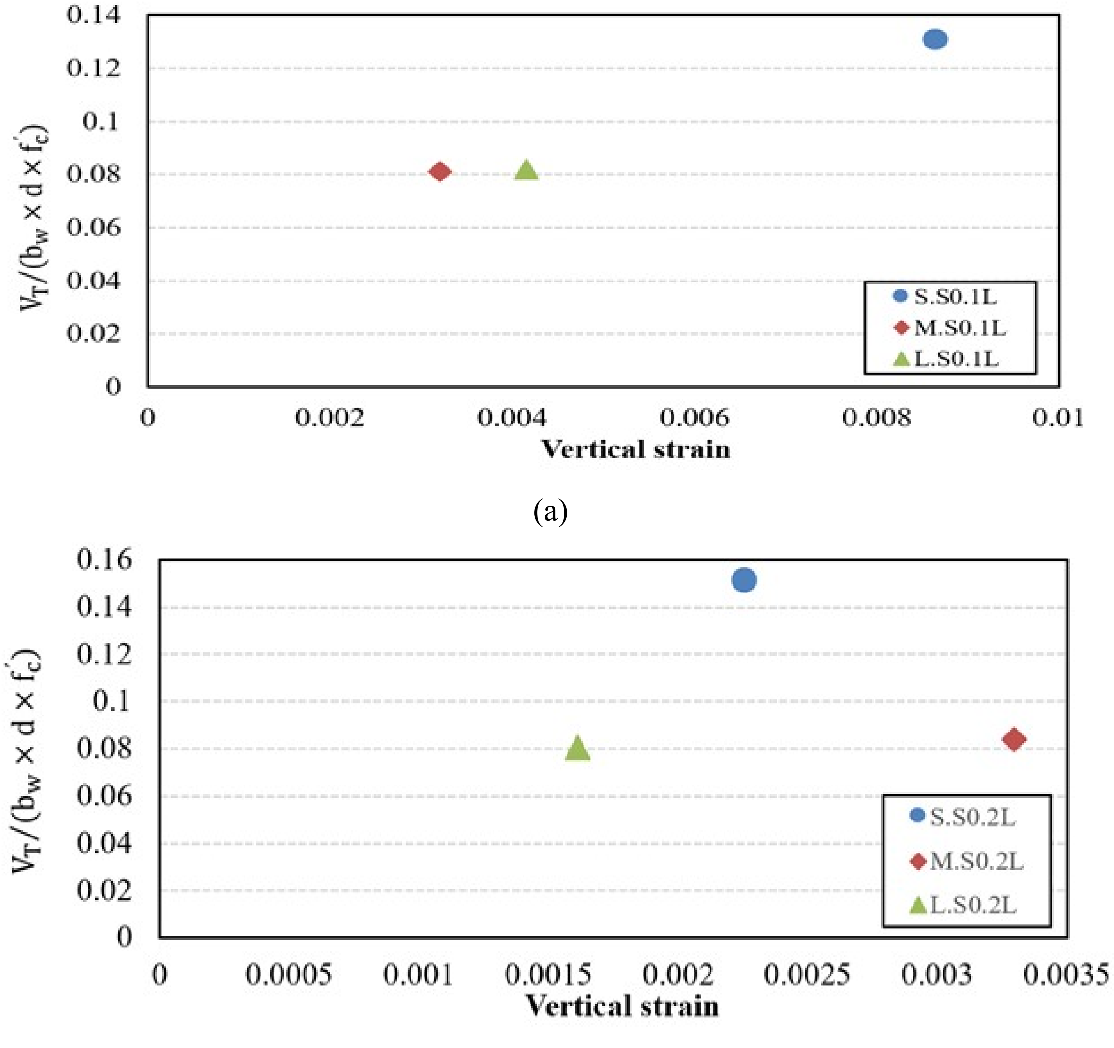

(a)

(b)

Figure 4.16 Correlation between maximum dimensionless shear capacity of specimens versus maximum strain along the fibre: (a) specimens strengthened by one layer of CFRP fabric; (b) specimens strengthened by two layers of CFRP fabric

4.7 Conclusions

This research study has reported on advanced FE modelling of RC beams strengthened in shear with EB-FRP fabrics, with emphasis on the size effect on the shear contribution of RC beams shear-strengthened with EB-CFRP. The results obtained from FEA were in good agreement with the experimental results. Nine RC-T beams (three control beams and six strengthened beams in shear with EB-FRP) were simulated in ABAQUS. The results obtained from the numerical model were related to shear crack patterns, load-deflection curve, shear stress contributed by concrete and CFRP fabric, distributions of strains on fibres crossed by normalized distance along the main diagonal shear path during the loading process, and correlation between maximum dimensionless shear capacity of specimens versus maximum strain along the fibres, demonstrating that the proposed FEA is capable of capturing the response of the RC-T beams with high accuracy if the assumptions are defined properly. Furthermore, compared to experimental tests, FEA provided more precise observations and parameters during loading. The following conclusions can be drawn from this study:

- By increasing the rigidity of EB-CFRP in small specimens, the shear contribution of EBCFRP showed a considerable increment, but in large specimens, EB-CFRP experienced a reduction in its absorption of shear stress due to the size effect.
- Delamination on the top parts of the diagonal shear cracks was the dominant failure mode compared to debonding, especially in medium and large specimens strengthened with EB-CFRP fabric.
- A reduction factor to account for size effect is of paramount importance. The reduction factor could be incorporated either into the effective strain or into the distribution factor, which are included in the model to express the shear contribution of EB-FRP
- The delamination failure initiated suddenly around the tips of the shear crack, where the bond length was minimal.
- Considering strain profiles and interfacial shear stress along with the fibres and the interface layers, when the strain profile reached its peak value or became constant, the interfacial shear stress became zero.

4.8 Acknowledgements

Financial support from the Natural Sciences and Engineering Research Council of Canada (NSERC) and from the Fonds de recherche du Québec – Nature et technologie (FRQ-NT) through operating grants is gratefully acknowledged.

CHAPTER 5

INVERSE INTERACTION BETWEEN STEEL STIRRUPS AND EB-CFRP IN RC BEAMS STRENGTHENED IN SHEAR: DEVELOPMENT OF ANALYTICAL AND NUMERICAL MODELS

Amirali Abbasi[1], Omar Chaallal[2] and Georges El-Saikaly[3]

[1,2,3] Department of Construction Engineering, École de Technologie Supérieure
1100 Notre-Dame St W, Montreal (Quebec) H3C 1K3, Canada

Paper submitted in Journal of *Reinforced Plastics and Composites*, September 2023.

5.1 Abstract

The main objective of the present study is to implement experimental and numerical tests to develop an analytical model for reinforced concrete (RC) beams strengthened in shear with externally bonded carbon fiber reinforced polymer (EB-CFRP). Emphasis is placed on the negative inverse interaction between the steel stirrups and the EB-CFRP as the ratio of EB-CFRP to steel stirrups increases. This interaction is not included in the design models proposed by most current guidelines, although it has a considerable effect on shear resistance as predicted by the guidelines. In fact, the shear contribution associated with EB-CFRP decreases as the ratio of EB-CFRP to steel stirrups increases. Therefore, proposing reliable effective strains by including this parameter improves the calculated shear contribution of EB-CFRPs. First, an analytical model is proposed for CFRP effective strain considering the inverse interaction between EB-CFRP and steel stirrups. Afterwards, a validation of the proposed model with experimental data is done by conducting a parametric study of the increasing trends with respect to the ratio of EB-CFRP to steel stirrups. A numerical finite-element model for the reduction factor and the corresponding effective strain based on the inverse interactions between EB-CFRPs and steel stirrups is also proposed, and the results are compared with various current guidelines. The results are presented in terms of shear crack patterns, load-midspan deflections, shear stresses, strain responses along the fibers, maximum strain profiles for all the CFRPs and specimens, applied shear forces and strains for all the steel stirrups and EB-CFRPs, and interactions between steel stirrups and EB-CFRPs based on their maximum

strain contributions at the maximum shear forces and the maximum strain they experience after shear failure.

Keywords: inverse interaction, externally bonded carbon fiber polymer, steel stirrups, finite-element model, analytical model, proposed model

5.2 Introduction

Fiber-reinforced polymers (FRP) have been extensively applied for various industrial purposes, including the construction industry, due to their numerous advantages such as high strength-to-weight ratio, high resistance at low temperature, low cost, and ease of installation. One of their applications in construction is to rehabilitate damaged concrete structures. Therefore, researchers have been conducting various experimental, analytical, and numerical investigations to calculate their contribution to the strengthening of concrete structures. Shear failures in reinforced concrete beams (RC) have always been a serious concern for practicing engineers because of their complexity and tendency to brittle failure without warning. However, there are many contradictions in the existing analytical models to calculate the shear contribution of FRP to the ultimate shear strength of RC beams strengthened with externally bonded FRP (EB-FRP). Various parameters are missing in these analytical models, which affect the accuracy of the guideline predictions for the contribution of EB-FRP to the ultimate load-carrying capacity of RC beams. The inverse interaction between steel stirrups and EB-FRP, the size effect, the angle of the shear crack, the distribution of the shear crack over the EB-FRP, and the effect of bond-slip between concrete and EB-FRP are examples of such parameters. The inverse interaction between EB-FRP and steel stirrups has been recently shown by researchers to have an important impact. Indeed, it was shown that increasing the amount of internal and external reinforcement resulted in various distributions of shear cracks, leading to less effective bond length (Chaallal et al., 2002; Guangming Chen, 2010; Khalifa et al., 1998; Mofidi & Chaallal, 2010; Pellegrino & Modena, 2002). In addition, there are some issues regarding these models that need to be questioned. Khalifa et al. (1998) proposed a model that relates the fraction of the effective strain and the ultimate strain to the EB-FRP ratio, where neither the shear-crack distribution nor the EB-FRP-to steel -stirrup ratio is considered. Chaallal et al. (2002) proposed a model where the effective strain is a function of the total reinforcement (EB-FRP + steel stirrups), in which the EB-FRP to steel stirrup ratio is not considered. Therefore, this model shows the effective strain for specimens that are not even strengthened with EB-FRP and does not consider inverse interaction between internal and external reinforcements. The reduction factor proposed by Pellegrino and Modena (2002) does not include the EB-FRP-to-steel stirrup ratio, but rather the reduction factor is a function that relates the shear gain due to EB-FRP to the ratio $A_s.E_s/\rho_f.E_f$. In addition, Guangming Chen (2010) defined a model in which the mobilization factors (reduction factors) were attributed to EB-FRP and steel stirrups where a single shear-crack opening is concerned, without considering the distribution or the nonlinearity of shear cracks. On the other hand, Mofidi and Chaallal (2010) considered the shear-crack distribution by converting the trapezoidal area to the rectangular area in the zone where EB-FRP contributes to the total shear resistance of the beam by including the effective bond length and width. Although similar to the model proposed by Chaallal et al. (2002), this model is based on the total ratio (i.e., internal steel stirrups plus external EB-FRP), not considering the ratio of the EB FRP to the steel stirrups.

The current research study aims to improve the model proposed by Mofidi and Chaallal (2010) by focusing on the effect of inverse interactions between EB-ERP and steel stirrups on the one hand and the shear-crack distribution on the other. First, a database of 100 previous experimental studies was gathered and analyzed; then, based on regression of laboratory test results, an analytical model was developed and compared to existing guidelines. After this, a parametric finite-element (FE) study was conducted considering different ratios of FRP to steel stirrups to evaluate FRP effective strain. The results of the numerical study were evaluated based on the shear-crack distributions, shear stress, and strain profiles with respect to the direction of fibers crossed by the main shear crack, the strain distribution factor, the effective strain, the load-deflection responses (concrete, steel stirrups, and fibers), and the amounts of EB-FRP and steel-stirrup strain versus the applied shear force.

5.3 Research significance

Research on the effect of the inverse interaction between EB-CFRP and steel stirrups is not considered in current guidelines, and the number of studies on this topic is limited. However, this phenomenon has a considerable influence on the components of an RC beam strengthened with EB-FRP, in the sense that not recognizing its effect results in misconceptions about the shear contributions of EB-FRP and steel stirrups. Furthermore, numerical studies of this inverse interaction are limited, although FEA facilitates the prediction of component responses during the loading process and paves the way for proposing models that consider the effect of major parameters. The present study plays a role in better understanding the inverse interaction between EB-FRP and steel stirrups and developing analytical and numerical models for future research.

5.4 Proposed model

The model proposed by Mofidi and Chaallal (2010) shows better accuracy than most current guidelines and considers the effect of total shear reinforcement on the shear-crack distribution because the effective bond length is reduced as the total amount of shear reinforcement increases. The accuracy of this model reflects its better prediction of EB-FRP shear contribution compared to the reviewed guidelines. This model replaces the trapezoidal areas with rectangular areas of effective length (L_e) and effective width (w_{fe}). The effective length was obtained based on the model of Neubauer and Rostasy (1997):

$$L_e = \sqrt{\frac{E_f t_f}{2 f_{ct}}} \tag{5.1}$$

$$f_{ct} = 0.53\sqrt{f_c'}. \tag{5.2}$$

For calculating w_{fe}, this model proves that both the number of stirrups $(\rho_s E_s)$ and the rigidity of FRP composites $(\rho_f E_f)$ affect the shear-crack distribution. Moreover, the proposed model shows that the crack pattern affects the bond length in FRP composites in such a way that as cracks propagate, less bond length is available, leading to less FRP contribution to shear resistance. Therefore, the effective width should be sufficient to provide an effective bond surface anchorage length. To calculate β_c and w_{fe}, the strut-and-tie method is used with a shear crack angle of 45º. The modification factor for each configuration (U-wrapped or side-bonded) is defined by the effective width and the distribution of shear cracks as follows:

$$w_{fe} = \frac{0.6}{\sqrt{\rho_f E_f + \rho_s E_s}} \times d_f \qquad U - Wrapped \qquad (5.3)$$

$$w_{fe} = \frac{0.43}{\sqrt{\rho_f E_f + \rho_s E_s}} \times d_f \qquad side - bonded \qquad (5.4)$$

$$\beta_c = \frac{w_{fe}}{d_f} = \frac{0.6}{\sqrt{\rho_f E_f + \rho_s E_s}} \qquad U - Wrapped \qquad (5.5)$$

$$\beta_c = \frac{w_{fe}}{d_f} = \frac{0.43}{\sqrt{\rho_f E_f + \rho_s E_s}} \qquad side - bonded \qquad (5.6)$$

The effective strain is given by:

$$\varepsilon_{fe} = \frac{\beta_c . \beta_L . \beta_w . \tau_{eff} . L_e}{t_f E_f} = 0.31 \beta_c . \beta_L . \beta_w \sqrt{\frac{f_c'}{t_f E_f}} \leq \varepsilon_{fu} \qquad (5.7)$$

The contribution of FRP composites to shear resistance can be determined using the following equation:

$$V_f = \frac{2 t_f . w_f . \varepsilon_{fe} . E_f . (\cot\theta + \cot\alpha) . sin\alpha . d_f}{s_f} = \rho_f . E_f . \varepsilon_{fe} . b . d_f . (cot\theta + cot\alpha) . sin\alpha \qquad (5.8)$$

The problem with this model is that it does not show how the shear-crack distribution changes as the EB-FRP-to steel-stirrups ratio increases. Because this model is based on the total ratio (i.e., internal steel plus external EB-FRP shear reinforcement), it is important to evaluate the reduction of EB-FRP shear contribution as a function of the steel-stirrup ratio.

In addition, the inverse interaction between steel stirrups and FRP is not considered in the model proposed by Mofidi and Chaallal (2010).

illustrates that the negative interaction has not yet been considered by existing codes. Therefore, in this research, by observing that inverse interaction, the model is developed by including a parameter related to the effect of the increasing ratio of $\rho_{FRP}.E_{FRP}/\rho_s.E_s$. The effective strain proposed by Mofidi and Chaallal (2010) includes a coefficient related to the shear-crack distribution (β_c).

Table 5.1Considering the influencing parameters of the shear strengthening in the existing codes

EB-FRP codes	years	Bond-slip stirrups & concrete	FRP& concrete bond	Effective strain	Crack patterns	Invers interaction FRP-stirrups	Crack angle	Size effect
CAN/CSA-S6	2019	×	×	✓	×	×	✓	×
CAN/CSA-S806	2012	×	×	✓	×	×	✓	×
ACI 440.2R	2017	×	×	✓	×	×	✓	×
fib-TG 5.1-19 (2019)	2019	×	✓	✓	×	×	✓	×
JSCE	2007	×	×	×	×	×	×	×
Mofidi's model	2012	×	×	✓	✓	×	✓	×

Therefore, the effective anchorage length is shorter than in the guidelines, which do not consider the effect of multiple shear-crack patterns. However, in this research, this factor is replaced by another factor that considers both the variation in shear-crack distribution as the shear reinforcement components increase and the inverse interaction between the ratio of EB-FRP and internal steel reinforcement. Previous studies (Chaallal et al., 2002; GM Chen et al., 2012; Pellegrino & Modena, 2002) demonstrated that by increasing both the ratios of EB-FRP and steel stirrups, shear cracks become more distributed compared to a single shear crack when there is no shear reinforcement. Therefore, as the anchorage length is reduced due to the appearance of major and minor shear cracks, EB-FRP offers less anchorage length, and this phenomenon accelerates EB-FRP debonding. The debonding process always starts at a major shear crack when the shear stresses exceeds the maximum shear stress at the FRP-concrete interface; this debonding area moves toward the immobilized area, where there is still enough anchorage length, until the entire debonding zone completely loses its strength (Carolin & Täljsten, 2005; GM Chen, Teng, et al., 2010). On the other hand, strengthening with EB-FRP is another reason for a wider distribution of shear cracks (GM Chen et al., 2012), which results in a reduction of the EB-FRP contribution to the total shear resistance of a beam when it comes to increasing the ratio of external reinforcement (FRP) to internal reinforcement. Therefore, if the reduction factor proposed by Mofidi and Chaallal (2010) is a function of total shear reinforcement, this model does not show how this trend is reduced by increasing the ratio of $\rho_{FRP}.E_{FRP}/\rho_S.E_s$. Moreover, it would be important to consider the crack-distribution coefficient (β_c) based on the ratio of external to internal reinforcement ($\rho_{FRP}.E_{FRP}/\rho_S.E_s$) instead of the total ratio of transverse steel and FRP. Because both bond-slip models (between FRP and concrete and between steel stirrups and concrete) are functions of the concrete strength, the maximum shear strength between concrete and EB-FRP calculated by Lu et al. (2005) ($\tau_{max} = \alpha_1.\beta_w.f_t$), and the maximum shear strength between concrete and steel stirrups proposed by Telford (1993) ($\tau_{max} = 2.0\sqrt{f_{ct}}$), it would be necessary to include the effect of concrete strength in the reduction factor (B_{ic}). Based on regression of the database of previous experimental studies, this reduction is observed when the ratio ($\rho_f.E_f/\rho_s E_s$) shows a rising trend (Figure 5.1a).

The following coefficient factors could be replaced with β_c. Therefore, in the proposed model by Mofidi and Chaallal (2010), the effective strain is implemented, and β_c is replaced with B_{ic} as follows:

$$B_{ic} = (W_e/d_f)^3 \times \sqrt{f_c'/f_{ct}} = 0.647 \times (\rho_f.E_f/\rho_s E_s)^{-0.637} \tag{5.9}$$

$$\varepsilon_{fe} = \frac{B_{ic}.\beta_L.\beta_w.\tau_{eff}.L_e}{t_f E_f} = 0.31 B_{ic}.\beta_L.\beta_w\sqrt{\frac{f_c'}{t_f E_f}} \leq \varepsilon_{fu} \tag{5.10}$$

where β_L is the reduction factor for FRP effective bond length when it is less than the maximum anchorage length proposed by J. F. Chen and Teng (2001), β_w is the coefficient factor for considering the effect of the strip-width-to-spacing ratio proposed by J. F. Chen and Teng (2001), ε_{fu} is the ultimate strength of the fibers, and W_e is the effective width proposed by Khalifa et al. (1998). The EB-FRP contribution is obtained based on Equations (5.1)– (5.8):

$$\beta_L = \begin{cases} 1 & if \quad \lambda \geq 1 \\ \sin\frac{\pi\lambda}{2} & if \quad \lambda < 1 \end{cases}; \quad \lambda = \frac{L_{max}}{L_e} \tag{5.11}$$

$$\beta_W = \sqrt{\frac{2 - W_f/S_f}{1 + W_f/S_f}} \tag{5.12}$$

$$w_e = d_f - L_e \tag{5.13}$$

5.5 Verification of the proposed model

A database of specimens strengthened in shear with U-shaped EB-CFRP and steel stirrups based on studies by Samb et al. (2020), Benzeguir et al. (2019), Bousselham and Chaallal (2004), Sayed et al. (2013), Abbasi, Benzeguir, et al. (2022), and Abbasi, Chaallal, and El-Saikaly (2022) was gathered to assess the validity of the proposed model (Figure 5.1b-g). All the database specimens were strengthened with steel stirrups and U-shaped EB-CFRP to evaluate and compare the shear resistance of EB-CFRP in the presence of steel stirrups. The comparison was drawn between the proposed model and the guidelines. Figure 5.1b-g presents the calculated $V_{f(cal)}$ according to current codes (CSA-S6-19, CSA-S806-12, ACI 440.2R-17, *fib*-TG 5.1-19, JSCE-07) versus experimental tests $V_{f(exp)}$ in terms of R^2, average, estimated standard deviation based on a sample (STDEV), and covariance. Obviously, the proposed model shows the highest R^2 ($R^2 = 0.5061$), with the Canadian guidelines (CAN/CSA-S6-19, CAN/CSA-S806-12) and those from the American Concrete Institute (ACI) showing the same R^2 value (0.42). The lowest R^2 is related to JSCE-07 ($R^2 = 0.28$), which does not use the effective strain for calculating V_f and *fib*-TG 5.1-19 ($R^2 = 0.15$). This demonstrates that the inverse shear interaction between internal and external shear reinforcement as well as the shear-crack distribution should be included in the calculation of V_f.

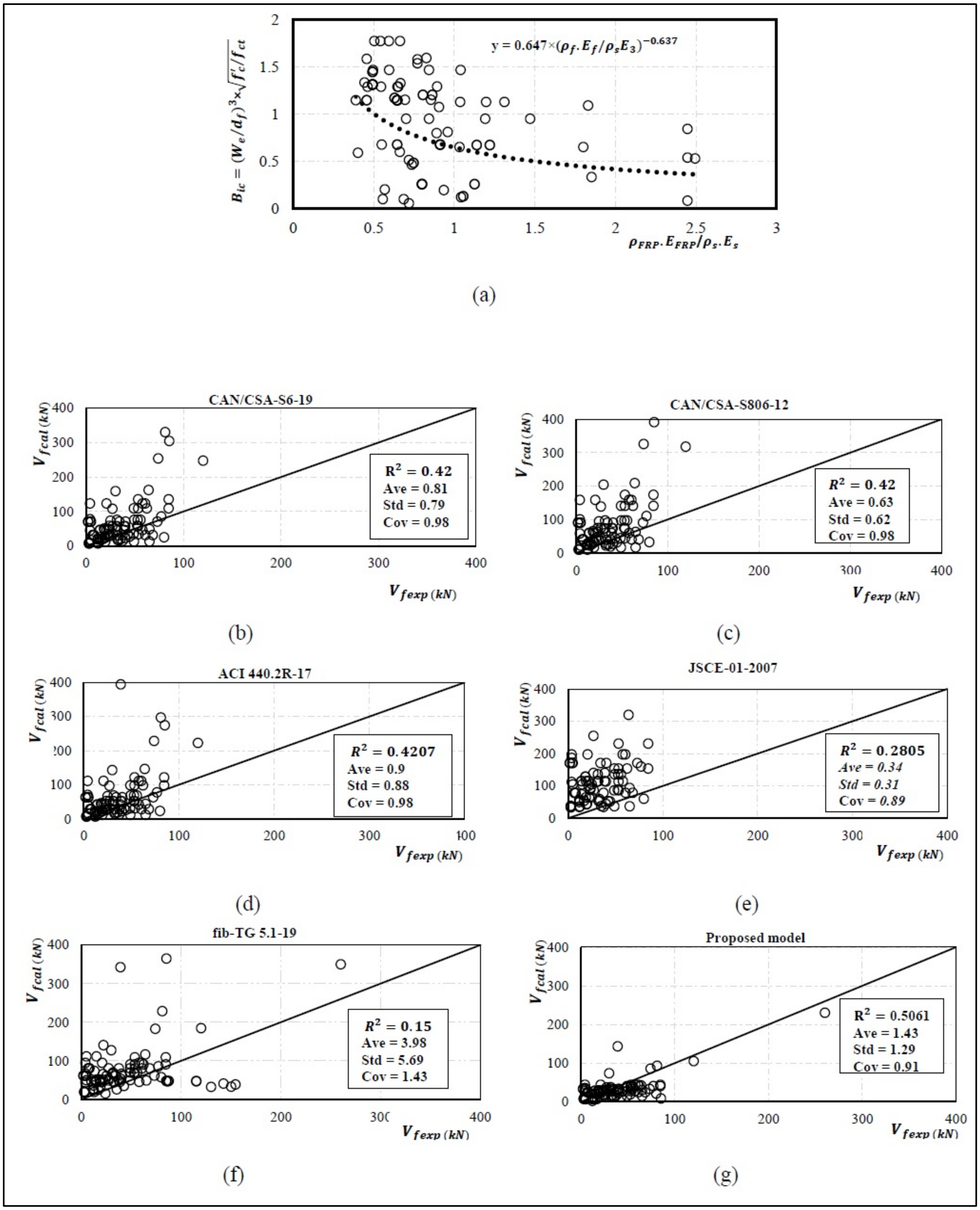

(a)

(b) (c)

(d) (e)

(f) (g)

Figure 5.1 (a) $(W_e/d_f)^3\times\sqrt{f_c'/f_{ct}}$ versus ratio of EB CFRP to the steel stirrups- Calculated versus experimental results for (b) CAN/CSA-S6-19 (c) CAN/CSA-S806-12 (d) ACI 440.2R-17 (e) JSCE-01-2007 (f) fib-TG 5.1-19 (g) the proposed model

5.6 Parametric finite-element analysis

5.6.1 Definitions of studied specimens

Parametric and numerical studies were carried out on 10 beams. The reference beam was adopted from the Matthys (2000) study, which used B3 (control beam) and B5 with small modifications in steel stirrups and concrete strength (using Y4 instead of Y6 for the steel stirrups and $f_c^{'} = 40$ MPa instead of $\mathrm{f_c^{'}} = 30$ MPa) to assess the negative inverse interaction between EB-FRP and steel stirrups as the ratio $\rho_{FRP}.E_{FRP}/\rho_S.E_S$ increases. However, to validate the numerical results of the experimental test, the original material properties and dimensions were used ($f_c^{'} = 30$ MPa for the concrete strength and Y6 for the steel stirrups). After simulation and validation of those specimens, a parametric study was carried out to evaluate the inverse interaction. Results were assessed in terms of the load-carrying capacity, the shear contribution of each component (concrete, EB-FRP, and steel stirrups), the strain distribution of EB-FRP along the fiber direction, the shear stress distribution of EB-FRP along the fiber direction, and the applied shear force versus the amount of strain in EB-FRP and steel stirrups. Figure 5.2Figure 5.2 shows the cross section and elevation of the studied beam. The specimens were classified into three groups, in which the ratio of steel stirrups was constant ($\rho_S = 0.0314\%$). In each group, there were three specimens, in which the thickness of EB-CFRP was increased to 0.444 mm and 1.8 mm from 0.111 mm, but the widths and distances between EB-CFRP strips remained constant. In the first series, the CFRP strips were 25 mm wide, and in the second and third series, they were 50 and 80 mm wide respectively.

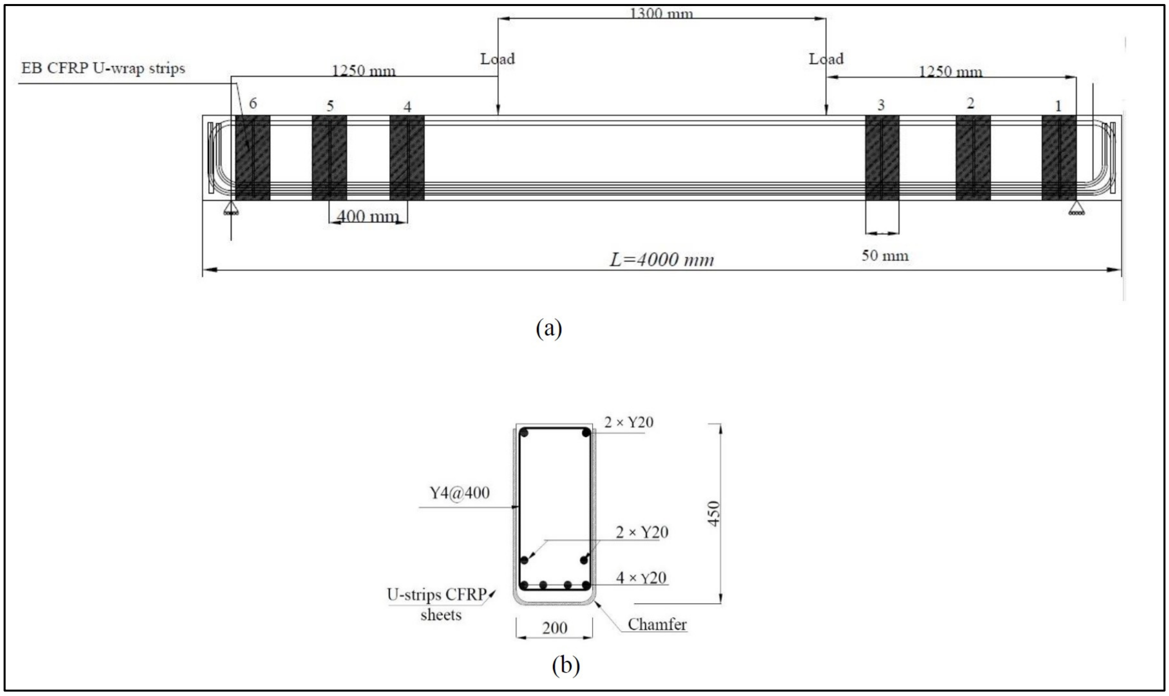

Figure 5.2 Details of beams: (a) Cross sections of the specimens (mm); and (b) Elevation of beam, and position of four points loading

The first letter (S) shows the number of the series, and the second and third letters (W, T) stand for the width and thickness of the CFRP strips. Details of the specimens are presented in Table 5.2 and Table 5.3.

Table 5.2 Property of material in studied beams by Matthys (2000)

Types	Dimesions (mm)	Yield strength ($\frac{N}{mm^2}$)	Tensile strength ($\frac{N}{mm^2}$)	Ultimate Strain (%)	Elasticisty Modulus ($\frac{N}{mm^2}$)
Y4	4 mm	560	590	5.1	200000
Y6	6 mm	560	590	5.1	200000
Y20	20 mm	530	620	11.9	200000
CFRP	0.111 mm	-	3500	1.25	233000

Table 5.3 Specimens and the amounts of EB FRP and steel stirrups in the current numerical parametric study

Specimens	Abbreviation name	$\rho_F\%$	$\rho_s\%$	FRP strips thickness (mm)	Distance between FRP strips (mm)	CFRP Width (mm)	$(\rho_F.E_F/\rho_s.E_s)$
Control beam	Control beam	-	0.0314	-	-	-	0
S1-W25-T0.11	R0.25	0.0061	0.0314	0.111	400	25	0.25
S1-W25-T0.44	R1.02	0.0246	0.0314	0.444	400	50	1.02
S1-W25-T1.8	R4.17	0.1	0.0314	1.8	400	80	4.17
S2-W50-T0.11	R0.51	0.0138	0.0314	0.111	400	25	0.51
S2-W50-T0.44	R2.05	0.0555	0.0314	0.444	400	50	2.05
S2-W50-T1.8	R8.34	0.225	0.0314	1.8	400	80	8.34
S3-W80-T0.11	R0.82	0.024	0.0314	0.111	400	25	0.82
S3-W80-T0.44	R3.39	0.096	0.0314	0.444	400	50	3.39
S3-W80-T1.8	R13.35	0.3891	0.0314	1.8	400	80	13.35

5.6.2 Suggested FE modeling

A summary of the nonlinear finite-element analysis (FEA) assumptions implemented in the current parametric study corresponding to the concrete materials, the definitions of a crack in concrete, steel reinforcement, CFRP sheet, bond-slip behavior between CFRP and concrete and between steel bars and concrete, and the types of analysis adopted for the simulation model is presented in this section (Figure 5.3 a-f).

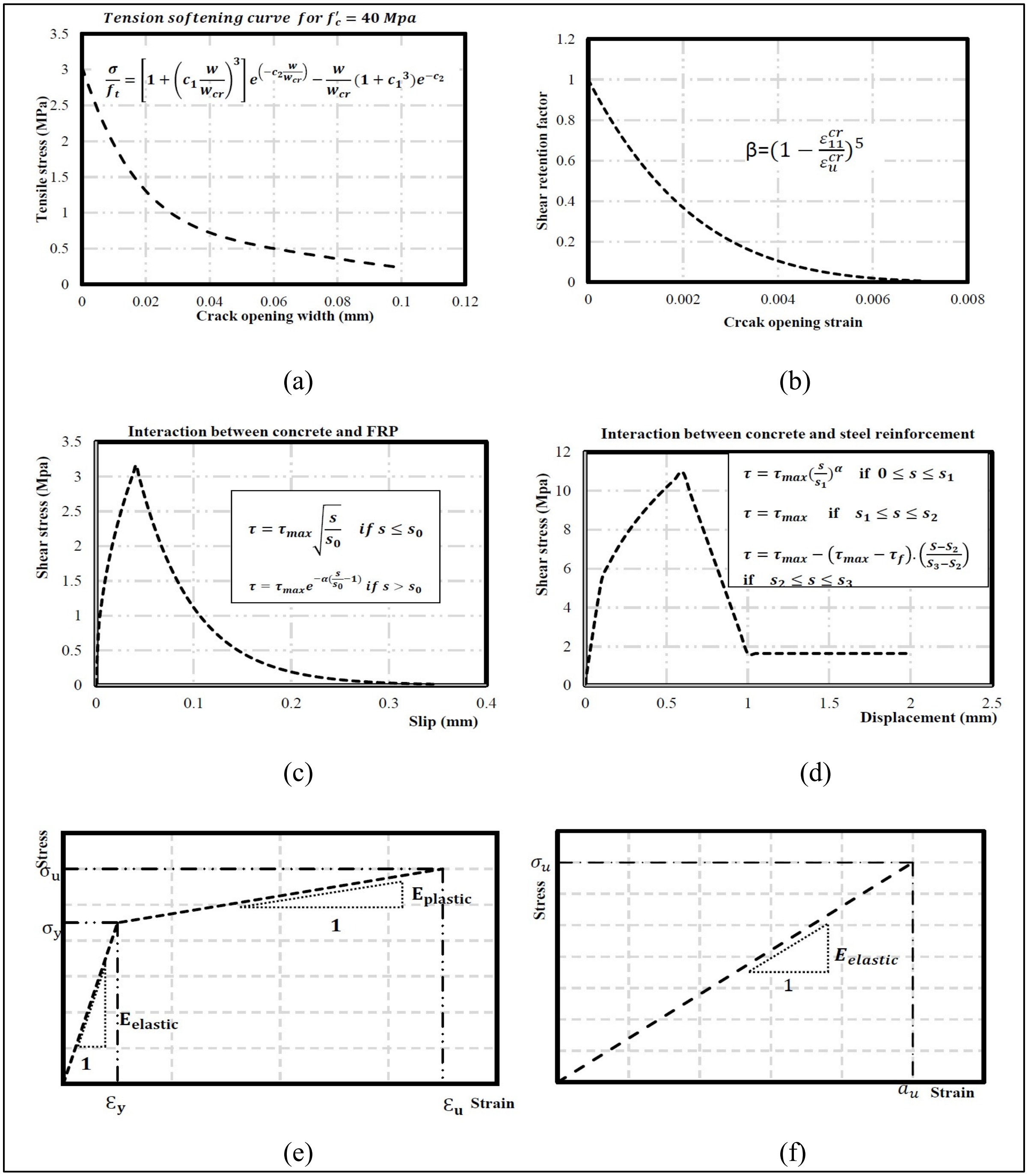

(a) (b)

(c) (d)

(e) (f)

Figure 5.3 Properties and assumption of the materials implemented in FE simulations (a) Tension softening curves for the concrete (Hordijk, 1991) (b) damage in the concrete versus shear retention factor (Rots, 1988) (c) Bond-slip model between concrete and CFRP (Lu et al., 2005) (d) Bond-slip model between concrete and steel stirrups (Telford, 1993) (e) Stress-strain relation for steel reinforcement (f) Stress-strain relation for CFRP fabrics

To reduce the time required for analysis and increase the accuracy of the results (by selecting a small discretization) and with regard to the behavior of the beam (bending in its own plane), two-dimensional (2D) FEA (plane stress technique) was applied for the concrete, the support, the load plate, and the cohesive layer between concrete and EB-CFRP, as well as for the cohesive layer between the concrete and the steel reinforcement. As for the CFRP sheets and the steel bars, two-dimensional truss elements were used to simply transfer the load in the direction of the truss elements. To avoid convergence challenges, especially post-failure of specimens (due to brittle behavior of concrete and nonlinearity of the bond-slip layer) produced by static analysis methods such as Newton-Raphson and arc-length analysis, explicit analysis (central difference analysis in ABAQUS) was used in this study (Guangming Chen, 2010). However, the options (load scheme, loading time, damping ratio, and time increment size) should be selected cautiously in the dynamic analysis to obtain a reliable response when solving static problems.

5.6.3 Constitutive models of materials

5.6.3.1 Concrete cracking models

Brittle cracking (BC) was assumed to represent the behavior of concrete in shear cracking (when shear failure is more probable than flexural failure). The BC model can predict the pattern of shear cracks in RC beams if the shear retention factor is defined precisely. The behavior of concrete in compression is considered to be elastic in the brittle cracking model. Various types of crack models are defined in FE programs, such as the discrete crack model, the rotating smeared crack model, and the fixed smeared crack model, but the fixed smeared crack model is implemented in the framework of brittle cracking in concrete. In this study, the shear retention factor was selected from Rots (1988) as follows:

$$\beta = (1 - \frac{\varepsilon_{11}^{cr}}{\varepsilon_{u}^{cr}})^{p} \tag{5.14}$$

where ε_{11}^{cr} is the principal tensile crack strain related to the crack width w in Equation (20), ε_{u}^{cr} is the stress-free crack normal strain related to w_{cr}, which can be obtained from Equation (21), and p is a factor to control the rate of shear degradation (GM Chen et al., 2012). The concrete modulus of elasticity is $E_c = 4730\sqrt{f_c^{'}}$ (MPa) (ACI 318).

To implement the tension-softening behavior of concrete, the formula defined by Hordijk (1991) based on the stress-crack width was used in this study as follows:

$$\frac{\sigma}{f_t} = \left[1 + \left(c_1 \frac{w}{w_{cr}}\right)^3\right] e^{\left(-c_2 \frac{w}{w_{cr}}\right)} - \frac{w}{w_{cr}}(1 + {c_1}^3)e^{-c_2} \tag{5.15}$$

$$w_{cr} = 5.14\frac{G_f}{f_t} \tag{5.16}$$

$$f_t = 1.4\left(\frac{f_c^{'}-8}{10}\right)^{\frac{2}{3}} \tag{5.17}$$

$$G_f = (0.0469{d_a}^2 - 0.5d_a + 26)\left(\frac{f_c^{'}}{10}\right)^{0.7} \tag{5.18}$$

where f_t is the maximum concrete tensile stress; σ is the tensile stress in the specimen during the stress-crack displacement test; G_f is the fracture energy, which can be obtained from the area of the stress-cracking width curve (Figure 3); $c_1 = 3$, $c_2 = 6.93$ are constant parameters proposed by Hordijk (1991); and d_a is the largest aggregate size. In this study, the concrete strength was assumed to be $f_c^{'} = 40\ MPa$.

5.6.3.2 Modeling internal steel reinforcement and EB-CFRP

As for the behavior of steel reinforcement materials, the linear and nonlinear response of steel materials was represented by a bilinear curve, as shown in Figure 3e-f. This approach to representing their elastic-plastic behavior was taken to reduce calculation time and avoid divergence in FEA. Regarding EB-CFRP, its behavior was assumed to be linear before rupture occurred. Detailed properties of materials are shown in Table 5.2 and Table 5.3.

5.6.3.3 Bond model between concrete and CFRP sheet

The ultimate load-carrying capacity of specimens is completely dependent on their bond-slip behavior. To obtain a reliable response from FEA, the parameters of the bond-slip modulus (the modulus of elasticity, the maximum shear stress, the fracture energy (which is the area under the shear stress curve along the cohesive layer), the maximum slip during failure, and the damage parameters) should be defined precisely. In this study, the properties of the interface layer between the concrete and the EB-FRP sheet were obtained from the model proposed by Lu et al. (2005) for $f_c' = 30\ MPa$:

$$\tau = \tau_{max}\sqrt{\frac{s}{s_0}} \qquad \text{if} \qquad s \leq s_0 \ , \tag{5.19}$$

$$\tau = \tau_{max} e^{-\alpha(\frac{s}{s_0}-1)} \qquad \text{if} \qquad s > s_0 \ , \tag{5.20}$$

where $s_0 = 0.0195\beta_w f_t$; $G_f = 0.308{\beta_w}^2\sqrt{f_t}$; $\alpha = \frac{1}{\frac{G_f}{\tau_{max}s_0}-\frac{2}{3}}$; $\beta_w = \sqrt{\frac{2-({w_f}/{(s_f \sin\beta)})}{1+({w_f}/{(s_f \sin\beta)})}}$; and $\beta =$ the fiber direction relative to the horizontal axis of the beam. Lu et al. (2005) introduced three bond-slip models: 1. the precise model, 2. the simplified model, and 3. the bilinear model. In this study, the bilinear model was chosen to assign two-dimensional and four-node-cohesive elements (COH2D4) from ABAQUS, where both debonding and delamination could be detected during and after shear failure.

5.6.3.4 Bond model between concrete and steel reinforcement

The same approach, cohesive elements (COH2D4), was used to describe the bond-slip behavior between concrete and steel reinforcement. The behavior of the cohesive layer for the deformation was assigned according to Telford (1993) and GM Chen et al. (2012) for $f_c' = 30\ MPa$: (Figure 5.3 d).

$$\tau = \tau_{max}(\frac{s}{s_1})^{\alpha} \quad \text{if} \quad 0 \leq s \leq s_1 \ ; \tau = \tau_{max} \ \text{if} \quad s_1 \leq s \leq s_2 \tag{5.21}$$

$$\tau = \tau_{max} - \left(\tau_{max} - \tau_f\right).\left(\frac{S - S_2}{S_3 - S_2}\right) \text{ if } \quad s_2 \leq s \leq s_3 \ ; \ \tau = \tau_f \text{ if } \quad s_3 \leq s \qquad (5.22)$$

where $\alpha = 0.4$, $s_1 = s_2 = 0.6\,mm$, $s_3 = 0.1\,mm$, $\tau_{max} = 2 \times \sqrt{f_{ck}}$, $\tau_f = 0.15 \times \tau_{max}$ for the deformed steel bars.

5.6.4 Validation of the proposed FE model

To verify the simulated model, the control beam (B3) and the beam strengthened with CFRP (B5) were selected from research conducted by Matthys (2000). Comparisons were drawn with experimental results to assess the accuracy of the numerical model. After the simulated models were validated, a parametric study was conducted to shed light on negative inverse interactions between internal and external shear reinforcement of RC beams strengthened in shear with U-shaped FRP sheets.

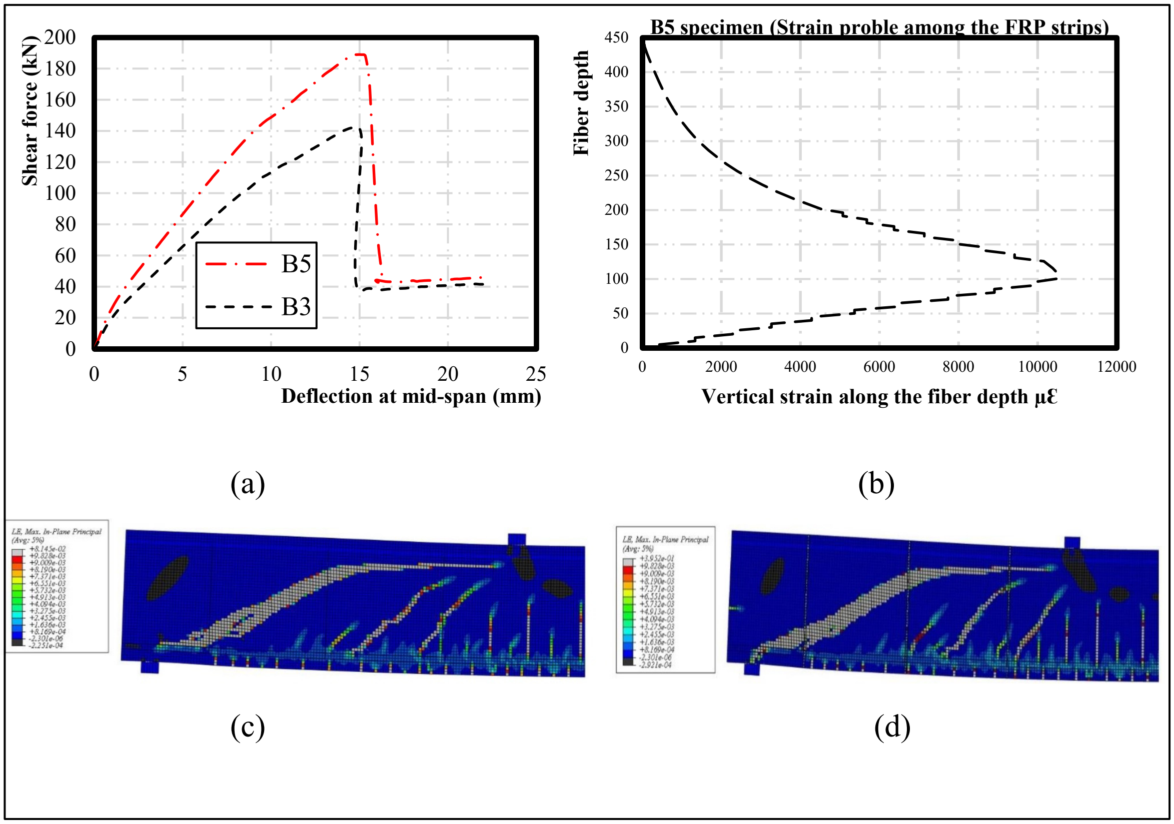

(a) (b)

(c) (d)

Figure 5.4 Verifications of the suggested FE models and experimental results (a) load-mid-span deflections for the specimens B3 (control beam not strengthened with EB CFRP) and B5 (Strengthened beam (b) strain response among CFRPs1 in the specimen B5 (c) distributions of the shear crack for the control beam at the ultimate state (d) distributions of the shear cracks for strengthened beam at the ultimate state

5.6.4.1 Failure modes, crack distributions, and shear force-midspan deflections

The failure modes for both specimens (B3, B5) were loss of shear resistance. However, for the strengthened specimen (B5), debonding occurred at the interface between concrete and CFRP1 strip (Figure 5.4a-d). The maximum strain on CFRP1 at the major shear crack obtained from FEA before shear failure was 10,254 µƐ at 110.637 mm from the lower surface of the beam, which was close to experimental results reported (9,900 µƐ) (Figure 5.4a-d).

5.7 Parametric study of the interaction between stirrups and CFRP strips

Specimens with different $\rho_F . E_F / \rho_S . E_S$ ratios were simulated to evaluate how both steel stirrups and EB-FRP contribute to the ultimate shear capacity of strengthened RC beams and what happens if these ratios (henceforth called R) are increased by keeping the ratio of steel stirrups constant ($\rho_s = 0.0314\%$).

5.7.1 Distribution and angle of shear cracks

Various parameters affect the pattern and angle of shear cracks, such as the number and arrangement of transverse reinforcements, the amount of fiber reinforcement, the shear span-to-depth ratio, the width of FRP strips and their corresponding spacing, and the size effect. As the shear-crack angle increases, the shear crack intercepts fewer FRP strips, and therefore less effective bond length is available to contribute to shear resistance. Moreover, considering a crack angle of 45º is too conservative because this angle changes based on the spacing between steel stirrups and other parameters. However, in this study, the average shear-crack angle varied from 19.23º for specimen (R=13.35) to 26.5º for specimen (R=0.25). When the spacing between steel stirrups was reduced, the shear-crack angle was also reduced because the stirrups tend to prevent shear cracks from propagating (Carolin & Täljsten, 2005; Mofidi & Chaallal, 2010). On the other hand, when the ratio of either steel stirrups or EB-FRP was increased, the pattern of shear cracks became more distributed, resulting in a reduction of the anchorage length offered by EB-FRP. It was proved that by increasing the ratio of steel stirrups and consequently having more distributed cracks, the bond length contributed less effectively to the shear resistance of EB-FRP (Bousselham & Chaallal, 2004; Chaallal et al., 2002; Pellegrino & Modena, 2002). It can be concluded therefore that increasing the ratio of steel stirrups reduces the shear contribution of EB-CFRPs. As was already mentioned, none of the design codes considers the effect of inverse interaction between steel stirrups and EB-FRP. The results of this numerical study represent the pattern of shear cracks as the ratio of CFRP to steel stirrups increases (R). The shear cracks are more distributed for specimens with a higher ratio (R), (Figure 5.7 a), demonstrating that similarly to internal reinforcements, external reinforcements affect crack patterns by producing more marginal shear cracks that reduce the effective bond length. This leads to a reduction in the FRP contribution to ultimate load-carrying capacity. However, it is expected that the greater the cross-section offered by the FRP strips, the greater will be the forecast contribution to the shear load by FRP. It is noteworthy that, unlike the case of a high steel-stirrup ratio (for example, reducing the spacing between steel stirrups), a greater number of shear cracks were more widely distributed (Mofidi & Chaallal, 2010). Multiple shear cracks developed in specimens with wider strips when the spacing between EB-FRP strips and the fiber thickness remained constant (Figure 5.7 a). This may be attributed to the wider strips, which offered a wider bridge to narrow the major shear cracks, and the fact that energy was released by producing marginal and more distributed shear cracks. Therefore, premature debonding happened when the fibers were intercepted by more marginal cracks, resulting in less effective bond length.

5.7.2 Load-deflection response for all components

The results obtained from the current parametric numerical study were evaluated in two ways. First, the EB-FRP contribution was assessed by increasing the FRP-to-steel stirrup ratio as the thickness of EB-FRP was increased from 0.111 mm to 0.444 and then to 1.8 mm. Second, the FRP-to-steel-stirrup ratio was increased by enlarging the width of EB-CFRP strips from 25 mm to 50 mm and then to 80 mm while holding EB-CFRP thickness and spacing constant. As presented in Figure 5.7 b, for the specimens with 25-mm strip width, as the thickness increased from 0.111 mm to 0.444 mm and then to 1.8 mm, the FRP shear contribution rose to 73.8% and 83% for specimens R1.02 and R4.17 compared to specimen R0.25. However, for the beams strengthened with 80-mm-wide FRP strips, the same thickness increases in EB-CFRP strips resulted in a 24.4% and 36.9% rise in EB-CFRP shear contributions for specimens R3.39 and R13.35 compared to specimen R0.82 (Figure 5.7 b). Therefore, increasing the thickness from 0.11 to 1.8 mm in an 80-mm-wide strip resulted in increasing the shear contribution by 36.9%, compared to 83% and 94.3% for specimens strengthened with 25-mm-wide and 50-mm-wide strips respectively. It can be concluded that the lowest increasing trend occurred in the specimens strengthened with 80-mm-wide FRP strips. This was associated with the fact that by increasing the FRP-to-steel stirrup ratio, more marginal shear cracks intercepted CFRP2 and CFRP3 strips, resulting in less effective bonding.

In the second experiments, the thickness of the EB-CFRP strips remained constant while the FRPs-to-steel-stirrup ratio was increased by using wider FRP strips. In the first series, when the strip widths were increased from 25 mm to 50 mm and then to 80 mm while the thickness (0.111 mm) and the spacing between FRP strips (400 mm) were kept constant, the rise in FRP shear contribution was 60% and 232.7% for specimens R0.51 and R0.82 compared to specimen R0.25 (Figure 5). However, in the third series, by increasing the ratio related to specimens R4.17, R8.43, and R13.35 with a constant thickness of 1.8 mm and increasing the widths similarly to series1 and series2, the shear contributions were increased to 36 kN, 61.2 kN, and 89.7 kN, consequently showing 46.6% and 149.1% rises in shear resistance. Therefore, to obtain higher shear contribution from EB-FRP, increasing the FRP width is more effective than increasing the thickness. Wider strips transferred more shear stress through the interface layer and increased the EB-FRP shear contribution.

5.7.3 Shear stress and strain profiles along the first CFRP strips intercepted by major shear cracks

5.7.3.1 Shear stress profiles along the CFRP1 direction

This section provides a brief explanation of bond-slip behavior by evaluating shear stress and strain profiles along the fibers on CFRP1 strips to assess how failure happens when the FRP-to-steel stirrup ratio is increased. The first CFRP strips were located on the widest parts of major shear cracks (crack ends), and the first CFRPs experienced the highest strain (after shear failure of the specimens).

Figure 5.5 a-b shows shear-stress profiles and strain distributions along the fiber depth in five mid-span deflection steps related to five states: (1) initiation of critical shear cracks in the lower part of the web; (2) development of major shear cracks when all cohesive layers experience shear stress as the shear cracks widen, but before they reach maximum stress at the interface; (3) complete formation of shear cracks and imposition of maximum strain on fibers; (4) initiation of debonding at the cohesive layers (reducing the anchorage lengths as cracks widen);

and (5) just before complete failure of the cohesive layers (almost all fibers lose their contribution to shear resistance). Moreover, the areas under the shear-stress profiles along the fibers were measured to evaluate the energies transferred through the interface layers by increasing the FRP-to-steel stirrup ratio, as presented in Figure 5.5 a-b

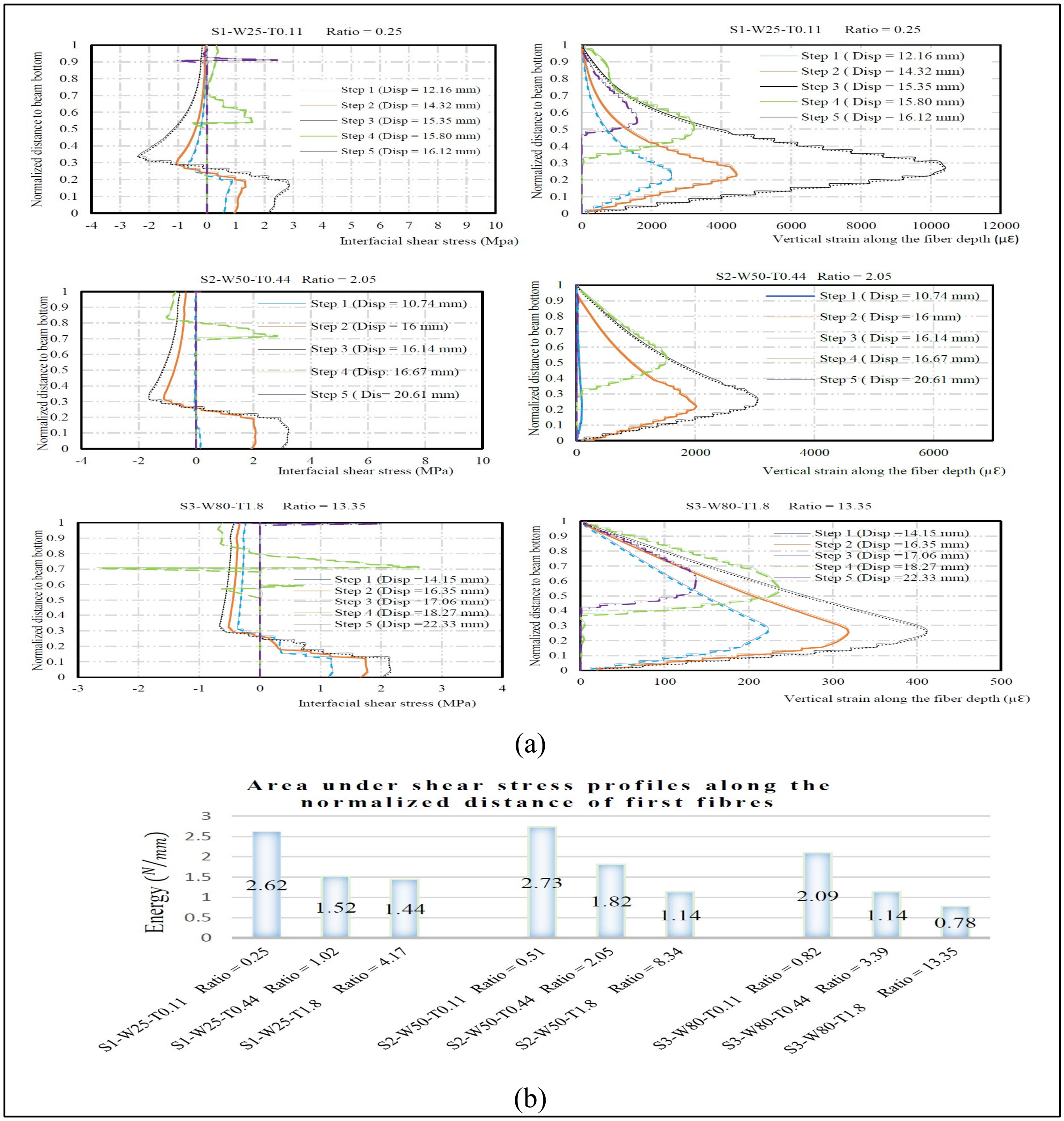

(a)

(b)

Figure 5.5 (a) Strain profiles and interfacial shear stresses along fibers and interface layers intercepted by maximum crack on CFRPs1 and Cohesivelayeres1 (b) Areas under shear stress profiles along the first fibers $(^{N}/_{mm})$

It is noteworthy that the shear stresses at the interface layers become zero whenever the strain responses reach any local pick point or become even. The first series, with the lowest FRP-to-steel stirrup ratio, experienced 2.62 (N/mm), 2.73 (N/mm), and 2.09 (N/mm) higher energies, corresponding to the R0.25, R0.51, and R0.82 specimens where all the specimens were 0.111 mm thick. The second series, with thicker EB-FRP (0.444 mm), was exposed to 1.52 (N/mm), 1.82 (N/mm), and 1.14 (N/mm) lower energies corresponding to the R1.02, R2.05, and R3.39 specimens, representing reductions of 42%, 33.5%, and 45.7% respectively. The lowest energy increases, 1.44 (N/mm), 1.14 (N/mm), and 0.78 (N/mm), were associated with the thickest specimens, R4.17, R8.34, and R13.35 and represented reductions of 44.8%, 58.3%, and 62.9% respectively (Figure 5.5).

The areas under the shear stresses among the cohesive-layer distances demonstrate that the higher the energy, the more benefits were removed from the full potential of the cohesive layer, and the greater was the number of mobilized zones in comparison to the immobilized zones (GM Chen, Teng, et al., 2010). Therefore, this phenomenon can be attributed to the fact that specimens with higher ratios (R) (by increasing FRP thickness) failed by premature debonding. It also proves that when R is increased by making the CFRP thicker, the shear stresses do not distribute properly all over the cohesive layer and do not benefit from the maximum potential shear stress in the interface layers. The same reduction in the amount of strain experienced by CFRPs1 strips can be observed as an increase in the FRP-to-steel stirrup ratio (Figure 5.5a) , as explained in the next section.

5.7.4 Maximum strain profiles along the direction of CFRPs

The FEA results show that the shear contribution of the first FRP strips (not intercepted by marginal shear cracks) was reduced as the EB-FRP-to-steel-stirrup ratio increased (Figure 5.6). The maximum strain on CFRPs1 was recorded for the first series of specimens, where the lowest R ratios were 10478 µƐ, 11219 µƐ, and 10140 µƐ for specimens R0.25, R0.51, and R0.82 respectively (Figure 5.6). However, the strain for the 50-mm-wide and 80-mm wide specimens was drastically reduced as the thickness increased from 0.111 mm to 0.44 mm and then to 1.8 mm.

For the second series, the maximum recorded strains before ultimate shear failure in specimens R1.02, R2.05, and R3.39 were 2487 µƐ, 3059 µƐ, and1909 µƐ respectively. For the third series, the maximum strains experienced by the first fibers were 655 µƐ, 639 µƐ, and 539 µƐ, associated with specimens R4.17, R8.34, and R13.35 (Figure 5.6). The first reason for these results might be the larger cross sections offered by the second and third series. The second reason might be premature debonding at the interface layers. Because of high stress concentrations around the major shear cracks, the shear stresses do not transfer proportionally along the whole of the cohesive layers. This results in not using the maximum potential of the interface layer in the upper parts of the shear cracks (Figure 5.6).

5.7.5 Effective strain

5.7.5.1 Vertical strains along the fiber depth

The maximum distributions of strain before the ultimate load-carrying capacities of specimens with increasing EB-FRP-to-steel stirrup ratio give a good indication of their contributions to shear resistance. However, to obtain the effective strain, all the fibers intercepted by the principal shear crack must be assessed to reach the limits of effective strain in all specimens. As presented in Figure 5.6, FRP responses at their ultimate state crossed by the main shear cracks are illustrated for CFRP1 strips in series1, which were subjected to higher strains where the maximum widths of cracks are located, compared to series2 and series3. It is noteworthy that there is only one pick point on the strain profile graphs for each CFRP1 in series1, indicating that these strips are not intercepted by minor shear cracks. However, because of marginal shear cracking, there is more than one pick point in CFRPs2 and CFRPs3 for series2 and series3 at the maximum strain states (Figure 5.6).

5.7.5.2 Maximum strain in CFRPs1 specimens

The maximum strain in specimens with 25-mm-wide strips was reduced by increasing FRP thickness (and thus the FRP-to-steel stirrup ratio) from 0.11 mm to 0.44 mm and then to 1.8 mm on CFRP1. The thicker specimens were subjected to 23.6% and 6.2% (for R1.02 and R4.17 respectively) of the maximum strain on specimen R0.25. These values were reduced by 2478 µƐ and 655 µƐ for specimens R1.02 and R4.17 respectively. As for the specimens with 80-mm-wide strips, as the thickness increased from 0.11 mm to 0.44 mm and then to 1.8 mm, the maximum strain was reduced from 10140 µƐ to 1909 µƐ and 539 µƐ for specimens R3.39 and R13.35 respectively. These values were 18.8% and 5.3% respectively of the maximum strain in specimen R0.82, as shown in Table 5.4 and Figure 5.6.

5.7.5.3 Maximum strain in CFRPs2 specimens

Evaluation of the maximum strain on the CFRPs2 strips, which were intercepted by more marginal shear cracks, showed less effective bonding than CFRP1 strips as the CFRP2 strip-to steel stirrup ratio increased. By increasing the ratio (R) for specimens with 25-mm-wide strips, as the thickness increased from 0.11 mm to 0.44 mm and then to 1.8 mm, the maximum strains experienced by specimens R0.25, R1.02, and R4.17 were 6505 µƐ, 3557 µƐ, and 937 µƐ respectively. In other words, they were exposed to 54.6% and 14.4% (for specimens R1.02 and R4.17) of the maximum strain in specimen R0.25.

With regard to the specimens strengthened by 80-mm-wide strips (R0.82, R3.39, and R13.35), by increasing the thickness (and consequently the ratio) from 0.111 mm to 0.444 mm and then to 1.8 mm, the maximum strains experienced by the CFRP2 strips were 5885 µƐ, 2190 µƐ, and 619 µƐ. These strains indicate that specimens R3.39 and R13.35 were subjected to 37% and 10% of the maximum strain in specimen R0.82, as shown in Table 5.4 and Figure 5.6.

5.7.5.4 Maximum strain in CFRP3 specimens

CFRP3 strips were located on the tips of major shear cracks, where crack width is at a minimum. Therefore, it is expected that most failures of CFRP3 strips occur because of premature debonding because they have the shortest effective length and are not subjected to the maximum strains experienced by the two previous sets of CFRP strips (Figure 5.6). Regarding the specimens strengthened with 80-mm-wide strips, by increasing the thickness for specimens R0.82, R3.39, and R13.35, the maximum strains reached were 1975 µƐ, 851 µƐ, and 271 µƐ respectively, which shows that the maximum amounts of strain in R3.39 and R13.35 were 29.9% and 14.5% of that in specimen R0.82 because of increasing ratio (R) (Table

5.4 and Figure 5.6). It can be concluded that the reduction in strain on CFRP3 can be attributed to the minor shear cracks that intercept the CFRP3 strips. Table 5.4 and Figure 5.6 show that increasing the ratio of CFRP strips results in more distributed shear cracks. Furthermore, as presented in Figure 5.6, CFRP2 and CFRP3 strips had more than one pick point on the maximum recorded strain profiles, which indicates that they were intercepted by marginal shear cracks.

Table 5.4 Maximum strains experienced by CFRPs crossed by the shear cracks after failure (μƐ)

Specimens	CFRP 1	CFRP 2	CFRP 3	CFRP 1%	CFRP 2%	CFRP 3%
S1-W25-T0.11 Ratio = 0.25	10478	6505	1614	100	100	100
S1-W25-T0.44 Ratio = 1.02	2478	3557	590	23.6	54.6	36.6
S1-W25-T1.8 Ratio = 4.17	655	937	219	6.2	14.4	13.6
S2-W50-T0.11 Ratio = 0.51	11219	7373	1822	100	100	100
S2-W50-T0.44 Ratio = 2.05	3059	2842	545	27.2	38.5	29.9
S2-W50-T1.8 Ratio = 8.34	639	665	265	5.7	9.02	14.5
S3-W80-T0.11 Ratio = 0.82	10140	5885	1975	100	100	100
S3-W80-T0.44 Ratio = 3.39	1909	2190	851	18.8	37.2	43.07
S3-W80-T1.8 Ratio = 13.35	539	619	271	5.3	10.5	13.72

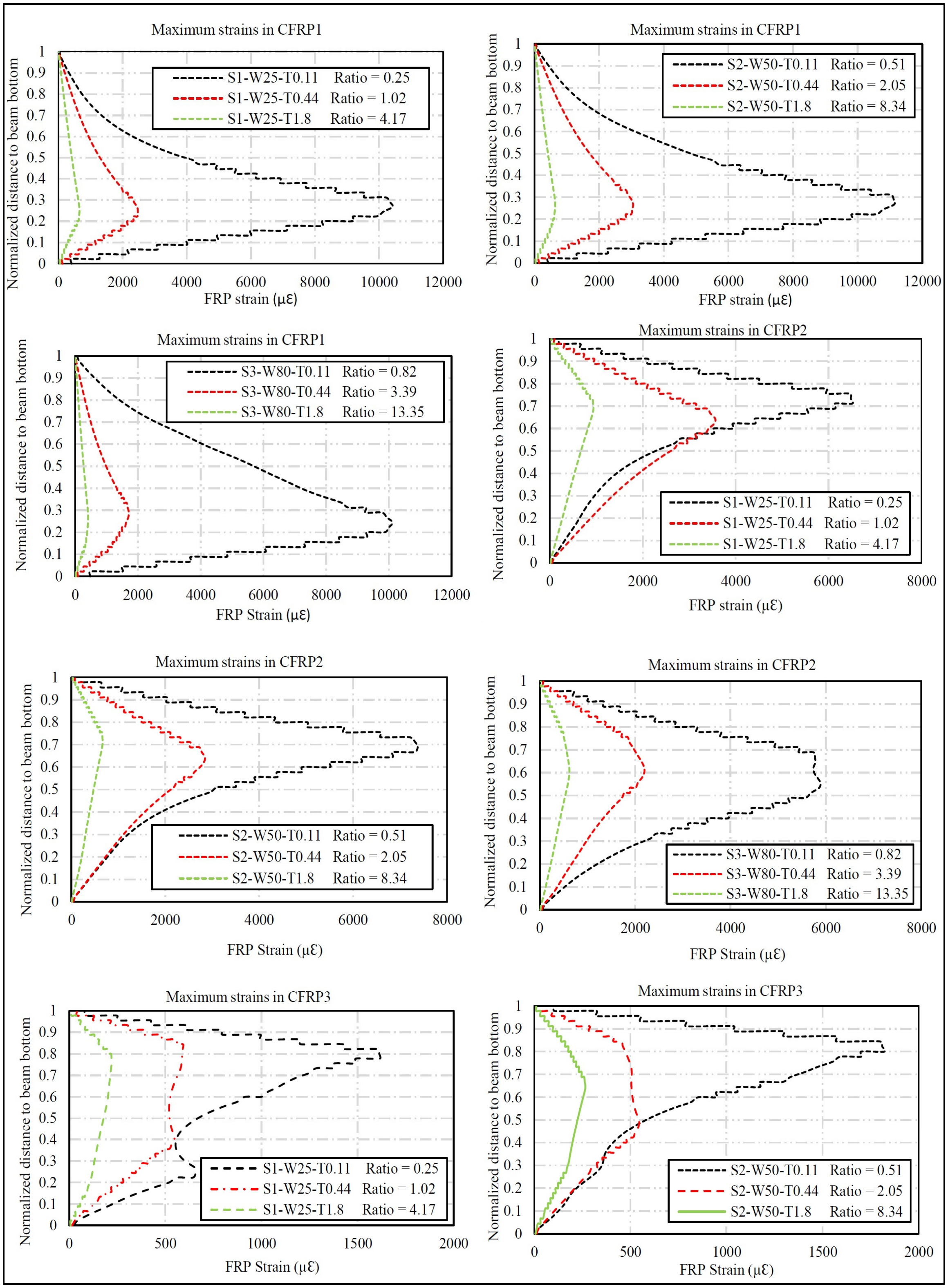

Figure 5.6 Maximum strains profiles among the fibres on CFRP1, CFRP2, and CFRP3 for the studied specimens (µƐ)

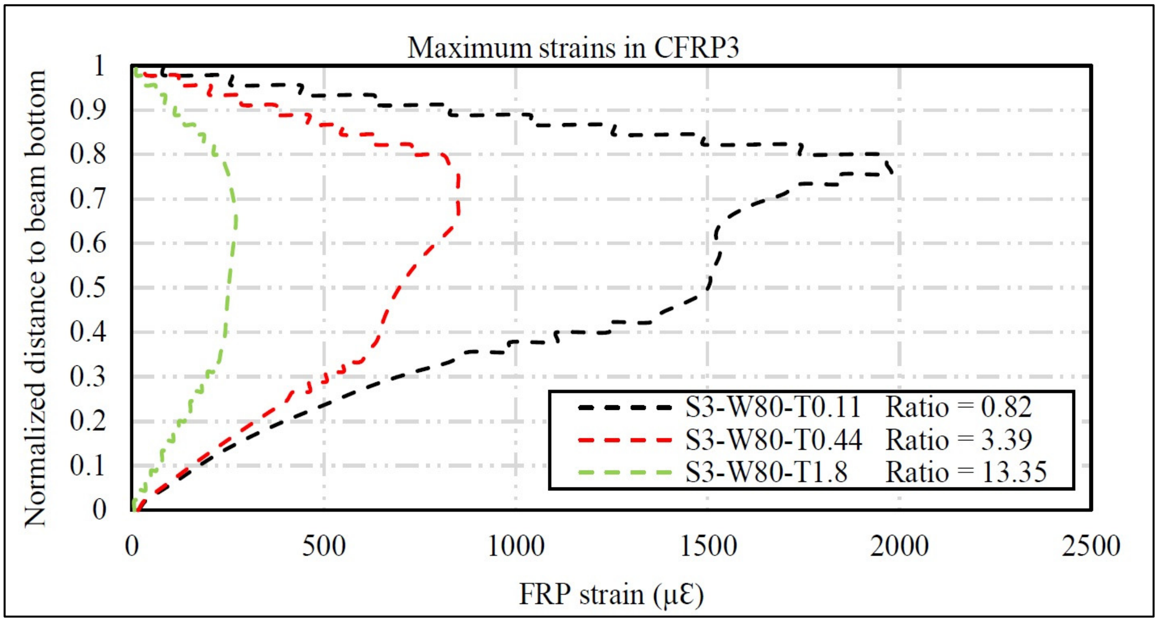

Figure 5.6 Maximum strains profiles among the fibres on CFRP1, CFRP2, and CFRP3 for the studied specimens (με) (Continued)

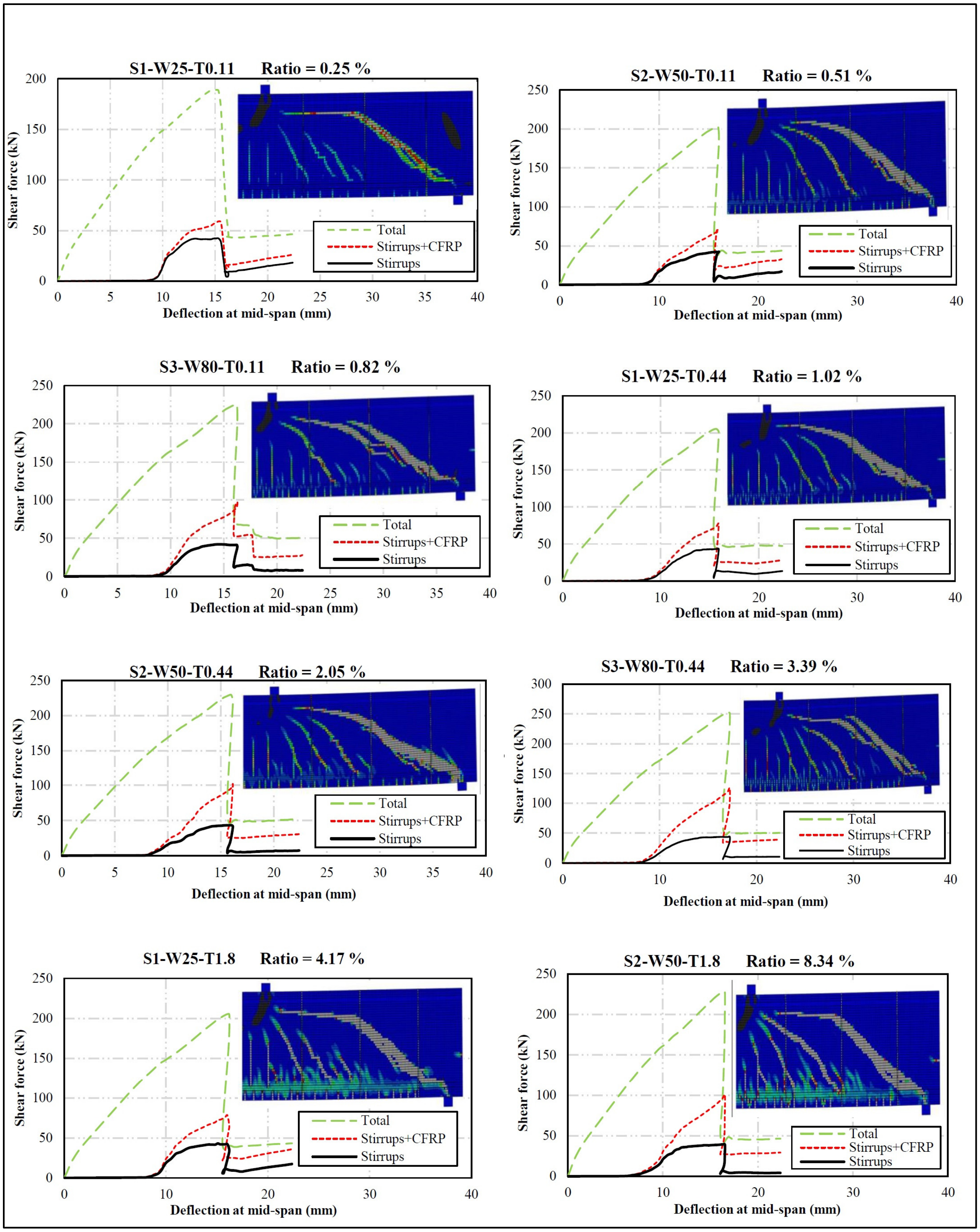

Figure 5.7 (a) Load-midspan deflections versus applied shear forces (kN) curve for the studied beams, steel stirrups, and steel stirrups + EB-CFRPs (b) Proportions of the Contributions for all the components resisting in shear forces (kN) (concretes, steel stirrups, steel stirrups+ EB-CFRPs)

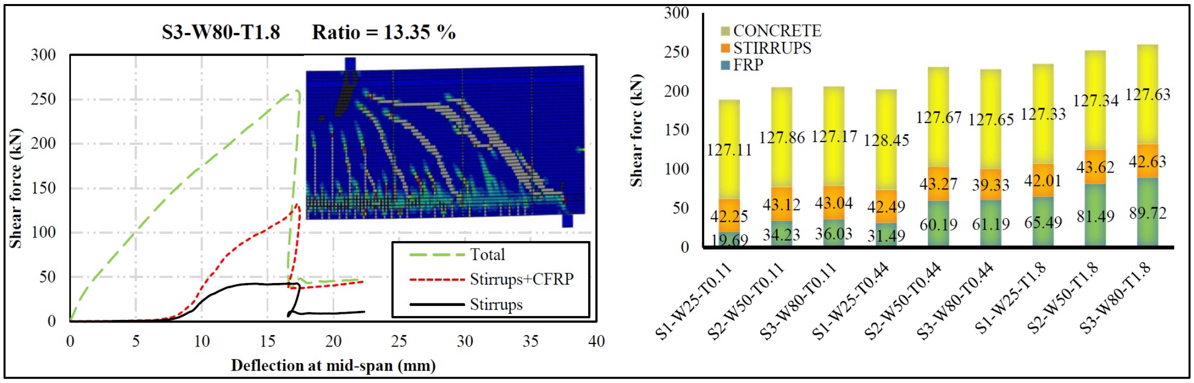

(a) (b)

Figure 5.7 (a) Load-midspan deflections versus applied shear forces (kN) curve for the studied beams, steel stirrups, and steel stirrups + EB-CFRPs (b) Proportions of the Contributions for all the components resisting in shear forces (kN) (concretes, steel stirrups, steel stirrups+ EB-CFRPs) (Continued)

5.7.5.5 Calculating and comparing the effective strains with other guidelines

After evaluating the maximum strains R on all specimens (Table 5.5, Figure 5.8), the distribution factor (D_{FRP}) and the effective strain $\left(\varepsilon_{f,e}\right)$ can be obtained from the model proposed by Guangming Chen (2010). D_{FRP} was calculated based on ε_{max} on the fiber experiencing the most strain among all the fibers and the average strain on the CFRP fibers crossed by major shear cracks before losing its contribution to shear resistance, as follows:

$$D_{FRP} = \frac{\sum_{i=1}^{n} \varepsilon_{FRP,i}}{n\varepsilon_{max}} \tag{5.23}$$

The model proposed by J. Chen and J. Teng (2003) for the shear contribution of EB-FRP is:

$$V_f = 2f_{f,e}t_f w_f \frac{h_{f,e}(\cot\theta + \cot\beta)\sin\beta}{s_f} \tag{5.24}$$

where $f_{f,e}$ is the effective stress on the FRP intercepted by the major shear crack and can be calculated as follows (Chen 2010):

$$f_{f,e} = E_f \varepsilon_{f,e} = E_f \varepsilon_{max} \mathrm{D}_{\mathrm{FRP}} \tag{5.25}$$

The effective strain was calculated for all specimens based on the results recorded from numerical analysis during displacement control. After this, they were compared to the guidelines and the proposed model (Table 5.5, Figure 5.8).

Table 5.5 Effective strains obtained from FEA for CFRPs intercepted by the shear cracks (μƐ)

$\varepsilon_{FRP,e}$						
Specimen	FEA	CAN/CSA-S6-19	CAN/CSA-S806-12	ACI 440.2R-17	*fib*-TG 5.1-19 (2019)	Proposed model
S1-W25-T0.11	6199	4 000	4 000	4 000	15105	5306
S1-W25-T0.44	2205	2400	2400	2400	3776	1975
S1-W25-T1.8	583	1100	1100	1100	931	434
S2-W50-T0.11	6075	4 000	4 000	4 000	15105	4790
S2-W50-T0.44	2188	2400	2400	2400	3776	1878
S2-W50-T1.8	522	1100	1100	1100	931	412
S3-W80-T0.11	5882	4 000	4 000	4 000	15105	4494
S3-W80-T0.44	1645	2400	2400	2400	3776	1762
S3-W80-T1.8	476	1100	1100	1100	931	387

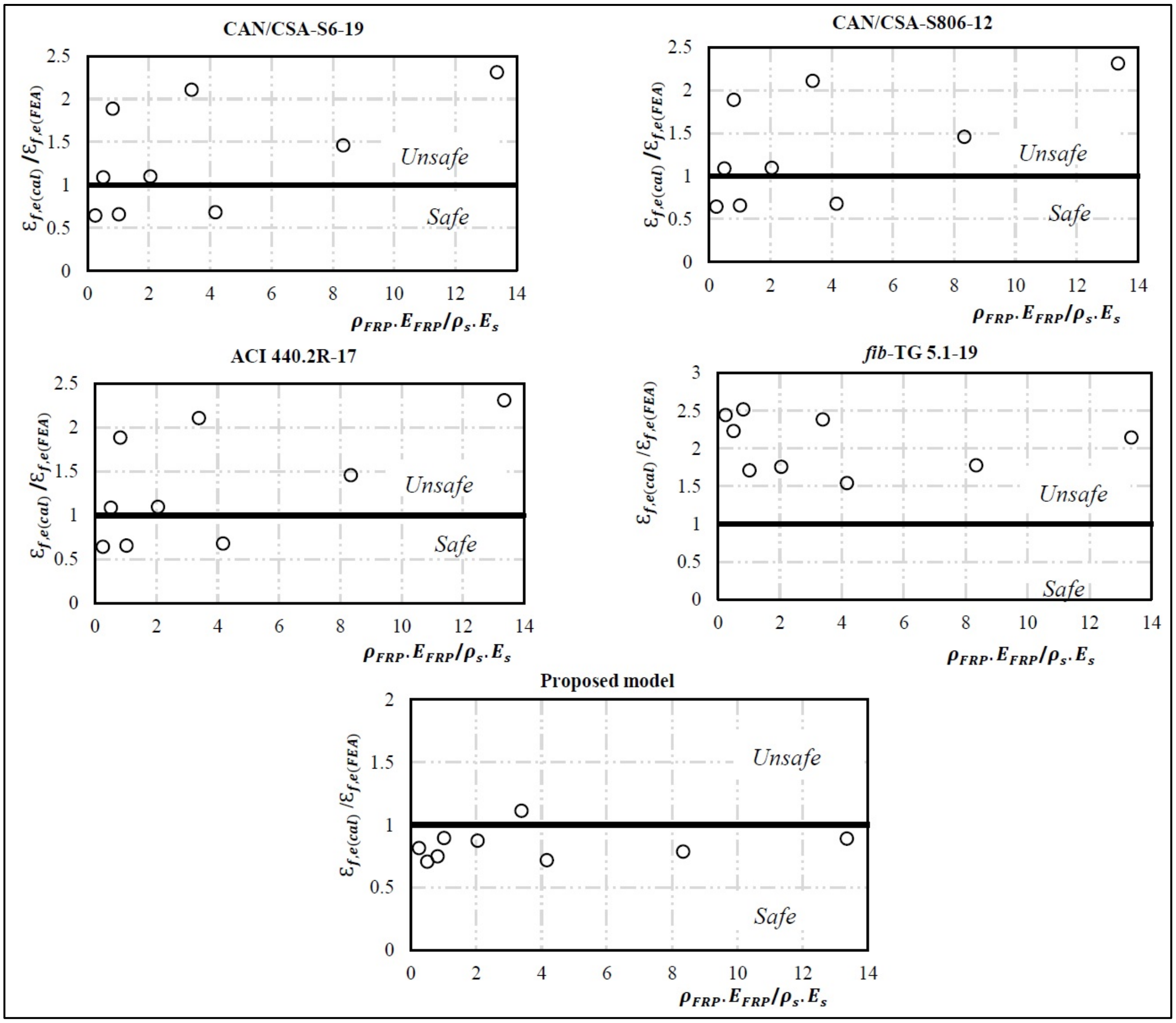

Figure 5.8 Compassion between the effective strains versus ratio of EB CFRPs-to-steel stirrups for the proposed models and the other guidelines

As presented in Table 5.5, the effective strains calculated by the proposed analytical model compared to the CAN/CSA-S6-19, ACI440.2R-17 CAN/CSA-S806-12, CEB-*fib*-TG 5.1-19 (2019) guidelines show higher accuracies for the effective strains obtained from numerical results, proving that the proposed model can be applied to obtain effective strains with high FRP-to-steel stirrup ratio. The maximum strain experienced by EB-CFRP increased slightly just after complete shear failure of the specimens, which was captured by FEA (Figure 5.9b). This might be attributed to the immobilized zones experiencing the strains released from the debonded areas.

Table 5.6 Comparison between the effective strains obtained from FEA versus the existing guidelines (μƐ)

Specimens	Strain on the CFRP stirrups intercepted by shear crack			Distribution factor (D_{FRP})	ε_{max}(μƐ)	Effective strain ($\varepsilon_{FRP,e}$)
	FRP1 (μƐ)	FRP2 (μƐ)	FRP3 (μƐ)			
S1-W25-T0.11 Ratio = 0.25	10478	6505	1614.58	0.5916	10478	6199
S1-W25-T0.44 Ratio = 1.02	2478	3557	590	0.6201	3557	2205
S1-W25-T1.8 Ratio = 4.17	655	937	219	0.6217	937	583
S2-W50-T0.11 Ratio = 0.51	11219	7373	1822	0.5415	11219	6075
S2-W50-T0.44 Ratio = 2.05	3059	2842	545	0.7154	3059	2188
S2-W50-T1.8 Ratio = 8.34	639	665	265	0.7854	665	522
S3-W80-T0.11 Ratio = 0.82	10140	5885	1975	0.5850	10140	5882
S3-W80-T0.44 Ratio = 3.39	1909	2190	851	0.7510	2190	1645
S3-W80 -T1.8 Ratio = 13.35	539	619	271	0.7688	619	476

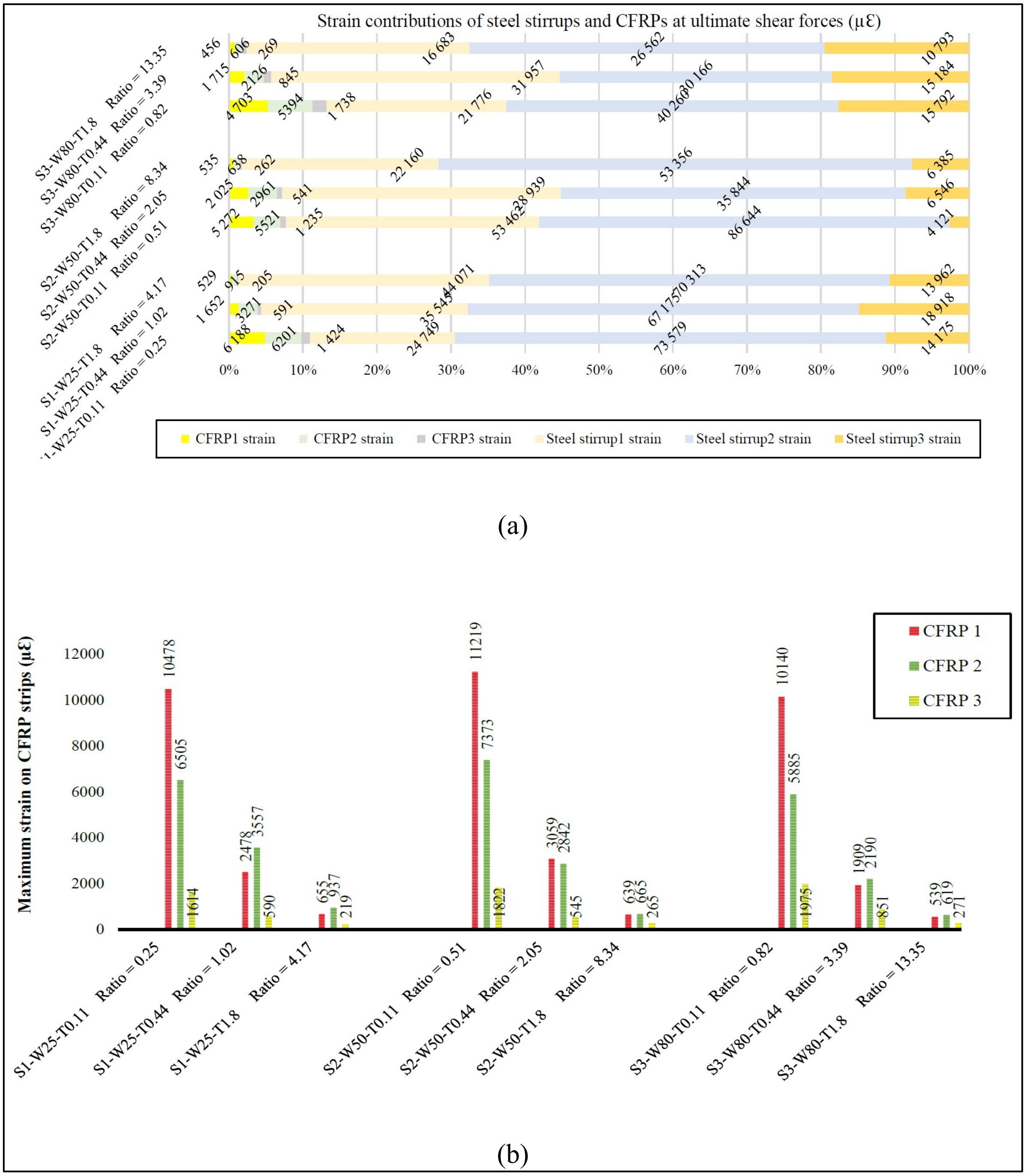

(a)

(b)

Figure 5.9 a) Maximum strains experienced by steel strirrups1,2,3 and CFRP1,2,3 strips at the maximum shear forces for the studied specimens (με) (interactions between steel stirrups and EB CFRPs) b) Maximum strains experienced by CFRP1, 2, 3 strips during the whole process of the loading (after complete failure of the specimens) for the studied specimens (με)

5.7.6 Inverse interaction between EB-CFRP and steel stirrups

The aim of the work described in this section was to develop an analytical model for North American guidelines (CAN/CSA-S6-19, ACI440.2R-17, CAN/CSA-S806-12) based on the results obtained from numerical analysis, which takes into account the inverse interaction between EB-FRP and steel stirrups as their ratio increases. The interaction for each CFRP strip and the corresponding steel stirrup was assessed, and the new effective strain was proposed to replace the existing effective strain in the guidelines. The new effective strain is a function of the ratio of the maximum strain on EB-FRP to that on steel stirrups, the ratio of maximum shear stresses between concrete and steel stirrups and to that between concrete and EB-CFRP, and the EB-FRP-to-steel stirrup ratio to develop analytical models by considering the inverse interaction between steel strips and concrete.

5.7.6.1 Interaction between CFRP1 and steel stirrups1

As shown in Figure 5.10 c, for 25-mm-wide EB-FRP strips, the CFRP starts to contribute to shear resistance when major shear cracks propagate at loads of 128.5 kN, 124.9 kN, and 125 kN for beams R0.25, R1.02, and R4.17 respectively. The ultimate loads of the specimens just before shear failure were 190.9 kN, 196.6 kN, and 205.3 kN, and the strains corresponding to these loads were 6188 µƐ, 1652 µƐ, and 529 µƐ respectively. The corresponding strains on the stirrups were 24749 µƐ, 35545 µƐ, and 44071 µƐ respectively. The strains to which CFRPs1 were subjected were 59%, 66%, and 80% of the maximum strain they experienced just after shear failure of concrete (Table 5.7, Table 5.8, Figure 5.9, and Figure 5.10).

Table 5.7 Comparison between the maximum strains experienced by CFRPs and steel stirrups at the maximum shear forces obtained from FEA (μƐ)

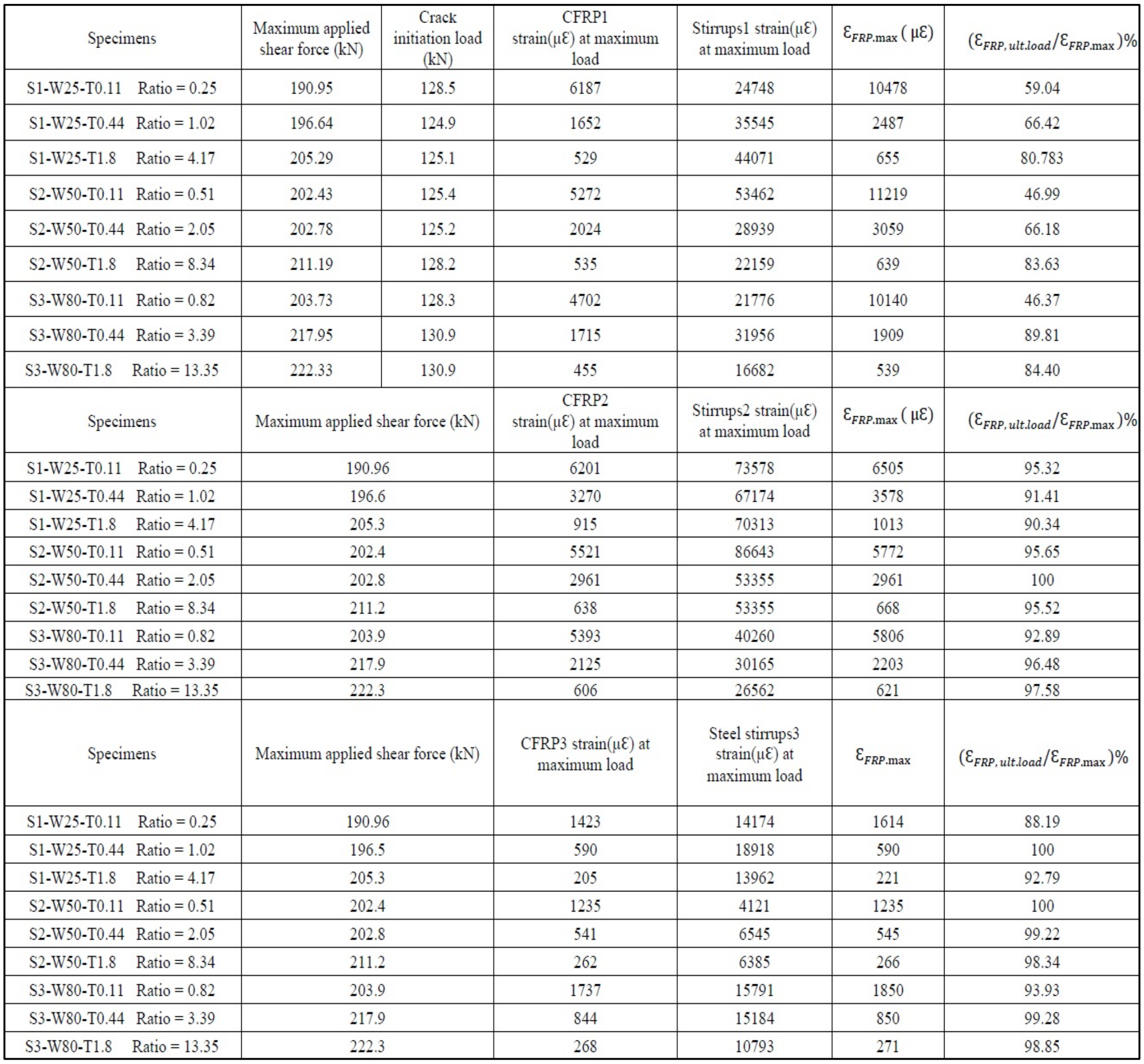

Specimens	Maximum applied shear force (kN)	Crack initiation load (kN)	CFRP1 strain(μƐ) at maximum load	Stirrups1 strain(μƐ) at maximum load	$\varepsilon_{FRP.\max}$ (με)	$(\varepsilon_{FRP,\,ult.load}/\varepsilon_{FRP.\max})\%$
S1-W25-T0.11 Ratio = 0.25	190.95	128.5	6187	24748	10478	59.04
S1-W25-T0.44 Ratio = 1.02	196.64	124.9	1652	35545	2487	66.42
S1-W25-T1.8 Ratio = 4.17	205.29	125.1	529	44071	655	80.783
S2-W50-T0.11 Ratio = 0.51	202.43	125.4	5272	53462	11219	46.99
S2-W50-T0.44 Ratio = 2.05	202.78	125.2	2024	28939	3059	66.18
S2-W50-T1.8 Ratio = 8.34	211.19	128.2	535	22159	639	83.63
S3-W80-T0.11 Ratio = 0.82	203.73	128.3	4702	21776	10140	46.37
S3-W80-T0.44 Ratio = 3.39	217.95	130.9	1715	31956	1909	89.81
S3-W80-T1.8 Ratio = 13.35	222.33	130.9	455	16682	539	84.40
Specimens	Maximum applied shear force (kN)		CFRP2 strain(μƐ) at maximum load	Stirrups2 strain(μƐ) at maximum load	$\varepsilon_{FRP.\max}$ (με)	$(\varepsilon_{FRP,\,ult.load}/\varepsilon_{FRP.\max})\%$
S1-W25-T0.11 Ratio = 0.25	190.96		6201	73578	6505	95.32
S1-W25-T0.44 Ratio = 1.02	196.6		3270	67174	3578	91.41
S1-W25-T1.8 Ratio = 4.17	205.3		915	70313	1013	90.34
S2-W50-T0.11 Ratio = 0.51	202.4		5521	86643	5772	95.65
S2-W50-T0.44 Ratio = 2.05	202.8		2961	53355	2961	100
S2-W50-T1.8 Ratio = 8.34	211.2		638	53355	668	95.52
S3-W80-T0.11 Ratio = 0.82	203.9		5393	40260	5806	92.89
S3-W80-T0.44 Ratio = 3.39	217.9		2125	30165	2203	96.48
S3-W80-T1.8 Ratio = 13.35	222.3		606	26562	621	97.58
Specimens	Maximum applied shear force (kN)		CFRP3 strain(μƐ) at maximum load	Steel stirrups3 strain(μƐ) at maximum load	$\varepsilon_{FRP.\max}$	$(\varepsilon_{FRP,\,ult.load}/\varepsilon_{FRP.\max})\%$
S1-W25-T0.11 Ratio = 0.25	190.96		1423	14174	1614	88.19
S1-W25-T0.44 Ratio = 1.02	196.5		590	18918	590	100
S1-W25-T1.8 Ratio = 4.17	205.3		205	13962	221	92.79
S2-W50-T0.11 Ratio = 0.51	202.4		1235	4121	1235	100
S2-W50-T0.44 Ratio = 2.05	202.8		541	6545	545	99.22
S2-W50-T1.8 Ratio = 8.34	211.2		262	6385	266	98.34
S3-W80-T0.11 Ratio = 0.82	203.9		1737	15791	1850	93.93
S3-W80-T0.44 Ratio = 3.39	217.9		844	15184	850	99.28
S3-W80-T1.8 Ratio = 13.35	222.3		268	10793	271	98.85

Table 5.8 Maximum strains experienced by CFRPs and steel stirrups after failures obtained from FEA (μƐ)

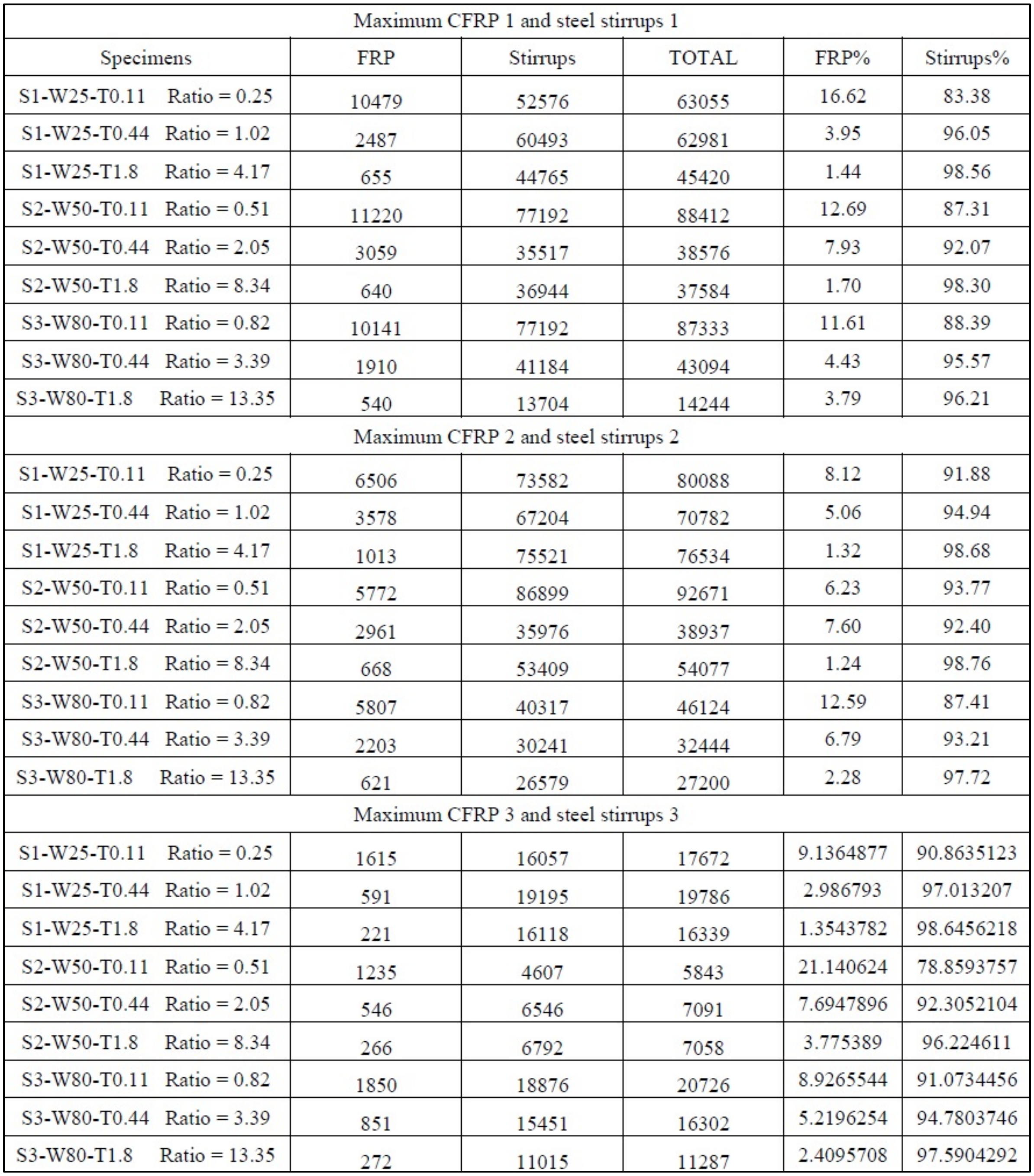

Maximum CFRP 1 and steel stirrups 1					
Specimens	FRP	Stirrups	TOTAL	FRP%	Stirrups%
S1-W25-T0.11 Ratio = 0.25	10479	52576	63055	16.62	83.38
S1-W25-T0.44 Ratio = 1.02	2487	60493	62981	3.95	96.05
S1-W25-T1.8 Ratio = 4.17	655	44765	45420	1.44	98.56
S2-W50-T0.11 Ratio = 0.51	11220	77192	88412	12.69	87.31
S2-W50-T0.44 Ratio = 2.05	3059	35517	38576	7.93	92.07
S2-W50-T1.8 Ratio = 8.34	640	36944	37584	1.70	98.30
S3-W80-T0.11 Ratio = 0.82	10141	77192	87333	11.61	88.39
S3-W80-T0.44 Ratio = 3.39	1910	41184	43094	4.43	95.57
S3-W80-T1.8 Ratio = 13.35	540	13704	14244	3.79	96.21
Maximum CFRP 2 and steel stirrups 2					
S1-W25-T0.11 Ratio = 0.25	6506	73582	80088	8.12	91.88
S1-W25-T0.44 Ratio = 1.02	3578	67204	70782	5.06	94.94
S1-W25-T1.8 Ratio = 4.17	1013	75521	76534	1.32	98.68
S2-W50-T0.11 Ratio = 0.51	5772	86899	92671	6.23	93.77
S2-W50-T0.44 Ratio = 2.05	2961	35976	38937	7.60	92.40
S2-W50-T1.8 Ratio = 8.34	668	53409	54077	1.24	98.76
S3-W80-T0.11 Ratio = 0.82	5807	40317	46124	12.59	87.41
S3-W80-T0.44 Ratio = 3.39	2203	30241	32444	6.79	93.21
S3-W80-T1.8 Ratio = 13.35	621	26579	27200	2.28	97.72
Maximum CFRP 3 and steel stirrups 3					
S1-W25-T0.11 Ratio = 0.25	1615	16057	17672	9.1364877	90.8635123
S1-W25-T0.44 Ratio = 1.02	591	19195	19786	2.986793	97.013207
S1-W25-T1.8 Ratio = 4.17	221	16118	16339	1.3543782	98.6456218
S2-W50-T0.11 Ratio = 0.51	1235	4607	5843	21.140624	78.8593757
S2-W50-T0.44 Ratio = 2.05	546	6546	7091	7.6947896	92.3052104
S2-W50-T1.8 Ratio = 8.34	266	6792	7058	3.775389	96.224611
S3-W80-T0.11 Ratio = 0.82	1850	18876	20726	8.9265544	91.0734456
S3-W80-T0.44 Ratio = 3.39	851	15451	16302	5.2196254	94.7803746
S3-W80-T1.8 Ratio = 13.35	272	11015	11287	2.4095708	97.5904292

Regarding the specimens strengthened with 80-mm-wide strips, by increasing the thickness (from 0.11 to 0.44 and then to 1.8 mm), the strains on the CFRPs1 at the ultimate load-carrying capacities of the beams were 4703 μƐ, 1715 μƐ, and 456 μƐ for specimens R0.82, R3.39, and

R13.35. These strains were 46%, 89%, and 84% of the maximum fiber strains experienced just after complete shear failure. The corresponding maximum stirrup strains were 21776 µƐ, 31957 µƐ, and 16683 µƐ, which were less than the yielding-point strain (51000 µƐ) (Table 5.7, Table 5.8, Figure 5.9, and Figure 5.10). In the CFRPs1, none of the steel stirrups reached the yielding point expected for specimen R0.51 (53462 µƐ).

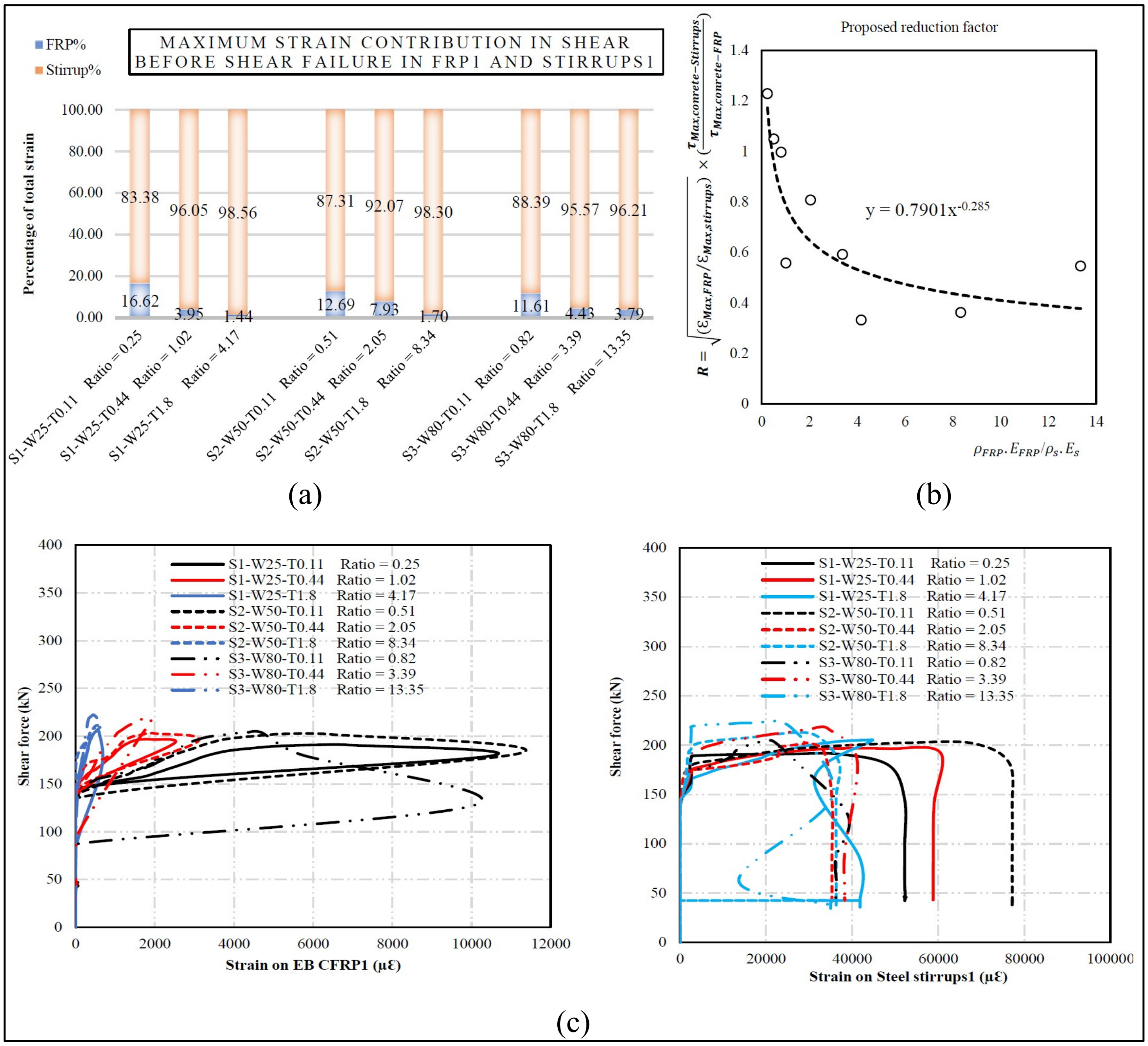

(a)

(b)

(c)

Figure 5.10 Interactions between strirrups1 and CFRP1 based on the maximum strain experience by fibers during the loading process (b) proposed reduction factor versus the ratio of EB CFRPs1-to-steel stirrups1 (c) Applied shear forces versus strains experienced by steel strirrups1 and CFRP1 for the studied specimens

5.7.6.2 Interaction between CFRP2 and steel stirrups2

Compared to the CFRPs1 and the steel stirrups1 specimens, the contribution of steel stirrups was greater in specimens strengthened with 25-mm-wide and 50-mm-wide CFRP strips before shear loss. This was the case because marginal shear cracks crossed a greater number of narrower strips, resulting in less effective bond length. However, unlike the CFRPs1 and steel-stirrups1 specimens, most of the steel stirrups reached their ultimate strain (51000 μƐ). This was due to major shear cracks that crossed the CFRPs2 and the steel stirrups2, intercepted the CFRPs1 and the steel stirrups1 (except for the specimens strengthened with 80-mm-wide strips), and then propagated towards the supports. Another reason may be that the second CFRPs were crossed by marginal shear cracks, which in turn reduced the bond length between concrete and CFRPs, leading to premature debonding and loss of concrete shear resistance because of more distributed shear cracks. Therefore, the greatest contributions to shear resistance were offered by steel stirrups until their yielding points. For specimens strengthened by 25-mm-wide strips, the maximum strains were 6201 μƐ, 3270 μƐ, and 915 μƐ. For specimens R0.25, R1.02, and R4.17, this occurred at an ultimate shear force of 190.9 kN, 196.6 kN, and 205.3 kN respectively. These strains were 95%, 91%, and 90% of the maximum strains on fibers experienced just after shear failure. The corresponding maximum strains recorded on steel stirrups were 73579 μƐ, 67175 μƐ, and 70313 μƐ respectively, indicating that all the steel stirrups had already yielded (Table 5.7, Table 5.8, Figure 5.9, and Figure 5.11).

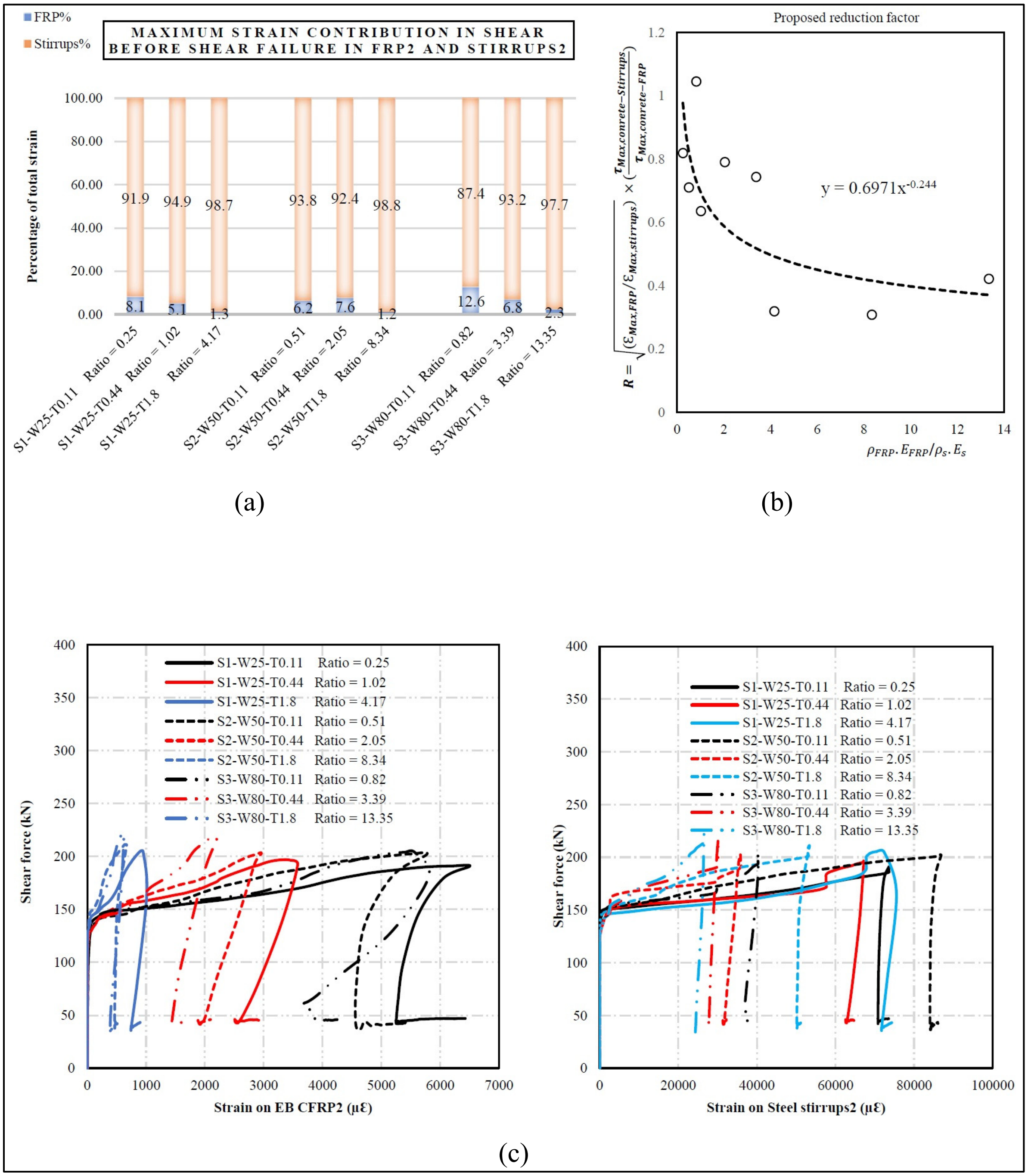

Figure 5.11 Interactions between strirrups2 and CFRs2 based on the maximum strain experience by fibers during the loading process (b) proposed reduction factor versus the ratio of EB CFRPs2-to-steel stirrups2 (c) Applied shear forces versus strains experienced by steel strirrups2 and CFRP2 for the studied specimens

5.7.6.3 Interaction between CFRP3 and steel stirrups3

Even though CFRPs3 and stirrups3, like CFRPs2 and stirrups2, were intercepted by the greatest number of marginal shear cracks with a high R ratio, they experienced less maximum strain than the first and second CFRPs and stirrups (Table 5.7, Table 5.8, Figure 5.9, and Figure 5.12). Regarding the specimens with 80-mm-wide strips (R0.82, R3.39, and R13.35), the maximum strains on the CFRP strips were 1738 µƐ, 845 µƐ, and 269 µƐ, and the corresponding strains on the stirrups were 15792 µƐ, 15184 µƐ, and 10793 µƐ respectively. The associated shear forces for these specimens were 203.8 kN, 217.9 kN, and 222.3 kN respectively. The maximum strains on CFRP3 strips and stirrups3 increased just after shear loss. For example, for the CFRP3 strips, the strains continued to increase until 1975 µƐ, 851 µƐ, and 271 µƐ for specimens R0.82, R3.39, and R13.35 respectively (Table 5.7, Table 5.8, Figure 5.9, and Figure 5.12).

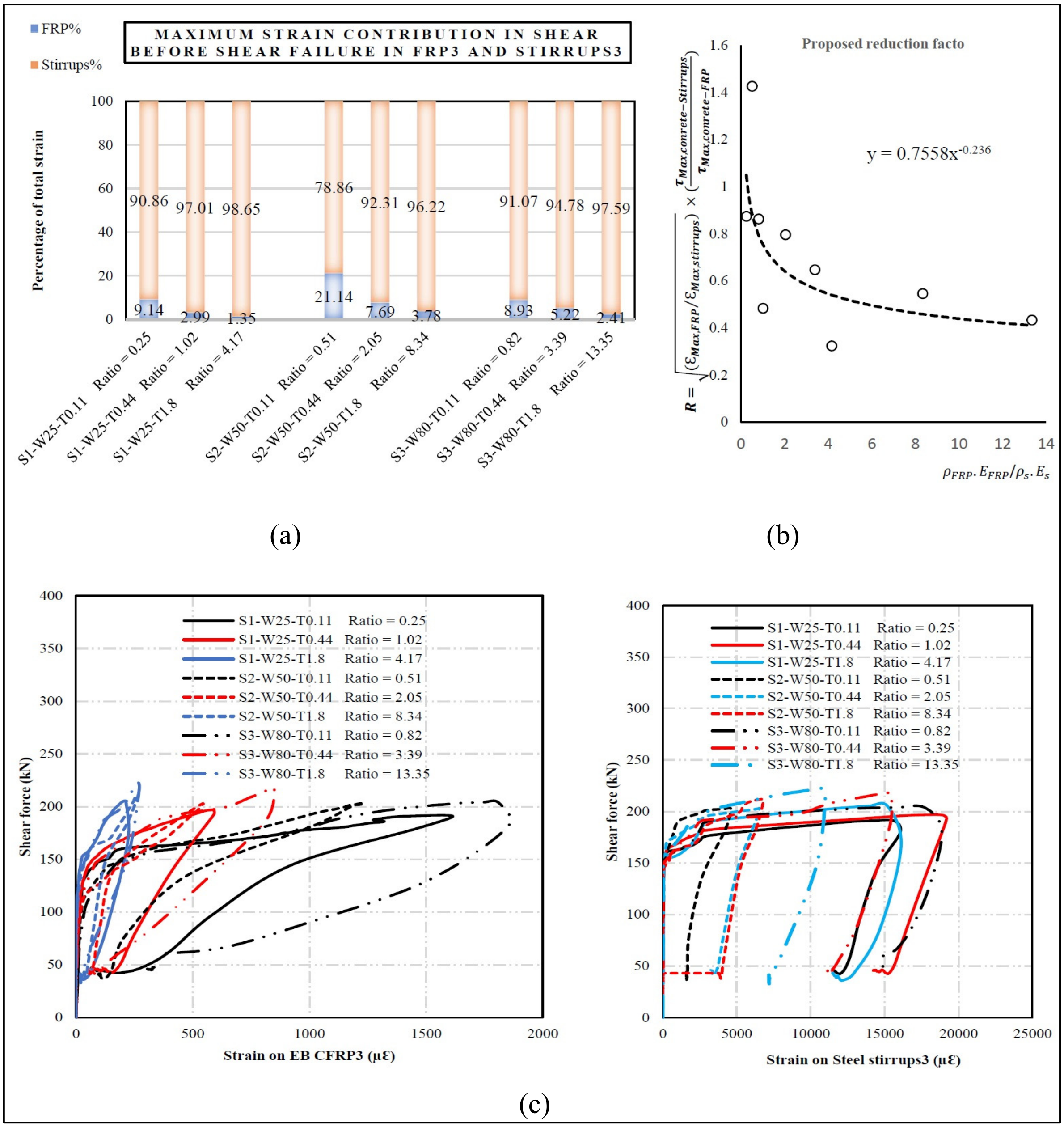

(a)

(b)

(c)

Figure 5.12 Interactions between strirrups3 and CFRs3 based on the maximum strain experience by fibers during the loading process (b) proposed reduction factor versus the ratio of EB CFRPs3-to-steel stirrups3 (c) Applied shear forces versus strains experienced by steel strirrups3 and CFRPs3 for the studied specimens

5.7.6.4 Discussion and evaluation of numerical results

It is obvious that steel stirrups are subjected to the highest strains in specimens with lower FRP-to-steel stirrup ratios. However, this depends on the strip width-to-strip spacing ratio, specifically for stirrups2 and stirrups1. As the ratio (R) increased, the stirrups experienced lower strains. For instance, for specimen R0.51, steel stirrups2 and steel stirrups1 experienced 86,644 μƐ and 53,462 μƐ respectively, but for the same steel stirrups in specimen R13.35, these figures were reduced to 26,562 μƐ and 16,683 μƐ, representing a reduction of 70% and 69% respectively. The same response occurred with EB-CFRPs, which means that when the R ratio was increased, their contributions to shear resistance had a reductive trend such that CFRPs2 and CFRPs1 experienced higher recorded strains. For example, consider specimens R0.51 and R13.35, where the amounts of strain for CFRPs2 and CFRPs1 were reduced from 5521 μƐ and 5272 μƐ to 606 μƐ and 456 μƐ respectively, representing reductions of 90% and 92% (Figure 9). By increasing the FRP-to-steel stirrup ratio, their performance was reduced compared to the lowest ratio (R), proving that an inverse interaction exists between EB-FRPs and steel stirrups. This inverse interaction should be included when calculating effective strain, as proposed in the next section.

5.8 Proposed effective strain

In this part of the paper, a new model is proposed for calculating effective strain for the North American guidelines. This model is a function of maximum shear stress in the bonds between concrete and steel stirrups and between concrete and EB-CFRP, the ratio of maximum strain on EB-CFRPs to that on steel stirrups, the EB-CFRP-to-steel stirrup ratio, and the ultimate strain on EB-CFRPs. The results of the proposed model are compared to CAN/CSA-S6-19, ACI440.2R-17, and CAN/CSA-S806-12 and demonstrate better predictions of the shear contributions of EB-CFRP. As presented in Figure 5.10, Figure 5.11, and Figure 5.12 the reduction factors based on interactions between internal and external reinforcements were obtained from the parametric numerical results based on increasing the EB-CFRP-to-steel stirrup ratio for U-shaped configuration specimens as follows:

$$R_1 = \sqrt{\varepsilon_{Max,FRP}/\varepsilon_{Max,stirrups}} \times \left(\frac{\tau_{Max,bond,concrete-Stirrups}}{\tau_{Max,bond,concrete-FRP}}\right) = 0.7901 \times (\frac{\rho_{FRP}.E_{FRP}}{\rho_s.E_s})^{-0.285}$$

for CFRP1 (5.26)

where $\varepsilon_{Max,FRP}$ and $\varepsilon_{Max,stirrups}$ are the maximum strains experienced by CFRP1 and steel stirrup1 during the whole loading process, even after complete failure of the beams as obtained from the numerical results; $\tau_{Max,bond,concrete-Stirrups}$ is the maximum shear stress on the bond between concrete and steel stirrups as proposed by Telford (1993); and $\tau_{Max,bond,concrete-FRP}$ is the maximum shear stress on the bond between concrete and steel stirrups proposed by Lu et al. (2005). Even though all three reduction factors follow the same trends (Figure 5.10b, Figure 5.11b, and Figure 5.12b), the authors propose Equation 5-26 as a reduction factor because it is less conservative. All North American guidelines limit the effective strain to be less than a portion of the ultimate strain proposed by Priestley et al. (1996):

$$\varepsilon_{f,e} = 0.004 \leq 0.75 \times \varepsilon_{f,u} \tag{5.27}$$

Therefore, to obtain the effective strain, Equation (5.26) should be multiplied by Equation (5.27), which results in:

$$\varepsilon_{f,e} = 0.75 \times \varepsilon_{f,u} \times R_1 = 0.75 \times \varepsilon_{f,u} \times (0.7901) \times \left(\frac{\rho_{FRP}.E_{FRP}}{\rho_s.E_s}\right)^{-0.285} \tag{5.28}$$

However, the maximum ratio (R), $R = (\frac{\rho_{FRP}.E_{FRP}}{\rho_s.E_s})$, should be restricted to 3.4 to let us use Equation 5.28. Otherwise, for $R \geq 3.4$, the following restriction should be used to reach the effective strain:

$$\varepsilon_{f,e} = \begin{Bmatrix} 0.75 \times \varepsilon_{f,u} \times R_1 = 0.75 \times \varepsilon_{f,u} \times (0.7901) \times \left(\frac{\rho_{FRP}.E_{FRP}}{\rho_s.E_s}\right)^{-0.285} & if \;\; 0.1 < R < 3.4 \\ 0.002 \qquad\qquad if & R \geq 3.4 \end{Bmatrix}$$

(5.29)

As presented in Figure 5.13a-c, after replacing the proposed effective strains for nine studied beams with different R ratios, R^2 for the North American codes was enhanced from 0.32, 0.32, and 0.35 to 0.75, 0.75, and 0.75 for all nine specimens respectively.

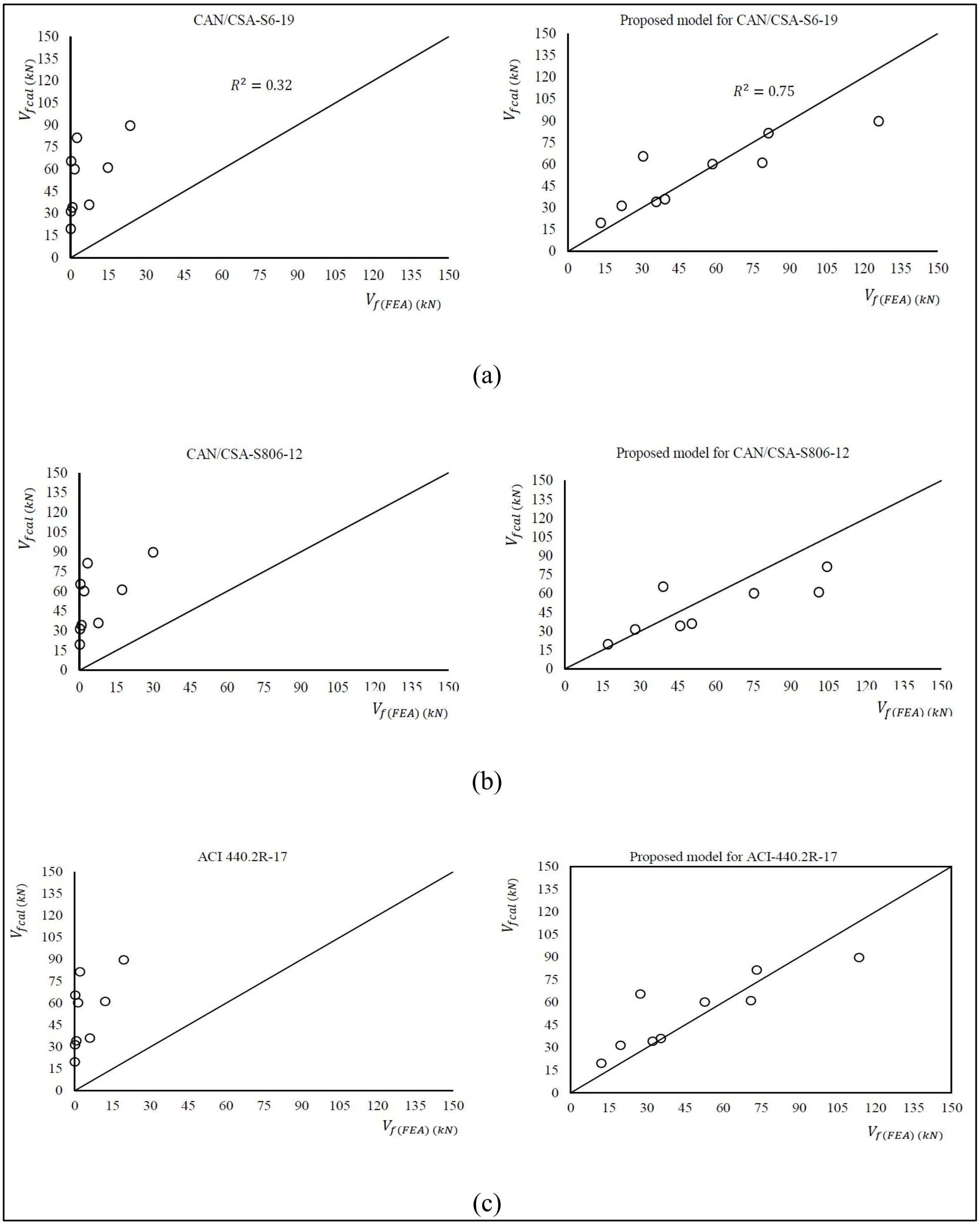

Figure 5.13 Comparison between calculated versus the proposed effective strains obtained from numerical results based on interactions between steel stirrups and CFRPs on the studied specimens for (a) CAN/CSA-S6-19 (b) CAN/CSA-S806-12 (c) ACI 440.2R-17

5.9 Conclusions

This research dealt with the inverse interaction of EB-FRP and steel stirrups for RC beams strengthened in shear with U-shaped configurations. The most applicable guidelines were evaluated and compared with experimental and FE numerical results. Analytical and numerical parametric studies were conducted to evaluate this inverse interaction. Some of the parameters that could not be evaluated from experimental studies were assessed: the contributions of concrete, steel stirrups, and EB-CFRPs to shear resistance; the behavior of interface layers and the strain responses along the fiber direction as obtained from FEA; and the inverse interaction between internal and external reinforcements by increasing the EB-CFRP-to-steel stirrup ratio. The following conclusions can be drawn from the current study:

- A new analytical model is proposed that considers the effect of the inverse interaction between EB-CFRPs and steel stirrups, showing higher accuracy compared to guidelines as the EB-CFRP-to-steel stirrup ratio increases.
- Increasing the ratio of EB-CFRP results in more distributed marginal shear cracks (similarly to increasing the ratio of steel stirrup).
- The areas under the shear stresses versus the distance along the interface layers are larger in specimens with lower EB-FRP-to-steel stirrup ratios. When these ratios are lower, more shear stress can be transferred through the interface layers and obtain more benefit from the potential of the cohesive layers. By increasing the EB-CFRP-to-steel stirrup ratio, shear stresses at the interface layers in the top parts of the main shear cracks do not increase as mid-span deflections increase.
- The effect of the inverse interaction becomes greater as the EB-CFRP-to-steel stirrup ratio increases, resulting in a smaller strain contribution offered by the steel stirrups and EB-CFRPs.
- Based on the parametric numerical results and the interaction between EB-CFRPs and steel stirrups, a reduction factor and an effective strain are proposed and compared with North American guidelines, demonstrating higher accuracy than the conservative effective strains proposed by the guidelines.

- An upper limit is proposed (0.002) for strains with higher EB CFRP-to-steel stirrup ratios ($R \geq 3.4$). Further investigations are needed based on more extensive data to enhance the effective strain based on the inverse interaction between EB-CFRPs and steel stirrups.

5.10 Data Availability Statement

Some or all data, models, or code that support the findings of this study are available from the corresponding author upon reasonable request.

5.11 Acknowledgments

The financial support of the Natural Sciences and Engineering Research Council of Canada (NSERC) and the Fonds de Recherche du Québec – Nature et Technologie (FRQnt) through operating grants is gratefully acknowledged.

CONCLUSIONS

Based on the objectives outlined in this research study, the following conclusions were achieved, highlighting both the advancements made and areas where further research may be needed:

1. Development of a Comprehensive Model:

The primary goal of the research was to propose a new model for the shear resistance of RC beams strengthened with EB-FRP plates/sheets. The study successfully developed advanced numerical and analytical models that consider various failure modes in shear and encompass U-shape schemes for shear strengthening of RC beams. This comprehensive model addresses the existing gap in the literature and serves as a valuable addition to the current state-of-the-art.

2. Thorough Study of FRP-RC Interaction:

The interaction between FRP sheets and plates employed for shear strengthening was thoroughly investigated using advanced finite element (FE) methods. This involved assessing the interaction between FRP composites and concrete, as well as the inverse interaction between EB-FRP and steel stirrups. The study contributes to a better understanding of the behavior of the interface layer, which has been a major challenge affecting the performance of FRP-strengthened RC beams.

3. Parametric Numerical Analysis:

Parametric numerical analyses were conducted to evaluate the inverse interaction between EB-FRP and steel stirrups. The study explored the influence of varying ratios of external shear reinforcement (EB-FRP) to internal shear reinforcement (steel stirrups) on the stress transferred through the bond between concrete and EB-FRP. This analysis enhances our understanding of the factors affecting the overall performance of the strengthened beams.

4. Consideration of Influencing Factors:

Various influencing factors, such as fracture mechanics of concrete, dimensions, configuration of FRP composites, and interactions between beam components, were taken into account. The study aimed to determine the effect of these factors on the behavior of the interface layer and, consequently, on the ultimate load-carrying capacity of beams.

5. Development of New Design Approaches:

The research proposed new theoretical and mathematical approaches to replace current design models in codes and standards. These approaches consider the complex interactions and influencing factors studied in the research, providing a more accurate representation of the behavior of FRP-strengthened RC beams. The intention is to enhance current design practices and offer a comprehensive design method for practicing engineers.

6. Enhancements to Design Codes:

It is projected that the proposed approaches will contribute to the enhancement of current design models in North American codes and standards. By considering a broader range of parameters and factors, the updated codes will provide more reliable guidelines for the design of RC beams strengthened in shear with EB-FRP.

7. Consideration of Size Effect:

The study addressed the size effect on the contribution of EB-FRP, taking into account interfacial shear stress and strain profile along the direction of fibers. This consideration provides valuable insights into how the size of the structure influences the effectiveness of EB-FRP in shear strengthening.

In conclusion, the research has made significant strides in advancing the understanding and design methodologies related to shear strengthening of RC beams with EB-FRP. While substantial progress has been achieved, the study also highlights the complexity of the interactions involved, suggesting avenues for future research to further refine and expand upon the proposed models.

RECOMMENDATIONS

This study represents progress in simulating FRP shear-strengthened beams and contributes to a deeper comprehension of their behavior. However, based on the results of the numerical analyses, additional research is warranted. Here are some suggestions for future investigations:

1. To assess the interaction between concrete and EB-FRP near significant shear cracks comprehensively, it is essential to conduct three-dimensional simulations. These simulations will enable the evaluation of the debonding process, which can, in turn, inform the calculation of effective bond length and height.

2. The differentiation should be considered between full-wrap and strips schemes for U-shape configurations to obtain precise effective strains, allowing to evaluate the impact of optimized strips length to those of width. Therefore, this ratio should be incorporated to reach the precise effective strain for U-shape strips and Fully U-wraps configurations.

3. The evaluation of the impact of strip length to strip width in U-shaped strip configurations in proportion to the thickness of EB-FRP needs to be performed to achieve accurate effective strains. This allows for the assessment of how the optimized length-to-width ratio based on the EB-FRP thickness impacts the results. Consequently, this ratio should be integrated to obtain precise effective strains for both U-shaped strips.

4. It is important to consider the effect of strip length-to-width ratio in U-shaped strip configurations to obtain precise effective strains. This assessment allows for an understanding of how the optimized length-to-width ratio of the strips influences the outcomes. Therefore, incorporating this ratio is essential to determine precise effective strains for U-shaped strips.

5. More simulations and parametric studies are recommended to evaluate the size effect and inverse interaction between EB-FRP and steel stirrups on shear contribution of EB-FRP to

capture more reliable results of the real-life behavior of structures retrofitted with EB-FRP systems without the need for the time consuming and costly experiments.

LIST OF BIBLIOGRAPHICAL REFERENCES

318, A. (1963). *Building code requirements for reinforced concrete (ACI 318-63).*

Abaqus, G. (2011). Abaqus 6.11. *Dassault Systemes Simulia Corporation, Providence, RI, USA*, 3.

Abbasi, A., Benzeguir, Z. E. A., Chaallal, O., & El-Saikaly, G. (2022). FE modelling and simulation of the size effect of RC T-beams strengthened in shear with externally bonded FRP fabrics. *Journal of Composites Science, 6*(4), 116.

Abbasi, A., Chaallal, O., & El-Saikaly, G. (2022). Shear strengthening of RC beams with FRP composites: Database of FE simulations and analysis of studied parameters. *Modelling and Simulation in Engineering, 2022*, 1-27.

ACI440.2R-17. Guide for the design and construction of externally bonded FRP systems for strengthening concrete structures (ACI 440.2 R-17). *American Concrete Institute, Farmington Hills, MI.*

Al-Mahaidi, R., Lee, K., & Taplin, G. (2001). Behavior and analysis of RC T-beams partially damaged in shear and repaired with CFRP laminates. In *Structures 2001: A Structural Engineering Odyssey* (pp. 1-8).

Al Jawahery, M. S., Gulsan, M. E., Albegmprli, H. M., Mansoori, I. A. H., & Cevik, A. (2019). Experimental investigation of rehabilitated RC haunched beams via CFRP with 3D-FE modeling analysis. *Engineering structures, 196*, 109301.

Amir, M. (1998). Analytical Study of Reinforced Concrete Beams Strengthened with Web-Bonded Fiber Reinforced Plastic Plates or Fabrics. *ACI structural journal, 95*(3), 12-16.

Arduini, M., Di Tommaso, A., & Nanni, A. (1997). Brittle failure in FRP plate and sheet bonded beams. *ACI structural journal, 94*(4), 363-370.

Bažant, Z. P., & Becq-Giraudon, E. (2002). Statistical prediction of fracture parameters of concrete and implications for choice of testing standard. *Cement and concrete research, 32*(4), 529-556.

Bazant, Z. P., & Kazemi, M. T. (1991). Size effect on diagonal shear failure of beams without stirrups. *ACI structural journal, 88*(3), 268-276.

Bazant, Z. P., & Planas, J. (1997). *Fracture and size effect in concrete and other quasibrittle materials* (Vol. 16): CRC press.

Benzeguir, Z. E. A., El-Saikaly, G., & Chaallal, O. (2017). Size effect in shear of conventional and shear-strengthened RC beams with EB-FRP: State of knowledge and research needs. *Global Journal of Advanced Engineering Technologies and Sciences, 4*(11), 1-23.

Benzeguir, Z. E. A., El-Saikaly, G., & Chaallal, O. (2019). Size effect in RC T-beams strengthened in shear with externally bonded CFRP sheets: Experimental study. *Journal of Composites for Construction, 23*(6), 04019048.

Bousselham, A., & Chaallal, O. (2004). Shear strengthening reinforced concrete beams with fiber-reinforced polymer: Assessment of influencing parameters and required research. *Structural Journal, 101*(2), 219-227.

Carolin, A., & Täljsten, B. (2005). Theoretical study of strengthening for increased shear bearing capacity. *Journal of Composites for Construction, 9*(6), 497-506.

Chaallal, O., Nollet, M.-J., & Perraton, D. (1998). Shear strengthening of RC beams by externally bonded side CFRP strips. *Journal of Composites for Construction, 2*(2), 111-113.

Chaallal, O., Shahawy, M., & Hassan, M. (2002). Performance of reinforced concrete T-girders strengthened in shear with carbon fiber-reinforced polymer fabric. *Structural Journal, 99*(3), 335-343.

Chen, G. (2010). *Behaviour and strength of RC beams shear-strengthened with externally bonded FRP reinforcement.* The Hong Kong Polytechnic University,

Chen, G., Chen, J., & Teng, J. (2012). On the finite element modelling of RC beams shear-strengthened with FRP. *Construction and Building Materials, 32*, 13-26.

Chen, G., Li, S., Zhang, S., Chen, J., & Teng, J. (2013). Numerical study on interaction between steel stirrups and shear-strengthening NSM FRP strips in RC beams.

Chen, G., Teng, J., & Chen, J. (2010). RC beams shear-strengthened with FRP: shear resistance contributed by FRP. *Magazine of Concrete Research, 62*(4), 301-311.

Chen, G., Teng, J., Chen, J., & Rosenboom, O. (2010). Interaction between steel stirrups and shear-strengthening FRP strips in RC beams. *Journal of Composites for Construction, 14*(5), 498-509.

Chen, G., Teng, J., Chen, J., & Xiao, Q. (2015). Finite element modeling of debonding failures in FRP-strengthened RC beams: A dynamic approach. *Computers & Structures, 158*, 167-183.

Chen, J.-F., & Teng, J. (2003). Shear capacity of FRP-strengthened RC beams: FRP debonding. *Construction and Building Materials, 17*(1), 27-41.

Chen, J., & Teng, J. (2003). Shear capacity of fiber-reinforced polymer-strengthened reinforced concrete beams: Fiber reinforced polymer rupture. *Journal of Structural Engineering, 129*(5), 615-625.

Chen, J. F., & Teng, J. (2001). Anchorage strength models for FRP and steel plates bonded to concrete. *Journal of Structural Engineering, 127*(7), 784-791.

Chen, J. F., & Teng, J. (2003). Shear capacity of fiber-reinforced polymer-strengthened reinforced concrete beams: Fiber reinforced polymer rupture. *Journal of Structural Engineering, 129*(5), 615-625.

Code, M. (1993). CEB-FIP model code 1990. *Bulletin d'information*(1996).

Collins, M. P., & Kuchma, D. (1999). How safe are our large, lightly reinforced concrete beams, slabs, and footings? *Structural Journal, 96*(4), 482-490.

Dai, J., & Ueda, T. (2003). Local bond stress slip relations for FRP sheets-concrete interfaces. In *Fibre-Reinforced Polymer Reinforcement for Concrete Structures: (In 2 Volumes)* (pp. 143-152): World Scientific.

Dirar, S., Lees, J. M., & Morley, C. (2012). Phased nonlinear finite-element analysis of precracked RC T-beams repaired in shear with CFRP sheets. *Journal of Composites for Construction, 17*(4), 476-487.

El-Saikaly, G. (2015). *Évaluation du comportement en fatigue des poutres en béton armé renforcées à l'effort tranchant à l'aide de polymères renforcés de fibres.* École de technologie supérieure,

Elyasian, I., Abdoli, N., & ROUNAGH, H. (2006). Evaluation of parameters effective in FRP shear strengthening of RC beams using FE method.

Engineers, J. S. o. C. (2001). Recommendations for upgrading of concrete structures with use of continuous fiber sheets. *JSCE Concr. Eng. Ser, 41*, 31-34.

Fang, C., Guo, X., Li, J., & Chen, G. (2023). Relations of Microstructural Attributes and Strength-Ductility of Zirconium Alloys with Hydrides. *Chinese Journal of Mechanical Engineering, 36*(1), 89.

Godat, A. (2008). *Finite element modelling of externally shear-strengthened beams using fibre reinforced polymers* (Vol. 69).

Godat, A., Chaallal, O., & Neale, K. W. (2013). Nonlinear finite element models for the embedded through-section FRP shear-strengthening method. *Computers & Structures, 119*, 12-22.

Godat, A., Labossière, P., & Neale, K. (2008). *Numerical prediction of shear crack angles for FRP shear-strengthened concrete beams.* Paper presented at the 4th International conference on FRP composites in civil engineering (CICE2008), Zurich, Switzerland.

Godat, A., Labossière, P., & Neale, K. (2012). Numerical investigation of the parameters influencing the behaviour of FRP shear-strengthened beams. *Construction and Building Materials, 32*, 90-98.

Godat, A., Labossière, P., Neale, K. W., & Chaallal, O. (2012). Behavior of RC members strengthened in shear with EB FRP: Assessment of models and FE simulation approaches. *Computers & Structures, 92*, 269-282.

Godat, A., Neale, K. W., & Labossière, P. (2007). Numerical modeling of FRP shear-strengthened reinforced concrete beams. *Journal of Composites for Construction, 11*(6), 640-649.

Godat, A., Qu, Z., Lu, X., Labossiere, P., Ye, L., & Neale, K. W. (2010). Size effects for reinforced concrete beams strengthened in shear with CFRP strips. *Journal of Composites for Construction, 14*(3), 260-271.

Guo, Z., Cao, S., Sun, W., & Lin, X. (2005). *Experimental study on bond stress-slip behaviour between FRP sheets and concrete.* Paper presented at the FRP in construction, proceedings of the international symposium on bond behaviour of FRP in structures.

Harper, P. W., & Hallett, S. R. (2010). A fatigue degradation law for cohesive interface elements–development and application to composite materials. *International Journal of Fatigue, 32*(11), 1774-1787.

Hii, A. K. Y. (2006). *Torsional strengthening of reinforced concrete members using carbon fibre reinforced polymer composites.* Monash University,

Hokelekli, E., & Yilmaz, B. N. (2019). Effect of cohesive contact of backfill with arch and spandrel walls of a historical masonry arch bridge on seismic response. *Periodica Polytechnica Civil Engineering, 63*(3), 926-937.

Hordijk, D. (1991). Local approach to fatigue of concrete, PhD thesis, Delft University of Technology, 1991.

Ibars, E. O., Ferreira, D., Bernat, A. M., & García, J. M. B. (2018). Numerical analysis of reinforced concrete beams strengthened in shear by externally bonded (EB) fibre reinforced polymer (FRP) sheets. *Hormigón y acero, 69*(285), 113-120.

Imperatore, S., Lavorato, D., Nuti, C., Santini, S., & Sguerri, L. (2012). *Numerical modeling of existing RC beams strengthened in shear with FRP U-sheets.* Paper presented at the Proceedings of the 6th International Conference on FRP Composites in Civil Engineering—CICE2012, Rome, Italy.

Jin, L., Xia, H., Xuan-ang, J., & Du, X. (2020). Size effect on shear failure of CFRP-strengthened concrete beams without web reinforcement: Meso-scale simulation and formulation. *Composite Structures*, 111895.

Kachlakev, D. I., Miller, T. H., Potisuk, T., Yim, S. C., & Chansawat, K. (2001). *Finite element modeling of reinforced concrete structures strengthened with FRP laminates*. Retrieved from

Kaliakin, V. N., Chajes, M. J., & Januszka, T. F. (1996). Analysis of concrete beams reinforced with externally bonded woven composite fabrics. *Composites Part B: Engineering, 27*(3-4), 235-244.

Kani, G. N. J. (1967). *How safe are our large reinforced concrete beams?* Paper presented at the Journal Proceedings.

Khalifa, A., Gold, W. J., Nanni, A., & MI, A. A. (1998). Contribution of externally bonded FRP to shear capacity of RC flexural members. *Journal of Composites for Construction, 2*(4), 195-202.

Kolanu, N. R., Raju, G., & Ramji, M. (2020). A unified numerical approach for the simulation of intra and inter laminar damage evolution in stiffened CFRP panels under compression. *Composites Part B: Engineering, 190*, 107931.

Lee, H.-K., Ha, S.-K., & Afzal, M. (2008). Finite element analysis of shear-deficient RC beams strengthened with CFRP strips/sheets. *Structural Engineering and Mechanics, 30*(2), 247-261.

Lee, J., & Fenves, G. L. (1998). Plastic-damage model for cyclic loading of concrete structures. *Journal of engineering mechanics, 124*(8), 892-900.

Lee, T. K. (2003). *Shear strength of reinforced concrete T-beams strengthened using carbon fibre reinforced polymer (CFRP) laminates.* Monash University,

Lee, T. K., Al-Mahaidi, R. S. H., & Taplin, G. R. (2000). *Non-linear finite element modelling of shear-damaged concrete T-beams repaired with CFRP laminates.* Paper presented at the ACUN-2 Int. Composites Conference.

Liotta, M. (2006). FRP Shear Strengthening in Shear Tests and Design Equations, Department of Struct Engineering & Geotechnology. *University Roma La Sapienza, Rome*.

Lu, X., Chen, J., Ye, L., Teng, J., & Rotter, J. (2009). RC beams shear-strengthened with FRP: Stress distributions in the FRP reinforcement. *Construction and Building Materials, 23*(4), 1544-1554.

Lu, X., Teng, J., Ye, L., & Jiang, J. (2005). Bond–slip models for FRP sheets/plates bonded to concrete. *Engineering structures, 27*(6), 920-937.

Lubliner, J., Oliver, J., Oller, S., & Onate, E. (1989). A plastic-damage model for concrete. *International Journal of Solids and Structures, 25*(3), 299-326.

Lubliner, J., Oliver, J., Oller, S., & Oñate, E. (1989). A plastic-damage model for concrete. *International Journal of Solids and Structures, 25*(3), 299-326.

Maeda, T. (1997). A study on bond mechanism of carbon fiber sheet. *FRPTCS3, 1*, 279-286.

Manos, G., Theofanous, M., & Katakalos, K. (2014). Numerical simulation of the shear behaviour of reinforced concrete rectangular beam specimens with or without FRP-strip shear reinforcement. *Advances in Engineering Software, 67*, 47-56.

Matthys, S. (2000). *Structural behaviour and design of concrete members strengthened with externally bonded FRP reinforcement.* Ghent University,

Matthys, S., & Group, f. W. (2019). *Externally applied FRP reinforcement for concrete structures* (Vol. 90): International Federation for Structural Concrete.

Mirza, S. A., MacGregor, J. G., & Hatzinikolas, M. (1979). Statistical descriptions of strength of concrete. *Journal of the Structural Division, 105*(6), 1021-1037.

Mofidi, A., & Chaallal, O. (2010). Shear strengthening of RC beams with EB FRP: Influencing factors and conceptual debonding model. *Journal of Composites for Construction, 15*(1), 62-74.

Monti, G. (2007). Tests and design equations for FRP-strengthening in shear. *Construction and Building Materials, 21*(4), 799-809.

Monti, G., Renzelli, M., & Luciani, P. (2003). FRP adhesion in uncracked and cracked concrete zones. In *Fibre-Reinforced Polymer Reinforcement for Concrete Structures: (In 2 Volumes)* (pp. 183-192): World Scientific.

Monti, G., Santinelli, F., & Liotta, M. A. (2004). *Mechanics of FRP shear strengthening of RC beams.* Paper presented at the Proc. ECCM.

Nakaba, K., Kanakubo, T., Furuta, T., & Yoshizawa, H. (2001). Bond behavior between fiber-reinforced polymer laminates and concrete. *Structural Journal, 98*(3), 359-367.

Neubauer, U., & Rostasy, F. (1997). *Design aspects of concrete structures strengthened with externally bonded CFRP-plates.* Paper presented at the PROCEEDINGS OF THE SEVENTH INTERNATIONAL CONFERENCE ON STRUCTURAL FAULTS AND REPAIR, 8 JULY 1997. VOLUME 2: CONCRETE AND COMPOSITES.

Obaidat, Y. T., Heyden, S., & Dahlblom, O. (2010). FEM study on the effect of CFRP stiffness and width on retrofitted reinforced concrete beam behaviour. *STRUCTURAL RETROFITTING OF REINFORCED CONCRETE BEAMS USING CARBON FIBRE REINFORCED POLYMER*, 57.

Parvin, A., & Syed Shah, T. (2016). Fiber reinforced polymer strengthening of structures by near-surface mounting method. *Polymers, 8*(8), 298.

Pellegrino, C., & Modena, C. (2002). Fiber reinforced polymer shear strengthening of reinforced concrete beams with transverse steel reinforcement. *Journal of Composites for Construction, 6*(2), 104-111.

Priestley, M. N., Seible, F., & Calvi, G. M. (1996). *Seismic design and retrofit of bridges*: John Wiley & Sons.

Qapo, M., Dirar, S., & Jemaa, Y. (2016). Finite element parametric study of reinforced concrete beams shear-strengthened with embedded FRP bars. *Composite Structures, 149*, 93-105.

Qapo, M., Dirar, S., Yang, J., & Elshafie, M. Z. (2015). Nonlinear finite element modelling and parametric study of CFRP shear-strengthened prestressed concrete girders. *Construction and Building Materials, 76*, 245-255.

Qu, Z., Lu, X.-Z., Ye, L.-P., Chen, J.-F., & Rotter, J. M. (2006). *Numerical modeling of FRP shear strengthened RC beams using compression field theory.* Paper presented at the Proceedings, third international conference on FRP composites in civil engineering (CICE 2006), Miami, Florida, USA.

Roberts, T. (1989). Approximate analysis of shear and normal stress concentrates in the adhesive layer of Plated RC Beams. *The structural engineer, 67*, 222-233.

Rots, J. G. (1988). Computational modeling of concrete fracture.

Rozylo, P. (2021). Failure analysis of thin-walled composite structures using independent advanced damage models. *Composite Structures, 262*, 113598.

Saenz, L. P. (1964). discussion of" Equation for the Stress-Strain Curve of Concrete" by Desayi and Krishnan. *Journal of the American Concrete Institute, 61*, 1229-1235.

Samb, N., El-Saikaly, G., & Chaallal, O. (2020). Effet de la rigidité, du taux du polymère renforcé de fibres (PRF) et de l'armature transversale interne sur la contribution à la résistance à l'effort tranchant d'un renfort en PRF collé en surface: état de l'art et besoins en recherche. *Canadian Journal of Civil Engineering, 47*(11), 1276-1296.

Santhakumar, R., Chandrasekaran, E., & Dhanaraj, R. (2004). Analysis of retrofitted reinforced concrete shear beams using carbon fiber composites. *Electronic Journal of structural engineering, 4*(1), 66-74.

Savoia, M., Ferracuti, B., & Mazzotti, C. (2003). Non linear bond-slip law for FRP-concrete interface. In *Fibre-Reinforced Polymer Reinforcement for Concrete Structures: (In 2 Volumes)* (pp. 163-172): World Scientific.

Sayed, A. M., Wang, X., & Wu, Z. (2013). Modeling of shear capacity of RC beams strengthened with FRP sheets based on FE simulation. *Journal of Composites for Construction, 17*(5), 687-701.

Shomali, A., Mostofinejad, D., & Esfahani, M. R. (2020). *Effective strain of CFRP in RC beams strengthened in shear with NSM reinforcements.* Paper presented at the Structures.

Smith, S. T., Otoom, O., & Foster, S. (2006). Finite element modelling of RC beams strengthened in shear with FRP composites.

Tan, P. (2014). Ballistic protection performance of curved armor systems with or without debondings/delaminations. *Materials & Design, 64*, 25-34.

Tao, Y., & Chen, J.-F. (2014). Concrete damage plasticity model for modeling FRP-to-concrete bond behavior. *Journal of Composites for Construction, 19*(1), 04014026.

Telford, T. (1993). CEB-FIP Modelcode 1990. *European Design Code, Lausanne, Switzerland*.

Teng, J., Chen, J.-F., Smith, S. T., & Lam, L. (2002a). *FRP: strengthened RC structures*.

Teng, J., Chen, J., Smith, S., & Lam, L. (2002b). FRP strengthened RC structures John Willey and Sons Ltd. *Chichester England*.

Triantafillou, T. C. (1998). Shear strengthening of reinforced concrete beams using epoxy-bonded FRP composites. *ACI structural journal, 95*, 107-115.

Triantafillou, T. C., & Antonopoulos, C. P. (2000). Design of concrete flexural members strengthened in shear with FRP. *Journal of Composites for Construction, 4*(4), 198-205.

Ueda, T., Dai, J., & Sato, Y. (2003). *A nonlinear bond stress-slip relationship for FRP sheet-concrete interface.* Paper presented at the Proc. of international symposium on latest achievement of technology and research on retrofitting concrete structures.

Valerio, P., Ibell, T. J., & Darby, A. P. (2009). Deep embedment of FRP for concrete shear strengthening. *Proceedings of the Institution of Civil Engineers-Structures and Buildings, 162*(5), 311-321.

Vecchio, F., & Bucci, F. (1999). Analysis of repaired reinforced concrete structures. *Journal of Structural Engineering, 125*(6), 644-652.

Wong, R. S., & Vecchio, F. J. (2003). Towards modeling of reinforced concrete members with externally bonded fiber-reinforced polymer composites. *ACI structural journal, 100*(1), 47-55.

You, Y.-M., Ayoub, A., & Belarbi, A. (2011). Three-dimensional nonlinear finite-element analysis of prestressed concrete beams strengthened in shear with FRP composites. *Journal of Composites for Construction, 15*(6), 896-907.